IMPROVING LAND SURFACE MODELING USING SATELLITE AND FIELD OBSERVATION DATA FOR A METEOROLOGY AND AIR QUALITY MODELING SYSTEM

Limei Ran

A dissertation submitted to the faculty of the University of North Carolina at Chapel Hill in partial fulfillment of the requirements for the degree of Doctor of Philosophy in the Curriculum for the Environment and Ecology.

Chapel Hill
2015

Approved by:

Larry E. Band

Francis S. Binkowski

Adel Hanna

Conghe Song

Jason West

ABSTRACT

LIMEI RAN: Improving Land Surface Modeling Using Satellite and Field Observation Data for a Meteorology and Air Quality Modeling System
(Under the direction of Larry E. Band)

Ingesting MODIS satellite derived leaf area index (LAI), fraction of absorbed photosynthetically active radiation (FPAR), and albedo into the Pleim-Xiu (PX) land surface model (LSM) in the combined meteorology and air quality modeling system WRF/CMAQ, composed of the Weather Research and Forecast (WRF) model and Community Multiscale Air Quality (CMAQ), adds realism to the system especially for vegetation fractional coverage in western drylands because the PX LSM intentionally exaggerates vegetation coverage in these sparsely vegetated areas for more effective soil moisture nudging for surface temperature and water vapor mixing ratio estimations. Initial simulations with realistic MODIS vegetation show mixed results with greater error and bias in daytime temperature and greater high bias for ozone concentrations but reduced error and bias in moisture over the western arid regions. Incorporating yearlong MODIS input into an updated WRF/CMAQ with recent improvements in vegetation, soil, and boundary layer processes results in improved 2 m temperature (*T*) and mixing ratio (*Q*), 10 m wind speed, and surface ozone simulations across the U.S. WRF/CMAQ 12km domain compared to the initial simulations. Yearlong MODIS input helps reduce bias of the 2 m *Q* estimation during the growing season from April to September. Improvements follow the green up in the southeast from April and move towards the west and north through August. A coupled photosynthesis-stomatal conductance model with two-big leaf canopy scaling (PX

PSN) is developed for the PX LSM in a diagnostic box model. The PX PSN shows distinct advantages in simulating latent heat over landscapes with short vegetation such as grassland and cropland. The advanced approach performs exceptionally well in simulating ozone deposition velocity and flux while the current PX approach significantly overestimates.

The future work is to implement the evaluated photosynthesis-based stomatal conductance model into WRF/CMAQ PX LSM with MODIS input. More research should be conducted to evaluate the influence of MODIS albedo with realistic diurnal and seasonable changes on the system. The final goal of this research is to implement and evaluate the impacts of air pollutants such as O_3 on CO_2 assimilation for ecosystem assessments.

To Jonathan, Andre, and Julianne Pleim and my parents Chao Ran and Dazhen Qi

ACKNOWLEDGEMENTS

I have many people to thank for supporting and helping me on this long study and research journey while working at the same time. I am very grateful to my advisor, Larry Band, for his valuable advice and continuous support. My committee has been helpful and supportive on guiding me through the research. Frank Binkowski has always been there to help and I learnt a lot not only from talking to him routinely but also from many research articles he sent to me related to my research. Adel Hanna is always supportive on my research and encouraged me year after year. Much of my knowledge on photosynthesis modeling is from Conghe Song from whom I took two classes which benefit my last chapter research greatly. I am thankful for his guidance on the photosynthesis research. My understanding on atmosphere chemistry and modeling is attributable to Jason West and it is very rewarding to take his class related to my research.

I am thankful to many research scientists at the U.S. Environmental Protection Agency for their support and help. Robert Gilliam kindly helped me on WRF simulations and input files. My research benefited a lot from his many suggestions on meteorology simulations and evaluations. Christian Hogrefe helped me on 2006 CONUS emission input and CMAQ initial and boundary condition inputs which were used for the AQMEII-2 study. His kindly suggestions and prompt helps on data input files and processing scripts made WRF/CMAQ simulations successful. John Walker kindly provided the measurements with ozone fluxes at Duke Forest Open Field/US-Dk1. Without his ozone flux measurement data, the last chapter

research will not be complete. K. Wyat Appel provided AMET air quality analysis scripts on processing CMAQ output data for evaluation.

I am grateful for the help from Aijun Xiu on WRF data assimilation method and the support from many of my friends who have always been there when I am in need.

My last and most important acknowledgement goes to my family. I am grateful to my husband's unconditional support not only on my research but also around the house. I thank his tireless explanations on the WRF/CMAQ modeling system and flux computation. The love and encouragement from my husband and my children kept me sane when I was busy around my work, research and housework. My parents' support and love are also the key to keep me going over these years in the program without quitting during difficult times. My sister Shunlan kindly took care of my children when there were meetings. I am also thankful for the support from my sister Lijun for taking care of my children when they were young. I am grateful to the support and help from my late father-in-law. He provided us so many wonderful meals at Carolina Meadows when we were busy. None of this would have been possible without the support, patience and love of my family over these years, to whom this dissertation is dedicated.

TABLE OF CONTENTS

LIST OF TABLES

LIST OF FIGURES

LIST OF ABBREVIATIONS

ACM2	Asymmetric Convective Model version 2
AE6	Aerosol 6 module
AMET	Atmospheric Model Evaluation Tool
APAR	Absorbed photosynthetically active radiation
AQ	Air quality
AQS	Air Quality System
AQMEII	Air Quality Model Evaluation International Initiative
ASOS	Automated Surface Observing System
AZ	Arizona
BIAS	Mean bias
BRDF	Bidirectional reflectance distribution function
BWB	the Ball-Woodrow-Berry
C_3	C_3 carbon fixation in photosynthesis
C_4	C_4 carbon fixation in photosynthesis
CA	California
"CAA"	Clean Air Act
CESM	Community Earth System Model
CB05	Carbon Bond mechanism
CLM	Community Land Model
cm	Centimeter
CO	Carbon monoxide
CO_2	Carbon dioxide
CMAQ	Community Multiscale Air Quality

DAMB	Difference of absolute mean biases
DMAE	Difference of mean absolute errors
E, ET	Evapotranspiration
EPA	Environmental Protection Agency
FLUXNET	Flux Network
FPAR	Fraction of absorbed photosynthetically active radiation
g	Grams
GCM	Global climate model
GEOV1	GEOLAND2 Version 1
GHGs	Greenhouse gases
GLASS	Global Land Surface Satellite
GLOBMAP	Global mapping
ha	Hectares
hPA	Hectopascal
IGBP	International Geosphere-Biosphere Programme
ISBA	Interactions Soil Biosphere Atmosphere
JRC-TIP	Joint Research Centre Two-stream Inversion Package
JULES	Joint UK Land Environment Simulator
K	Kevin
KDAG	ASOS site at the Barstow-Daggett airport, CA, US
KF2	Kain–Fritsch 2
kg	Kilograms
KPGA	ASOS site at the Page Municipal Airport, Arizona, US
L2	Level 2
LAADS	Level 1 and Atmosphere Archive and Distribution System

LAI	Leaf area index
LBC	Lateral boundary conditions
LE, LH	Latent heat
LSM	Land surface model
m	Meter
MACC-II	Monitoring Atmospheric Composition and Climate Interim Implementation
MADIS	Meteorological Assimilation Data Ingest System
MAE	Mean absolute error
MB	Mean bias
MCD43A1	MODIS BRDF/Albedo Model Parameters product
MCD43A2	MODIS BRDF/Albedo Quality product
MCD43A3	MODIS Albedo product at 500m resolution
MCIP	Meteorology-Chemistry Interface Processor
mm	Millimetre
MOD15A2GFS	Gap-Filled, smoothed MODIS LAI/FPAR products
MODIS	Moderate Resolution Imaging Spectroradiometer
MOST	Monin-Obukov similarity theory
NACP	North American Carbon Program
NADP	National Atmospheric Deposition Program
NAM	North American Model
λE	Latent heat ($W\ m^{-2}$)
NASA	National Aeronautics and Space Administration
NCAR	National Center for Atmospheric Research
NDVI	Normalized Difference Vegetation Index

netCDF	Network Common Data Form
NH_3	Ammonia
NH_4	Ammonium
NIR	Near infrared radiation
NLCD	National Land Cover Database
NMB	Normalized mean bias
NME	Normalized mean error
NO_2	Nitrogen dioxide
NOAA	Oceanic and Atmospheric Administration
NOx	Nitrogen oxides
O_3	Ozone
OBS	Observation
PAR	Photosynthetically active (visible) radiation
PBL	Planetary boundary layer
PBLH	Planetary boundary layer height
PEP	Phosphoenolpyruvate
PFT	Plant function type
$PM_{2.5}$	Fine particulate matter
ppb	Parts per billion
ppmV	Parts per million by volume
PRISM	Parameter-elevation Relationships on Independent Slopes Model
PX	Pleim-Xiu
PX PSN	Photosynthesis-based stomatal conductance model for the PX LSM
RAMS	Regional Atmospheric Modeling System
RMSE	Root-mean-squared-error

RRTMG	WRF Rapid Radiative Transfer Model for GCMs
SH	Sensible heat
SFDDA	Surface four-dimensional data assimilation
SO_2	Sulfur dioxide
StDev	Standard deviation
SURFRAD	SURFace RADiation Budget Measurement
SW	South west
SZA	Solar zenith angle
μg	Microgram
UK	United Kingdom
U.S.	United States
US-Dk1	U.S. FLUXNET Duke Forest Open Field in North Carolina
US-IB2	U.S. FLUXNET Fermi Prairie in Illinois
US-Ha1	U.S. FLUXNET Harvard Forest in Massachusetts
US-MOz	U.S. FLUXNET Missouri Ozark
US-Ne1	U.S. FLUXNET Mead irrigated maize in Nebraska
US-Ne2	U.S. FLUXNET Mead irrigated rotation in Nebraska
US-Ton	U.S. FLUXNET Tonzi Ranch in California
US-Wrc	U.S. FLUXNET Wind River Field Station in Washington
UV	Ultraviolet
U/V	Wind u (zonal velocity) and v (meridional velocity) components
UTC	Coordinated Universal Time
VF	Vegetation fraction
VOCs	Volatile organic compounds
$W\ m^{-2}$	Watts per square meters

WRF	Weather Research and Forecast
WS	Wind speed
Z	UTC time

LIST OF SYMBOLES

A	Leaf CO_2 assimilation rate (mol CO_2 m^{-2} s^{-1})
A_c	Leaf CO_2 assimilation rate limited by Rubisco (mol CO_2 m^{-2} s^{-1})
A_{cnet}	Net CO_2 assimilation rate at the canopy scale (mol CO_2 m^{-2} s^{-1})
A_e	Leaf CO_2 assimilation rate limited by transport of photosynthetic products for C_3 plants or phosphoenolpyruvate (PEP) carboxylase limitation for C_4 plants (mol CO_2 m^{-2} s^{-1})
A_i	Smoothed minimum of A_c and A_j leaf CO_2 assimilation rate (mol CO_2 m^{-2} s^{-1})
A_j	Leaf CO_2 assimilation rate limited by light (mol CO_2 m^{-2} s^{-1})
α	Constant (set to 1) in surface soil layer temperature T_g computation
α_{BSA}	Black-sky albedo (direct)
α_{BLUE}	Blue-sky albedo (actual)
α_{leaf}	Leaf absorptivity
α_{WSA}	White-sky albedo (diffuse)
A_{net}	Net CO_2 assimilation rate at the leaf scale (mol CO_2 m^{-2} s^{-1})
A_{net_shd}	Net CO_2 assimilation rate at the shaded leaf scale (mol CO_2 m^{-2} s^{-1})
A_{net_sun}	Net CO_2 assimilation rate at the sunlit leaf scale (mol CO_2 m^{-2} s^{-1})
ANIR	Absorbed NIR at the leaf (sunlit or shaded) (W m^{-2})
APAR	Absorbed PAR at the leaf (sunlit or shaded) (W m^{-2})
b	Slope of the retention curve varying with soil texture in soil resistance computation
β	Factor of the volumetric water content of the top soil layer and at field capacity
c_c	CO_2 compensation point in the absence of non-photorespiratory respiration (Pa)

c_h	Volumetric heat capacity (J m^{-3} k^{-1})
c_i	CO_2 partial pressure inside the leaf stomata (Pa)
c_s	CO_2 partial pressure at the leaf surface (Pa)
C_t	Coefficient that is inversely proportional to heat capacity (K m^2 J^{-1})
C_g	C_t for the soil surface in a grid cell (K m^2 J^{-1})
C_v	C_t for vegetation in a grid cell and set to 1.2×10^{-5} (K m^2 J^{-1})
d	Damping depth of the diurnal temperature wave (m)
d_1	Top soil layer thickness which is set to 1.75 cm
D	Diffuse radiation fraction
D_0	Molecular diffusion coefficient of water vapor in the atmosphere and is set to a constant 2.59 × 10-5 (m^2 s^{-1})
D_s	Reduced soil vapor diffusivity soil for soil resistance computation (m^2 s^{-1})
e	Constant 2.71828
E_g	Evaporation from the soil surface (kg m^{-2} s^{-1})
e_i	Saturation vapor pressure (Pa) inside the leaf stomata at the vegetation surface temperature (T_s)
ε	Quantum yield in photosynthesis (mol CO_2 mol^{-1} photon)
ε_j	Computed electron transport quantum use efficiency in photosynthesis (mol CO_2 mol^{-1} photon)
e_s	Vapor pressure at the leaf surface (Pa)
E_{ss}	Evaporation from the bare soil surface (kg m^{-2} s^{-1})
ET_c	*E*vapotranspiration from the canopy (kg m^{-2} s^{-1})
E_{vs}	Evaporation from the vegetation surface (kg m^{-2} s^{-1})
F_1	Fractional degree (0 to 1) of stomatal closure caused by photosynthetically active radiation (*PAR*)

F_2	Fractional degree (0 to 1) of stomatal closure caused by Root-depth (1 m) volumetric soil moisture (w_2)
F_3	Fractional degree (0 to 1) of stomatal closure caused by relative humidity at the leaf surface (RHs)
F_4	Fractional degree (0 to 1) of stomatal closure caused by air temperature in the canopy (T_{ic})
f_{dr}	Dark respiration coefficient which is set as 0.015 for C3 plants and 0.025 for C4 plants following JULES [*Clark et al*., 2011]
f_{iso}, f_{vol}, f_{geo}	MODIS BRDF/albedo anisotropy three parameters (Isotropic, RossThick, LiSparseR)
f_{LW}	Scaling factor of the longwave radiation to the canopy
f_{seas}	Seasonal adjustment factor for LAI and VF
G	Ground heat flux (W m^{-2})
Gc	Canopy stomatal conductance (m s^{-1})
g_0	Minimum leaf stomatal conductance (mol CO_2 m^{-2} s^{-1}). Set 0.01 for C_3 plants and 0.04 for C4 plants.
g_{0iso}, g_{1iso}, g_{2iso}	MODIS BRDF/albedo Isotropic constants
g_{0vol}, g_{1vol}, g_{2vol}	MODIS BRDF/albedo RossThick constants
g_{0geo}, g_{1geo}, g_{2geo}	MODIS BRDF/albedo LiSparseR constants
g_{iso}, g_{vol}, g_{geo}	Computed MODIS BRDF/albedo anisotropy three functions (Isotropic, RossThick, LiSparseR) with solar zenith angle
g_{st}	Leaf stomatal conductance for CO_2 (mol CO_2 m^{-2} s^{-1})
g_{st_shd}	Shaded leaf stomatal conductance for CO_2 (mol CO_2 m^{-2} s^{-1})
g_{st_sun}	Sunlit leaf stomatal conductance for CO_2 (mol CO_2 m^{-2} s^{-1})
g_{stw_sun}	Sunlit leaf stomatal conductance for water vapor (m s^{-1})
G_{st}	Canopy stomatal conductance for water vapor (m s^{-1})
$G(t)$	Surface energy forcing (W m^{-2})

H	Sensible heat flux (W m^{-2})
I_{apar}	Absorbed photosynthetically active radiation (APAR) by the leaf (mol photon m^{-2} s^{-1})
J	Rate of electron transport in photosynthesis (mol electron m^{-2} s^{-1})
J_{max}	Maximum electron transport rate in photosynthesis (mol electron m^{-2} s^{-1})
K_c	Michaelis-Menten constant for CO_2 defined by equation 9 by *Clark et al*. [2011] (Pa)
K_{dif}	Extinction (attenuation) coefficient for diffuse light within the canopy
K_{dir}	Extinction coefficient for direct beam within the canopy
K_n	Foliage nitrogen decay coefficient and defined as 0.17 [*Bonan et al*., 2011]
K_o	Michaelis-Menten constant for O_2 defined by equation 10 by *Clark et al*. [2011] (Pa)
LAI	Leaf area index (m^2 m^{-2})
LAI_{min}	Minimum leaf area index (m^2 m^{-2})
LAI_{max}	Maximum leaf area index (m^2 m^{-2})
LAI_{shd}	LAI for the shaded leaves (m^2 m^{-2})
LAI_{sun}	LAI for the sunlit leaves (m^2 m^{-2})
L_s	Estimated soil dry layer path length (m) in soil resistance computation
LW_{air}	Long wave radiation from air (W m-2)
LW_{canopy}	Long wave radiation from the canopy (W m-2)
LW_{floor}	Long wave radiation from the floor (W m-2)
λ	Latent heat of evaporation (k J kg^{-1})
λ_t	Thermal conductivity (W m^{-2} K^{-1})
λE	Latent heat flux (W m^{-2})
m_g	Plant-type parameter which is 9 for C_3 plants and 4 for C_4 plants
M_i	Estimated daily total flux at day i

NMB	Normalized mean bias
NME	Normalized mean error
O_a	Partial pressure of atmospheric oxygen (Pa)
O_i	Observed daily total flux at day *i*
P_a	Atmospheric pressure (Pa)
PAR	Photosynthetically active radiation (W m^{-2})
π	Pi constant
Q	Mixing ratio (g kg^{-1})
q_a	Water vapor mixing ratio at the lowest atmospheric layer (kg kg^{-1})
$q_s(T_{s\_sun})$	Saturated mixing ratio for water vapor at the sunlit leaf temperature T_{s_sun} (kg kg^{-1})
$q_{sat}(T_s)$	Saturated water vapor mixing ratio (kg kg^{-1}) at the soil surface temperature (T_s)
R_a	Aerodynamic resistance (s m^{-1})
R_{aw}	Equal to $R_a + R_{bw}$ (s m^{-1})
R_{bw}	Quasi-laminar boundary layer resistance for water vapor (s m^{-1})
R_g	Incoming solar radiation at the surface (W m^{-2})
R_{gl}	Limiting factor with 30 (W m-2) for forest types and 100 (W m-2) for other vegetation types in computing F_1
RH_s	Relative humidity at the leaf surface
R_{net}	Net radiation for the sunlit or shaded leaf (W m^{-2})
R_s	Soil resistance (s m^{-1})
ρ_a	Density of dry air (kg m^{-3})
R_{stmin}, R_{stmax}	Minimum and maximum stomatal resistances (s m^{-1})
t	Time step (s)

T	Temperature (K)
T_2	Deep soil layer (1 m) temperature (K)
τ	Diurnal time scale (s)
τ_{dir}	Transmittance of beam radiation for non-horizontal scattering leaves
τ_{dif}	Transmittance for diffuse radiation over the entire upper hemisphere
T_g	Surface soil layer (1 cm) temperature (K)
T_{ic}	Air temperature in the canopy (K)
T_{low}	Lower limit of the optimal temperature range defined for PFT types in JULES [Clark et al., 2011] (°C)
θ_{sun}	Solar zenith angle (radians)
TR_c	Transpiration from the canopy (kg m^{-2} s^{-1})
TR_{c_shd}	Transpiration from the shaded leaf canopy (kg m^{-2} s^{-1})
TR_{c_sun}	Transpiration from the sunlit leaf canopy (kg m^{-2} s^{-1})
T_s	Canopy leaf surface temperature (°C)
T_{ssl}	Soil surface temperature (K)
T_{up}	Upper limit of the optimal temperature range defined for PFT types in JULES [Clark et al., 2011] (°C)
u_*	Friction velocity (m s^{-1})
V_{cmax}	Maximum rate of carboxylation of Rubisco (mol CO_2 m^{-2} s^{-1})
V_{cmax25}	V_{cmax} at 25°C (mol CO_2 m^{-2} s^{-1})
V_{cmax25_0}	V_{cmax25} at the top of the canopy (mol CO_2 m^{-2} s^{-1})
$vegF$	Vegetation fraction for a grid cell
VF_{min}	Minimum vegetation fraction
VF_{max}	Maximum vegetation fraction

w	Parameter which controls the concavity of the curve and is set to 5 for the exponential shape in soil resistance computation
w_2	Root-depth (1 m) volumetric soil moisture ($m^3\ m^{-3}$)
w_{2avl}	Available volumetric soil water content at root depth ($m^3\ m^{-3}$)
$w_{2\ mxav}$	Maximum available volumetric soil water content at root depth ($m^3\ m^{-3}$)
w_{fc}	Volumetric soil water content at field capacity ($m^3\ m^{-3}$)
w_g	Volumetric soil water content of the top soil layer ($m^3\ m^{-3}$)
w_{sat}	Volumetric soil water content at saturation ($m^3\ m^{-3}$)
w_{res}	Volumetric soil residual water content ($m^3\ m^{-3}$)
w_{wlt}	Volumetric soil water content at the wilting point ($m^3\ m^{-3}$)
x	Canopy leaf orientation parameter with 0 for vertical leaves and 1 for spherical leaf orientation (randomly oriented)

CHAPTER 1: INTRODUCTION

1.1 Introduction

The combined meteorology and air quality modeling system composed of the Weather Research and Forecast (WRF) model and Community Multiscale Air Quality (CMAQ) model is an important decision support tool that is used in research and regulatory decisions related to emission, meteorology, climate, and chemical transport around the world. The land surface model (LSM) is an important component in WRF/CMAQ for simulating the exchange of heat, moisture, momentum, and trace atmospheric chemicals between the land surface and the atmosphere. Vegetation transpiration is a crucial component in the surface energy budget and the water and carbon cycles of LSMs. Vegetation is also a source and sink of many atmospheric chemicals such as O_3 and volatile organic compounds (VOCs).

The Pleim-Xiu (PX) LSM is commonly used in retrospective WRF/CMAQ simulations for research and policy making. Different from LSMs in climate earth system models with complex dynamic vegetation processes, the LSM has much simpler vegetation treatment with a big-leaf empirical function stomatal conductance approach to model vegetation transpiration and pollutant deposition. Surface characteristics including vegetation parameters and surface albedo are specified in LSM land use look-up tables and plant phenological dynamics are modeled using simple time and temperature dependent functions. With data assimilation the LSM has demonstrated strong capabilities in modeling the land surface processes for meteorology and air quality modeling. However, with increased needs to conduct year-long retrospective WRF/CMAQ simulations, the LSM clearly show limitations in capturing seasonal landscape

changes (e.g. phenology) and disturbances (e.g. fires, storm damages). In addition, lacking a biochemically-based photosynthesis-conductance scheme could limit not only the model's dynamic responses to environmental conditions such as temperature, air pollutants (e.g. O_3) and CO_2 concentration but also their applications in assessing the coupling effects of air quality and vegetation productivity in changing climate.

1.2 Objective

The objective of this research is to improve land surface processes in retrospective WRF/CMAQ modeling by:

1) Incorporating satellite-derived temporal vegetation and albedo data for faithful surface representation and
2) Advancing the vegetation processes with a biochemically-based photosynthesis-stomatal conductance approach.

The two components of this research are synergistic because accurate vegetation representation is essential for estimating canopy CO_2 assimilation and stomatal conductance using the biochemically-based photosynthesis approach. As WRF/CMAQ is an important decision support tool for mitigating harmful effects of air pollution on human health and ecosystems, improving the tool through development of more advanced science processes and incorporation of satellite observations will have direct benefit to society.

1.3 Method

The PX LSM is routinely selected for retrospective WRF/CMAQ simulations because PX LSM in WRF is designed especially for air quality applications and particularly for use with CMAQ to have consistent LSM and planetary boundary layer (PBL) treatments for meteorology

and atmospheric chemistry. The research focuses on improving the land surface representation and vegetation processes in the PX LSM through the following three incremental studies:

1) Evaluate the sensitivity of WRF/CMAQ with PX LSM to MODIS LAI, FPAR, and albedo,
2) Assess impacts of MODIS input on seasonality during a yearlong simulation using an updated WRF/CMAQ modeling system, and
3) Develop, test, and evaluate a coupled photosynthesis-based stomatal conductance approach in PX LSM to advance the vegetation processes in WRF/CMAQ with direct connection to CO_2 level and vegetation productivity.

The science questions to be addressed by this research are:

1) How well does current WRF/CMAQ with PX LSM represent vegetation and surface albedo?
2) How does the WRF/CMAQ with PX LSM respond to the more realistic surface representation from MODIS input?
3) Can the WRF/CMAQ model be modified to produce improved results when using the MODIS input?
4) Can phenology from MODIS input help improve multi-seasonal WRF/CMAQ simulations?
5) Can a coupled photosynthesis-stomatal conductance approach perform as well as the PX Jarvis stomatal conductance approach?
6) Does the photosynthesis-based approach have advantages in modeling latent heat and ozone fluxes in comparison with the current approach?

The three incremental studies are presented in chapters 2, 3, and 4 in sequence as independent papers. Research summary, future work and significance are presented in the last Chapter.

1.4 Expected Results

The research results in an advanced WRF/CMAQ model including MODIS vegetation and albedo input and a coupled photosynthesis and stomatal conductance approach incorporated into the PX LSM. Assimilating MODIS vegetation and albedo into the modeling system can provide up-to-date landscape information with more accurate phenology and disturbance representation. The photosynthesis-based stomatal conductance approach provides responses of C_3 and C_4 plants to environmental conditions through biochemically-based processes associated with CO_2 assimilation. The realistic surface representation from satellite observations and improved vegetation processes likely improve surface flux estimation and reduce overall uncertainty in WRF/CMAQ modeling for scientific and regulatory studies.

CHAPTER 2: SENSITIVITY OF THE WEATHER RESEARCH AND FORECAST/COMMUNITY MULTISCALE AIR QUALITY MODELING SYSTEM TO MODIS LAI, FPAR, AND ALBEDO[1]

Abstract

This study aims to improve land surface processes in a retrospective meteorology and air quality modeling system through the use of Moderate Resolution Imaging Spectroradiometer (MODIS) vegetation and albedo products for more realistic vegetation and surface representation. MODIS leaf area index (LAI), fraction of absorbed photosynthetically active radiation (FPAR), and albedo are incorporated into the Pleim-Xiu land surface model (PX LSM) used in a combined meteorology and air quality modeling system. The current PX LSM intentionally exaggerates vegetation coverage and LAI in western drylands so that its soil moisture nudging scheme is more effective in simulating surface temperature and mixing ratio. Reduced vegetation coverage from the PX LSM with MODIS input results in hotter and dryer daytime conditions with reduced ozone dry deposition velocities in much of western North America. Evaluations of the new system indicate greater error and bias in temperature, but reduced error and bias in moisture with the MODIS vegetation input. Hotter daytime temperatures and reduced dry deposition result in greater ozone concentrations in the western arid regions even with deeper boundary layer depths. MODIS albedo has much less impact on the meteorology simulations than MODIS LAI and FPAR. The MODIS vegetation and albedo input does not

[1] This chapter previously appeared as an article in the Journal of Geophysical Research: Atmospheres. The original citation is as follows: Ran, L., R. Gilliam, F. S. Binkowski, A. Xiu, J. Pleim, and L. Band (2015), "Sensitivity of the Weather Research and Forecast/Community Multiscale Air Quality modeling system to MODIS LAI, FPAR, and albedo" Journal of Geophysical Research: Atmospheres, 120, 8491–8511.

have much influence in the east where differences in vegetation and albedo parameters are less extreme. Evaluation results showing increased temperature errors with more accurate representation of vegetation suggests that improvements are needed in the model surface physics, particularly the soil processes in the PX LSM.

2.1 Introduction

Degraded air quality (AQ) is a persistent environmental problem that causes serious health, ecological, and climate consequences (e.g. mortality, eutrophication, biodiversity loss, climate forcing). To improve AQ and mitigate the deleterious effects on human health, ecosystems and climate, policy makers and scientists rely on comprehensive computer modeling systems that simulate emissions, transport, chemistry, and deposition of air pollutants to design emission control strategies for achieving healthy sustainable AQ [*Cohan et al.*, 2007]. The combined meteorology and air quality modeling system WRF/CMAQ - composed of the National Center for Atmospheric Research (NCAR) Weather Research and Forecast (WRF) model [*Skamarock et al.*, 2008] and the United States (US) Environmental Protection Agency (EPA) Community Multiscale Air Quality (CMAQ) model [*Byun and Schere*, 2006] is an important decision support tool that is used to help understand the chemical and physical processes involved in AQ degradation and to develop policy to mitigate harmful effects of air pollution on human health and the environment around the world [*Isakov et al.*, 2007; *Wang et al.*, 2010; *Compton et al.*, 2011]. Improving spatial and temporal distributions of modeled air pollutant concentrations and deposition, particularly O_3, $PM_{2.5}$, and NH_4, will help reduce the uncertainties involved in quantifying risk assessment to human health and the environment. Despite significant advances in the modeling system over the past ten years, there are still many uncertainties in the system [*Foley et al.*, 2010; *Appel et al.* 2011]. Many factors including

emissions, transport, photolysis rates, photochemistry, and land surface exchange may contribute to errors in the current modeling system. Our research focuses on improving land surface model (LSM) processes in the WRF/CMAQ, which includes both meteorological (heat, moisture, and momentum) and chemical (dry deposition and bi-directional exchange) surface fluxes, through using satellite-derived land surface data.

The two commonly used LSMs for meso-scale WRF meteorology modeling are the Noah [*Chen and Dudhia*, 2001] and PX LSMs [*Pleim and Xiu*, 1995; *Xiu and Pleim*, 2001]. Unlike climate LSMs (e.g. *Oleson et al.*, 2013; *Clark et al.*, 2011) with complex hydrology and dynamic vegetation coupled with climate to model processes over decadal to century future periods, these two LSMs rely heavily on data initialization and assimilation for high accuracy over relative short periods (days to years). Thus, both the LSMs have simple canopy treatments with a big-leaf empirical function stomatal conductance following the approach described by *Noilhan and Planton* [1989] as well as simple soil hydrology and snow processes. When applied retrospectively for long term simulations, such as for full years, accurate Noah WRF simulations rely on frequent (e.g. every 2-5 days) re-start of simulations with re-initialized soil conditions [e.g. *Hogrefe et al.*, 2014] while the PX LSM uses continuous data assimilation for dynamic nudging of soil moisture [*Pleim and Xiu*, 2003] and temperature [*Pleim and Gilliam*, 2009] to optimize surface fluxes. The PX LSM is mainly designed for air quality simulations using the WRF/CMAQ system where the WRF LSM parameters (e.g. stomatal and aerodynamic resistances) are consistently used in the AQ dry deposition model.

WRF/CMAQ with the PX LSM scheme has been routinely used to retrospectively simulate for months to years continuously without re-initialization using the indirect soil moisture and temperature nudging schemes that leverages re-analysis fields [*Appel et al.*, 2011;

Rogers et al., 2013; *Hogrefe et al.*, 2014]. At the start of an extended run, the soil moisture fields can be very quickly and effectively spun up from simple generic initializations (e.g. from moisture availability factors by land use type) in about 5 days [*Pleim and Gilliam,* 2009]. To ensure good model performance when using the PX LSM, the key is to configure the WRF simulation with the PX LSM indirect soil moisture and temperature nudging. For example, *Miao et al.* [2007] described a modeling study comparing the Noah and PX LSMs implemented in MM5 and concluded that soil moisture initialization is crucial for the PX LSM performance. However, since they did not use data assimilation in their study the soil moisture nudging scheme was not activated in the simulation with the PX LSM scheme. The PX LSM dynamic continuous data assimilation has the strength to continuously and effectively adjust soil temperature and moisture without re-starting the simulation for reducing error growth in atmospheric variables such as 2 m temperature (T) and mixing ratio (Q) [Pleim and Xiu, 2003; Pleim and Gilliam, 2009]. However, it has the drawback that the assimilation may compensate and mask errors in model physics and it may cause changes in soil moisture when the atmospheric model's temperature and relative humidity errors are not related to surface fluxes. In addition, the PX LSM treats modeling grids with land cover fractions instead of the dominant land cover type in each grid cell used by the WRF Noah LSM. As a result, the PX LSM can take better advantage of high resolution land cover data such as the 500 meter Moderate-resolution Imaging Spectroradiometer (MODIS) data and the 30 meter National Land Cover Database (NLCD) to describe heterogeneous land surface types for model grid cells which are normally coarser than land cover data resolutions [*Ran et al.*, 2010].

Accurate description of surface characteristics is important in meteorology and AQ modeling for simulating the exchange of heat, moisture, momentum, and trace atmospheric

chemicals between the land surface and the atmosphere. Leaf area index (LAI), vegetation fraction (VF), and albedo are important land surface parameters which are typically specified in LSM land-use category look-up tables or derived from monthly averaged satellite vegetation parameters [Hong et al, 2009]. LAI and VF are crucial vegetation parameters used for scaling leaf level fluxes to the canopy level [*Bonan*, 2008] and then to the grid cell level as well as for controlling deposition of various atmospheric gases and particles [*Pleim and Ran*, 2011]. Surface albedo affects not only the surface energy budget and fluxes but also photolysis rates in the air quality model [*Rappenglück et al.*, 2014]. With the availability of many global satellite products at temporal scales ranging from daily to annual, satellite vegetation data and surface products such as MODIS leaf area index (LAI) and albedo have been used to improve LSM performance [*Liang et al.*, 2005; *Alton*, 2009; *Moore et al.*, 2010]. For example, *Moore et al.* [2010] assimilated MODIS dynamic LAI and vegetative fractional cover products into the Regional Atmospheric Modeling System (RAMS) for model simulations of East Africa. Their results show dramatic improvement in land surface temperature simulation both spatially and temporally for most of the year. Other studies [*Buermann et al.*, 2001; *Masson et al.*, 2003; *Rodell et al.*, 2004; *Baker et al.*, 2010; *Lawrence et al.*, 2011; *Barbu et al.*, 2011] have also used satellite derived LAI and vegetation index in LSMs for global and mesoscale atmospheric modeling. However, for operational retrospective meteorology and air quality WRF/CMAQ simulations LAI, VF, and albedo along with other surface and soil parameters are still specified in the LSM tables with some simple seasonal adjustments [*Pleim and Xiu*, 1995, *Chen and Dudhia*, 2001, *Walko et al.*, 2000, *Xiu and Pleim*, 2001]. For year-long retrospective WRF/CMAQ simulations, these LSMs using simple canopy treatment with table prescribed surface representations from out-of-date land use data [*Ran et al.*, 2010] clearly show limitations

in capturing seasonal landscape changes (e.g. phenology and albedo) and disturbances (e.g. fires, storm damages). Thus, assimilating satellite data derived LAI, VF, and albedo into the WRF/CMAQ simulations can provide more up-to-date, accurate, and detailed landscape information and likely improve model performance.

The objective of this research is to reduce overall error and uncertainty in retrospective WRF/CMAQ simulations by improving LSM processes through using MODIS LAI, FPAR and surface albedo products to better describe spatial and temporal variations in vegetation and land surface. The questions which the papers addresses are: (i) how well does the current WRF/CAMQ with PX LSM represent vegetation and albedo compared with satellite observations, (ii) how does MODIS vegetation and albedo input influence the performance of meteorology, and (iii) how does MODIS vegetation and albedo influence the performance of air quality? This study focuses on WRF/CMAQ meteorology and air quality simulations for the US 12km grid resolution modeling domain over a period from August to September 2006. The LAI, VF, and albedo from the current WRF/CMAQ configuration will be first evaluated against observation data from MODIS products, FLUXNET, and the SURFace RADiation Budget Measurement (SURFRAD) network measurements in Section 2. MODIS data and the methodologies used in processing and the model simulations are presented in Section 3. Simulated meteorology results are compared and evaluated in detail among different simulations with table prescribed surface data and with MODIS inputs against measurement data to demonstrate benefits and issues in Section 4. Some AQ results from CMAQ simulations are also presented in this section. Conclusions and future plans are presented in the last section.

2.2 Evaluation of Current WRF/CMAQ

The limitations of the surface characteristics description in the current WRF/CMAQ system and the possible benefit in using the satellite surface data are demonstrated through comparing LAI, VF, and albedo from 2006 PX LSM WRF/CMAQ simulations over the continental US 12km domain and MODIS surface data with site observations from FLUXNET and SURFRAD. 2006 gap-filled and smoothed MODIS LAI and FPAR data MOD15A2GFS at 1km resolution and every 8 days [*Gao et al.*, 2008; *Myneni et al.*, 2011] from the US North American Carbon Program (NACP) are processed and re-gridded onto the WRF/CMAQ 12km grid cells. LAI FLUXNET measurements [*Baldocchi*, 2008], which are often very limited and generally only available for a few selected days each year, are obtained from three FLUXNET sites (US Ha1 - Harvard Forest in Massachusetts; US-Ne1 - Mead irrigated maize in Nebraska; and US-Ton - Tonzi Ranch in California). LAI data are also extracted from 2006 WRF simulations and gridded MODIS LAI/FPAR data set for these site locations. MODIS albedo product MCD43A3 at 500m resolution and every 8 day (16 days running averages) including the white-sky albedos and the black-sky albedos at local solar noon [*Schaaf et al.*, 2002] are obtained and processed onto the 12km grid domain. Surface radiation measurements are obtained from three SURFRAD sites in Illinois, Montana, and Pennsylvania. Albedo data for the three SURFRAD sites are also extracted from PX LSM WRF and gridded MODIS data.

2.2.1 Leaf Area Index

LAI is a measure of the foliage amount in a plant canopy and it is often defined as the projected or one-sided area of leaves per unit area of ground (m^2 m^{-2}, often goes from 0 to 8). The gridded LAI used in the PX LSM WRF is an averaged LAI value for vegetated fraction of a model cell. Thus, gridded MODIS cell-averaged LAI is divided by gridded MODIS FPAR,

which is used as a surrogate for vegetation cover fraction [Los et al., 2000; Mu et al., 2011], to be consistent with the WRF LAI. LAI from FLUXNET, 2006 PX LSM WRF simulation, and 2006 MODIS for the 12km domain are compared for the three selected FLUXNET sites and the whole 12km domain (figure 2.1). For the Harvard Forest Tower site, the MODIS, FLUXNET, and WRF LAI values match relatively well although the WRF summer peak LAI values are too low and the winter LAI are too high. In the PX LSM, LAI is calculated based on the deep soil temperature (T_2) (average T in 1 m soil layer) and minimum and maximum LAI values (LAI_{min}, LAI_{max}) prescribed for each vegetation type as:

$$f_{seas} = \max\left(1.0 - 0.015626 * (290.0 - T_2)^2, 0.0\right), \quad f_{seas} = 1.0 \text{ if } T_2 \geq 290.0 \tag{2.1}$$

$$LAI = LAI_{\min} + f_{seas}\left(LAI_{\max} - LAI_{\min}\right) \tag{2.2}$$

where f_{seas} is a seasonal adjustment factor when762 m the 1-m soil column is cooler than 290 K. When T_2 is $\geq$ 290 K, the LAI is set to the maximum value. While this computation scheme captures the general seasonal variations in temperate climates, LAI values can fluctuate erroneously for winter days with warm spells, as is evident near the end of year at the Harvard site (see figure 2.1). These issues are exacerbated by the deep soil temperature nudging scheme in the PX LSM that can sometimes cause T_2 to fluctuate in an unrealistic manner. Such spurious variations should be easily resolved with a better seasonal adjustment factor using a running average T_2 value over a period instead of the instantaneous T_2 value.

For the Nebraska maize site, it is clear that MODIS and WRF LAI are too low during the peak growing season. Because PX LSM WRF and MODIS land cover datasets do not distinguish among different crops, average LAI is assigned for the general cropland category. Thus, it is difficult to estimate individual crop LAI using the average prescribed values unless detailed crops are included in the LSM. For the California Tonzi Ranch site which is classified

as Woody Savanna in the MODIS land cover, WRF LAI is clearly too high through most of the year and does not capture the peak greenness as MODIS does in the spring following the rainy winter months followed by the dry summer and fall. However, the MODIS LAI values are higher than FLUXNET LAI possibly partially due to grid cell averaging used for MODIS data.

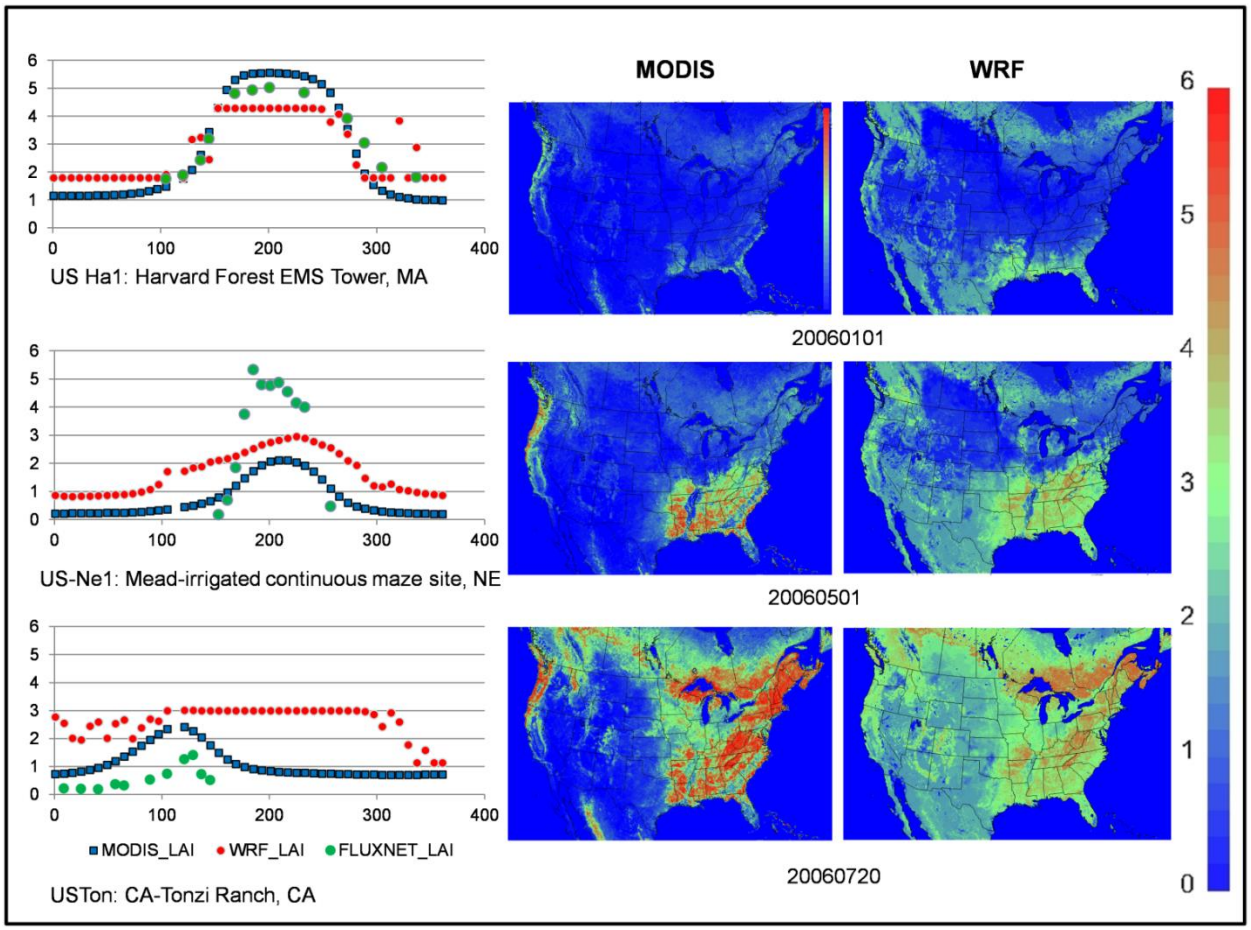

Figure 2.1. PX LSM WRF, MODIS, and FLUNXET LAI comparisons. The LAI graphs on the left have LAI on the vertical axis and day of year with 1 for Jan. 1, 2006 on the horizontal axis.

For the domain-wide comparison, PX LSM WRF LAI does show similar spatial distributions and seasonal changes as MODIS LAI, but with different magnitudes. Broad land use categories with the average minimum and maximum LAI values for vegetation categories used in the PX LSM tend to dampen the extremes of LAI. It is clear that WRF LAI is relatively

high during the cold seasons and low during the peak green summer. WRF LAI is also too high in the west dryland areas and northern boreal regions during the warm seasons. The LAI spatial evaluation points to an additional issue in the PX LSM simple seasonal LAI adjustments. In western dryland regions, LAI is controlled primarily by moisture conditions rather than temperature during summer and autumn seasons. Thus, in addition to the need to use a running average T_2 in adjusting LAI to avoid unphysical short-term fluctuations in LAI, accounting for the effects of drought conditions by including deep soil moisture into the LAI seasonal adjustments in equation 2.1 should produce more realistic LAI in the western drylands. Overall, MODIS LAI does capture seasonal and spatial variation much better than the prescribed WRF LAI, particularly in the north and west regions.

2.2.2 Vegetation Fraction

Vegetation fraction in the PX LSM is prescribed based on the minimum and maximum VF values (VF_{min}, VF_{max}) for each land cover class specified in the LSM landuse lookup tables using the same seasonal adjustment factor as for LAI:

$$VF = VF_{\min} + f_{seas}\left(VF_{\max} - VF_{\min}\right) \tag{2.3}$$

The PX WRF VF and MODIS FPAR used as a surrogate for VF are compared for a typical summer day (08/10/2006) in figure 2.2. In the West and North, PX WRF vegetation fraction is clearly over-estimated compared to MODIS VF particularly in the western dryland areas. The PX LSM scheme was originally designed for the eastern US where there is much more vegetation cover. The PX LSM deep soil moisture nudging scheme computes the nudging strengths from model parameters such as solar radiation, temperature, leaf area, vegetation coverage, and aerodynamic resistance [*Pleim and Xiu*, 2003] rather than from statistically derived functions [*Mahfouf*, 1991; *Bouttier et al.*, 1993; *Douville et al.*, 2000]. Thus, it is most

effective in vegetated areas through its influence on transpiration and surface fluxes. The PX LSM exaggerates VF values for many vegetation categories to allow the soil moisture nudging scheme to be more effective. Although this exaggerated VF helps reduce the model's daytime biases in 2 m *T*, it could have erroneous consequences such as over prediction of moisture fluxes and air humidity as well as over estimates of trace atmospheric chemical surface fluxes related to the vegetation pathway.

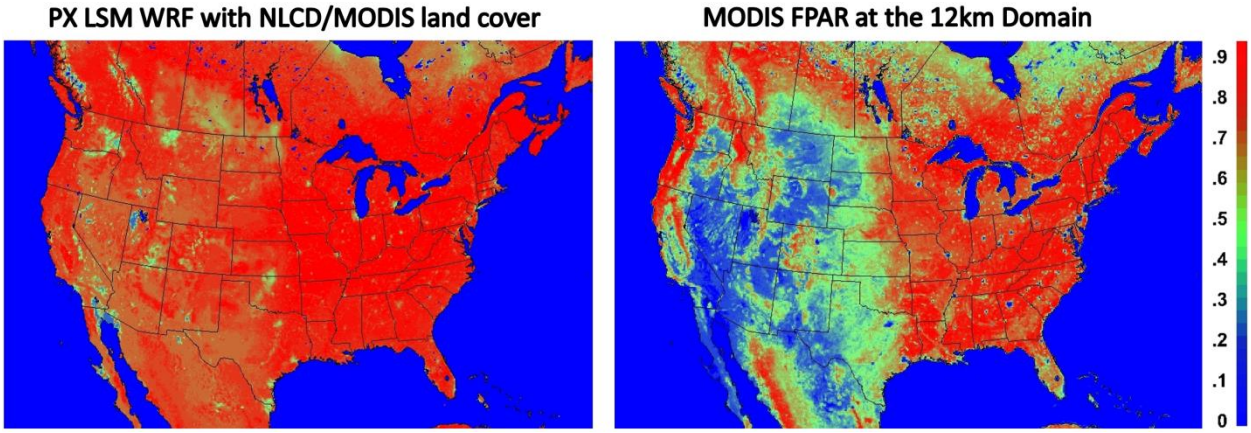

Figure 2.2. PX WRF vegetation cover and MODIS gridded FPAR used as the surrogate of vegetation cover fraction for 2006-08-10.

2.2.3 Albedo

Albedo is an important parameter in meteorology and air quality modeling systems such as the WRF/CMAQ because it affects the surface energy budget, which in turn influences heat and moisture fluxes and the evolution of the planetary boundary layer (PBL). Changing the PBL height (PBLH) will affect air quality due to changes in dilution of air pollutant concentrations near the surface. The impact of changing albedo on the actinic flux in the UV bands is particularly important for photochemical pollutants such as ozone and NO_x. For example, rapid increases in ozone concentration right after the onset of snow cover has been observed in western valleys with abundant NO_x from the rapidly expanding unconventional oil and gas drilling

operations [*Rappenglück et al.*, 2014]. Thus, correctly representing surface albedo is crucial in systems like WRF/CMAQ. Albedo changes diurnally like a "U" shape with the sun zenith angle and seasonally with the sun inclination angle along with changing surface conditions. MODIS combined Terra and Aqua BRDF/Albedo product (MCD43A3) provides two types of albedo around local solar noon: black-sky albedos (α_{BSA}) (directional-hemispherical reflectance - direct) and white-sky albedos (α_{WSA}) (bi-hemispherical reflectance - diffuse) for MODIS 7 bands and three broad bands. The actual albedo, which is also called blue-sky albedo (α_{BLUE}), can be calculated based on the equation derived by *Lewis and Barnsley* [1994] with an assumed constant white-sky albedo at low solar zenith angles (less than 70°-75°) as:

$$\alpha_{BLUE} = \alpha_{BSA}(\theta_{sun})(1-D) + \alpha_{WSA} * D \tag{2.4}$$

where D is the diffuse radiation fraction.

MODIS shortwave black sky and white sky albedo (0.3-5.0μm) is compared with PX WRF and SURFRAD albedo in figure 2.3. The diurnal difference is examined by comparing WRF and SURFRAD albedo values for a winter (01/01/2006) and summer day (07/04/2006). It is clear that WRF albedo is missing the diurnal and seasonal changes which are evident in the SURFRAD measurements. However, at the Montana site, WRF snow assimilation captured the snow cover well with the high albedo similar to the SURFRAD values. But for the Pennsylvania site, WRF albedo values are much lower than the SURFRAD data. Spatial plots of the two days from WRF and MODIS data over the domain show similar patterns. However, MODIS black and white sky albedo values display more variations, particularly for areas in the north and in the west. Using 16-day MODIS albedo composites (with the Julian date in the file name representing the first day of the 16-day period) to compare with the Julian date WRF albedo likely causes some mismatch in the comparison, especially in the northern regions with high

snow albedo for the winter day. Since snow coverage can vary significantly on a daily basis it is more appropriate to use daily snow analyses to define snow coverage for albedo estimation in WRF simulations. Nevertheless, the MODIS albedo excluding the snow coverage areas does capture the heterogeneous surface better in comparison with the albedo calculation in the current PX LSM WRF.

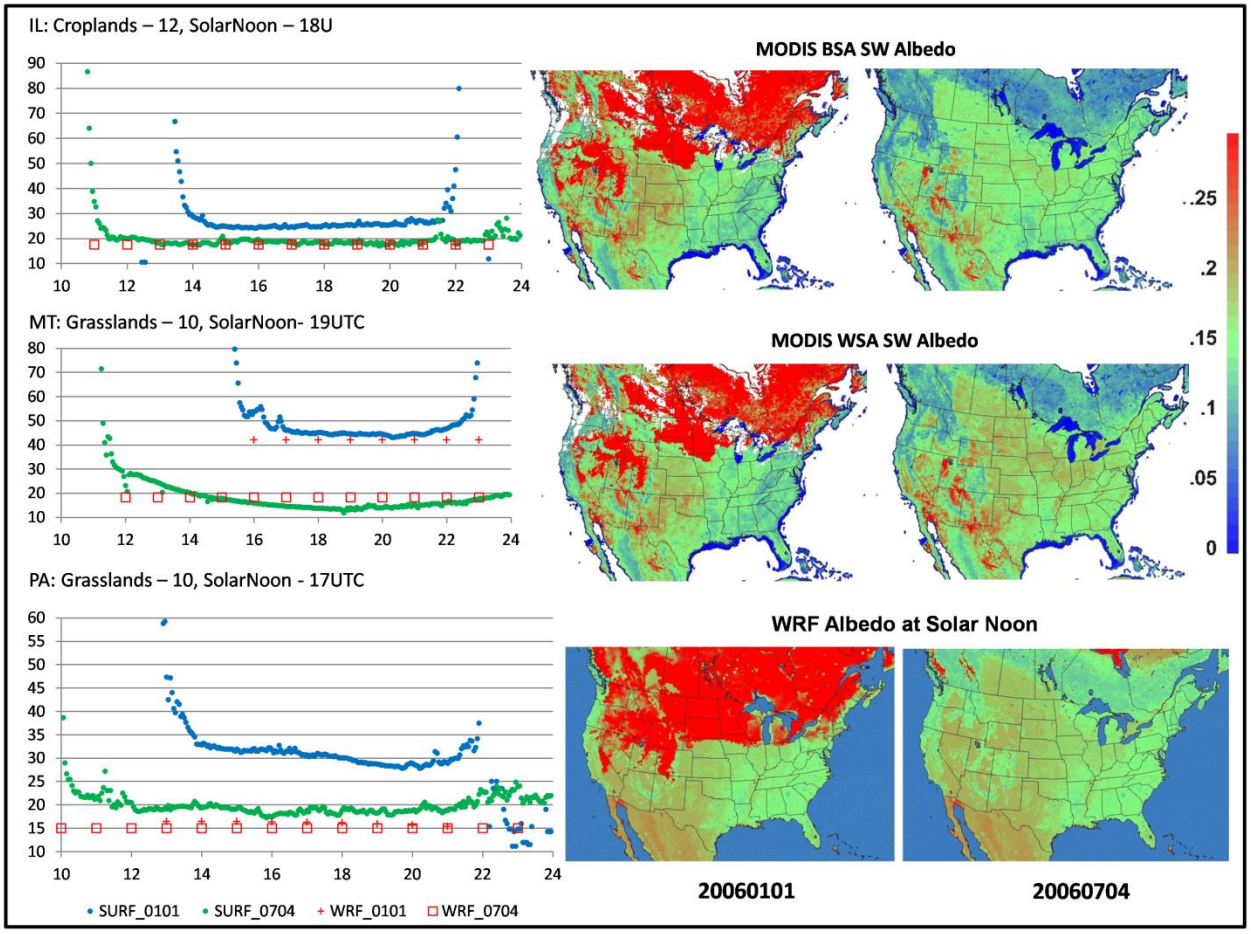

Figure 2.3. PX WRF, SURFRAD, and MODIS albedo comparisons. The albedo graphs on the left have albedo (%) on the vertical axis and local time zone hour of day on the horizontal axis.

2.3 Data and Methods

MODIS LAI, FPAR and albedo data are freely available at the Level 1 and Atmosphere Archive and Distribution System (LAADS) web site from the US National Aeronautics and

Space Administration (NASA). Users can choose the needed data set from several MODIS LAI, FPAR and albedo products which are processed from different satellite platforms (Terra, Aqua or combined), at different resolutions, and for different applications. This section first describes MODIS data selected for this research in detail and methods used to process the data for WRF/CMAQ. Then, it presents the methods used to apply MODIS data in WRF, WRF/CMAQ configurations, and modeling scenario design for evaluation.

2.3.1 MODIS Data

Because MODIS products such as LAI, FPAR and albedo products are derived from surface reflectance measurements, uncertainties exist in these products due to aerosol, cloud, and snow contaminations. For example, the MODIS Collection 4 LAI/FPAR products tend to be overestimated by around 12% based on the study by *Yang et al.* [2006b], which is similar to the conclusion from the evaluation by *Fensholt et al.* [2004] that MODIS LAI is overestimated by around 2 to 15% and FPAR is overestimated by 8 to 20% on average in a semi-arid area. In addition, MODIS LAI could show unrealistic temporal variations during the growing and winter seasons because of cloud/snow contaminations [*Cohen et al.*, 2006]. The MODIS LAI/FPAR algorithm contains a radiative transfer algorithm for the best quality estimates and a back-up empirical algorithm based on NDVI(Normalized Difference Vegetation Index)-LAI relationships with poor quality for high LAI (saturation) or areas with cloud, aerosol, or snow contamination [*Myneni et al.*, 1997; *Yang et al.*, 2006a]. The overestimation of the product is mostly caused by misclassified biomes and higher uncertainties in the back-up algorithm. The current release of MODIS Collection 5 LAI/FPAR products has significant refinements to the algorithm, particularly for woody vegetation - broadleaf and needle leaf forests which are subdivided into deciduous and evergreen subclasses [*Myneni et al.*, 2011]. *Fang et al.* [2013] described MODIS

LAI and four new global LAI products (GEOV1, GLASS, GLOBMAP, and JRC-TIP) in detail and compared and analyzed them at 0.01 degree resolution at a monthly time step for the 2003 to 2010 period. By analyzing the product's quantitative quality indicators, they found that MODIS LAI has the lowest average uncertainty and relative uncertainty (0.17, 11.5%) among the five products. For applying MODIS LAI/FPAR data in land surface processes, the data often need to be gap-filled and smoothed for improving spatial and temporal continuity and consistency. The NACP gap-filled and smoothed MODIS Collection 5 LAI and FPAR data (MOD15A2GFS), which are also used in the WRF/CMAQ LAI and VF evaluation in the previous section, are selected for WRF/CMAQ simulations.

MODIS albedo products are derived using a kernel-based semi-empirical bidirectional reflectance distribution function (BRDF) model to characterize isotropic, volumetric and geometric scattering [*Wanner et al.*, 1995*; Lucht et al.*, 2000; *Schaaf et al.*, 2002, 2011]. MODIS BRDF/albedo parameter products contain three parameters corresponding to the weights for isotropic kernel, volumetric kernel and geometric kernel. MCD43A1 MODIS BRDF/albedo parameter product and corresponding MCD43A2 MODIS BRDF/albedo quality product are generated every 8 days at 500m resolution with the following 16 days of MODIS surface reflectance input. While MODIS albedo products at local solar noon are used in the previous section albedo evaluation, MODIS BRDF/albedo parameters retrieved are more appropriate for WRF/CMAQ simulations with changing solar zenith angle (SZA, θ_{sun}). The MODIS product can be used to characterize the actual albedo at a location throughout the better part of the diurnal cycle with some confidence based on the study by *Liu et al.* [2009]. Although many surface conditions (such as soil conditions, canopy, surface heterogeneity, and spatial scale) affect surface albedo; direct-beam albedo may be predominately influenced by SZA [*Yang et al.*,

2008]. The three MODIS BRDF/albedo parameters (f_{iso}, f_{vol}, f_{geo}) are used to compute both black-sky albedo and white-sky albedo using simple polynomial [*Lucht et al.*, 2000; *Schaaf et al.*, 2011] equations as:

$$\alpha_{BSA}(\theta_{sun},\lambda) = f_{iso}(\lambda)g_{iso}(\theta_{sun}) + f_{vol}(\lambda)g_{vol}(\theta_{sun}) + f_{geo}(\lambda)g_{geo}(\theta_{sun}) \quad (2.5)$$

$$\alpha_{WSA}(\theta_{sun},\lambda) = f_{iso}(\lambda)g_{3iso} + f_{vol}(\lambda)g_{3vol} + f_{geo}(\lambda)g_{3geo} \quad (2.6)$$

$$g_{iso}(\theta_{sun}) = g_{0iso} + g_{1iso}\theta_{sun}^2 + g_{2iso}\theta_{sun}^3 \quad (2.7)$$

$$g_{vol}(\theta_{sun}) = g_{0vol} + g_{1vol}\theta_{sun}^2 + g_{2vol}\theta_{sun}^3 \quad (2.8)$$

$$g_{geo}(\theta_{sun}) = g_{0geo} + g_{1geo}\theta_{sun}^2 + g_{2geo}\theta_{sun}^3 \quad (2.9)$$

where g_{0-2iso}, g_{0-2vol}, and g_{0-2geo} are constant and the blue sky albedo can be computed based on equation 2.4. MODIS BRDF/albedo parameters are available for MODIS seven spectral bands as well as for three broad bands (0.3-0.7μm, 0.7-5.0μm, and 0.3-5.0μm). For this study, processed MODIS BRDF/albedo parameters for the shortwave (0.3-5.0μm) are used for computing black sky, white sky, and blue sky albedo.

2006 MODIS LAI and FPAR products as well as MODIS BRDF/albedo parameter MCD43A1 and quality MCD43A2 products are processed, projected, and averaged over the WRF/CMAQ model 12km grid cells. The generated temporal data are stored in a netCDF file for WRF simulations. MODIS albedo products over snow are not reliable because it is often difficult to discriminate between snow and clouds which have similar visible spectral reflectance features [*Gao et al.*, 2011] and also the 16-day composite product can easily miss ephemeral snow on the ground. Thus, the BRDF/albedo quality product is used to filter out snow cover cells in averaging MODIS albedo parameters for WRF/CMAQ modeling grid cell parameters.

2.3.2 WRF/CMAQ Modeling

WRF version 3.4 is used for this study and many WRF modules are modified for ingesting gridded MODIS LAI, FPAR, and three albedo parameter data through the WRF simulation namelist control. The average MODIS LAI over a modeling grid cell is divided by FPAR to represent the LAI of the vegetated portion of the model grid cell and MODIS FPAR is used directly as VF. Black, white, and blue sky albedos are computed based on equations 2.4-2.6 when SZA is less or equal to 70 degrees. When SZA is greater than 70 degrees, albedo is computed using 70-degree SZA because the MODIS data are less reliable at SZA above 70. WRF snow albedo is computed based on the daily snow analyses and weighted in the final albedo computation based on the fractional snow coverage. While the computed blue sky albedo is used in the PX LSM for surface energy budgeting, black sky and white sky albedo values are passed to the WRF Rapid Radiative Transfer Model for GCMs (RRTMG) radiation model [*Iacono et al*., 2008] for the short wave (SW) and long wave (LW) radiation computation.

The WRF modeling system is prepared and configured in the same way as described by *Gilliam and Pleim* [2010]. It is important to note that the PX LSM scheme has the regular nudging scheme turned on for analysis nudging (U/V wind, *T*, *Q*) above the PBL and for indirect soil moisture and T nudging from accurate 2 m *T* and *Q* analyses or re-analyses in the surface four-dimensional data assimilation input file (SFDDA). Other important WRF physics options include the Asymmetric Convective Model version 2 (ACM2), for PBL [*Pleim*, 2007a, 2007b], the Morrison double-moment cloud microphysics scheme [*Morrison et al.*, 2009], and version 2 of the Kain–Fritsch (KF2) cumulus parameterization [*Kain*, 2004]. The 12-km North American Model (NAM) data are used as lateral boundary conditions for the WRF simulation. The Meteorology-Chemistry Interface Processor (MCIP) [*Otte and Pleim*, 2010] version 4.1.3 is used to process the WRF output for CMAQ simulations. CMAQ version 5.0.2 and its configuration

used for the study is described in detail by *Hogrefe et al.* [2014] for the second phase of the Air Quality Model Evaluation International Initiative (AQMEII) study with the difference being that the offline version of CMAQ is used in this research. The CMAQ model uses the Carbon Bond mechanism CB05 for gas-phase chemistry, aerosol 6 module (AE6), and in-line point source, biogenic and dust emissions. The CMAQ model uses the same ACM2 PBL scheme as the WRF simulations for consistent PBL evolution, which is crucial for modeling boundary layer mixings of air pollutant concentrations. The AQ simulation uses 2006 CMAQ-ready emission data which are generated for the AQMEII Phase 2 study and are described in detail by *Pouliot et al.* [2014]. The chemical boundary conditions are based on the Monitoring Atmospheric Composition and Climate Interim Implementation (MACC-II) as described by *Innes et al.* [2013].

The WRF simulations are conducted over the 40-day period from August 1 to September 9, 2006 and the CMAQ simulations are conducted for the 30 days from August 1 to August 30 over the North America 12km domain. The 12-km domain covers the conterminous US, southern Canada, and northern Mexico with 299 by 459 grid cells and 34 vertical levels extending from the surface to the 50-hPA level. The land use data used are processed from 2006 NLCD at 30m resolution for the US and MODIS land cover data at 500m resolution for the areas outside the US using the Spatial Allocator Raster Tools [Ran and Hanna, 2014]. For the base model albedo is specified by the land use category lookup table along with the maximum and minimum LAI and VF used in equations 2.2 and 2.3. The following four WRF simulation scenarios and two CMAQ simulation scenarios are conducted for evaluation:

Four WRF scenarios:

1. Base case: standard WRF
2. LAI-FPAR case: modified WRF with MODIS LAI and FPAR input

3. Albedo case: modified WRF with MODIS BRDF/albedo parameter input
4. LAI-FPAR-albedo case: modified WRF with MODIS LAI, FPAR, albedo parameter input

Two CMAQ scenarios:

1. Base case: CMAQ with WRF Base case meteorology
2. LAI-FPAR-albedo case: CMAQ with WRF LAI-FPAR-albedo case meteorology

Pair-comparison, statistical evaluation, and visualization of WRF/CMAQ simulation performance compared to observations are conducted using the Atmospheric Model Evaluation Tool (AMET) [*Gilliam et al.* 2005, *Appel et al.*, 2010]. The Meteorological Assimilation Data Ingest System (MADIS) observation data from the US National Oceanic and Atmospheric Administration (NOAA) are used for meteorology comparison. The US EPA Air Quality System (AQS), the National Atmospheric Deposition Program (NADP), and other air quality network data are used for AQ evaluation. In addition, surface flux measurements from FLUXNET and precipitation analysis data from the Parameter-elevation Relationships on Independent Slopes Model (PRISM) [Daly et al., 2008] are also used in evaluating the simulation results. Similar to many other WRF/CMAQ studies [e.g. *Gilliam and Pleim,* 2010; *Appel et al.* 2011; *Hogrefe et al.*, 2014], interpolation or any other types of adjustments are not applied in the evaluation to account for the difference between the site observations and the model estimates at the grid cell level.

2.4 Results and Analysis

Evaluations of meteorology simulations and their impacts on air quality have been the focus of many studies [*Gego et al*., 2005*; Gilliam et al*., 2006; *Vautard et al*., 2012]. Grid cell volume-averaged results of temperature, moisture, wind speed, and precipitation from

meteorology simulations are often compared with surface-based point measurements. Statistics such as mean bias (BIAS), mean absolute error (MAE), root-mean-squared-error (RMSE), standard deviation (StDev) and index of agreement for the model-to-observation differences are often computed for model grids with surface measurements to evaluate model performance. For this paper BIAS in space over a period will be mainly used to evaluate how the model performs spatially with the input of MODIS data. Overall domain-wide evaluation statistics (BIAS, MAE, and StDev) for 2 m *T* and *Q* and 10-m wind speed for the four meteorology scenarios are similar and well within typical model performance benchmarks [e.g. *Gilliam et al.*, 2006]. The 10-m wind evaluation statistics are very much the same for the four scenarios. Thus, surface temperature and mixing ratio, surface fluxes of sensible and latent heat, O3 concentration and dry deposition velocity, and NH4 wet deposition are the foci in the following comparisons and evaluation.

2.4.1 Surface T, Q and O3

Figure 2.4 shows the 2 m *T* and *Q* statistical metrics of BIAS, MAE, and StDev from the base case and LAI-FPAR case versus observation range. The statistical metrics are computed using all MADIS sites within the domain and their matched-grid simulated meteorology over the period from Aug. 10 – Sept. 9, 2006. The first 9 days of simulation are excluded from the analysis because soil moisture fields need to be sufficiently spun up from the simple generic initializations. The 2 m *T* StDev is fairly constant at around 2 K over the observed temperature range for both cases while the MAE is below 2 K for all but the lowest end of the observed temperature range. The main differences between the 2 cases are the reduced error and cold bias at the high end of the observed 2 m *T* range for the MODIS LAI-FPAR run and the practical elimination of the wet bias in 2 m *Q* below 14 (g kg^{-1}).

Figure 2.5 shows differences in 2 m *T* (top) and *Q* (bottom) biases between the LAI-FPAR case and the base case for all MADIS observation sites averaged over Aug. 10 – Sept. 9, 2006. The absolute value of the bias is less for the LAI-FPAR case at all sites where the bias difference is negative and greater for all sites with positive differences. Thus, these statistics do not indicate which case is hotter or wetter at each site but rather which has less absolute bias. However, in this analysis it is clear that the LAI-FPAR case which has much lower VF than the base case in the drylands of the west is generally hotter and dryer in these areas because more surface radiation is partitioned into SH and less into LE resulting in higher 2 m *T* and lower 2 m *Q*. Thus, in the areas where the LAI-FPAR case is hotter and dryer, the warm bias is increased but wet bias decreased compared to the base case. This suggests that the exaggerated VF and LAI in the western drylands for the base case tends to reduce an inherent tendency toward hot biases in the 2 m *T* at the expense of increased wet biases in the 2 m *Q*. Thus, using more accurate vegetation descriptions, such as from MODIS data, gives mixed results compared to the base case with greater warm bias in 2 m *T* but reduced bias in 2 m *Q*.

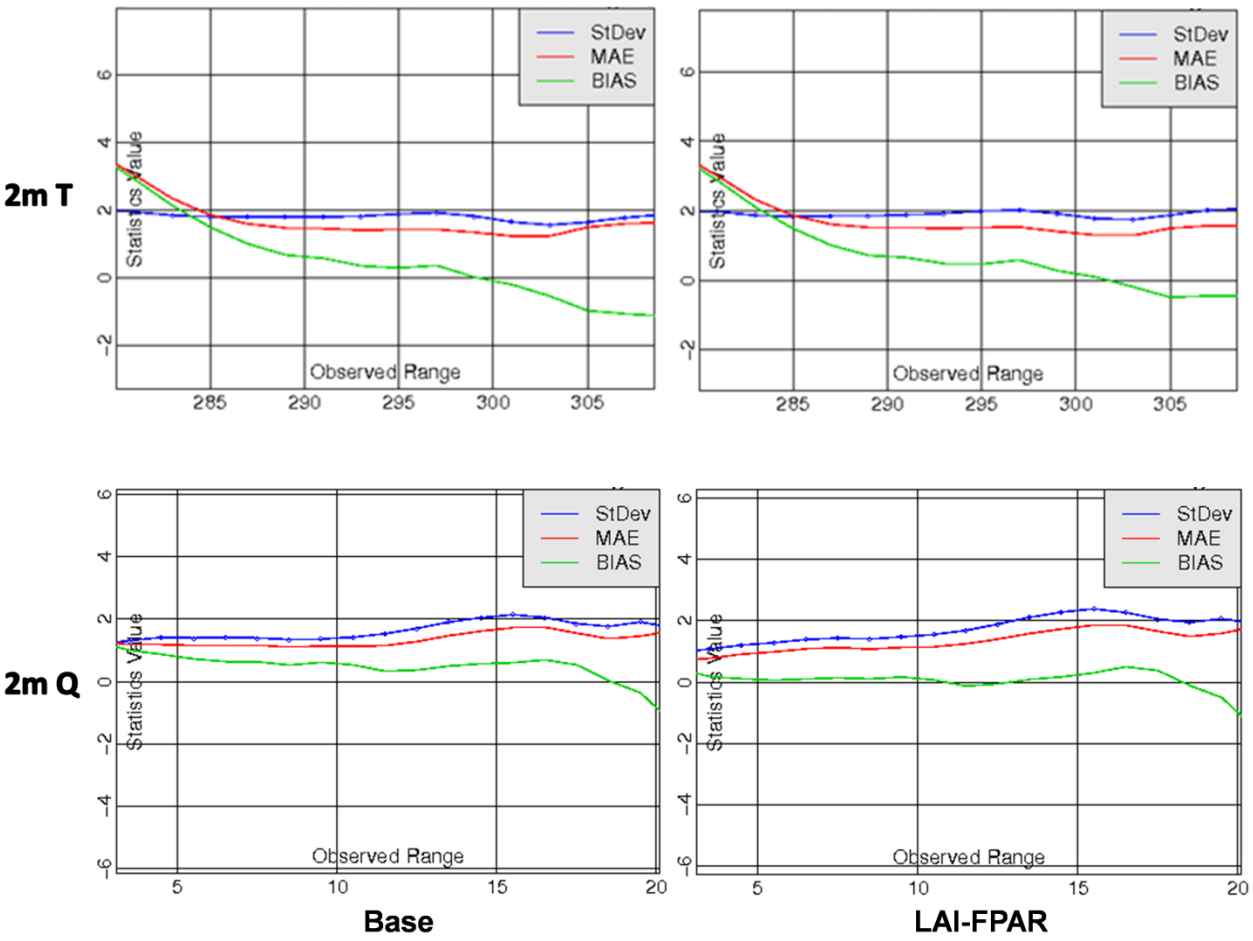

Figure 2.4. Statistical metrics (y axis) vs. observation range (x axis) for 2 m *T* (K) and Q (g kg^{-1}) over the period from Aug. 10 – Sept. 9, 2006. The top plots are for 2 m *T* and the bottom for 2 m *Q*. The two plots on the left are from the base case meteorology and the plots on the right are from the LAI-FPAR case.

The plots from the albedo case and LAI-FPAR-albedo case are not included in figure 2.4 because the albedo case 2 m *T* and Q plots are very similar to the base case plots and the LAI-FPAR-albedo case plots are similar to the LAI-FPAR case plots. On the average for this summer period simulation, albedo has little impacts on the system performance. This is likely attributable to the similarity of the MODIS albedo to the base albedo prescribed by the land use lookup table during the summer season (see figure 2.3). However, during the winter and

especially the spring and fall transitional seasons, the MODIS albedo differs from the base albedo to a much greater degree. This will be investigated further in future work.

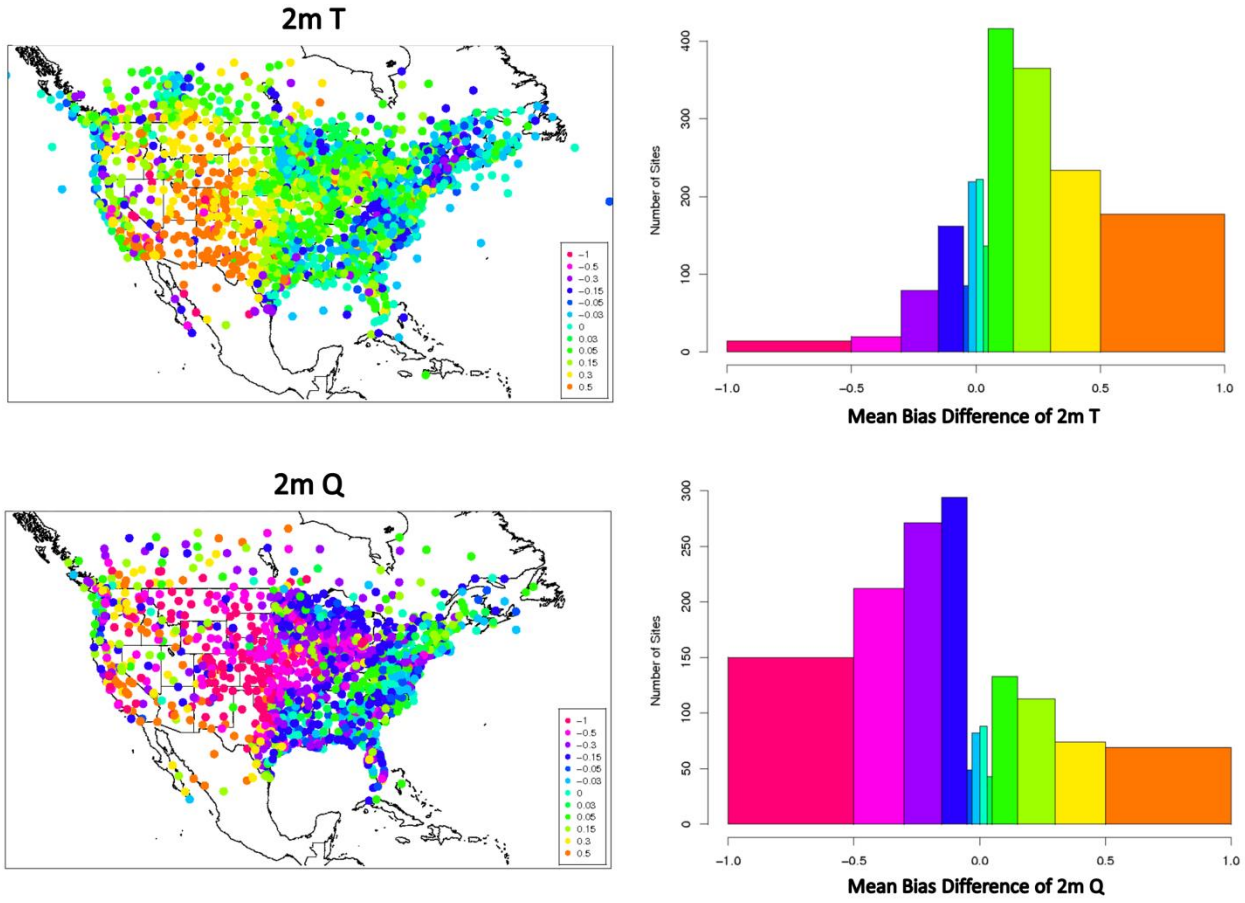

Figure 2.5. Mean Bias Difference (LAI-FPAR Case – Base Case) spatial and histogram plots over the period from Aug. 10 – Sept. 9, 2006. The top row is for 2 m *T* (K) and the bottom row is for Q(g kg^{-1}).

The differences of 2 m *T* and *Q* in the two cases are further investigated through comparisons against two ASOS observation sites that are typical of very dry climates in the US southwest over an 11-day period (figures 2.6 and 2.7). The KDAG site is located at Barstow Daggett County Airport, California, which is in a sparsely vegetated dry desert landscape. The 2 m *Q* from the LAI-FPAR case is reduced in comparison with the base case and closer to the

measurements for most hours after Aug. 20. For 2 m *T*, the LAI-FPAR case performs much better compared to measurements for the peak 2 m *T* than the base case for most of the days . Thus, in general, reduced VF in the LAI-FPAR case causes reduced 2 m *Q* and increased 2 m *T*. Note that modeled daily minimum 2 m *T* is too warm for both cases which results in average daily biases that are lower for the base case even though the LAI-FPAR shows significantly better daily maximum 2 m *T*.

The KPGA site is located at the Page Municipal Airport, Arizona where to the east is sparsely vegetated desert land, to the west is the small city of Page, AZ, and to the north is Lake Powell that extends into Utah. Similar to the KDAG site, the LAI-FPAR case has much lower 2 m *Q* than the base case. From August 18 to 23, the modeled 2 m *Q* in the LAI-FPAR case matches the observations quite well while the base case is much wetter. At this site, the LAI-FPAR case has the peak 2 m *T* consistently too high and the base case has the peak 2 m *T* matching the observations well. Unlike the KDAG site, daily minimum 2 m *T* agrees well with the measurements for both cases. Thus, the smaller daily average 2 m *T* bias for the base case reflects a more accurate simulation throughout the diurnal cycle than the LAI-FPAR case. In conclusion, the LAI-FPAR case reduces the wet bias in the base case at both sites; but it reduces cool bias in the peak 2 m *T* for one site and causes warm bias in the peak 2 m *T* for another site.

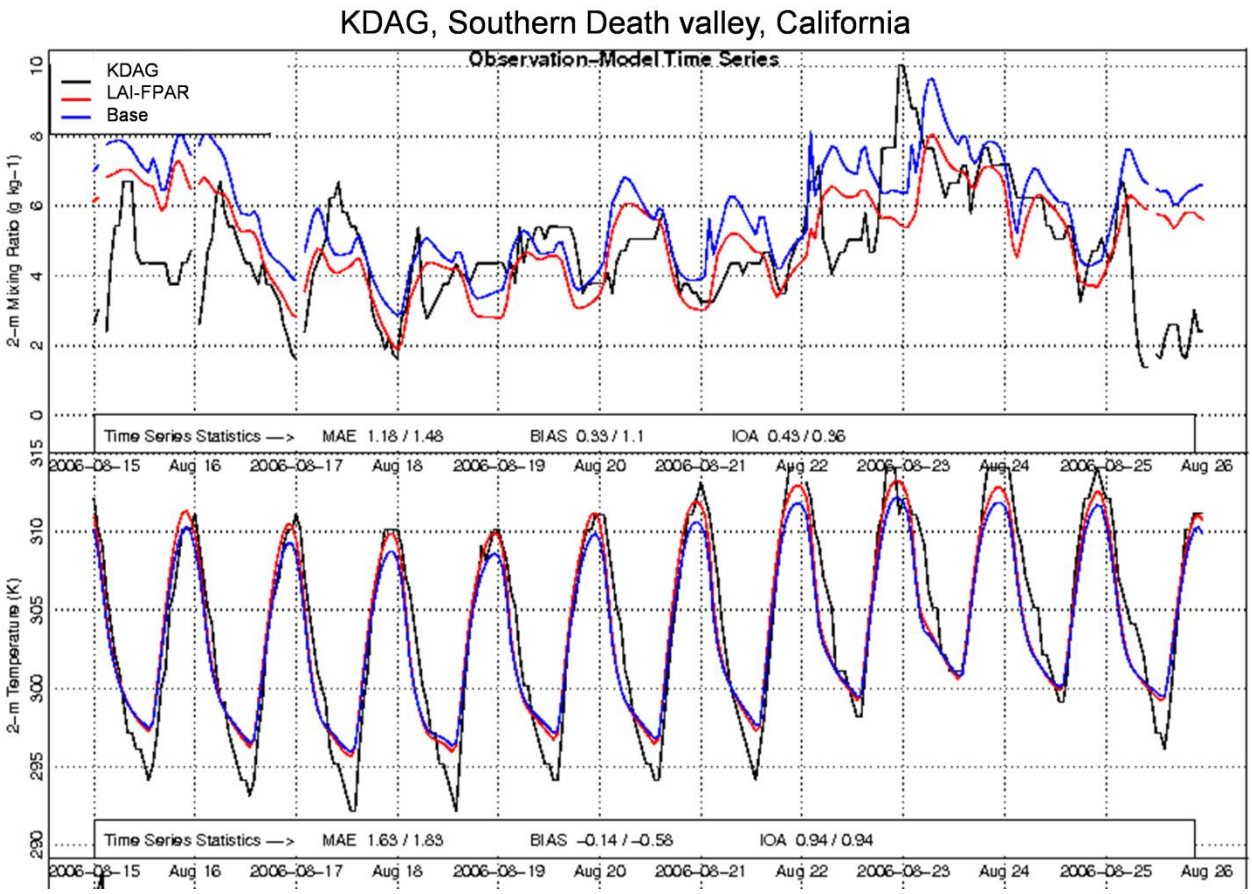

Figure 2.6. ASOS measurement site 2 m *T* (K) and Q (g kg^{-1}) time series comparison for the period from Aug. 15-25, 2006. KDAG site is in black line, LAI-FPAR case is in red line, and base case is in blue line. Site grid cell has VF 0.669 and LAI 2.282 for the base case and VF 0.186 and LAI 1.258 for the LAI-FPAR case.

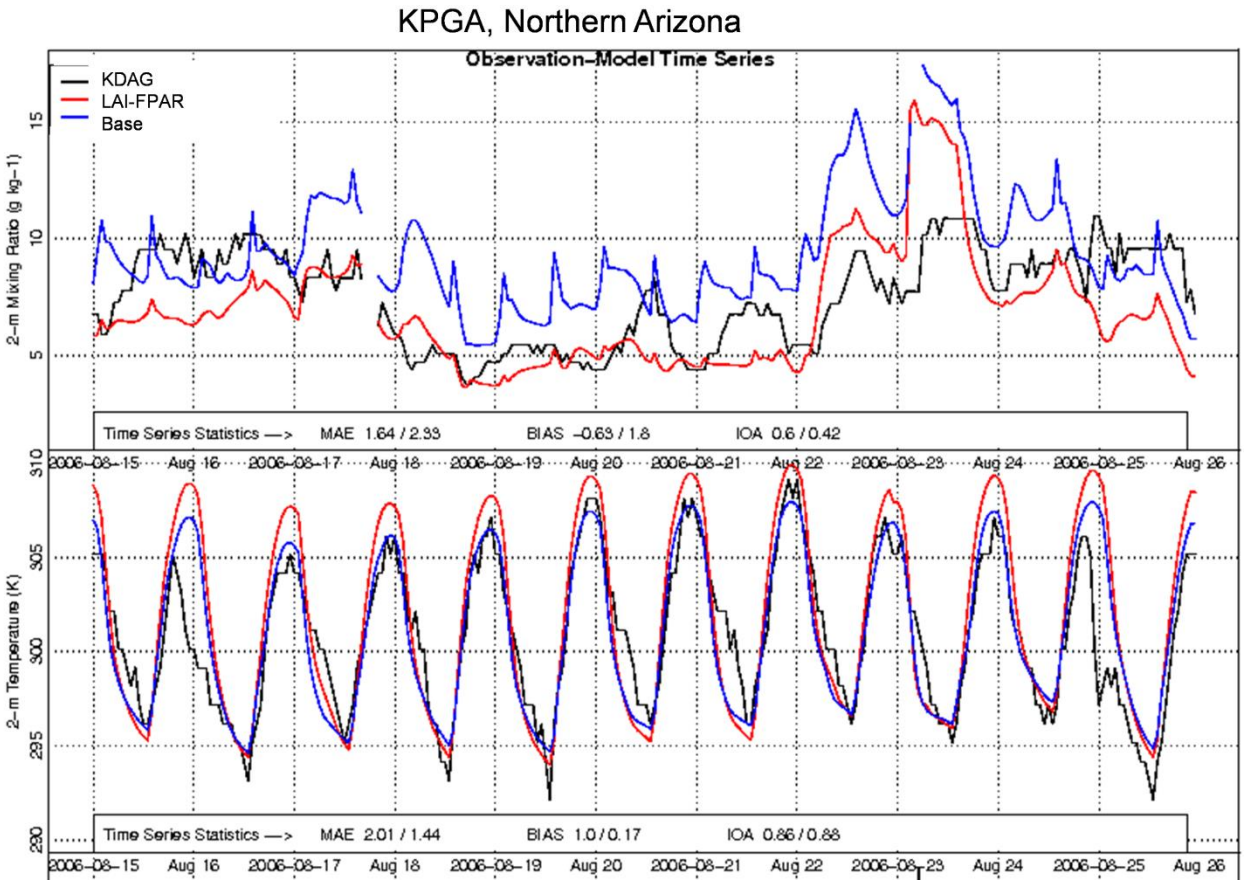

Figure 2.7. ASOS measurement site 2 m *T* (K) and Q (g kg^{-1}) time series comparison for the period from Aug. 15-25, 2006. KPGA site is in black line, LAI-FPAR case is in red line, and base case is in blue line. Site grid cell has VF 0.580 and LAI 1.918 for the base case and VF 0.105 and LAI 1.227 for the LAI-FPAR case.

The temperature (particularly day time temperature) has strong influence on ozone formation in the atmospheric boundary layer [*Rasmussen et al.*, 2012]. The impacts of the MODIS LAI-FPAR input on the near surface ozone concentration in the PX LSM WRF/CMAQ system is demonstrated in figure 2.8 which shows mean bias difference between the LAI-FPAR-Albedo case and base case CMAQ simulation over the period from Aug. 10-30, 2006. The mean bias difference spatial plot shows that the daily maximum 8-hour average O_3 (ppb) from the LAI-FPAR-Albedo case is increased for most of the AQS sites in the west, particularly in the

southwest where 2 m *T* increases the most. Many AQS sites (in grey color) in the east show very little change for the modeled O_3 and some (in green) show improvement in the O_3 estimation in the same areas of improved 2 m *T* (compare to figure 2.5). Overall the modeled ozone in the CMAQ run with MODIS input meteorology has a greater high bias: 12.6 ppb in comparison with the high bias of 9.94 ppb in the base model due to hotter 2 m *T*, particularly in the SW. Figure 2.9 shows that most of the ozone high bias occurs when the observed ozone concentration is low for both model cases. This tendency to over predict at the low end of the concentration range and under predict at the high end is a persistent characteristic of most air quality models [*Im et al.*, 2015; *Solazzo el al.*, 2012; *Foley et al.*, 2010]. With the MODIS input, under prediction at the high end is slightly improved. For limited area regional modeling the lateral boundary conditions (LBC) have strong influence on daytime ozone concentrations. Comparisons of 16 model applications of eight different air quality models as part of the AQMEII study, reported by *Im et al.* [2015], showed that all models have highest maximum 8-hr average ozone concentration biases at the low end of the observed range and nearly all greatly under estimate the high end of the range. For their study all models used 3-D daily LBC from the MACC re-analysis [*Inness et al.*, 2013] produced by assimilating satellite observations of O_3, CO and NO_2 in the coupled system IFS-MOZART [*Flemming et al.*, 2009]. Analysis of MACC data along with the model results showed the same behavior of overestimating the low end and underestimating the high end [*Im et al.*, 2015].

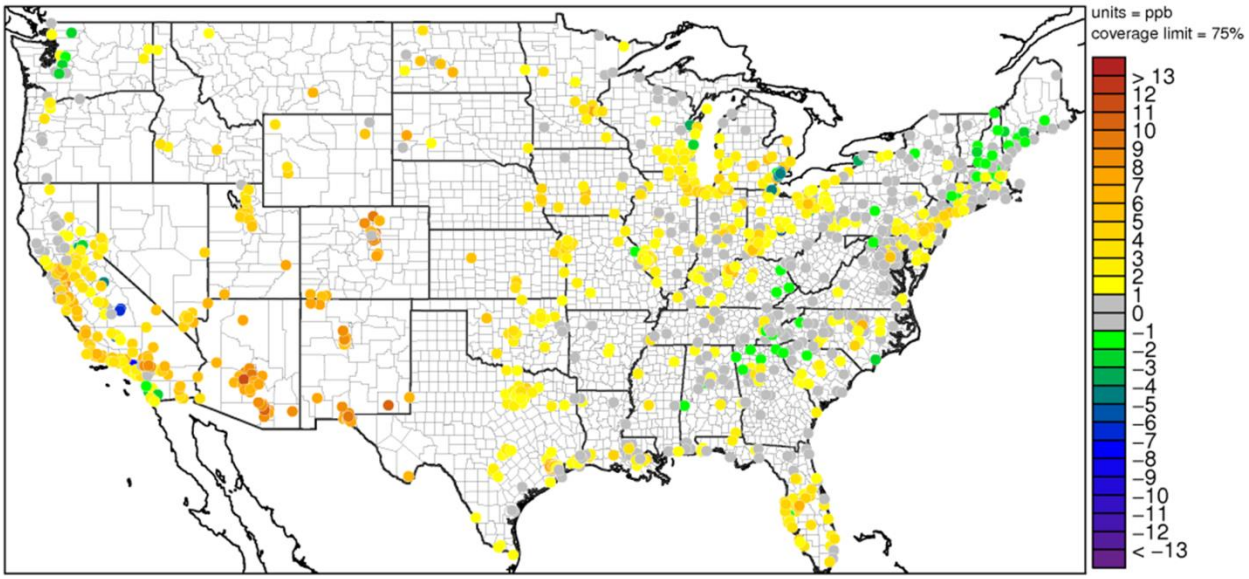

Figure 2.8. Mean bias difference (CMAQ LAI-FPAR-Albedo Case – Base Case) spatial plot for daily maximum 8-hour average O_3 (ppb) over the period from Aug. 10-30, 2006.

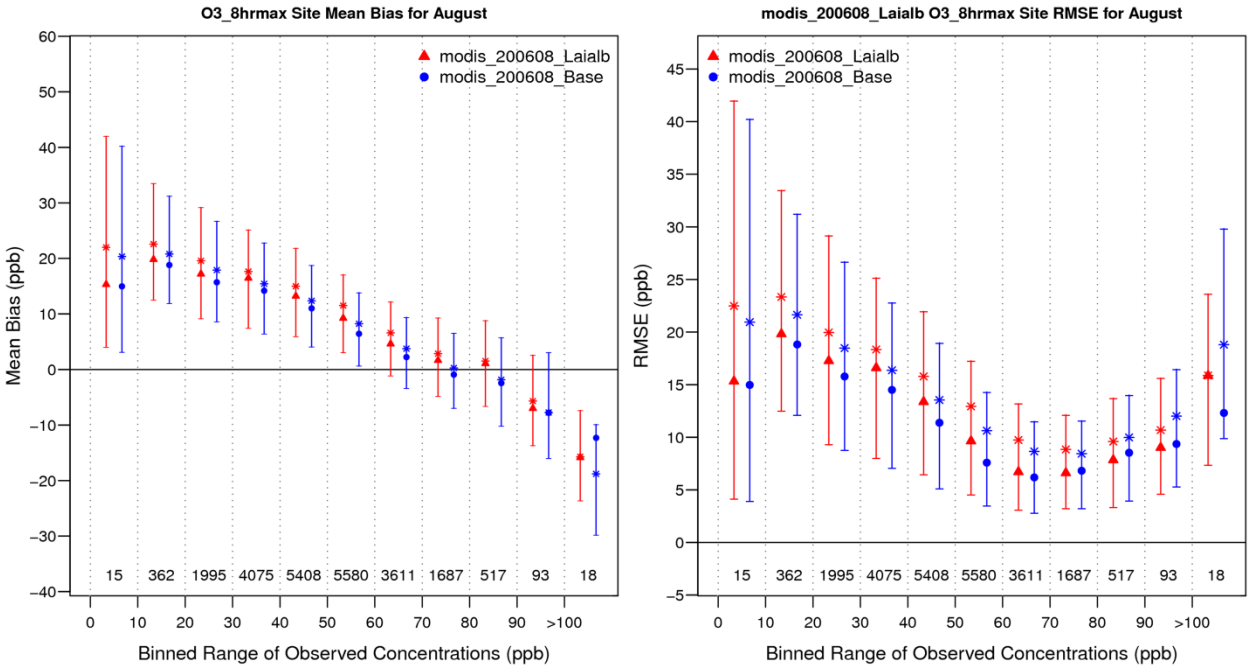

Figure 2.9. Mean bias (MB) and root mean square error (RMSE) of daily maximum 8-hour average O3 (ppb) over the binned observation range for CMAQ LAI-FPAR-Albedo Case (in red)

and Base Case (in blue) from Aug. 10-30, 2006. Line length is for the range of MB and RMSE, triangle for the median, and asterisk for the mean.

2.4.2 Surface Fluxes and PBLH

The changed surface characteristics through the use of the MODIS input have direct impacts on surface fluxes and PBLH. Modeled latent heat (LE) and sensible heat (SH) fluxes from the base case and the LAI-FPAR case are compared with the FLUXNET measurements at the Tonzi Ranch site in California. Figure 2.10 shows that LE from the base case (in red) is much too high in comparison with the LAI-FAPR case (green) and the site measurements (blue). LE from the LAI-FPAR case matches the site observations much better for the period. SH from the base case is too low and SH from the LAI-FPAR case is higher and agrees better with the FLUXNET measurements. The Tonzi Ranch site, which is used in the LAI evaluation in Section 2 (see figure 2.1), has too high LAI and VF in the base case that compensates for high 2 m *T* bias by increasing soil moisture through the PX LSM soil moisture nudging scheme. The increased soil moisture causes more surface radiation energy being partitioned into LE (too high LE) and less energy into SH (too low SH). In contrast, much more realistic low LAI and VF from the MODIS input in the LAI-FPAR run result in much better LE and SH estimates.

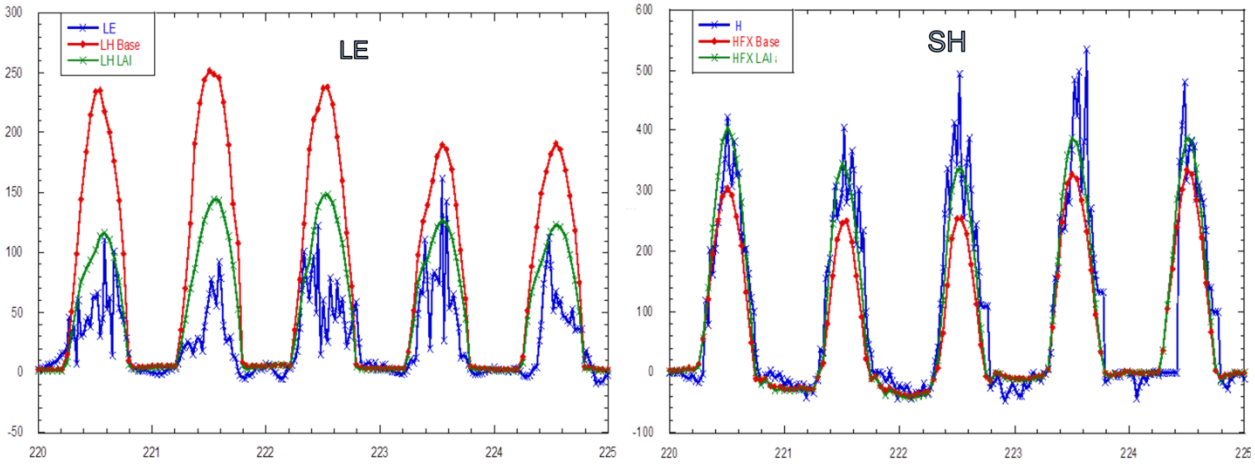

Figure 2.10. Tonzi-CA FLUXNET measurement latent and sensible Heat (W m^{-2}) comparison for the period from Aug. 8-13, 2006. FLUXNET site is in blue line, base case is in red line, and LAI-FPAR case is in green line.

Spatial differences between the model with MODIS input and the base model are also evaluated by examining differences at 20 UTC each day averaged over the period from August 10 to September 9. Figure 2.11 shows the differences of modeled LE, 2 m *T*, and PBLH between the LAI-FPAR and base model runs. MODIS LAI is higher (around 6) in heavily vegetated areas and lower (around 1) in the dryland west. MODIS LAI is lower in Florida as well as in the boreal forest areas compared to the base WRF LAI. As expected, LE from the LAI-FPAR case is much lower in the west, particularly in the southwest where MODIS LAI is much lower than the base WRF LAI and correspondingly LE in this region is 100 to 150 (W m^{-2}) lower than that in the base case. Some boreal regions and Florida also have lower LE (around 50 – 100 W m^{-2}) in the LAI-FPAR case due to the reduced LAI from MODIS input. 2 m *T* is around 1 to 2.5 degrees higher in most of the west and around 0.5 degree higher in Florida and many boreal areas where LE is lower. The PBLH from the LAI-FPAR case is much higher by around 300 m to 500 m in many western areas and is higher (about 100 m) in many boreal areas and Florida

where surface layer T is also higher. However, differences of LE, 2 m *T*, and PBLH are not obvious in the heavily vegetated areas in most of the eastern US.

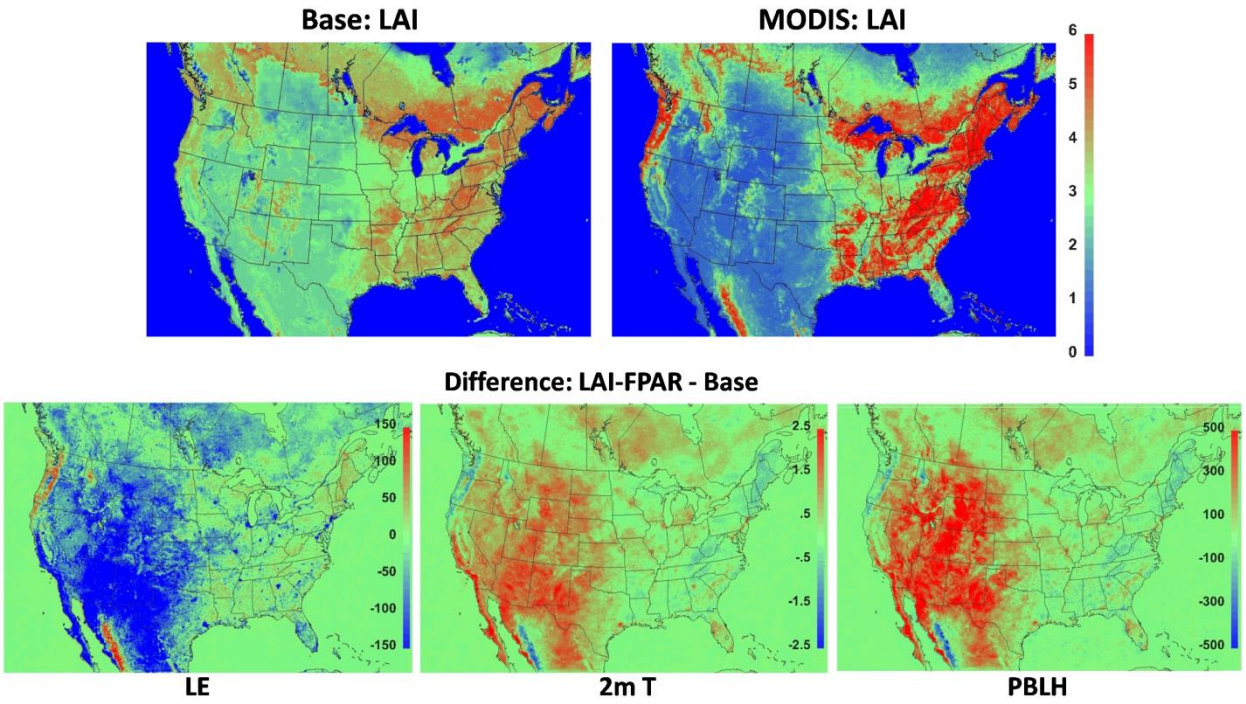

Figure 2.11. LAI for 20Z, August 10, 2006 and average differences of latent heat (W m^{-2}), 2 m *T* (K), and PBLH (m) between the LAI-FPAR case and base case for 20 UTC from August 10 to September 09, 2006.

The PX WRF albedo does not show diurnal changes and has much less spatial variation than the MODIS albedo, which is computed with varying SZA from BRDF/albedo parameters (figure 2.12). The MODIS albedo is generally lower in vegetated areas, particularly coniferous forests in the south, boreal regions, and high mountains in the west. Barren and desert areas in the west, particularly salt flats west of the Great Salt Lake in Utah and parts of Arizona and New Mexico, have much higher albedo (more than 30%). The higher albedo areas have lower surface skin temperature (by around 1.5 degree) in the MODIS albedo case. In contrast, the lower

albedo areas over coniferous forest regions have higher surface skin temperature by around 0.5 to1.5 degrees). Over cooler surface areas, 2 m *T* is proportionally lower (by around 1 degree) and warmer surface areas have higher 2 m *T* by around 0.5 to 1 degree. The PBLH difference has similar patterns as the surface skin T and 2 m *T* differences, particularly over the salt flats in Utah where PBLH is about 200 m lower in the albedo case than for the base model. It is important to note that the legend scales are much smaller in figure 2.12 than those in figure 2.11. MODIS albedo has much less impacts than MODIS LAI and FPAR on the meteorology simulations in general.

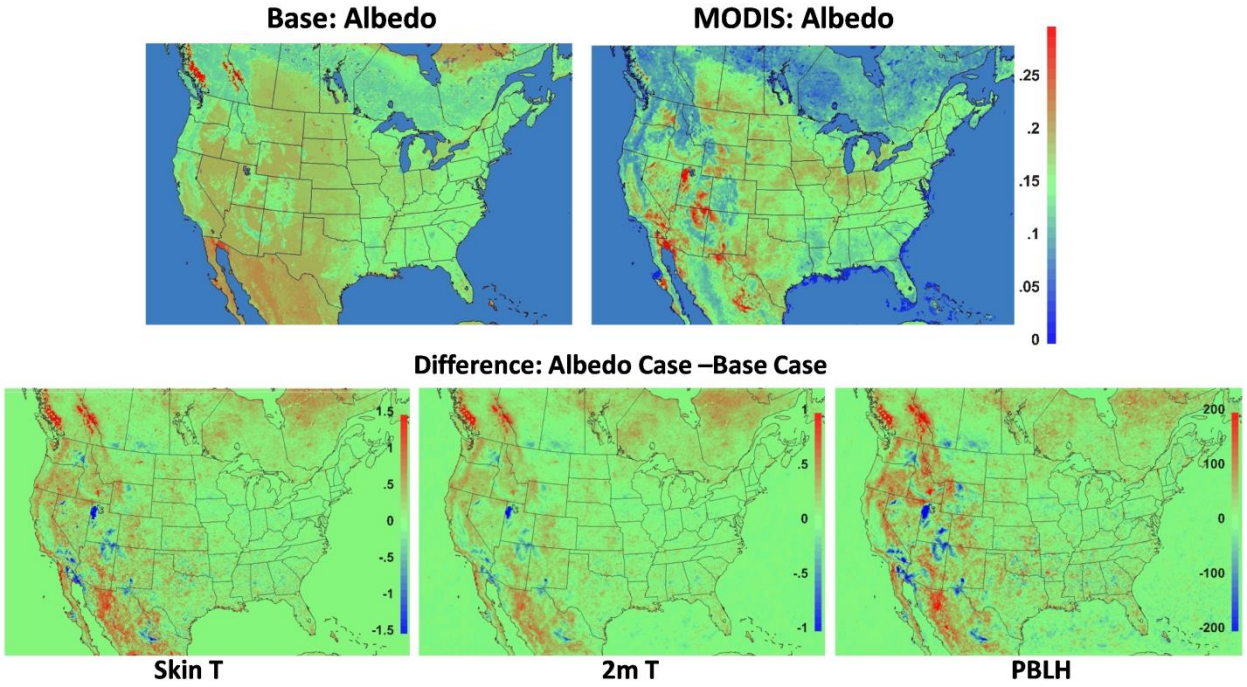

Figure 2.12. Albedo (fraction) for 20Z, August 10, 2006 and average differences of surface skin *T* (K), 2 m *T* (K) and PBLH (m) between the albedo case and the base case for 20 UTC from August 10 to September 09, 2006.

The ozone dry deposition flux has a strong stomatal pathway in vegetated areas [*Wesely et al.*, 1982; *Padro*, 1996; *Fuentes et al.*, 1992]. In CMAQ the dry deposition model is designed

to use the same aerodynamic and bulk stomatal conductance computed for evapotranspiration in WRF with the PX LSM [*Pleim et al.*, 2001] for consistency. Thus, the change of surface vegetation characteristics with the MODIS input as well as the resulting meteorology have significant impacts on the surface ozone flux and further effects on ozone concentration. The change of ozone deposition velocity and surface-layer concentration due to the use of the MODIS input is demonstrated in figure 2.13 for 20Z on August 10, 2006. The difference in ozone deposition velocity between the CMAQ LAI-FPAR-albedo case and base case follows the same pattern as LE differences resulting from the changed LAI and vegetation cover (see figure 2.11 and figure2. 2). The deposition velocity is lower in the west, the boreal regions, and Florida due to the lower LAI and vegetation cover with the MODIS vegetation input and relatively high in the dense vegetation areas such as the east, Pacific Northwest, and Sierra Madres Occidental (western Mexico). The surface ozone concentration differences exhibit corresponding patterns resulting primarily from the 2 m temperature differences and deposition velocity differences. With the MODIS input, the areas with the low deposition velocity and high 2 m *T* tend to have higher surface ozone concentration by up to 10 ppb even though there is a substantial increase in PBLH in these same areas that increases dilution.

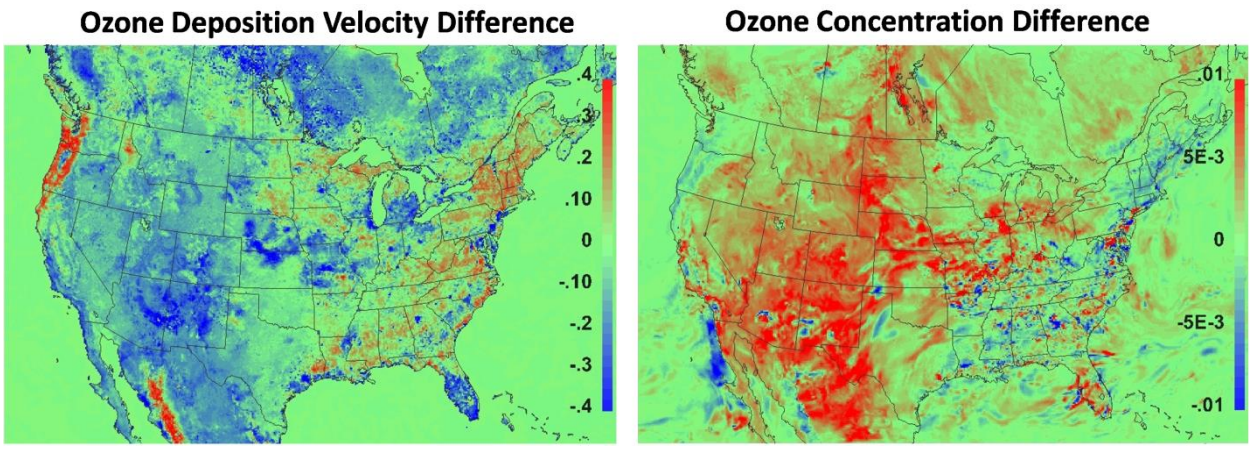

Figure 2.13. Difference of ozone deposition velocity (cm s^{-1}) and ozone concentration (ppmV) at the surface layer between the CMAQ LAI-FPAR-albedo case and base case for 20Z, August 10, 2006.

2.4.3 Precipitation and NH4 Wet Deposition

Differences in surface fluxes, temperature, mixing ratio, and PBLH also affect cloud formation and precipitation. Figure 2.14 shows the August domain-wide precipitation differences between the base case and the PRISM precipitation (left plot) and between the LAI-FPAR case and PRISM precipitation (right plot). The greatest difference between the two cases is that the large overestimation of precipitation in the Southwest (SW) plains and Colorado (CO) and New Mexico (NM) Mountains in the base case is greatly reduced in the LAI-FPAR case while the dry bias in the desert SW is increased. In general, precipitation is less in the western drylands in the LAI-FPAR case compared to the base case resulting in reduced biases where the base model was too wet (e.g. northern mountains and parts of Texas) but larger biases where the base model was too dry (e.g. Northern plains and desert SW). However, the MODIS vegetation input does not have much influence on the precipitation in the east where difference in LAI and VF are less extreme.

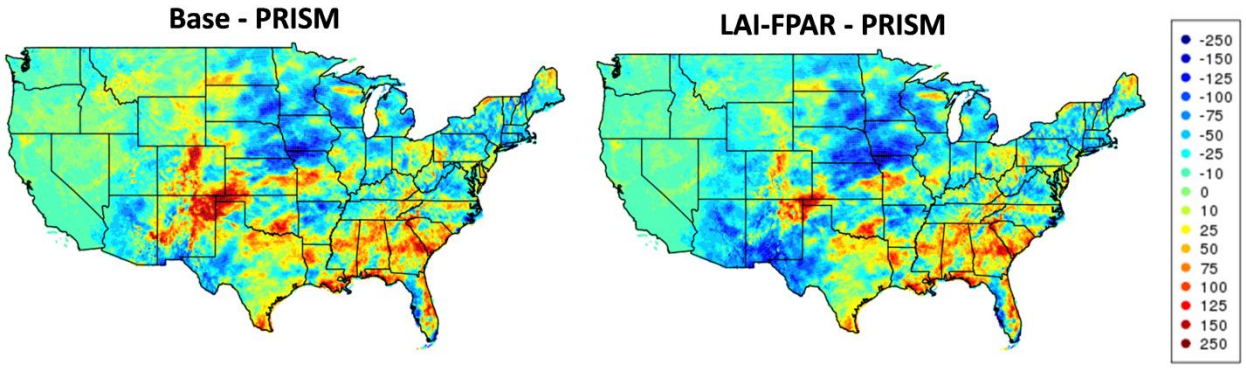

Figure 2.14. Monthly precipitation difference (mm) of the LAI-FPAR case and the base case from the PRISM precipitation for August 2006.

The precipitation modeled by the two cases is also evaluated against precipitation measured at the NADP sites in figure 2.15. While, a majority of the sites do not show big differences (grey color) between the two cases, the sites in the SW plains and CO and NM Mountains show big improvements with much less precipitation bias in the LAI-FPAR-Albedo case, which is consistent with the results displayed in figure 2.14. Many sites in the central plains also show modest improvements (green colors). Precipitation mean biases at most NADP sites in the east do not show much difference with the input of MODIS data. Overall, with the MODIS input the average mean bias for the NADP site precipitation is reduced to -14.22 mm dry bias from 40.89 mm wet bias in the base model for the month of August 2006. Despite the improved precipitation, the modeled wet deposition of NH_4 at the NADP sites with the input of MODIS data (figure 2.16) did not show clear similar improvement patterns as the precipitation. Many NADP sites such as those near the Great Lakes show some improvement and others, such as a few sites in North Carolina show increased bias. Overall, the simulation with the MODIS input has same mean bias (-0.02kg ha^{-1}) as the base simulation for the month of August 2006.

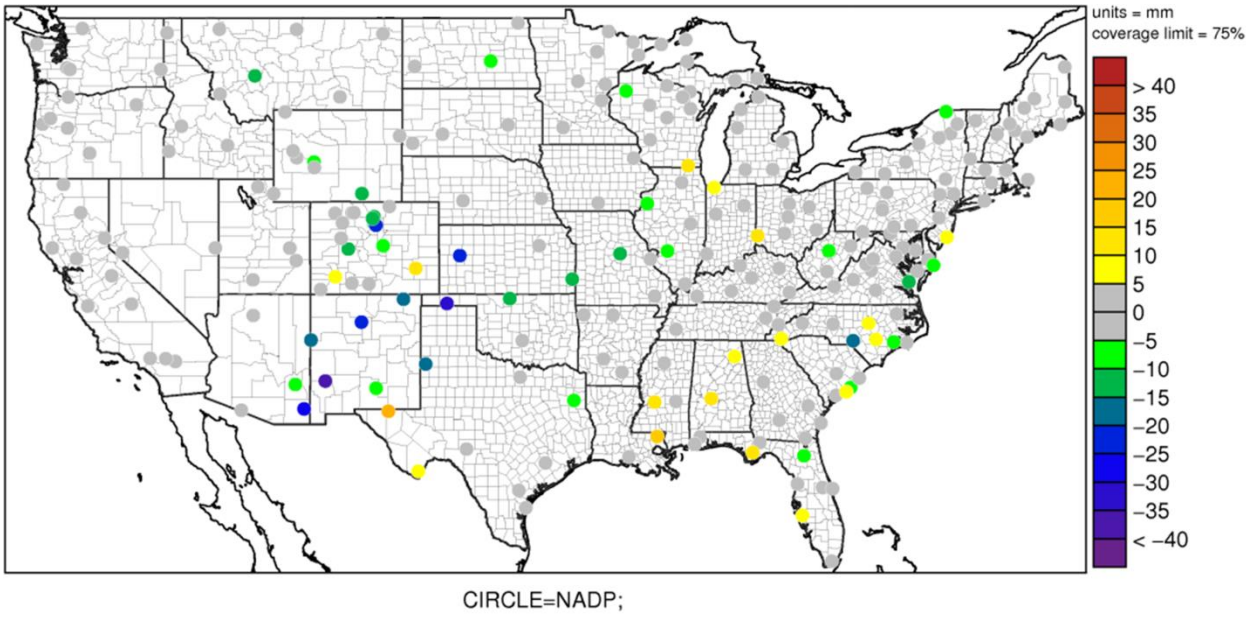

Figure 2.15. Mean bias difference of precipitation (mm) between the LAI-FPAR-Albedo case and the base case at the National Atmospheric Deposition Program (NADP) sites for August.

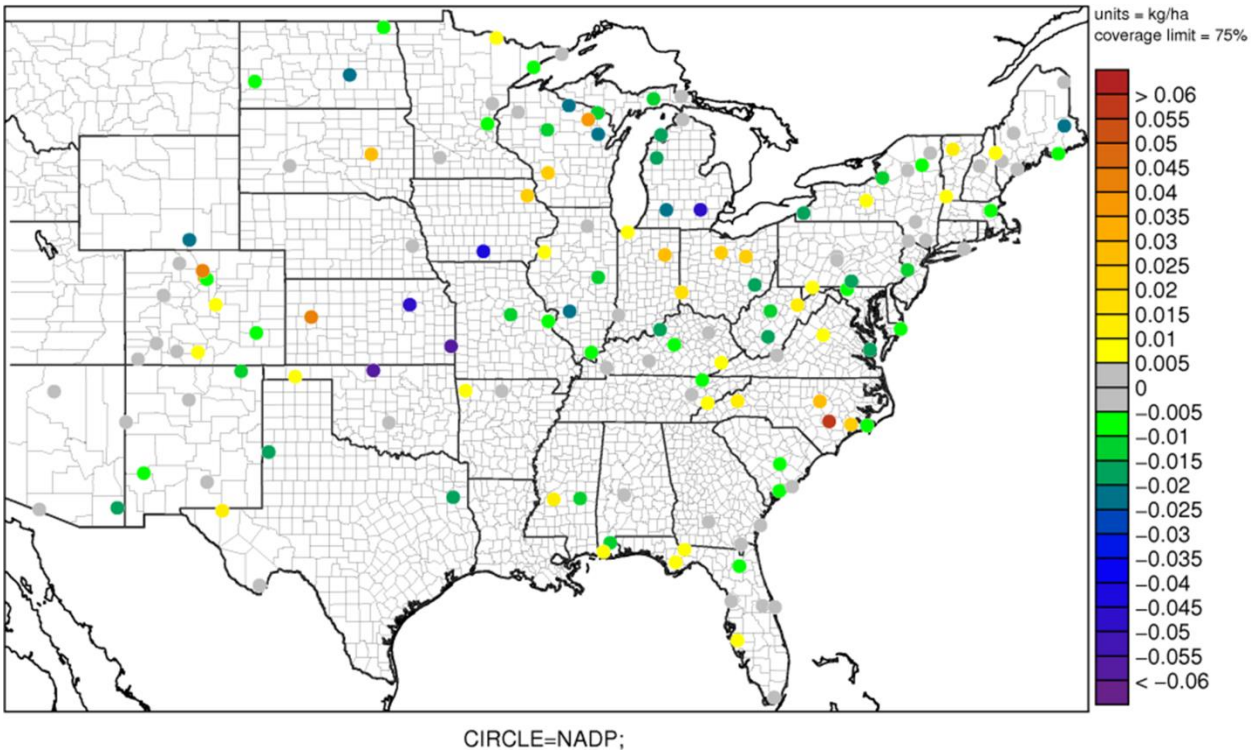

Figure 2.16. Mean bias difference of NH4 wet deposition (kg ha^{-1}) between the LAI-FPAR-Albedo case and the base case at the National Atmospheric Deposition Program (NADP) sites for August.

2.5 Conclusions and Future Work

The replacement of vegetation characteristics (LAI and VF) and surface albedo, which are currently specified by LSM land-use category look-up tables, with MODIS satellite products in the PX LSM is clearly a significant advance adding more realism to the WRF-CMAQ modeling system. However, comparisons between model simulations including the MODIS inputs and the base model show mixed results. The largest effect of the MODIS inputs is hotter and dryer conditions in the dry climate regions of western North America due to substantially less vegetation coverage (derived from MODIS FPAR) and LAI. Clearly, the more accurate, reduced vegetation has strong effects reducing LE and 2 m *Q* while increasing surface skin T, 2 m *T* and PBLH. The sparser vegetation described by the MODIS data substantially reduces

evapotranspiration and ozone dry deposition velocity. The combined effects of reduced deposition and higher temperatures in the western arid regions result in greater ozone concentrations even though deeper PBL depths tend to increase dilution of surface air pollutants. Thus, including the MODIS vegetation description tends to increase over-prediction of ozone at the low end of the observed concentration range but decrease under-prediction at the high end of the concentration range.

Evaluation of the two WRF modeling cases generally indicates greater error and bias in 2 m *T* but reduced error and bias in 2 m *Q* for the MODIS case compared to the base case. However, site meteorology measurement comparisons indicate improvement of peak 2 m *T* for some areas due to improved LE estimates. The input of MODIS vegetation and albedo data seems to have little effect on minimum 2 m *T* based on the two ASOS site comparison results. Thus, the increase in daily average 2 m *T* bias for the LAI-FPAR case that is widespread over the west may not always reflect degraded model performance depending on the model biases in minimum 2 m *T*. In some cases (e.g. KDAG shown in Fig 6) the base case has lower daily average 2 m *T* bias because the minimum 2 m *T* is over-predicted while the maximum 2 m *T* is under-predicted. Meanwhile, the MODIS case better matches the observed maximum 2 m *T* at this site but similarly over-predicts the minimum 2 m *T* resulting in a larger diurnal average bias. Thus, good daily average temperature performance in the base model is sometimes the result of compensating errors and masks separate problems in simulating processes determining daytime minimum and maximum temperatures.

In comparison with the MODIS LAI and FPAR, MODIS albedo has much less impact on the meteorology simulations in general. Even though overall domain-wide evaluation statistics (BIAS, MAE, and StDEV) for 2 m *T* and *Q* and 10-m wind speed are almost identical between

the simulations with and without MODIS albedo input, model-to-model 20 UTC 30-day average comparisons of skin T, 2 m *T*, and PBLH between the two simulations do show differences due to changed albedo. Barrens and deserts in the west tend to have higher albedo which results in lower surface skin T, 2 m *T*, and PBLH while coniferous forest in the south, boreal regions and high mountains in the west tends to have lower albedo which corresponds to higher skin *T*, 2 m *T*, and PBLH.

With the input of MODIS LAI and FPAR, precipitation is reduced compared to the base case which results in lower biases where the model tended to be too wet but increased low biases where the model tended to be too dry. Overall, with the MODIS input the average mean bias for the NADP sites precipitation is reduced while the modeled NH_4 wet deposition at the NADP sites with the input of MODIS data did not show clear similar improvement patterns as the precipitation. Note that the LAI and VF in the PX LSM were intentionally over-estimated in the base model so that the soil moisture nudging scheme could be more effective in optimizing surface T and Q. As a result, the base model achieved low errors in 2 m *T* by exaggerating LE both by the inflated vegetation and by the soil moisture nudging scheme which increases root zone soil moisture in response to hot and dry biases.

A significant conclusion of this study is that in the current PX LSM the combination of the soil moisture nudging scheme and the exaggerated base vegetation coverage and LAI in the western arid regions compensates for an inherent tendency toward hot biases in low vegetation areas. This conclusion suggests that improvements should be made in the model physics, particularly the LSM. Upgrades to the PX LSM are underway, including a biochemically-based photosynthesis-conductance scheme following the studies for climate LSMs [*Sellers et al.*, 1996; *Calvet et al.*, 1998; *Dai et al.*, 2004; *Krinner et al.*, 2005; *Bonan et al.*, 2011; *Clark et al.*, 2011;

Kowalczyk et al., 2013; *Oleson et al.*, 2013]. As WRF/CMAQ with the PX LSM has been applied for annual simulations, the lack of the coupled leaf photosynthesis and stomatal conductance could limit not only the model's dynamic responses to environmental conditions such as temperature, air pollutants (e.g. O_3) and CO_2 concentration but also their applications in assessing the coupling effects of air quality and vegetation productivity in changing climate [*Sitch et al.*, 2007; *Lombardozzi et al.*, 2012]. The addition of a third soil layer to the force-restore soil model following the advances in ISBA described by Boone et al. [1999] may allow the LSM to simulate deep root zone moisture better (e.g. vegetation in the dryland west). Furthermore, there is an ongoing effort to improve the PX LSM land use scheme with biome, phenology, rainfed and irrigated crop, and C_3/C_4 grass information for better landscape characterization. Since this analysis focusses only on a short period in the summer (August-September 2006) the advantages of satellite derived vegetation and albedo data for describing seasonal changes are not included. Year-long modeling studies that cover entire annual cycles are ongoing and the effects of more accurate representation of seasonal changes in natural and cultivated vegetation and changes due to human and natural disturbances (e.g. severe drought, fire and storm damages, and construction activities) will be fully explored in the coming research.

REFERENCES

Alton, P. (2009), A simple retrieval of ground albedo and vegetation absorptance from MODIS satellite data for parameterisation of global land-surface models, Agricultural and Forest Meteorology, 149(10), 1769-1775.

Appel, K. W., K. M. Foley, J. O. Bash, P. W. Pinder, R. L. Dennis, D. J. Allen, and K. A. Pickering (2011), Multi-resolution assessment of the Community Multiscale Air Quality (CMAQ) model v4.7 wet deposition estimates for 2002-2006, Geosci. Model Dev, 4, 357–371.

Appel, K. W., R. C. Gilliam, N. Davis, and A. Zubrow (2011), Overview of the Atmospheric Model Evaluation Tool (AMET) v1.1 for evaluating meteorological and air quality models, Environ. Modell. Softw., 26(4), 434–443.

Baker, I. T., A. S. Denning, N. Hanan, L. Prihodko, P. L. Vidale, K. Davis, and P. Bakwin (2010), North American gross primary productivity: regional characterization and interannual variability, Tellus, 62B, 533–549.

Baldocchi, D. (2008), TURNER REVIEW No. 15, 'Breathing' of the terrestrial biosphere: lessons learned from a global network of carbon dioxide flux measurement systems, Australian Journal of Botany, 56(1),1-26.

Barbu, A. L., J. C. Calvet, J. F. Mahfouf, C. Albergel, and S. Lafont (2011), Assimilation of Soil Wetness Index and Leaf Area Index into the ISBA-A-gs land surface model: grassland case study, Biogeosciences, 8, 1971–1986.

Bonan, G. B. (2008), Ecological climatology: concepts and applications, Cambridge University Press, New York.

Bonan, G. B., P. J. Lawrence, K. W. Oleson, S. Levis, M. Jung, M. Reichstein, D. M. Lawrence, and S. C. Swenson (2011), Improving canopy processes in the Community Land Model version 4 (CLM4) using global flux fields empirically inferred from FLUXNET data, Journal of Geophysical Research: Biogeosciences (2005–2012), 116(G2).

Boone, A., J. C. Calvet, and J. Noilhan (1999), Inclusion of a third soil layer in a land surface scheme using the force-restore method, J. Appl. Meteorol., 38, 1611–1630.

Bouttier, F., J. F. Mahfouf, and J. Noilhan (1993), Sequential assimilation of soil moisture from atmospheric low-level parameters. Part I: Sensitivity and calibration studies, J. Appl. Meteor., 32, 1335–1351.

Buermann, W., J. Dong, X. Zeng, R. B. Myneni, and R. E. Dickinson (2001), Evaluation of the utility of satellite-based vegetation leaf area index data for climate simulations, Journal of Climate, 14(17), 3536-3550.

Byun, D. W. and K. L. Schere (2006), Review of the governing equations, computational algorithms, and other components of the Models-3 Community Multiscale Air Quality (CMAQ) modeling system, Appl. Mech. Rev., 59, 51-77.

Calvet, J. C., J. Noilhan, J. L. Roujean, P. Bessemoulin, M. Cabelguenne, A. Olioso, and J. P. Wigneron (1998), An interactive vegetation SVAT model tested against data from six contrasting sites, Agric. For. Meteorol., 92,73– 95.

Chen, F., and J. Dudhia (2001), Coupling an advanced land-surface/hydrology model with the Penn State/NCAR MM5 modeling system. Part I: Model implementation and sensitivity. Mon. Wea. Rev., 129:569-585.

Clark, D. B., L. M. Mercado, S. Sitch, C. D. Jones, N. Gedney, M. Pryor, G. G. Rooney, R. L. H. Essery, E. Blyth1, O. Boucher, R. J. Harding, C. Huntingford, and P. M. Cox (2011), The joint UK land environment simulator (JULES), model description–Part 2: carbon fluxes and vegetation dynamics, Geoscientific Model Development, 4(3), 701-722.

Cohan, D. S., J. W. Boylan, A. Marmur, and M. N. Khan (2007), An Integrated Framework for Multipollutant Air Quality Management and Its Application in Georgia, Environ. Manage., 40, 545–554.

Cohen, W. B., T. K. Maiersperger, D. P. Turner, W. D. Ritts, D. Pflugmacher, R. E. Kennedy, A. Kirschbaum, S.W. Running, M. Costa, and S. T. Gower (2006), MODIS land cover and LAI collection 4 product quality across nine sites in the western hemisphere, IEEE Transactions on Geoscience and Remote Sensing, 44,1843−1857.

Compton, J. E., J. A. Harrison, R. L. Dennis, T. L. Greaver, B. H. Hill, S. J. Jordan, H. Walker, and H. V. Campbell (2011), Ecosystem services altered by human changes in the nitrogen cycle: a new perspective for US decision making, Ecology Letters, 14, 804–815.

Dai, Y., R. E. Dickinson, and Y. P. Wang (2004), A two-big-leaf model for canopy temperature, photosynthesis, and stomatal conductance, J. Clim., 17, 2281-2299.

Daly, C., M. Halbleib, J. I. Smith, W. P. Gibson, M. K. Doggett, G. H. Taylor, J. Curtis, and P. P. Pasteris (2008), Physiographically sensitive mapping of climatological temperature and precipitation across the conterminous United States, International journal of climatology, 28(15), 2031-2064.

Douville, H., P. Viterbo, J. F. Mahfouf, and A. C. M. Beljaars (2000), Evaluation of the optimum interpolation and nudging techniques for soil moisture analysis using FIFE data, Mon. Wea. Rev., 128, 1733–1756.

Fang, H., C. Jiang, W. Li, S. Wei, F. Baret, J. Chen, J. Garcia-Haro, R. Liu, R. Myneni, R., B. Pinty, Z. Xiao, and Z. Zhu (2013), Characterization and intercomparison of global moderate resolution leaf area index (LAI) products: Analysis of climatologies and theoretical uncertainties, Journal of Geophysical Research – Biospheres, 118, 529-548.

Fensholt, R., I. Sandholt, and M. S. Rasmussen (2004), Evaluation of MODIS LAI, fAPAR and the relation between fAPAR and NDVI in a semi-arid environment using in situ measurements, Remote Sensing of Environment, 91(3), 490-507.

Flemming, J., A. Inness, H. Flentje, V. Huijnen, P. Moinat, M. G. Schultz, and O. Stein (2009), Coupling global chemistry transport models to ECMWF's integrated forecast system, Geosci. Model Dev., 2, 253–265, doi:10.5194/gmd-2-253-2009.

Foley, K. M., S. J. Roselle, K. W. Appel, P. V. Bhave, J. E. Pleim, T. L. Otte, R. Mathur et al. (2010), Incremental testing of the Community Multiscale Air Quality (CMAQ) modeling system version 4.7, Geoscientific Model Development, 3(1), 205-226.

Fuentes, J. D., T. J. Gillespie, G. den Hartog, G. and H. H. Neumann (1992), Ozone deposition onto a deciduous forest during dry and wet conditions, Agric. For. Meteorol., 62, 1-18.

Gao, F., J. Morisette, R. Wolfe, G. Ederer, J. Pedelty, E. Masuoka, R. Myneni, B. Tan, and J. Nightingale (2008), An Algorithm to Produce Temporally and Spatially Continuous MODIS-LAI Time Series, IEEE Geoscience and Remote Sensing Letters, 5(1), 60-64.

Gao, Y., N. Lu, and T. Yao T. (2011), Evaluation of a cloud-gap-filled MODIS daily snow cover product over the Pacific Northwest USA, Journal of Hydrology, 404, 157–165.

Gego, E., C. Hogrefe, G. Kallos, A. Voudouri, J.S. Irwin, and S.T., Rao (2005), Examination of model predictions at different horizontal grid resolutions, Environmental Fluid Mechanics, 5, 63–85.

Gilliam, R. C., W. Appel, and S. Philips (2005), The Atmospheric Evaluation Tool (AMET): Meteorology module, Extended Abstracts, Fourth Annual Community Analysis and Modeling System Conf., Chapel Hill, NC, University of North Carolina Institute for the Environment, 6 pp. [Available online at http://www.cmascenter.org/conference/2005/abstracts/6_1.pdf].

Gilliam, R. C., C. Hogrefe, and S. T. Rao (2006), New methods for evaluating meteorological models used in air quality applications, Atmospheric Environment, 40, 5073-5086.

Gilliam, R. C., and J. E. Pleim (2010), Performance assessment of new land surface and planetary boundary layer physics in the WRF-ARW, Journal of Applied Meteorology and Climatology, 49(4), 760-774.

Hogrefe, C., G. Pouliot, D. Wong, A. Torian, S. Roselle, J. Pleim, and R. Mathur (2014), Annual application and evaluation of the online coupled WRF–CMAQ system over North America under AQMEII phase 2, Atmospheric Environment.

Hong, S., V. Lakshmi, E. E. Small, F. Chen, M. Tewari, and K. W. Manning (2009), Effects of vegetation and soil moisture on the simulated land surface processes from the coupled WRF/Noah model, J. Geophys. Res., 114, D18118, doi:10.1029/2008JD011249.

Iacono, M.J., J. S. Delamere, E. J.Mlawer, M. W. Shephard, S. A. Clough, W. D. Collins (2008), Radiative forcing by long-lived greenhouse gases: calculations with the AER radiative transfer models, J. Geophys. Res., 113, D13103. doi:10.1029/2008JD009944.

Im, U., R. Bianconi, E. Solazzo, I. Kioutsioukis, A. Badia, A. Balzarini, ... and S. Galmarini (2014), Evaluation of operational on-line-coupled regional air quality models over Europe and North America in the context of AQMEII phase 2. Part I: Ozone, Atmospheric Environment.

Inness, A., F. Baier, A. Benedetti, I. Bouarar, S. Chabrillat, H. Clark, ... and C. Zerefos (2013), The MACC reanalysis: an 8 yr data set of atmospheric composition, Atmos. Chem. Phys., 13, 4073-109.

Isakov, V., J. Irwin, and J. Ching (2007), Using CMAQ for Exposure Modeling and Characterizing the Subgrid Variability for Exposure Estimates, J. Appl. Meteor. Climatol., 46, 1354–1371.

Kain, J. S. (2004), The Kain–Fritsch convective parameterization: An update. J. Appl. Meteor., 43, 170–181.

Kowalczyk, E. A., L. Stevens, R. M. Law, M. Dix, Y. P. Wang, I. N. Harman, ... and T. Ziehn (2013), The land surface model component of ACCESS: description and impact on the simulated surface climatology, Australian Meteorological and Oceanographic Journal, 63(1), 65-82.

Krinner, G., N. Viovy, N. de Noblet-Ducoudre´, J. Oge´e, J. Polcher, P. Friedlingstein, P. Ciais, S. Sitch, and I. C. Prentice (2005), A dynamic global vegetation model for studies of the coupled atmosphere-biosphere system, Global Biogeochem. Cycles, 19(1).

Lawrence, D., K. W. Oleson, M. G. Flanner, P. E. Thorton, S. C. Swenson, P. J. Lawrence, X. Zeng, Z. L. Yang, S. Levis, K. Skaguchi, G. B. Bonan and A. G. Slater (2011), Parameterization Improvements and Functional and Structural Advances in Version 4 of the Community Land Model, J. Adv. Model. Earth Syst., 3(1).

Lewis, P., and M. J. Barnsley (1994), Influence of the sky radiance distribution on various formulations of the earth surface albedo, In 6th International Symposium on Physical Measurements and Signatures in Remote Sensing, ISPRS, 707-715.

Liang, X. Z., M. Xu, W. Gao, K. Kunkel, J. Slusser, Y. Dai, Q. Min, … and F. Gao (2005), Development of land surface albedo parameterization based on Moderate Resolution Imaging Spectroradiometer (MODIS) data, Journal of Geophysical Research: Atmospheres (1984–2012), 110(D11).

Liu, J., C. Schaaf, A. Strahler, Z. Jiao, Y. Shuai, Q. Zhang, ... and E. G. Dutton (2009), Validation of Moderate Resolution Imaging Spectroradiometer (MODIS) albedo retrieval algorithm: Dependence of albedo on solar zenith angle, Journal of Geophysical Research: Atmospheres (1984–2012), 114(D1).

Lombardozzi, D., S. Levis, G. Bonan, and J. P. Sparks (2012), Predicting photosynthesis and transpiration responses to ozone: decoupling modeled photosynthesis and stomatal conductance, Biogeosciences, 9, 3113-3130, doi:10.5194/bg-9-3113-2012.

Los, S. O., N. H. Pollack, M. T. Parris, G. J. Collatz, C. J. Tucker, P. J. Sellers, ... and D. A. Dazlich (2000), A global 9-yr biophysical land surface dataset from NOAA AVHRR data, Journal of Hydrometeorology, 1(2), 183-199.

Lucht, W., C. B. Schaaf, and A. H. Strahler (2000), An algorithm for the retrieval of albedo from space using semiempirical BRDF models, IEEE Trans. Geosci. Remote Sens., 38, 977– 998, doi:10.1109/36.841980.

Mahfouf, J. F. (1991), Analysis of soil moisture from near-surface parameters: A feasibility study, J. Appl. Meteorol., 30, 506– 526.

Masson, V., J. L. Champeaux, F. Chauvin, C. Meriguet, and R. Lacaze (2003), A Global Database of Land Surface Parameters at 1-km Resolution in Meteorological and Climate Models, J. Climate, 16, 1261–1282.

Miao, J. F., D. Chen, and K. Borne (2007), Evaluation and comparison of Noah and Pleim-Xiu land surface models in MM5 using GÖTE2001 data: Spatial and temporal variations in near-surface air temperature, Journal of Applied Meteorology and Climatology, 46(10), 1587-1605.

Moore, N., N. Torbick, B. Lofgren, J. Wang, B. Pijanowski, J. Andresen, D. Y. Kim, and J. Olson (2010), Adapting MODIS-derived LAI and fractional cover into the RAMS in East Africa, Int. J. Clim., 30, 1954–1969.

Morrison, H., G. Thompson, V. Tatarskii (2009), Impact of Cloud Microphysics on the Development of Trailing Stratiform Precipitation in a Simulated Squall Line: Comparison of One– and Two–Moment Schemes, Mon. Wea. Rev., 137, 991–1007.

Mu, Q., F. A. Heinsch, M. Zhao, and S. W. Running (2011), Improvements to a MODIS global terrestrial evapotranspiration algorithm, Remote Sensing of Environment 115, 1781-1800.

Myneni, R., Y. Knyazikhin, and N. Shabanov (2011), Leaf Area Index and Fraction of Absorbed PAR Products from Terra and Aqua MODIS Sensors: Analysis, Validation, and Refinement. Land Remote Sensing and Global Environmental Change, Remote Sensing and Digital Image Processing, 11, 603-633.

Myneni, R. B., R. R. Nemani, and S. W. Running (1997), Algorithm for the estimation of global land cover, LAI and FPAR based on radiative transfer models, IEEE Trans. Geosc. Remote Sens., 35(6), 1380-1393.

Noilhan, J. and S. Planton (1989), A simple parameterization of land surface processes for meteorological models, Mon. Wea. Rev., 117, 536-549.

Oleson, K. W., D. M. Lawrence, G. B. Bonan, B. Drewniak, M. Huang, C. D. Koven, S. Levis, F. Li, W. J. Riley, Z. M. Subin, S. C. Swenson, P. E. Thornton, A. Bozbiyik, R. Fisher, E. Kluzek, J. F. Lamarque, P. J. Lawrence, L. R. Leung, W. Lipscomb, S. Muszala, D. M. Ricciuto, W. Sacks, Y. Sun, J. Tang, and Z. L. Yang (2013), Technical Description of version 4.5 of the Community Land Model (CLM). Ncar Technical Note NCAR/TN-503+STR, National Center for Atmospheric Research, Boulder, CO, 422 pp, DOI: 10.5065/D6RR1W7M.

Otte, T. L. and J. E. Pleim (2010), The Meteorology-Chemistry Interface Processor (MCIP) for the CMAQ modeling system: updates through MCIPv3. 4.1, Geoscientific Model Development, 3(1), 243-256.

Padro, J. (1996), Summary of ozone dry deposition velocity measurements and model estimates over vineyard, cotton, grass and deciduous forest in summer, Atmospheric Environment, 30(13), 2363-2369.

Pleim, J. E. (2007a), A combined local and nonlocal closure model for the atmospheric boundary layer. Part I: model description and testing, J. Appl. Meteor. Clim., 46, 1383–1395.

Pleim, J. E. (2007b), A combined local and nonlocal closure model for the atmospheric boundary layer. Part II: application and evaluation in a mesoscale meteorological model, J. Appl. Meteor. Clim., 46, 1396–1409.

Pleim J. E. and R. Gilliam (2009), An indirect data assimilation scheme for deep soil temperature in the Pleim-Xiu land surface model, J. Appl. Meteor. Clim., 48, 1362-1376.

Pleim, J. E. and L. Ran (2011), Surface Flux Modeling for Air Quality Applications, Atmosphere, 2(3), 271-302.

Pleim, J. E. and A. Xiu (1995), Development and testing of a surface flux and planetary boundary layer model for application in mesoscale models, J. Appl. Meteorol., 34, 16–32.

Pleim, J. E. and A. Xiu (2003), Development of a Land Surface Model. Part II: Data Assimilation, J. Appl. Meteor., 42, 1811–1822.

Pleim, J. E., A. Xiu, P. L. Finkelstein, and T. L. Otte (2001), A coupled land-surface and dry deposition model and comparison to field measurements of surface heat, moisture, and ozone fluxes. Water, Air and Soil Pollution: Focus, 1(5-6), 243-252.

Pouliot, G., H. A. D. van der Gon, J. Kuenen, J. Zhang, M. D. Moran, and P. A. Makar (2014), Analysis of the emission inventories and model-ready emission datasets of Europe and North America for phase 2 of the AQMEII project, Atmospheric Environment.

Ran, L. and A. Hanna (2014), Spatial Allocator Raster Tools v4.2: User's Guide, the Community Modeling and System analysis at the University of North Carolina, Chapel Hill. Available at: https://www.cmascenter.org/sa-tools/documentation/4.2/html/raster/Raster_Users_Guide_4_2.pdf, (last access: December 2014), 15 pp.

Ran, L., J. Pleim, and A. R. Gilliam (2010), Impact of High Resolution Land-Use Data in Meteorology and Air Quality Modeling Systems, in Air Pollution Modeling and its Applications XX, edited by Douw G. Steyn and S. Trivikrama Rao, Springer Netherlands, C(section 1.1):3-7.

Rappenglück, B., L. Ackermann, S. Alvarez, J. Golovko, M. Buhr, R. A. Field, J. Soltis, … and C. Keslar (2014), Strong wintertime ozone events in the Upper Green River basin, Wyoming, Atmospheric Chemistry and Physics, 14(10), 4909-4934.

Rasmussen, D. J., A. M. Fiore, V. Naik, L. W. Horowitz, S. J. McGinnis, M. G. Schultz (2012), Surface ozone-temperature relationships in the eastern US: A monthly climatology for evaluating chemistry-climate models, Atmospheric Environment, 47, 142-153.

Rodell, M., P. R. Houser, U. Jambor, J. Gottschalck, K. Mitchell, C. J. Meng, K. Arsenault, B. Cosgrove, J. Radakovich, M. Bosilovich, … and D. Toll (2004), The global land data assimilation system, Bull. Am. Meteorol. Soc., 85, 381–394.

Rogers, R. E., A. Deng, D. R. Stauffer, B. J. Gaudet, Y. Jia, S. T. Soong, and S. Tanrikulu (2013), Application of the Weather Research and Forecasting Model for Air Quality Modeling in the San Francisco Bay Area, Journal of Applied Meteorology & Climatology, 52(9).

Schaaf, C. B., F. Gao, A. H. Strahler, W. Lucht, X. Li, T. Tsang, N. C. Strugnell, X. Zhang, Y. Jin, J. P. Muller, P. Lewis, M. Barnsley, P. Hobson, M. Disney, G. Roberts, M. Dunderdale, C. Doll, R. d'Entremont, B. Hu, S. Liang, and J. L. Privette (2002), First Operational BRDF, Albedo and Nadir Reflectance Products from MODIS, Remote Sens. Environ., 83, 135-148.

Schaaf, C. B., J. Liu, F. Gao and A. H. Strahler (2011), MODIS Albedo and Reflectance Anisotropy Products from Aqua and Terra, In Land Remote Sensing and Global Environmental Change: NASA's Earch Observing System and the Science of ASTER and MODIS, Remote Sensing and Digital Image Processing Series, Vol.11, edited by B. Ramachandran, C. Justice, and M. Abrams, Springer-Cerlag, 873 pp.

Sellers, P. J., D. A. Randall, G. J. Collatz, J. A. Berry, C. B. Field, D. A. Dazlich, C. Zhang, G. D. Collelo, and L. Bounoua (1996), A revised land surface parameterization (SiB2) for atmospheric GCMs. Part I: Model formulation, J. Clim., 9, 676–705.

Skamarock, W. C., J. B. Klemp, J. Dudhia, D. O. Gill, D. M. Barker, W. Wang, and J. G. Powers (2008), A description of the advanced research WRF version 3. NCAR Tech Note, NCAR/TN 475+STR: 125 pp.

Sitch, S., P. M. Cox, W. J. Collins, and C. Huntingford (2007), Indirect radiative forcing of climate change through ozone effects on the land-carbon sink, Nature, 448, 791–794.

Solazzo, E., R. Bianconi, G. Pirovano, M. D. Moran, R. Vautard, C. Hogrefe, K. W. Appel, V. Matthias, P. Grossi, B. Bessagnet, J. Brandt, C. Chemel, J. H. Christensen, R. Forkel, X. V. Francis, A. B. Hansen, S. McKeen, U. Nopmongcol, M. Prank, K. N. Sartelet, A. Segers, J. D. Silver, G. Yarwood, J. Werhahn, J. Zhang, S. T. Rao, S. Galmarini (2013), Evaluating the

capability of regional-scale air quality models to capture the vertical distribution of pollutants, Geoscientific Model Development, 6, 791-818.

Vautard, R., M. D. Moran, E. Solazzo, R. C. Gilliam, V. Matthias, R. Bianconi, ... and S. Galmarini (2012), Evaluation of the meteorological forcing used for the Air Quality Model Evaluation International Initiative (AQMEII) air quality simulations. Atmospheric Environment, 53, 15-37.

Walko, R. L. Band, L. E. Baron, J. Kittel, T. G. F. Lammers, R. Lee, T. J. Ojima, D. Pielke, R. A. Taylor, and C. Tague (2000), Coupled Atmosphere-Biophysics-Hydrology Models for Environmental Modeling, J. Appl. Meteor., 39(6), 931-944.

Wang, S. X., M. Zhao, J. Xing, Y. Wu, Y. Zhou, Y. Lei, K. B. He, L. X. Fu, and J. M. Hao (2010), Quantifying the air pollutants emission reduction during the 2008 Olympic Games in Beijing, Environ. Sci. Technol., 44, 2490-2496.

Wanner, W., X. Li, and A. H. Strahler (1995), On the derivation of kernels for kernel-driven models of bidirectional reflectance, J. Geophys. Res., 100, 21,077– 21,090.

Wesely, M. L., J. A. Eastman, D. H. Stedman, and E. D. Yalvac (1982), An eddy correlation measurement of NO_2 flux to vegetation and comparison to O_3 flux, Atmos. Environ., 16, 815-820.

Xiu, A. and J. E. Pleim (2001), Development of a Land Surface Model. Part I: Application in a Mesoscale Meteorological Model, J. Appl. Meteor., 40, 192-209.

Yang, F., K. Mitchell, Y. T. Hou, Y. Dai, X. Zeng, Z. Wang, and X. Z. Liang (2008), Dependence of land surface albedo on solar zenith angle: Observations and model parameterization, Journal of applied meteorology and climatology, 47(11), 2963-2982.

Yang, W., N. V. Shabanov, D. Huang, W. Wang, R. E. Dickinson, R. R. Nemani, Y. Knyazikhin, and R. B. Myneni (2006a), Analysis of leaf area index products from combination of MODIS Terra and Aqua data, Remote Sensing of Environment, 104(3), 297-312.

Yang, W., B. Tan, D. Huang, M. Rautiainen, N. V. Shabanov, Y. Wang, J. L. Privette, … and R. B. Myneni (2006b), MODIS leaf area index products: From validation to algorithm improvement, Geoscience and Remote Sensing, IEEE Transactions, 44(7), 1885-1898.

CHAPTER 3: IMPROVED METEOROLOGY FROM AN UPDATED WRF/CMAQ MODELING SYSTEM WITH MODIS VEGETATION AND ALBEDO[2]

Abstract

Realistic vegetation characteristics and phenology from the Moderate Resolution Imaging Spectroradiometer (MODIS) products improve the simulation for the meteorology and air quality modeling system WRF/CMAQ (Weather Research and Forecast model and Community Multiscale Air Quality model) that employs the Pleim-Xiu land surface model (PX LSM). Recently, PX LSM WRF/CMAQ has been updated in vegetation, soil, and boundary layer processes resulting in improved 2 m temperature (*T*) and mixing ratio (*Q*), 10 m wind speed, and surface ozone simulations across the domain compared to the previous version for a period around August 2006. Yearlong meteorology simulations with the updated system demonstrate that MODIS input helps reduce bias of the 2 m *Q* estimation during the growing season from April to September. Improvements follow the green up in the southeast from April and move towards the west and north through August. From October to March, MODIS input does not have much influence on the system because vegetation is not as active. The greatest effects of MODIS input include more accurate phenology, better representation of leaf area index (LAI) for various forest ecosystems and agricultural areas, and realistically sparse vegetation coverage in the western drylands. Despite the improved meteorology, MODIS input causes higher bias for the surface O_3 simulation in April, August, and September in areas where MODIS LAI is much

[2] This chapter is accepted as an article in the Journal of Geophysical Research: Atmospheres in January 2016. The article is submitted as: Ran, L., J. Pleim, R. Gilliam, F. S. Binkowski, C. Hogrefe, and L. Band "Improved Meteorology from an Updated WRF/CMAQ Modeling System with MODIS Vegetation and Albedo".

less than the base LAI. Thus, improvements may be needed in the CMAQ dry deposition model for low LAI areas where deposition on the soil surface becomes important.

3.1 Introduction

Air quality (AQ) modeling systems are generally composed of three major components representing emissions, meteorology, and chemical transport and transformation. The National Center for Atmospheric Research (NCAR) Weather Research and Forecast (WRF) model [*Skamarock et al.*, 2008] and the United States (U.S.) Environmental Protection Agency (EPA) Community Multiscale Air Quality (CMAQ) model [*Byun and Schere*, 2006] – WRF/CMAQ, is an important combined meteorology and air quality modeling system which has been used around the world for various AQ and climate studies as well as policy development [*Wang et al.*, 2010; *Compton et al.*, 2011; *Hogrefe et al.*, 2014; *Xing et al.*, 2015]. The accuracy of the modeling system depends not only on the completeness of the model algorithms for key processes but also the accuracy of input data including emission sources, meteorology and AQ initial and boundary conditions, and geospatial data describing surface characteristics such as land cover, vegetation, and albedo. Improving spatial and temporal distributions of modeled air pollutant concentrations and deposition in WRF/CMAQ is an ongoing effort [e.g., *Pleim at al.*, 2013; *Sarwar et al.*, 2014] because uncertainties still exist [*Foley et al.*, 2010; *Appel et al. 2011a*] in many components of this complex modeling system including emissions, transport, photochemistry, and land surface exchange. Our research aims to use spatial and temporal land surface data generated from the Moderate Resolution Imaging Spectroradiometer (MODIS) vegetation and albedo products to improve the land surface model (LSM) processes, which simulates the exchange of heat, moisture, momentum, and trace atmospheric chemicals between the land surface and the atmosphere in retrospective WRF/CMAQ modeling.

Among the LSMs available in WRF, the Pleim-Xiu (PX) LSM [*Pleim and Xiu*, 1995; *Xiu and Pleim*, 2001] is often used in retrospective WRF/CMAQ simulations [*Appel et al.*, 2011a; *Rogers et al.*, 2013; *Hogrefe et al.*, 2014] because it is mainly designed for air quality simulations where the WRF LSM parameters (e.g. stomatal and aerodynamic resistances) are consistently used in the CMAQ dry deposition model. In addition, the same planetary boundary layer (PBL) model, the Asymmetric Convective Model version 2 (ACM2) [*Pleim*, 2007a, 2007b], can be used in both WRF and CMAQ consistently. The PX LSM was developed based on the Interactions Soil Biosphere Atmosphere (ISBA) LSM model from Meteo-France and originally designed for mesoscale meteorology modeling [*Noilhan and Planton*, 1989; *Noilhan and Mahfouf*, 1996]. Following the consideration by *Noilhan and Planton* [1989] to minimize the parameters required in describing the physics (particularly for soil processes with many uncertainties and heterogeneities within the mesoscale grid scale), PX LSM has relatively simple process schemes with a modified ISBA Jarvis-type stomatal conductance approach [*Jarvis*, 1976] and two-layer soil model (top 1 cm and the 1 m whole soil column) using the force restore algorithm to estimate soil temperature [*Bhumralkar*, 1975; *Blackadar*, 1976] and moisture [*Deardorff*, 1977]. A simple indirect data assimilation scheme is used for retrospective meteorology simulations where soil moisture and temperature are continuously adjusted to minimize model errors in 2 m temperature (T) and mixing ratio (Q), compared to observed surface analyses with nudging coefficients based on model parameters such as solar radiation, temperature, leaf area, vegetation coverage, and aerodynamic resistance [*Pleim and Xiu*, 2003; *Pleim and Gilliam*, 2009], in contrast with the statistically derived data assimilation functions [*Mahfouf*, 1991; *Bouttier et al.*, 1993; *Douville et al.*, 2000] used in ISBA. While the nudging coefficients are designed to be most effective when the coupling between the soil and the air is

strongest (i.e. when surface fluxes are large), there can occasionally be other model errors, such as erroneous modeled precipitation or cloud cover, that cause the indirect soil data assimilation scheme to degrade results. Despite these issues, continuously adjusting soil moisture and temperature in PX LSM based on re-analysis fields effectively reduces overall errors in simulating surface 2 m *T* and *Q* as well as 10 m wind [*Rogers et al.*, 2013; *Carvalho et al*., 2014].

Improvements to LSMs can be approached from two directions. One is by including sufficiently realistic representations of physical processes including slow vegetation processes such as those in Earth system models [*Bonan et al.*, 2011; *Clark et al.*, 2011; *Niu et al*., 2011; *Kowalczyk et al.*, 2013; *Oleson et al.*, 2013]. The other is by parameter constraints or data assimilation based on ground or satellite observations to have more realistic surface representation and to optimize parameter estimation [*Douville et al.*, 2000; *Pleim and Gilliam*, 2009; *Moore et al.*, 2010; *Baker et al.*, 2010; *Lawrence et al.*, 2011; *Barbu et al.*, 2011; *Dee et al.*, 2011; *Ran et al.*, 2015]. *Prentice et al.* [2015] suggests that the dominant paradigm in current generation LSM development emphasizes too much on realistic representation of physical processes including unknown variability at the expense of model reliability and robustness. They propose that parameter constraints for biological and hydrological processes with unknown variability and data assimilation techniques for model evaluation and enhancement should be included in the next-generation LSMs. For retrospective WRF/CMAQ simulations, the proposed direction is particularly relevant because reliability and accuracy are key goals of the modeling system that is often used as an air quality policy decision support tool.

Leaf area index (LAI), vegetation fraction (VF), and surface albedo are important parameters controlling surface energy partitioning, latent heat (LH) and sensible heat fluxes, and

the deposition of various atmospheric gases and particles in WRF/CMAQ. ,Many studies have demonstrated a benefit of using satellite surface data for more accurate model parameters that improve model performance [*Liang et al.*, 2005; *Alton*, 2009; *Baker et al., 2010*; *Lawrence et al.*, 2011; *Moore et al.*, 2010; *Barbu et al*., 2011; *Boussetta et al.*, 2015]. Despite many satellite surface products currently available in near real-time, retrospective WRF/CMAQ simulations for studies related to air quality assessment, policies, and applications [*Eder et al.*, 2009; *Kelly et al.*, 2014; *Hogrefe et al.*, 2014] still use vegetation parameters and surface albedo that are specified in LSM look-up tables and rely on simple deep soil temperature dependent functions to model plant phenological dynamics [*Xiu and Pleim*, 2001]. *Ran et al.* [2015] evaluated LAI, VF, and surface albedo prescribed in the current PX LSM look-up tables in comparison with the Moderate Resolution Imaging Spectroradiometer (MODIS) vegetation parameters and surface albedo and against ground measurement data. They show that the current PX LSM intentionally exaggerates LAI and VF in arid regions in order to have more effective soil moisture nudging in simulating 2 m *T* and *Q*. The PX LSM simple seasonal LAI and VF adjustment fails to capture the western dryland vegetation patterns because greenness in the west is mainly controlled by available moisture rather than temperature during dry and hot seasons (summer and autumn). In contrast, seasonal and spatial vegetation variations are well captured in MODIS data, particularly in the north and west regions. In addition, the MODIS vegetation data captures more spatial heterogeneity than the land use category based lookup tables, which can influence model bulk results. Their evaluation also shows that albedo from the current PX LSM WRF lacks diurnal and seasonal variation with changing solar zenith angle (SZA) and land surface properties. Compared with the albedo calculated in the current PX LSM WRF, MODIS albedo does well in describing the heterogeneous surface for areas without snow coverage. However, the evaluation

of incorporating MODIS LAI, fraction of absorbed photosynthetically active radiation (FPAR) (used as surrogate for VF), and albedo into WRF/CMAQ simulations for more than a month summer period in 2006 show mixed results with overall reduced bias and error in *Q* but greater bias and error in *T*. The raised *T* and reduced ozone dry deposition velocities in the much less vegetated western North America resulted in higher ozone estimation. The mixed results from the WRF/CMAQ simulations with more accurate MODIS surface representation suggest that improvements may be needed in the surface physics of the modeling system [*Ran et al.*, 2015].

The most recent version of the WRF/CMAQ modeling system developed at EPA since the study by *Ran et al.* [2015] has improvements and updates in the soil, vegetation, and planetary boundary layer (PBL) processes [*Pleim et al., 2015*]. This research presented here furthers the work by *Ran et al.* [2015] through using the improved WRF/CMAQ for an annual simulation. The goal of this study is to apply year-long MODIS LAI, FPAR, and albedo to the updated WRF/CMAQ system and demonstrate the benefit of using the annual MODIS data with realistic spatial and temporal surface and vegetation variations (e.g. phenology). The questions which the papers addresses are: (i) how does MODIS input influence the updated WRF/CMAQ modeling system meteorology (*T*, *Q*, and wind speed) , (ii) does phenology from MODIS vegetation help improve meteorology simulations over the changing seasons, and (iii) how does MODIS input influence air quality simulations in the updated system (O_3)? The study focuses on the annual WRF simulations and a subset of CMAQ simulations over three selected periods in spring, summer, and fall of 2006 using a U.S. 12-km grid domain. The improvements to the vegetation and soil processes in the WRF/CMAQ system since the study by *Ran et al.* [2015] are presented in section 2. The methodologies, MODIS vegetation and albedo data, and ground measurements used in the model simulations and evaluation are described in section 3. Results

and analyses are presented in section 4 with simulated yearlong meteorology and three season AQ results using the improved system comparing simulations that used table-prescribed surface data to simulations using MODIS inputs. Both model runs are evaluated in detail against ground measurements and the simulation results from the previous research by *Ran et al.* [2015] to show value added and limitations of the revised model. The last section presents conclusions and future plans.

3.2 Vegetation and Soil Process Improvements

The updated WRF/CMAQ contains changes to vegetation and soil processes in the PX LSM as well as to PBL processes in ACM2 [*Pleim et al.*, 2015]. The improvements to the vegetation and PBL processes are included in the releases of WRF version 3.7 (WRF v3.7) and CMAQ version 5.1 (CMAQ v5.1). The description of changes to the ACM2 PBL processes are outlined by *Pleim et al.* [2015]; but the modifications to vegetation and soil processes in PX LSM are described in detail here. An essential function of LSMs is partitioning of net radiation absorbed at the surface into sensible heat flux (H), LH flux (λE), which is expressed as the product of LH of evaporation (λ) times evaporative water flux (E, also called evapotranspiration - ET), and ground heat flux (G). ET includes evaporation from biotic leaf transpiration and abiotic water evaporation from soil pores, plant litters, open water bodies, and leaf cuticle surfaces [*Bonan*, 2008]. In heavily vegetated areas, such as forest and agriculture lands, transpiration is usually the dominant pathway for ET [*Budyko*, 1974] during the growing season. The importance of ET is well recognized not only in atmospheric processes related to the surface energy budget but also hydrologic processes related to the water cycle. Changes to LSM vegetation and soil processes affect H, λE, and G estimations and in turn influence convective turbulence which vertically mixes heat, moisture, momentum, and air pollutants within the PBL

and dilutes ground level concentration [*Wyngaard,* 2010]. Uplifted LH by atmospheric turbulence may be released to the atmosphere at higher altitude during condensation to form clouds that may result in precipitation [*Sellers et al.*, 1997; *Pielke et al.*, 1998].

3.2.1 Vegetation Processes

The stomatal conductance is a crucial parameter in estimating not only ET from biotic leaf transpiration [*Katul et al.*, 2012] but also atmospheric chemicals including CO_2 and gas-phase chemical species such as O_3 and NH_3 [*Pleim and Ran,* 2011]. The PX LSM treats the whole canopy as a single leaf (big-leaf model) in modeling a canopy stomatal conductance (G_c) to gasses following the Jarvis approach at the leaf scale [*Jarvis,* 1976], presented in the ISBA LSM [*Noilhan and Planton,* 1989] with modifications [*Pleim and Xiu,* 1995] as:

$$G_c = LAI * \left[\frac{1}{R_{st\min}} F_1(PAR) F_2(w_2) F_3(RH_s) F_4(T_{ic}) \right] \tag{3.1}$$

where R_{stmin} as well as R_{stmax} in the following equation 3.2 are the minimum and maximum stomatal resistances for each land cover type specified in the LSM land cover lookup tables. The functions F_{1-4} represent the fractional degree (0 to 1) of stomatal closure caused by the environmental factors: photosynthetically active radiation (*PAR*), root-depth soil moisture (w_2), relative humidity at the leaf surface (RH_s), and air temperature in the canopy (T_{ic}). Different from the original Jarvis approach, the influence of ambient CO_2 concentration is not included in the modified approach with the assumption that the CO_2 concentration is constant for relatively short period mesoscale meteorology simulations. F_1 measures the impact of *PAR* (light intensity) on stomatal conductance or photosynthesis and is computed in the original PX LSM as:

$$F_1 = \frac{R_{st\min} / R_{st\max} + f}{1 + f} \tag{3.2}$$

with

$$f = \frac{PAR}{R_{gl}} \frac{2}{LAI}, \quad PAR = 0.55 R_g$$

where R_{gl} is a limiting factor with 30 (W m^{-2}) for forest types and 100 (W m^{-2}) for other vegetation types and R_g is the incoming solar radiation at the surface. In the new version of the PX LSM in WRF v3.7, the F_1 function is changed to:

$$F_1 = MAX\left[\frac{Rst\,\min}{Rst\,\max}, F_{1\max}\left(\frac{2}{1+\exp(-0.014PAR)} - 1\right)\right] \tag{3.3}$$

with

$$F_{1\max} = 1.0 - 0.03LAI, \quad \text{if } R_{st\,\min} > 130 \text{ (for forest types)}$$

$$F_{1\max} = 1.0 - 0.05LAI, \quad \text{if } R_{st\,\min} \le 130 \text{ (for other vegetation types)}$$

$$PAR = 0.45 R_g$$

where *PAR* is changed to be 45% of solar radiation at the ground, which is a fraction commonly used and close to values reported in many studies [*Weiss and Norman*, 1985; *Yu et al.*, 2015]. The function was developed based on the relationship of gross primary production with *PAR* measurements shown by *Clark et al.* [2011] and the relationship of stomatal conductance with *PAR* measurements displayed by *Bonan* [2008]. Figure 3.1 displays the change of original *F1* (F1_old) and improved *F1* (F1_new) functions with R_g. The reason for changing the *F1* function is to slightly reduce G_c in low solar radiation regimes, particularly during the evening transition [*Pleim et al.*, 2015]. Thus, a reduced G_c will result in lower LH flux and more energy can be partitioned into sensible heat to delay the evening transition to stable conditions. Thus, the improved function can help reduce wet bias tendency of 2 m *Q* and maintain atmosphere mixing longer during the evening transition in WRF/CMAQ thereby mitigating the tendency of

WRF/CMAQ to overestimate emitted pollutants near surface concentrations (e.g. NOx) and underestimate ozone.

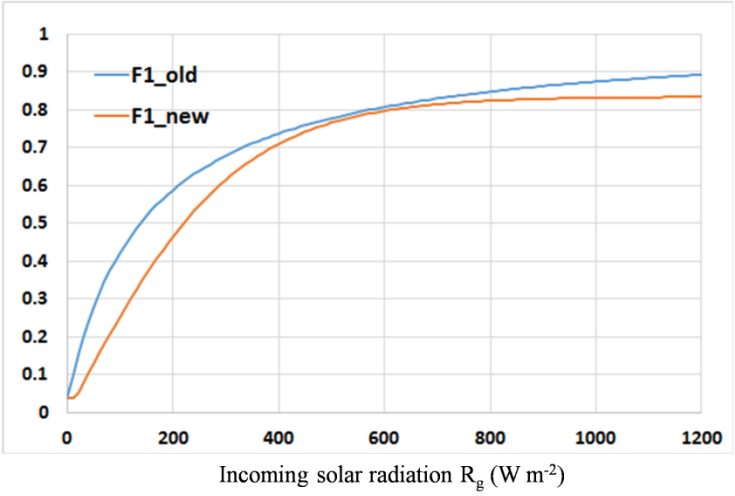

Figure 3.1. Original (F1_old) and improved (F1_new) *F1* functions with incoming solar radiation R_g (W m^{-2}) in the PX LSM Jarvis stomatal conductance function. *F1* (scalar) represents the impact of R_g on stomatal conductance or photosynthesis when other factors are at optimal conditions. *F1* is computed for broadleaf forest type with assumed R_{stmin}=200 (s m^{-1}), R_{stmax}=5000.0 (s m^{-1}), and LAI=5.5(m^2 m^{-2}).

Vegetation heat capacity is reduced in the PX LSM to mitigate observed model warm bias in daily low temperature (e.g. predawn) and cold bias during warming up hours in the post-dawn morning. The surface temperature equation in the force-restore model used in the PX-LSM is taken directly from the ISBA LSM [*Noilhan and Planton*, 1989] as,

$$\frac{\partial T_g}{\partial t} = C_t G(t) - \frac{2\pi}{\tau}(T_g - T_2) \tag{3.4}$$

where T_g is the surface soil layer (1 cm) temperature and T_2 is the deep soil layer (1 m) temperature, $G(t)$ is the surface energy forcing and τ is the diurnal time scale. C_t is a coefficient

that is inversely proportional to heat capacity and can be derived from the force-restore model [*Bhumralkar*, 1975; *Blackadar*, 1976] as:

$$C_t = \frac{2}{cd\alpha} \text{ , with } d = \left(\frac{\lambda}{c\pi}\right)^{1/2} \tag{3.5}$$

where c is the volumetric heat capacity, d is the damping depth of the diurnal temperature wave, α is set to 1, and λ is the thermal conductivity. The grid cell surface soil and vegetation heat capacity coefficient (C_t) in the PX LSM is computed based on area-weighted parameters for soil (C_g) and vegetation (C_v) as:

$$C_t = \left(\frac{1 - vegF}{C_g} + \frac{vegF}{C_v}\right)^{-1} \tag{3.6}$$

where *vegF* is the vegetation fraction for a grid cell. C_g is a function of deep soil moisture and soil texture type as described by *Noilhan and Mahfouf* [1996]. Previous versions of the PX LSM set C_v to an empirical value of 8×10^{-6} K m^2 J^{-1} based on the value used by *Giard and Bazile* [2000]. As vegetation canopy characteristics changes spatially and seasonally with different vegetation types, the empirical value C_v contains great uncertainty. The value was first defined in the ISBA LSM as 3×10^{-3} K m^2 J^{-1} [*Noilhan and Planton*, 1989] and later revised to 2×10^{-5} K m^2 J^{-1} [*Manzi and Planton*, 1994]. In the new version of the PX LSM in WRF v3.7, C_v is computed from equation 3.5 using the high end of the ranges of the leaf mass density, specific heat, and thermal conductivity reported by *Jayalakshmy and Philip* [2010] resulting in a value of $C_v = 1.2\times10^{-5}$ K m^2 J^{-1}.

3.2.2 Soil Processes

Soil resistance is a crucial parameter in controlling ET from the bare-soil surface in LSMs and as a result it influences soil moisture as well as the water cycle in both atmosphere

and the land surface [*Camillo et al.*, 1986; *Sellers et al*., 1992]. Evaporation from the soil surface (E_g) in the PX LSM is estimated as:

$$E_g = \rho_a (1 - vegF) \frac{q_{sat}(T_{ss}) - q_a}{R_a + R_{bw} + R_s} \tag{3.7}$$

where ρ_a is the density of dry air, $q_{sat}(T_{ss})$ is the saturated water vapor mixing ratio at the soil surface temperature (T_{ss}), q_a is the water vapor mixing ratio at the lowest atmospheric layer, R_a is the aerodynamic resistance, R_{bw} is the quasi-laminar boundary layer resistance for water vapor, and R_s is the soil resistance. In the release of WRF v3.7, R_s is computed based on the empirical so-called β factor from *Lee and Pielke* [1992] as:

$$R_s = R_{aw}\left(\frac{1}{\beta} - 1\right) \tag{3.8}$$

with

$$\beta = \frac{1}{4}\left[1 - \cos\left(\frac{w_g}{w_{fc}}\pi\right)\right]^2 \quad \text{for } w_g < w_{fc}; \quad \beta = 1 \quad \text{for} \quad w_g \geq w_{fc} \tag{3.9}$$

where $R_{aw} = R_a + R_{bw}$ for water vapor and β is a function of the volumetric water content of the top soil layer (w_g) and at the field capacity (w_{fc}). The β based soil resistance formulation is commonly used in large scale LSMs such as the Community Land Model version 4.5 [*Oleson et al.*, 2013] because of its simplicity. The problem with the β based soil resistance is that the resistance approaches to zero too fast with increasing soil water content such that $R_s = 0$ for $w_g \geq w_{fc}$ (figure 3.2). While this might be realistic at a specific homogenous site, a more gradual function is preferable for representation of large area grid cells which implicitly include a significant amount of soil moisture heterogeneity. The improved WRF uses the surface resistance based on the Fick's diffusion, which is presented by *Sakaguchi and Zeng* [2009] as:

$$R_s = \frac{L_s}{D_s} \tag{3.10}$$

with

$$L_s = \frac{d_1}{e-1}\left[\exp\left\{(1 - w_g / w_{sat})^w\right\} - 1\right] \tag{3.11}$$

$$D_s = D_0 w_{sat}^2 \left(1 - \frac{w_{res}}{w_{sat}}\right)^{2+3b} \tag{3.12}$$

where L_s is the estimated dry layer path length as a function of soil water content relative to saturation (w_{sat}) [*Kondo et al.*, 1990], d_1 is the top soil layer thickness which is set to 1.75 cm, e is the constant 2.71828, and w is a parameter which controls the concavity of the curve and is set to 5 for the exponential shape. D_s is the reduced vapor diffusivity ($m^2\ s^{-1}$) in the soil based on *Moldrup et al.* [1999]. D_0 is the molecular diffusion coefficient of water vapor in the atmosphere and is set to a constant $2.59 \times 10^{-5}\ m^2\ s^{-1}$. w_{res} is the residual water content which is computed based on the formulation by *Rawls et al.* [1982]. b is the slope of the retention curve varying with soil texture and is estimated based on the formation described by *Noilhan and Mahfouf* [1996]. In the current release of WRF v3.7, b is specified in the LSM lookup tables according to *Noilhan and Planton* [1989]. As displayed in figure 3.2, the soil resistance (green line) computed based on the Fick's diffusion formulation by *Sakaguchi and Zeng* [2009] tails off more gradually when soil is approaching to field capacity where the formulations by *Kondo et al.* [1990] and *Lee and Pielke* [1992] have almost no resistance. This adopted soil resistance, which lies between the formulations of *Sellers et al.* [1992] and *Lee and Pielke* [1992], is also adapted and well tested in the CMAQ bi-directional NH_3 model with field measurements [*Pleim et al.*, 2013].

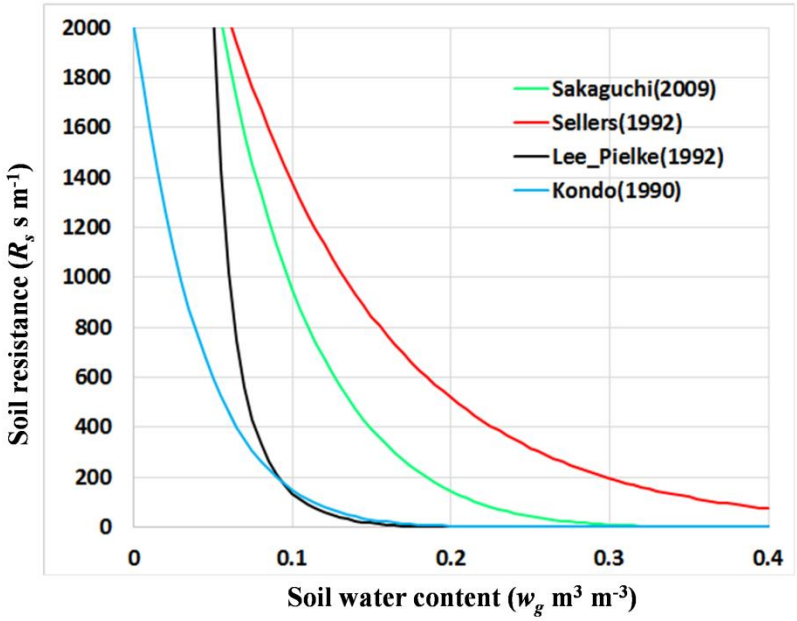

Figure 3.2. Comparison of soil resistances computed based four formulations described by *Sakaguchi and Zeng* [2009], *Sellers et al.* [1992], *Lee and Pielke* [1992], and *Kondo et al.* [1990] for sandy loam soil. Soil resistances are computed with w_{fc}=0.195 m^3 m^{-3}, w_{sat}=0.435 m^3 m^{-3}, w_{res}=0.01 m^3 m^{-3}, b=4.9, d_1=1.75 cm, and R_{aw}=50 s m^{-1}.

3.3 Data and Methods

2006 MODIS LAI, FPAR and albedo data, obtained freely from the U.S. National Aeronautics and Space Administration (NASA) web site, are averaged over the WRF/CMAQ model 12-km grid cells and stored in a netCDF file for WRF simulations. WRF/CMAQ simulations are conducted for two scenarios with/without MODIS input using improved WRF version 3.4 (WRF v3.4) and CMAQ version 5.0.2 (CMAQ v 5.0.2) models with the physics options typically configured for EPA AQ simulations [*Gilliam and Pleim*, 2010; *Hogrefe et al*., 2014]. Detailed information on MODIS products used and WRF/CMAQ physics configurations is also presented in the study by *Ran et al*. [2015]. The meteorology and air quality simulation results are statistically analyzed and visualized in comparison with observations and the

simulations performed by *Ran et al.* [2015] using the Atmospheric Model Evaluation Tool (AMET) [*Gilliam et al*,. 2005; *Appel et al.*, 2011b]. The evaluation analysis does not apply any interpolation or adjustments to account for the difference between the site observations and the model results at the grid cell level.

3.3.1 MODIS Data

Gap-filled and smoothed 2006 MODIS Collection 5 LAI and FPAR data (MOD15A2GFS) [*Gao et al.*, 2008; *Myneni et al*., 2011] from the U.S. North American Carbon Program are used for WRF/CMAQ simulations. The MODIS LAI and FPAR data at 1-km resolution and every 8 days are re-gridded onto the WRF/CMAQ 12-km grid cells at daily time steps with constant LAI and FPAR values for each 8 day period. As the PX LSM uses an averaged LAI value for the vegetation area of a model cell, gridded MODIS cell-averaged LAI is divided by gridded MODIS FPAR, which is used as a surrogate for vegetation cover fraction [*Los et al.*, 2000; *Mu et al.*, 2011]. Uncertainties exist in the MODIS products because they are derived from snap shot reflectance measurements which contain aerosol, cloud, and snow contaminations [*Yang et al.*, 2006; *Fensholt et al.*, 2004; *Cohen et al.*, 2006]. For example, cloud or snow contaminations could cause unrealistic temporal variations in MODIS LAI during the growing and winter seasons. Nevertheless, MODIS LAI data shows relative good qualities in comparison with other LAI products as demonstrated by *Fang et al.* [2013]. The gap-filled and smoothed MODIS LAI and FPAR products are selected to be used in yearlong WRF simulations for spatial and temporal continuity and consistency.

MODIS albedo products contain isotropic, volumetric and geometric scattering parameters which are derived using a kernel-based semi-empirical bidirectional reflectance distribution function (BRDF) model [*Wanner et al.*, 1995*; Lucht et al.*, 2000; *Schaaf et al.*, 2002,

2011]. 2006 MCD43A1 MODIS BRDF/albedo parameters for the shortwave (0.3-5.0μm) and corresponding MCD43A2 MODIS BRDF/albedo quality product at 500 m resolution and every 8 days with the following 16 days of MODIS surface reflectance input are used in the WRF PX LSM at daily time steps with constant parameters for each 8 day period. Black-sky albedo (directional-hemispherical reflectance - direct) and white-sky albedo (bi-hemispherical reflectance - diffuse) are computed in PX LSM with the three MODIS BRDF/albedo parameters and changing SZA using simple polynomial equations [*Lucht et al.*, 2000; *Schaaf et al.*, 2011]. Then, the blue-sky albedo (actual hemispherical reflectance), is calculated based on computed black-sky and white-sky albedos weighted by diffuse radiation fraction [*Lewis and Barnsley*, 1994]. MODIS snow cover cells identified from the BRDF/albedo quality product are filtered out in averaging albedo parameters for WRF/CMAQ modeling grid cells because of high uncertainties in MODIS albedo products over snow areas [*Gao et al.*, 2011].

3.3.2 WRF and CMAQ Modeling

The updated WRF v3.4 and CMAQ v5.0.2 which also take MODIS LAI, FPAR, and albedo input are used for this study. The input of gridded MODIS LAI, FPAR, and three albedo parameter data are specified through the WRF namelist control. The final albedo in the PX LSM is weighted by the fractional snow coverage with the WRF snow albedo based on the daily snow analyses. The WRF simulations use the 12-km North American Model (NAM) data for lateral boundary conditions. The CMAQ simulations use the chemical boundary conditions that are generated from the Monitoring Atmospheric Composition and Climate Interim Implementation (MACC-II) as described by *Innes et al.* [2013] and used for the Air Quality Model Evaluation International Initiative (AQMEII) Phase 2 study [*Hogrefe et al.*, 2014]. The key WRF physics options are the PX LSM scheme with indirect soil nudging [*Pleim and Xiu*, 2003; *Pleim and*

Gilliam, 2009], the WRF Rapid Radiative Transfer Model for GCMs (RRTMG) radiation model [*Iacono et al*., 2008], the Asymmetric Convective Model version 2 (ACM2), for PBL [*Pleim*, 2007a, 2007b], version 2 of the Kain–Fritsch (KF2) cumulus parameterization [*Kain*, 2004], and the Morrison double-moment cloud microphysics scheme [*Morrison et al.*, 2009]. Grid nudging or Four-Dimensional Data Assimilation (FDDA) [*Staufer and Seaman*, 1990; *Stauffer et al.*, 1991] was used above the PBL. The WRF output is processed using the Meteorology-Chemistry Interface Processor (MCIP) [*Otte and Pleim*, 2010] version 4.1.3 for CMAQ. The CMAQ simulations use 2006 CMAQ-ready emission data which are generated for the AQMEII Phase 2 study [*Pouliot et al.*, 2014]. The AQ simulations are configured with the Carbon Bond mechanism CB05 for gas-phase chemistry [*Whitten et al*., 2010], aerosol 6 module (AE6) [*Binkowski and Roselle*, 2003], and in-line point source, biogenic and dust emissions. 2006 National Land Cover Database (NLCD) at 30 m resolution for the U.S. and MODIS land cover data at 500 m resolution for the areas outside the U.S. are processed into 40 land cover types for the PX LSM using the Spatial Allocator Raster Tools [*Ran and Hanna*, 2014].

The CMAQ 12-km domain with 299 by 459 grid cells is nested within the WRF 12-km domain with 311 by 471 grid cells that covers the conterminous U.S., southern Canada, and northern Mexico. The modeling system is configured with 35 vertical levels from the surface to the 50-hPA level. The WRF simulations are conducted from 27 December 2005 to 31 December 2006 and CMAQ AQ is simulated for three selected periods of 25 March to 30 April, 25 July to 31 August, and 24 September to 31 October 2006. Two WRF scenarios are conducted as follows: (i) Base case: standard WRF and (ii) MODIS case: modified WRF with MODIS LAI, FPAR, albedo parameter input. Two CMAQ scenarios for each CMAQ period are performed as follows: (i) Base case: CMAQ with standard WRF meteorology and (ii) MODIS case: CMAQ

with WRF MODIS case meteorology. Excluding a few days at the start of the simulations for spin-up, WRF output for 2006 and CMAQ output for April, August and October are used in evaluation and analysis. Observation data from the Meteorological Assimilation Data Ingest System (MADIS) at the U.S. National Oceanic and Atmospheric Administration (NOAA) and the U.S. EPA Air Quality System (AQS) with other air quality network data are used for meteorology and air quality comparison and evaluation.

3.4 Data and Methods

Meteorology and AQ results are first evaluated in comparison with the simulations conducted in the previous study by *Ran et al.* [2015] against observation data to assess the impact of the updated WRF/CMAQ for this study. Then, the yearlong simulated meteorology and the air quality results for April, August, and October are presented and analyzed to assess influences of realistic surface seasonality from the MODIS input. The improved WRF/CMAQ with MODIS input does not have large impact on 10 m wind, ground level $PM_{2.5}$, and most other species concentrations and depositions based on overall monthly statistical evaluations. Thus, the comparison and evaluation for this paper mainly focus on 2 m T, 2 m Q, and surface O_3 in relationship with vegetation change as albedo has much less influence on the system in comparison with vegetation [*Ran et al*, 2015]. The simulated meteorology and air quality are compared with surface-based point measurements following standard evaluation methods proposed and used by many other studies [e.g., *Gego et al.*, 2005; *Gilliam et al.*, 2006; *Vautard et al.*, 2012; *Appel et al.*, 2011]. Model performance is evaluated using statistical metrics such as mean bias (MB), difference of absolute mean biases (DAMB), mean absolute error (MAE), difference of mean absolute errors, (DMAE), root mean squared error (RMSE), and standard deviation (StDev).

3.4.1 Assessment of Updated WRF/CMAQ

Table 3.1 shows domain-wide statistics metrics (MB, MAE, and StDev) for simulated 2 m *T*, 2 m *Q*, and 10 m wind speed (WS) using the WRF in the previous study and the updated WRF against MADIS observations over the period from 10 August to 9 September 2006. Overall, the MB, MAE, and StDev for the simulated variables are similar for the base and MODIS scenarios using the same WRF model and they are well within typical model performance benchmarks [e.g. *Gilliam et al.,* 2006]. Simulated 2 m *T*, 2 m *Q*, and 10-m WS from the updated WRF for both the base and MODIS cases show clear improvements with reduced MB, MAE, and StDev. Particularly, using the updated WRF, 2 m *T* and *Q* show much reduced MAE and MB and 10 m WS has almost no bias. Most importantly, MODIS input in the updated WRF does not result in much higher warm bias (0.168 K) for 2 m *T* in comparison with the base case (0.163 K), which is quite different from the previous WRF simulations with MB 0.607 K for the MODIS case and 0.415 K for the base case. While domain-wide statistics may mask regional differences, the spatial statistics plots shown below (figure 3.6) demonstrate that the 2 m T improved in all parts of the country. Similar to the previous WRF, using the MODIS input significantly reduces 2 m *Q* wet bias in the updated WRF simulation. In addition, the updated WRF reduces the wet bias (0.506 g kg^{-1}) in the previous base model to 0.359 (g kg^{-1}) in the updated base. This is consistent with the new soil resistance [*Sakaguchi and Zeng*, 2009] implemented for reducing soil ET when soil moisture is approaching and exceeding field capacity.

Table 3.1. Domain-wide statistical metrics for simulated 2 m T, 2 m Q, and 10 m WS using the previous WRF [Ran et al., 2015] and the updated WRF for the base and MODIS cases against MADIS observations over the period from 10 August to 9 September 2006.

WRF Simulations		2m T (K)			2m Q (g/kg)			10m WS (m/s)		
WRF	Scenario	StDev	MAE	MB	StDev	MAE	MB	StDev	MAE	MB
Previous	Base	1.981	1.520	0.415	1.676	1.313	0.506	1.603	1.219	0.109
Previous	MODIS	2.032	1.584	0.607	1.816	1.355	0.095	1.603	1.220	0.137
Updated	Base	1.927	1.447	0.163	1.603	1.239	0.359	1.573	1.199	0.056
Updated	MODIS	1.950	1.460	0.168	1.645	1.234	0.080	1.575	1.198	0.050

The diurnal performances of 2 m *T* and *Q* domain-wide using the updated WRF in comparison with the previous WRF are examined in figures 3.2 and 3.3. The warm bias at night and in the late afternoon from the left column of figure 3.3 has been reduced with the updated WRF (the right column) for both base and MODIS runs. The improvements in the updated WRF also help reduce 2 m *T* MAE for both the base and MODIS case simulations (not shown). With the updated WRF, 2 m *T* for the simulation with MODIS input has almost the same diurnal performance as the base simulation without MODIS input (only slightly warmer between 18 to 3 UTC).

The updated model did not change diurnal performance of 2 m *Q* greatly in comparison with the previous WRF although BIAS and MAE for 2 m Q show slight improvements between 17 and 1 UTC for the updated model with MODIS input (bottom row in figure 3.4). Both the base cases without MODIS input using the previous and updated WRF have wet bias over almost all hours (top row in figure 3.4); but lower wet bias over UTC 23 to 3 are observed in the updated WRF base simulations. MODIS input results in dryer conditions for both models, particularly between UTC 17 to 22 (early afternoon in the U.S. summer time) because of lower ET from less vegetation coverage in the MODIS LAI and FPAR products in comparison with the

base WRF PX LSM table-prescribed LAI and VF. With the realistic vegetation coverage from MODIS, the estimated 2 m *Q* has much reduced bias suggesting that the excessive LAI and VF in the base model over estimate transpiration

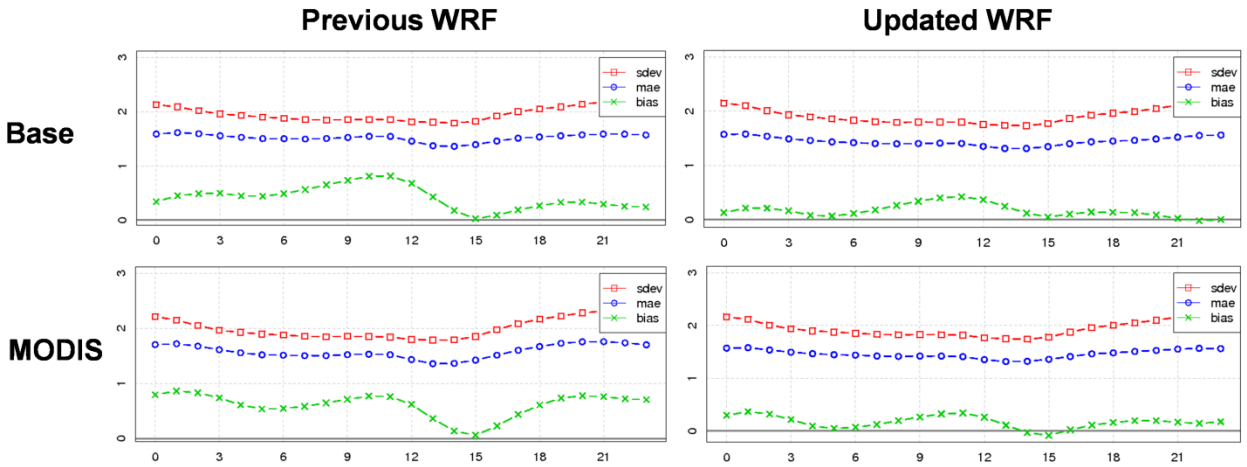

Figure 3.3. Diurnal domain-wide statistical metrics (y axis) for simulated 2 m *T* (K) against MADIS observations over the period from 10 August to 9 September 2006. The x axis is time of day with UTC hours. The left column is for the previous WRF [*Ran et al.*, 2015] and the right column is for the updated WRF. The top row is for the base case simulations without MODIS input and the bottom row is for the MODIS case simulations.

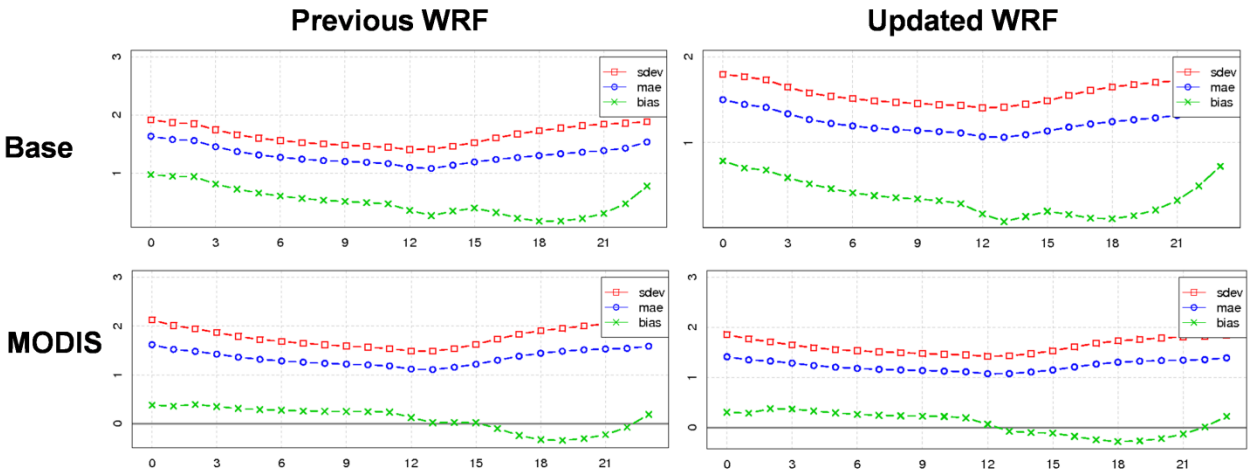

Figure 3.4. Diurnal domain-wide statistical metrics (y axis) for simulated 2 m *Q* (g kg^{-1}) against MADIS observations over the period from 10 August to 9 September 2006. The x axis is time of day with UTC hours. The left column is for the previous WRF [*Ran et al.*, 2015] and the right column is for the updated WRF. The top row is for the base case simulations without MODIS input and the bottom row is for the MODIS case simulations.

The spatial patterns of the model performance are evaluated by figures 3.5 and 3.6. The difference in the absolute MB for 2 m *T* and *Q* between the MODIS case and the base case using the previous WRF (left column) and the updated WRF (right column) for all MADIS observation sites averaged over 10 August to 9 September 2006 are displayed in figure 3.5. Figure 3.5 shows the improvement from the base to the MODIS case using the improved model in comparison with the base and MODIS case simulations conducted in the previous study. The impact of the improved model processes on 2 m *T* and *Q* is further examined spatially in figure 3.6 using MB, DAMB, and DMAE metrics to display the influence of the improved model using MODIS input in comparison with the previous model with the MODIS input. The absolute statistical metrics such as DAMB and DMAE used in figures 3.5 and 3.6 do not indicate which case is hotter or wetter at each site but rather which has more (displayed in purple) or less (in green) bias and

absolute error. The MB and MAE spatial plots for each case (not all displayed in the paper) are also evaluated for hotter/cooler, wetter/dryer, and better/worse indication.

It is clear that MODIS input has great impacts in the western drylands (figure 3.5) due to the great vegetation difference from the PX LSM table-prescribed LAI and VF which were intentionally exaggerated in the region [*Ran et al*., 2015]. The much higher DAMB (greater than 0.3) for both temperature and mixing ratio using the previous model (left column plots), which is the result of hotter and dryer estimations in this region from much lower VF and LAI in the MODIS input, has been reduced with the updated model (right column plots). The improved 2 m *T* performance with reduction in warm bias is particularly distinct from the west to the central Plains. With the updated model, the realistic surface representation from MODIS input helps improve 2 m *T* estimation for 56% of the MADIS sites in comparison with 26% of the sites from the previous model over the domain. Although the number of sites with 2 m *Q* MB improvement is very much the same for both models with MODIS input (around 64%, the bottom row in figure 3.5), the updated model helps reduce the dry bias in the west, particularly in the northwest. The improved processes in the updated model (particularly the updated soil resistance which was evaluated independently and not displayed in this paper), alleviate an inherent tendency of the previous model toward hot biases in the 2 m *T*. Thus, the updated model performs much better in estimating 2 m *T* in comparison with the previous model with MODIS input (figure 3.6) with overall domain wide warm bias and MAE reduction (around 78% of the sites with lower DAMB and DMAE in the top row of figure 3.6). The dry bias in the west and wet bias in the east along with MAE of 2 m *Q* with MODIS input are also reduced using the updated model for many sites (64% of the sites with lower DAMB and 80% of the sites with lower DMAE in the bottom row of figure 3.6).

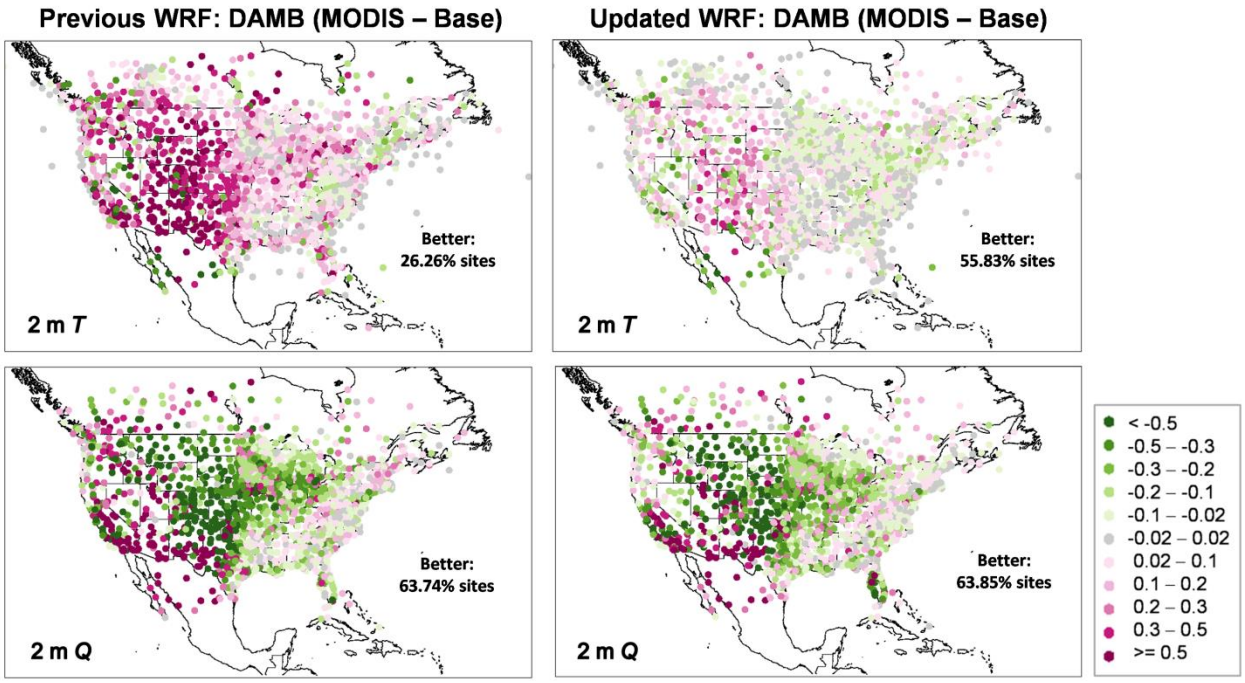

Figure 3.5. Spatial plots for the differences of the absolute mean biases (MODIS case – base case) for WRF simulations against MADIS observation sites over the period from 10 August to 9 September 2006. The left column is for the previous WRF [*Ran et al.*, 2015] and the right column is for the updated WRF. The top row is for 2 m *T* (K) and the bottom row is for 2 m *Q* (g kg^{-1}).

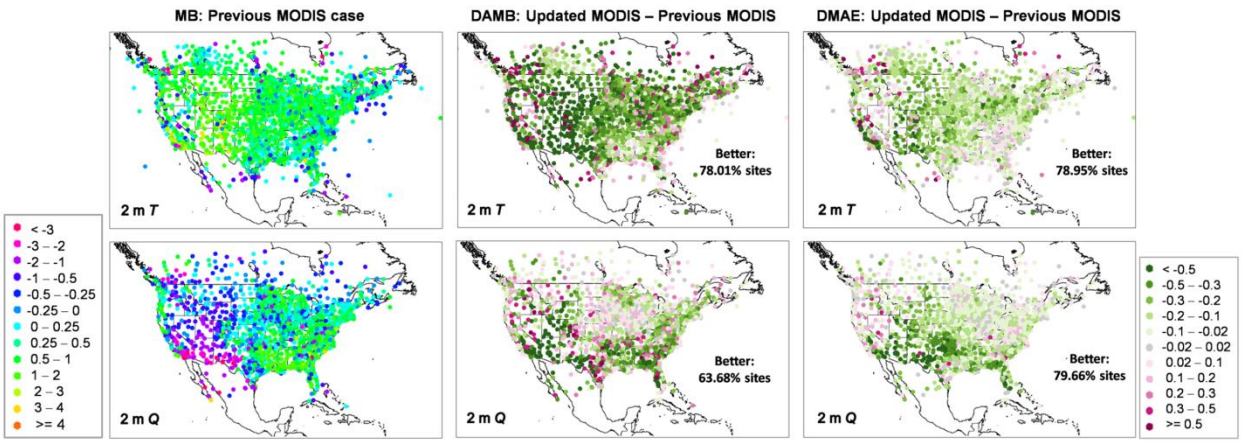

Figure 3.6. Spatial plots of statistical metrics for WRF simulations with MODIS input against MADIS observation sites over the period from 10 August to 9 September 2006. The left column is for the mean bias of the MODIS case using the previous model [*Ran et al.*, 2015], the middle column is for the difference of the absolute mean biases between the MODIS cases using the updated model and previous model, and the right column is for the difference of the mean absolute errors. The top row is for 2 m *T* (K) and the bottom row is for 2 m *Q* (g kg^{-1}).

The near surface ozone flux and concentration are greatly influenced by both the temperature (particularly day time) in the atmospheric boundary layer [*Rasmussen et al.*, 2012] and vegetation coverage because of a strong stomatal pathway of the ozone dry deposition flux [*Wesely et al*., 1982; *Padro*, 1996; *Fuentes et al*., 1992]. The improvement of 2 m *T* estimation with MODIS input using the updated model helps reduce errors in near surface ozone concentrations (figure 3.7). The domain average of the estimated daily maximum 8 h average O_3 (ppb) with MODIS input from using the updated WRF/CMAQ system (red line in the top graph of figure 3.7) against all AQS sites (black line) is reduced by 5.9 ppb on average (around 4 to 9 ppb reduction) from the previous model estimation (blue line) over the period from 10 to 30 August 2006. The DAMB spatial plot (bottom plot of figure 3.7) shows overall domain-wide bias reduction of the daily maximum 8-hour average O_3 (ppb) using the updated system with

MODIS input in comparison with the previous system for many AQS sites (in green and blue). Though many AQS sites (in grey) in the northeast show very little change for the modeled O_3, almost all AQS sites in the south, particularly the southwest where 2 m *T* and *Q* improve most, show great improvement of the O_3 estimation with more than 10 ppb bias reduction for many sites. In summary, with MODIS input the modeled ozone using the updated system has a reduced bias of 6.73 ppb and MAE of 10.4 ppb in comparison with the high bias of 12.6 ppb and MAE of 14.5 ppb in the previous system [*Ran et al*., 2015]. The MB and RMSE for daily maximum 8-hour average O_3 modeled by the updated and previous systems with MODIS input are also evaluated against binned ranges of observations in figure 3.8. It is clear that the system tends to over predict at the low end of the concentration range and under predict at the high end. This tendency is a persistent issue to many air quality modeling systems [*Im et al.*, 2014; *Solazzo el al.*, 2013; *Foley et al.*, 2010]. Over prediction with MODIS input at the low end is reduced with the updated system while the under prediction at the high end (note the much smaller sampling sites) is worse. Most importantly, there is clear MB and RMSE reduction at the concentration range around 60 to 70 ppb that is critical in policy decision related to potential lower O_3 standard in the U.S.

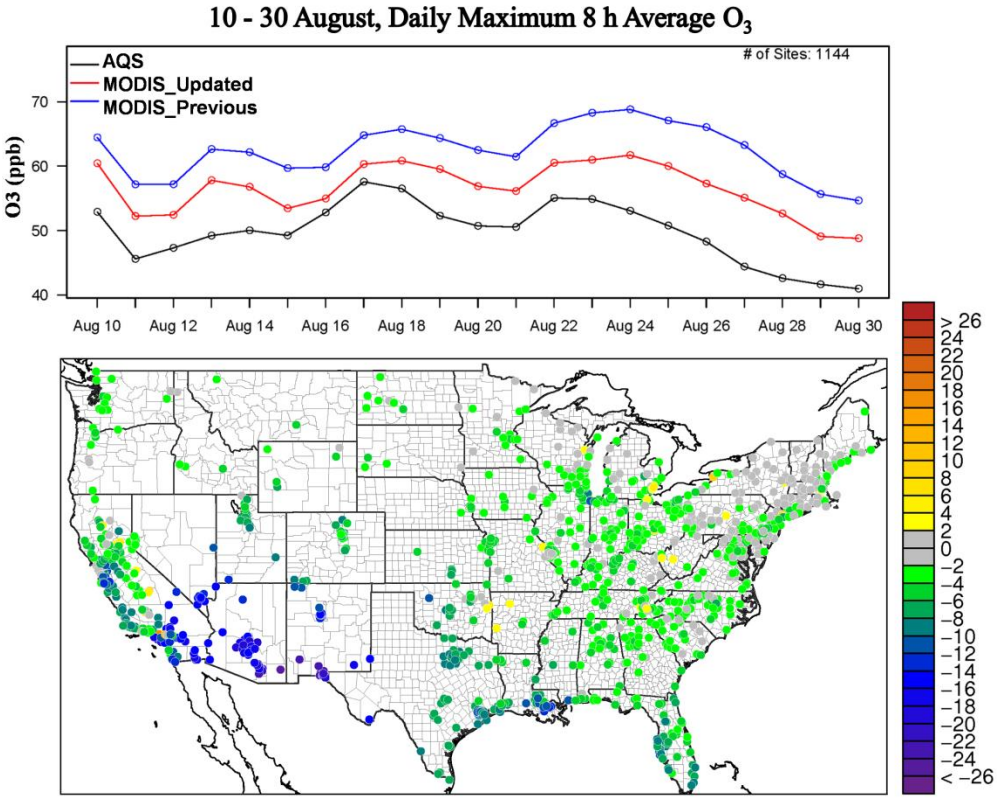

Figure 3.7. Evaluation of daily maximum 8 h average O_3 (ppb) simulated with MODIS input using the updated WRF/CMAQ and the previous WRF/CMAQ [*Ran et al.*, 2015] over the period from 10 to 30 August 2006 against the EPA AQS sites. The top plot displays mean of daily maximum 8 h average O_3 from the previous system (blue line), updated system (red line) and all AQS sites (black line). The spatial plot shows the difference of absolute mean bias for daily maximum 8 h average O_3 between the updated system and previous system.

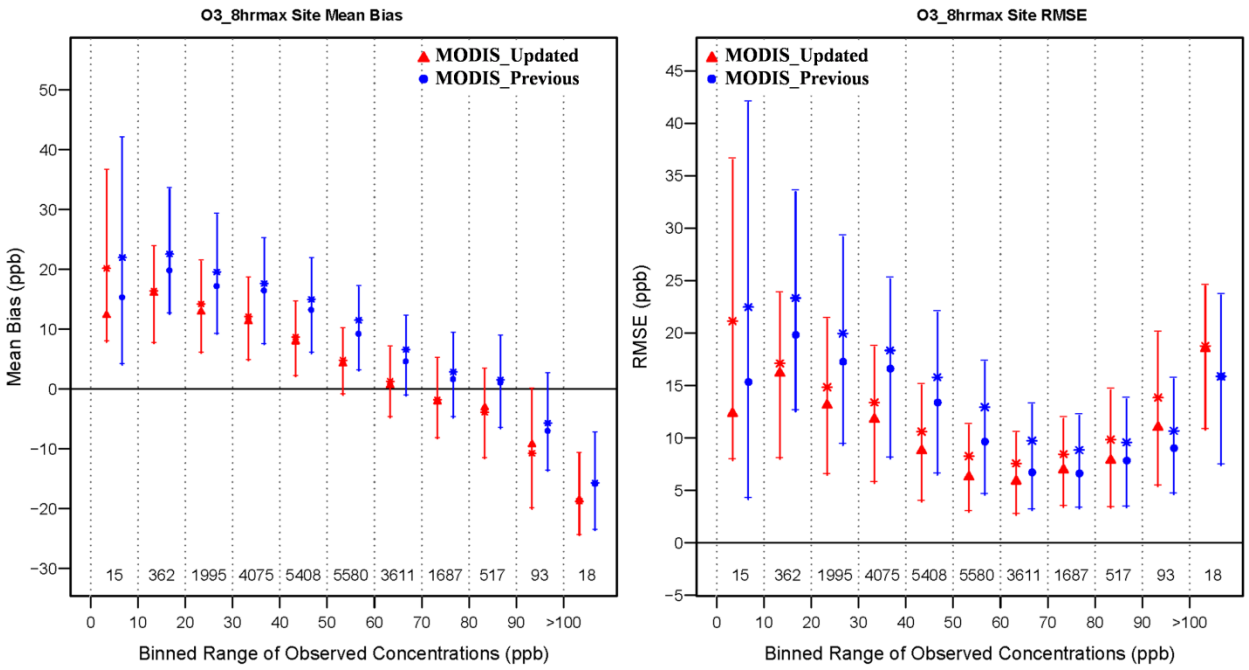

Figure 3.8. Mean bias (MB, left plot) and root-mean-square error (RMSE, right plot) of daily maximum 8 h average O_3 (ppb) simulated with MODIS input using the updated WRF/CMAQ (in red) and the previous WRF/CMAQ (in blue) [*Ran et al.*, 2015] over the period from 10 to 30 August 2006 against the binned AQS observation ranges. Line length is for the inner quartile range of MB and RMSE, triangle and circle for the median, and asterisk for the mean.

Nudging has significant impacts on the system - as is demonstrated by *Ran et al.* [2015]. In the base case, nudging helps reduce 2 m *T* bias with exaggerated vegetation. With MODIS input, there is more warm bias in the 2 m *T* in the west with much less vegetation because the soil moisture nudging is less effective in non-vegetated areas since the indirect soil moisture nudging scheme works most effectively in modulating stomatal conductance through its relationship to deep (root zone) soil moisture. This suggested that the model physics for evaporation from bare soil needed to be improved. Therefore, the soil resistance has been modified in the updated model (equations 3.10-3.12).

Evaluations for vegetation, PBL, and soil changes from the updated model are conducted independently. The soil resistance change shows the largest impact on temperature and humidity, especially in the western drylands where the warm bias with MODIS input is reduced while humidity is slightly increased. This result seems counter-intuitive since the updated soil resistance is greater than the in the base model for all but the very driest conditions (see figure 3.2). The explanation is that the greater soil resistance reduced soil evaporation in the morning thereby retaining more surface moisture into the mid-day hours when 2 m *T* peaks resulting greater LH and lower 2 m *T* and reduced O_3 bias. While the base model typically has minimum surface soil moisture in mid-day the updated model often has a bit more.

3.4.2 Annual WRF Simulations

The updated WRF/CMAQ system with MODIS input shows clear improvements by reducing the wet bias of 2 m *Q* estimation while minimizing the change of warm bias for 2 m *T* estimation for the summer period demonstrated above (figure 3.5). Since the results are from a peak growing period for vegetation and a hot and dry season for the west, the model performance may not be representative for other seasons. Thus, annual WRF simulations are important for assessing how the realistic MODIS vegetation phenology affects the system, particularly during vegetation green-up and green-down periods. Domain-wide statistical analyses (MB, MAE, and RMSE) are conducted for yearlong 2 m *T*, *Q*, and 10 m WS simulated using the updated model with and without MODIS input against the MADIS observations. The monthly average domain-wide statistics for 2 m *T* and 10 m WS are similar for the base and MODIS scenarios. Thus, the yearlong simulation analysis focuses on 2 m *Q*, LH, and LAI which are most directly related to vegetation seasonal changes. Figure 3.9 shows monthly averages of MB and MAE (left plot)

and daily averages of MB and RMSE (right plot) for 2 m *Q* simulated from the base and MODIS case scenarios. The monthly average MAE and daily average RMSE are similar for the two scenarios. MODIS input clearly helps reduce 2 m *Q* wet bias during growing season from April to September despites the slight wet bias during the cold seasons from November to February. Except for October, the base model without MODIS input tends to have wet bias, which is likely caused by the exaggerated vegetation coverage in the base PX LSM. During the growing seasons, the simulated moisture from the system responds better to the realistic vegetation coverage and LAI from MODIS input.

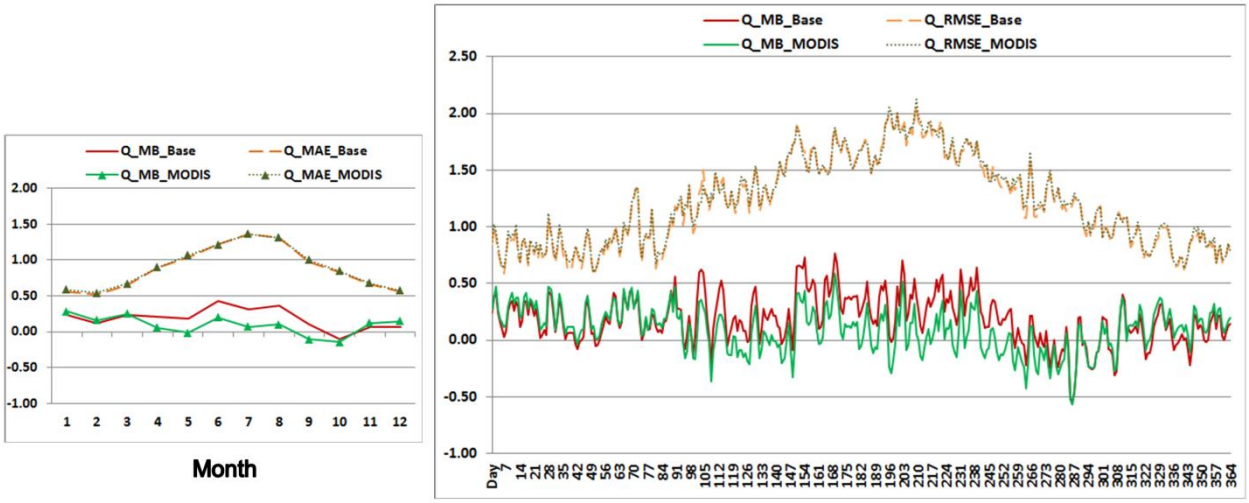

Figure 3.9. 2006 monthly and daily average statistical metrics for 2 m *Q* (g kg^{-1}, y axis) domain-wide for the base and MODIS WRF simulations against MADIS observations. The left graph is for the monthly averages of the mean biases and mean absolute errors. The right graph is for the daily average of the mean biases and root mean square errors.

Monthly average spatial performance of 2 m *Q* from the base and MODIS scenarios is evaluated by examining mean bias metrics with changes in LAI and LH. Figures 3.10 to 3.15 show the evaluation results for five selected months – April, May, June, August, and October. The spatial performances of the two scenarios are very similar during the cold seasons because

vegetation is not active and the dominant influence is often from large scale weather. Though the pattern of vegetation green-up starts showing difference from March in the south with the too fast green-up in the base scenario, the domain-wide March average MB of 2 m *Q* is very similar for the two scenarios (figure 3.9). The green-up difference is clearly displayed by the April LAI plots in the top row of figure 3.10. The April green-up in the base model is too fast into the northeast reaching Vermont and New Hampshire while MODIS vegetation shows the green-up only reaching Virginia. In general, the MODIS scenario for April has much lower LAI for most of the southern half of the domain, except for some greened areas in the southeast. The Pacific temperate rain forest in the northwest, dominated by coastal redwood, Douglas-fir, and western red cedar with much higher LAI [*Leverenz and Hinckley*, 1990] than the evergreen forest LAI (maximum 5 m^2 m^{-2} and minimum 3 m^2 m^{-2}) prescribed by the base PX LSM, shows much higher LAI from MODIS input throughout the year. But, the southern coniferous forests dominant by Longleaf and Loblolly pine (Florida and the southeast coastal plain) and the Rocky Mountains and the boreal coniferous forest regions in Canada tend to have lower LAI [*Chen et al*., 1997] from the MODIS scenario for all seasons. The difference of the monthly average LH (bottom left plot in figures 3.10 to 3.15) as well as 2 m *Q* (not displayed in the paper) between the MODIS and base scenarios averaged over all days in the month at 20 UTC closely follows the differences in the monthly average LAI over the growing vegetation regions. In general, the MODIS scenario as well as the base is too wet across the domain (bottom row middle plot). The difference in the absolute MB between the MODIS and base scenario (bottom row right plot) stands out in the southeast where the MODIS scenario has slower green-up than the base but higher LAI in some greened areas. With MODIS input, many sites in the southeast show the reduction of MB (green color) with decreased wet bias by more than 0.3 g kg^{-1} in comparison

with the base scenario. Meanwhile, MODIS input causes some sites in the central Plains down to Mexico to become too dry by more than 0.3 g kg^{-1} 2 m *Q* reduction (purple color). Overall, with MODIS input 55% of those MADIS sites show bias reduction for April.

In May (figure 3.11), the base simulation again shows accelerated green-up reaching into southern Canada compared to MODIS which shows green-up just beginning in Pennsylvania. The MODIS scenario has full green-up in the south with much higher LAI (more than 1.5 m^2 m^{-2}) than the base. Thus, the LAI difference is greater in the south and the base LAI is greater in the north. As the vegetation becomes more active the pattern of the LH difference closely follows the LAI difference between the two scenarios throughout the domain. The higher LH of the MODIS scenario is apparent in the southeast and the northwest U.S. where LAI is high. The wet bias pattern and the difference in absolute MB seem to follow the northward progression of the green-up from the MODIS scenario. Both the base and MODIS scenarios have wet bias in much the southern U.S. and dry bias particularly in the Midwest and northern Plains. In most of the southern and eastern U.S., reductions in absolute MB for MODIS coincide with lower LAI while in the northern plains and Midwest the absolute MB is increased in the MODIS case since the dry bias is worsened by the lower LAI in these areas. Overall, MODIS input helps reduce bias for 55 % of the MADIS sites.

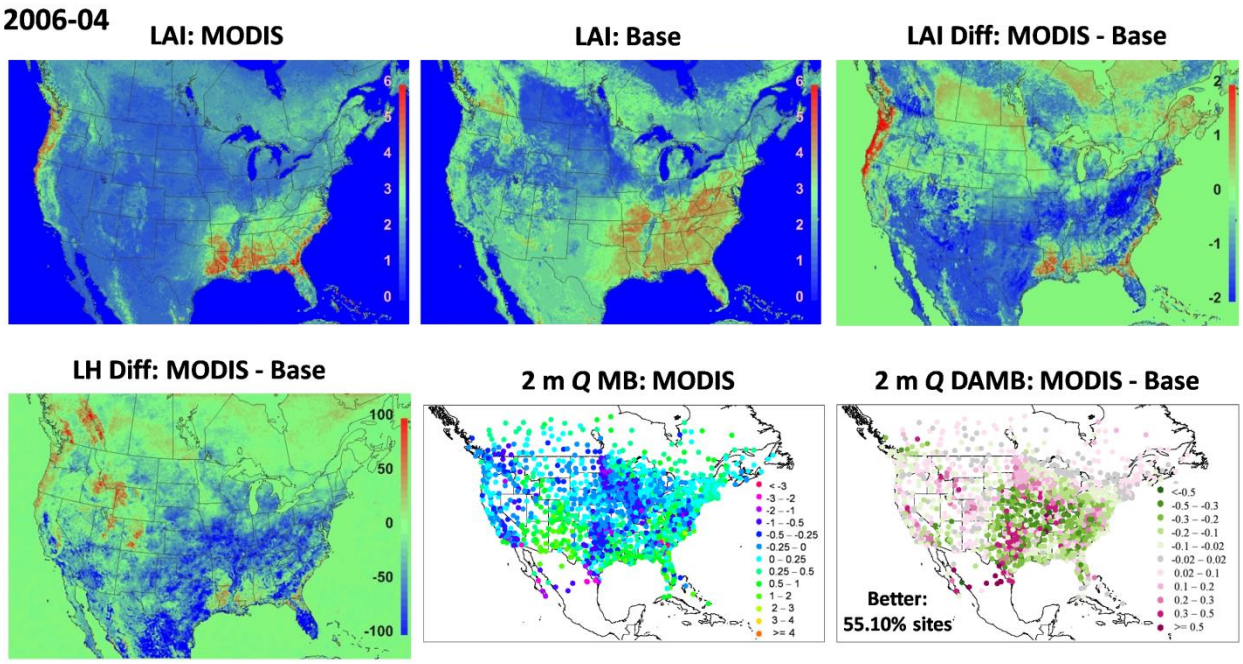

Figure 3.10. April 2006 LAI (m^2 m^{-2}), latent heat (W m^{-2}), and 2 m *Q* (g kg^{-1}) spatial evaluation. The top row is for the monthly average LAI from the MODIS case (top left) and base case (top middle) and for the difference of the average LAI between the two cases (top right). The bottom left plot is for the difference of the monthly average latent heat between the two cases for 20 UTC. The bottom middle plot is for the mean bias of 2 m *Q* from the MODIS case against MADIS observations. The bottom right plot is the difference of absolute mean bias for 2 m *Q* between the two cases.

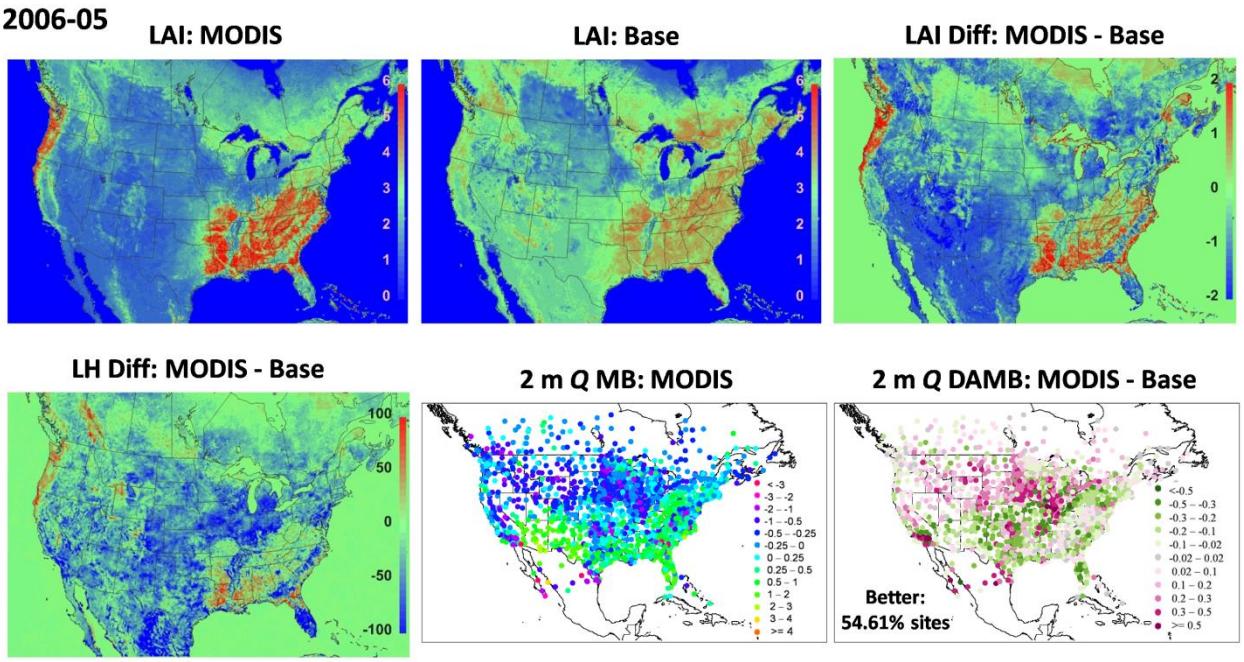

Figure 3.11. May 2006 LAI (m^2 m^{-2}), latent heat (W m^{-2}), and 2 m *Q* (g kg^{-1}) spatial evaluation. Plot descriptions are the same as those in the figure 3.10 caption.

In June (figure 3.12), both the MODIS and base scenarios have the full vegetation green up. However, the MODIS scenario has much higher LAI for forest areas in the east and north and lower LAI in most of the west. Also, in this early part of the growing season the base scenario overestimates the LAI in agricultural areas of the Midwest and Plains as compared to MODIS. With active vegetation growth in June, the difference of LH for 20 UTC shows distinct patterns from the south to north over the domain following the LAI difference. The pattern of the wet bias from the MODIS scenario moves northward as the growing season progresses but still with more dry bias in the north, particularly the northwest where both the scenarios show high dry bias. The MODIS and base scenarios show similar performance for the 2 m *Q* simulation in most of the south and east coastal regions with some clear improvement in Florida and Pennsylvania because of MODIS input. The bias improvement (green in the bottom row right plot) from using MODIS input increases along an axis from the desert southwest to the

northeast U.S. as the growing season progresses. In general, the MODIS scenario shows reduced absolute MB in areas where MODIS LAI is less than the base, such as the central Plains and agricultural regions of the Midwest, but slightly greater absolute MB in areas where MODIS LAI is greater, such as most of the south and east. With MODIS input, 61% of the MADIS sites show bias reduction in comparison with the base scenario.

The spatial distribution of LAI and the performance of 2 m *Q* for July with the MODIS input are very similar to those displayed for August in figure 3.13. The MODIS scenario shows more vegetation growth in the northern forest (north and east of the Great Lakes) and higher cropland LAI in the central corn-belt region (around Iowa). The much higher LAI (by around 2 m^2 m^{-2}) from MODIS input over the Sierra Madre Occidental in the western Mexico stands out from the LAI difference plot for August (July and September as well). The MODIS input captures the peak green up of the forests in the Sierra Madre Occidental following the monsoon precipitation after the spring dry season. The MODIS scenario shows much higher average LH at 20 UTC for this region during this hot summer month but much lower LH for the surrounding drylands in northern Mexico and the southwest U.S. With MODIS input, the southwest becomes much too dry for many sites with 2 m *Q* MB less than -1.0 g kg^{-1}. In the east both scenarios show similar performance for the 2 m *Q* estimation. The area of the greatest bias improvement with MODIS moves further west and north. The sites with the largest bias improvement (in forest green) with the reductions of more than 0.3 g kg^{-1} are in the central Plains and Rocky Mountains from the northern Texas to the Canada border, where the base model is too wet. Overall, MODIS input helps reduce 2 m *Q* bias for 61% of the MADIS sites in August.

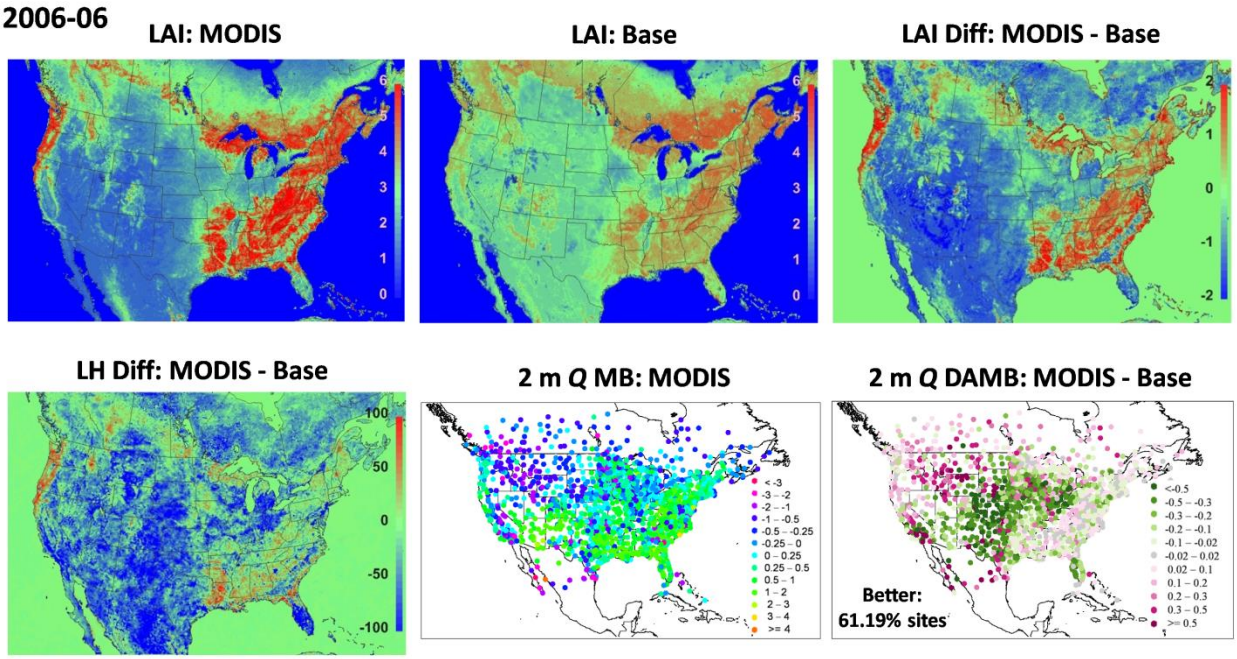

Figure 3.12. June 2006 LAI (m^2 m^{-2}), latent heat (W m^{-2}), and 2 m *Q* (g kg^{-1}) spatial evaluation. Plot descriptions are the same as those in the figure 3.10 caption.

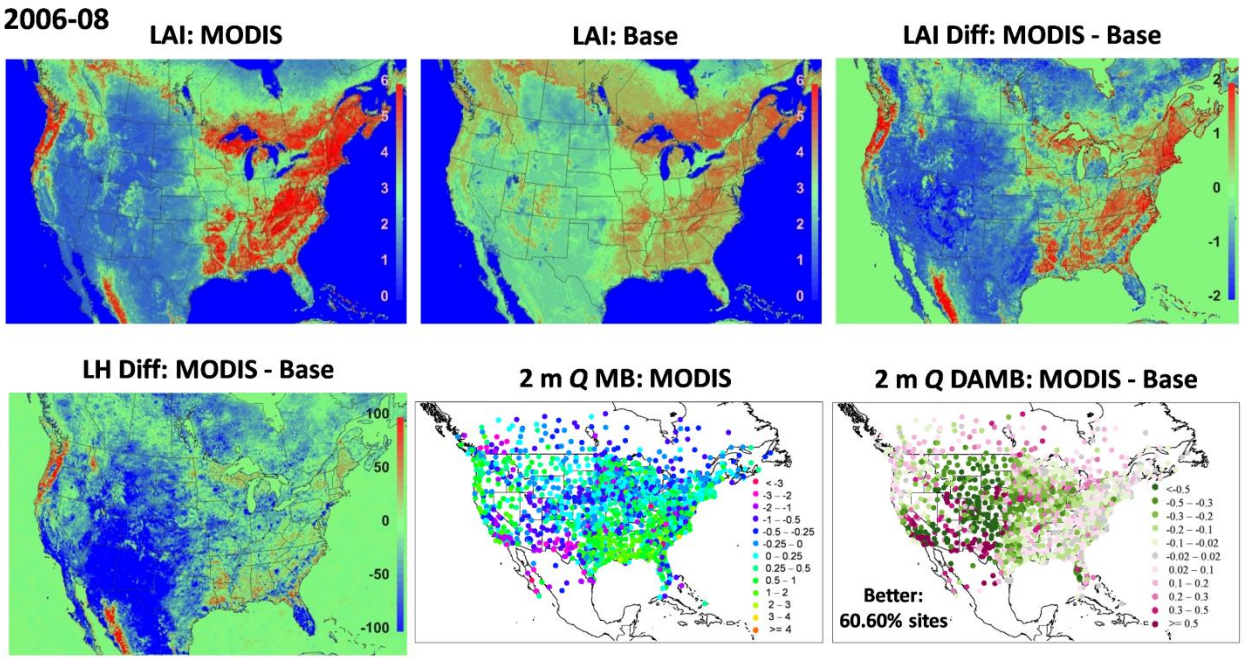

Figure 3.13. August 2006 LAI (m^2 m^{-2}), latent heat (W m^{-2}), and 2 m *Q* (g kg^{-1}) spatial evaluation. Plot descriptions are the same as those in the figure 3.10 caption.

The green-down of the northern forests starts in September and the timing of the green-down for both the MODIS and base scenarios is quite similar as demonstrated by the October LAI plots in figure 3.14. The pattern of the LAI difference for September (not displayed in the paper) is similar to that displayed by figure 3.13 for August but with lesser magnitudes. Following the green-down of the vegetation from north to south, the effect of LAI on LH is diminishing in the north where vegetation becomes inactive through the fall season. Thus, the LH difference no longer follows the pattern of the LAI difference in the north starting from September as shown in figure 3.14 for October. With leaf fall and less active vegetation, 55% of the MADIS sites show bias reduction with the MODIS input for September in comparison with the base scenario. In October, the LAI difference over the domain is relatively small between the two scenarios, except in the southwest dryland areas where the MODIS LAI is much lower and the Pacific temperate rain forest and the Sierra Madres Occidental where the MODIS LAI is much higher. Both the MODIS and base scenarios have very similar MB spatial patterns. Thus, the difference plot of the absolute MB shows that most sites, particularly in the north, show very small bias differences. Both scenarios are too dry from the Mid-Atlantic region to the corn-belt region and the southern Plains into Mexico with 2 m Q more than 0.25 g kg^{-1} lower than observations for many sites. Overall, MODIS input helps bias reduction at 44% of the MADIS observation sites in October and causes a dryer simulation, particularly for the southeast. From November to March, the monthly spatial plots (not displayed in the paper) for the difference of the absolute MB are similar to the October plot in figure 3.14 but with much smaller magnitudes with the MODIS run slightly wetter (figure 3.9) in the west.

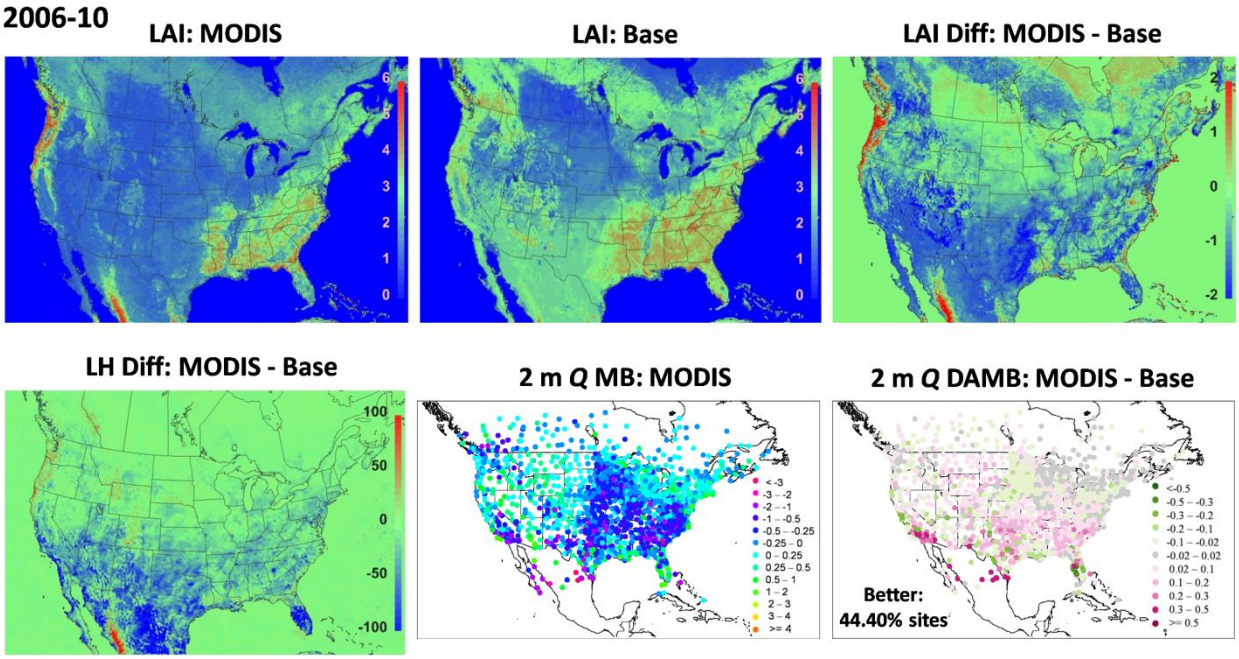

Figure 3.14. October 2006 LAI (m^2 m^{-2}), latent heat (W m^{-2}), and 2 m *Q* (g kg^{-1}) spatial evaluation. Plot descriptions are the same as those in the figure 3.10 caption.

3.4.3 April-August-October Ozone Simulations

The change of vegetation from MODIS input has significant impacts not only on the meteorology but also the surface ozone flux and ozone concentration because the dry deposition model in CMAQ uses the same aerodynamic and bulk stomatal conductance computed for LH estimation in the PX LSM WRF [*Pleim et al.*, 2001]. The monthly average difference of the ozone deposition velocities and surface-layer concentrations between the MODIS and base scenarios at 20 UTC as well as the monthly LAI difference are demonstrated in figure 3.15 for April, August and October 2006. The modeled O_3 concentrations are evaluated over different UTC hours across the domain and it appears that O_3 shows the biggest effects of MODIS input around 20 UTC which corresponds to 13:00 and 14:00 local time for the Pacific and Mountain Daylight summer time zones. Thus, 20 UTC is used to display the monthly average difference for O_3 as well as LH displayed in the previous annual evaluation. With the strong stomatal

pathway of the ozone dry deposition [*Padro*, 1996], the difference in ozone deposition velocity (the middle row in figure 3.15) between the CMAQ MODIS and base scenarios generally follows the LAI difference (the top rows in figure 3.15) as well as the LH difference (figures 3.10, 3.13, and 3.14) for each of the three months. Consequently, the largest O_3 concentration increases (the bottom row) appear in areas with largest decreases in LAI and O_3 deposition. The O_3 concentration difference is consistently high for the three months in Florida where the O_3 deposition velocity difference is low due to lower LAI from MODIS input in all seasons.

In April, the central east has much lower ozone deposition velocity (with more than 0.20 cm s^{-1} less) from using MODIS input due to quicker green-up in the base model. MODIS input causes the O_3 concentration to increase by more than 3 ppb over the base run in most of these areas. In August, the ozone deposition velocity is much lower for the MODIS case in the west where not only the LAI is much lower but also some warm bias still exists in this hot and dry region from using MODIS input (the top row right plot in figure 3.5). Most of the west, outside of the Pacific temperate rain forest and the Sierra Madres Occidental, has much higher ozone concentrations by more than 5 ppb. In October, the higher O_3 concentration region from using MODIS input is shifted to the south where temperature is warmer. As the ozone formation in the atmospheric boundary layer is also strongly influenced by the temperature [*Rasmussen et al.*, 2012], the ozone concentration difference is smaller in the north where temperature is relatively low, despite the big LAI differences, in all three months. Table 3.2 summaries the domain-wide statistical metrics for the simulated daily maximum 8 h average O_3 concentration (ppb) from the base and MODIS cases against EPA AQS site observations for the three months. Though the ozone is the highest in August and the lowest in October, MODIS input causes the domain-wide

mean and average MB to be higher by no more than 2.7 ppb and RMSE and MAE higher by no more than 1.39 ppb for all three months.

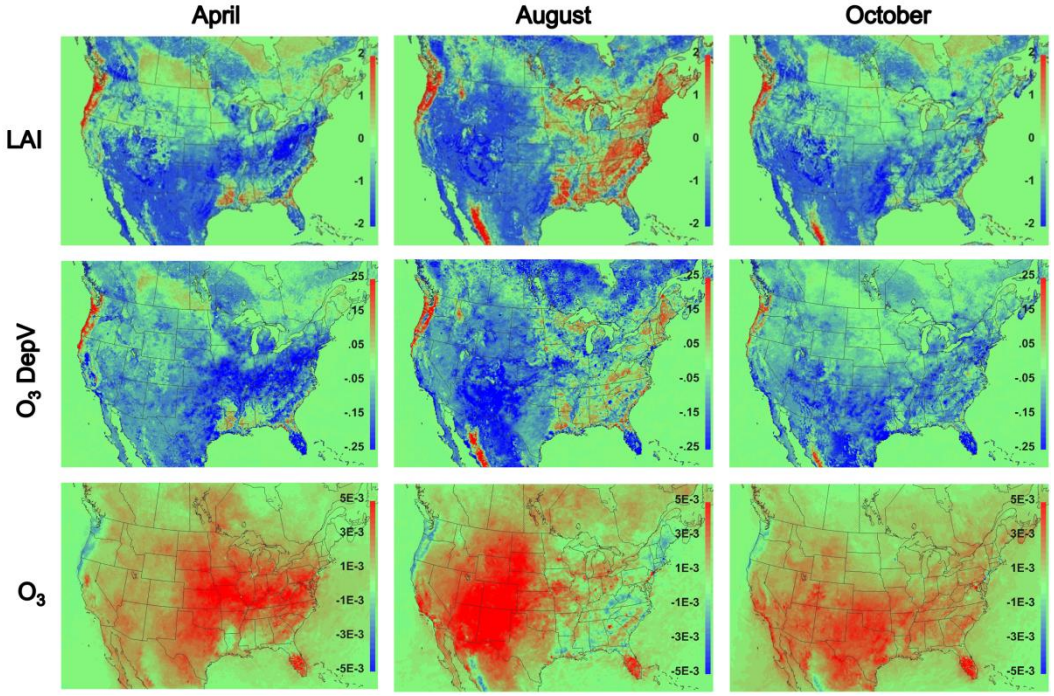

Figure 3.15. Monthly average difference of LAI (m^2 m^{-2}), ozone deposition velocity (cm s^{-1}), and ozone concentration (ppmV) at the surface layer between the MODIS case and base case for 20 UTC over April, August, and October 2006.

Table 3.2. Domain-wide statistical metrics for the simulated daily maximum 8 h average O3 concentration (ppb) from the base and MODIS cases against EPA AQS site observations for April, August, and October 2006.

CMAQ		April O_3 (ppb)				August O_3 (ppb)				October O_3 (ppb)		
Scenario	Mean	RMSE	MAE	MB	Mean	RMSE	MAE	MB	Mean	RMSE	MAE	MB
Base	52.70	9.51	7.33	3.94	55.00	12.80	9.70	4.84	42.20	10.10	8.20	5.34
MODIS	55.40	10.90	8.64	6.62	57.10	13.80	10.50	6.89	44.60	11.30	9.51	7.72
MODIS-Base	2.70	1.39	1.31	2.68	2.10	1.00	0.80	2.05	2.40	1.20	1.31	2.38

Since ozone is most important in the warm season, the simulated daily maximum 8 h average O_3 concentration in August is further evaluated by the daily mean graph and DAMB spatial plot in figure 3.16. The domain average of the estimated daily maximum 8 h average O_3 (ppb) with MODIS input (red line in the top graph of figure 3.16) is consistently higher than that from the base scenario (by around 2 ppb) and compared to the AQS observations by 2.17 to 11.15 ppb (6.89 on average). The DAMB spatial plot (bottom plot of figure 3.16) shows the areas where the MODIS run absolute mean bias of the daily maximum 8-hour average O_3 (ppb) is greater than the base run (yellow and orange dots) are mostly in California, the Southwest, Florida and the Gulf coast, and the upper Midwest. Many AQS sites (in grey and green) in the east and northwest show very little change and some improvement for the modeled O_3 using the MODIS input. Despite the big improvement on the over prediction of 2 m *T* with MODIS input using the updated WRF/CMAQ modeling system (figure 3.7), the ozone estimation is still higher in general in comparison with the observations. As the west is realistically much less vegetated with MODIS input, the dry deposition onto barren soil becomes an important pathway influencing the atmospheric O_3 concentration. This suggests that the CMAQ dry deposition model should be evaluated for possible improvements in the dry deposition onto barren

landscapes, which is common in the west where the ozone concentration generally has the greatest high bias.

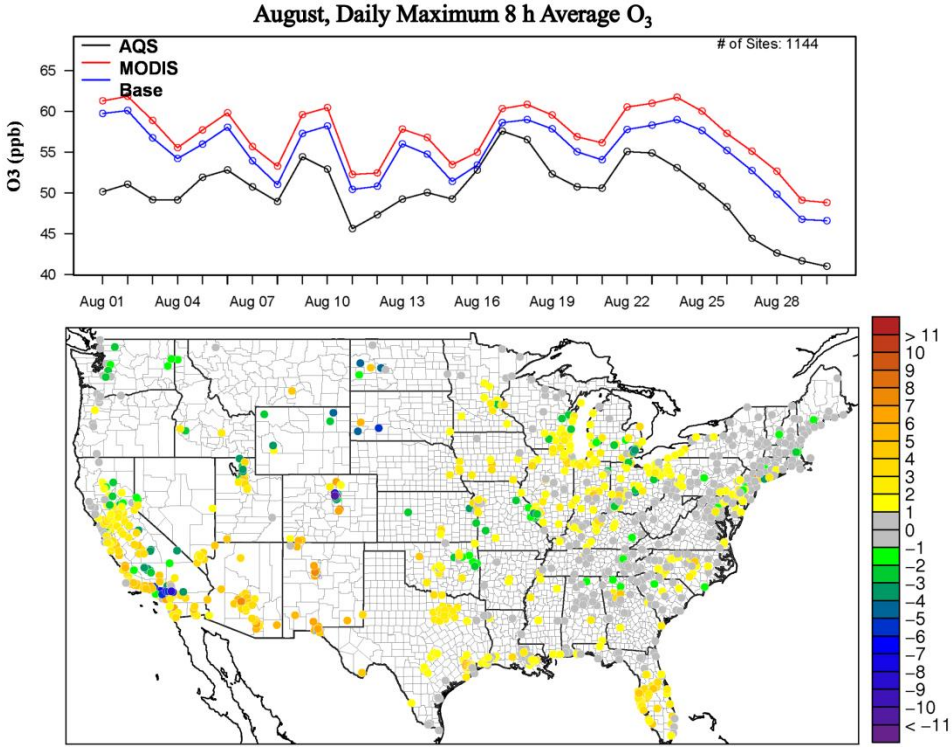

Figure 3.16. Evaluation of daily maximum 8 h average O3 (ppb) simulated from the base and MODIS case WRF/CMAQ over August 2006 again the EPA AQS sites. The top plot displays mean of daily maximum 8 h average O_3 from the base case (blue line), MODIS case (red line) and all AQS sites (black line). The bottom plot is the difference spatial plot of absolute mean bias for daily maximum 8 h average O_3 between the MODIS case and the base case.

3.5 Conclusions and Future Plans

Ingesting the MODIS satellite products, particularly MODIS LAI/FPAR product, into the WRF/CMAQ modeling system with the PX LSM, has significant influences on the simulated meteorology and air quality. The MODIS vegetation products (LAI and VF) clearly add realistic vegetation characteristics and phenology to the WRF/CMAQ system in comparison with the

vegetation characteristics currently specified by the PX LSM land-use category look-up tables. The previous study using the standard WRF v3.4 modified for MODIS input and CMAQ v5.0.2 over the period from 10 August to 9 September 2006 shows mixed results with much hotter and dryer conditions in much of western North America where MODIS vegetation shows substantially less coverage [*Ran et al*., 2015]. Based on the results from the previous study, the WRF/CMAQ modeling system is updated to include recent improvements [*Pleim et al*., 2015] in the PX LSM vegetation (in WRF v3.7) and soil (not in public release) processes and in the ACM2 PBL processes (in WRF v3.7 and CMAQ v5.1). The updated WRF/CMAQ modeling system demonstrates clear improvements in the 2 m *T* and *Q*, 10 m WS, and near surface ozone concentration simulations with and without MODIS input for this period around August. The warm bias in the west from using MODIS input has significant reduction while the bias and MAE of 2 m *Q* get reduced as well in many areas in the south in comparison with the simulations using the previous system. The improved meteorology propagates through the air quality system which results in much improved O_3 concentration estimations. The simulated O_3 concentration using the updated system with MODIS input shows significant error reduction across the domain (by 6 ppb for bias and 4 ppb for MAE on average) in comparison with the previous system with MODIS input. However, ozone concentrations in the updated model still show greater biases and errors for the MODIS case compared the base case. Just as improvements to the meteorology model were instigated by the earlier study that showed degraded 2 m T statistics using MODIS these results for ozone may promote improvements in the ozone dry deposition model in CMAQ.

The yearlong meteorology simulations and selected three-month (April, August, and October) air quality simulations using the updated system are conducted with and without

MODIS input for impact assessments. Preliminary evaluations show that 2 m *T*, 10 m WS, and other air quality do not show big differences on a monthly average basis from using MODIS input although differences do exist over space and time. Thus, the evaluations of the simulated meteorology and air quality focus on 2 m *Q* and surface ozone with the change of vegetation (change of albedo has much less influence in comparison with vegetation). The more realistic vegetation characteristics and phenology from MODIS input [Zh*ang et al*., 2006] improve the system through not only better spatial and temporal representation but also different LAI magnitudes from diverse natural and cultivated vegetation types which the LSM general land cover look-up tables cannot capture. For instance, MODIS LAI is consistently much higher than the base for the Pacific temperate rain forest where dominant redwood, Douglas-fir, and western red cedar have much higher LAI than LAI prescribed for evergreen forest type in the base model LSM. Conversely, MODIS LAI for the boreal forests in Canada and southeast coniferous forests (e.g. in Florida) have lower LAI than the prescribed LAI for evergreen forests. The influence of the North American monsoon on the green up in the Sierra Madres Occidental forest is distinctly captured by MODIS input from July to September. In addition, MODIS LAI has great advantage by capturing changes of LAI of cultivated lands such as crop lands because LAI in these areas is greatly influenced by human activities such as planting, fertilizing, irrigating, and harvesting which are very difficult to model correctly in the LSM on a specific year basis. Overall, for 2006 the base model green up is too fast but the green down is similar to the MODIS vegetation. The differences of LH and 2 m *Q* simulated from the MODIS and base scenarios closely follow the difference of LAI in areas with growing vegetation.

The area with improved 2 m *Q* from MODIS input follows the green up from April in the southeast and extends towards the west and north in May. In June, the distinct improvement area

moves to the Midwest and the southwest where the landscape is dominated by agriculture. In peak summer July and August, the improvement area is further expanded into the north, reaching Canada. Along with the improved performance of 2 m *Q* for many MADIS observation sites from April to September, there are also many sites which show increased bias and error, such as the southwest U.S. near the Mexican border where it gets too dry from August through September with MODIS input. From October to March, MODIS input does not have big influence on 2 m *Q* because of vegetation green down. MODIS input increases the existing high bias in the base model for the simulated ozone concentration by no more than 3 ppb for domain-wide monthly average in April, August, and October. The areas with high ozone bias follow where MODIS input has much lower LAI in comparison with the base model LAI. With the much improved vegetation representation and improved meteorology simulations, the surface ozone simulations do not show any improvement but have consistently higher bias for all selected months, particularly in areas where MODIS LAI is lower than for the base. This suggests that the CMAQ dry deposition model may need to be evaluated for possible improvements in low LAI areas where deposition to the soil surface is the dominant pathway.

In conclusion, this study shows that realistic vegetation characteristics and phenology from MODIS input help improve the meteorology simulations during the growing seasons with the use of the updated PX LSM WRF/CMAQ modeling system. Possible improvements for the CMAQ dry deposition model particularly for bare soil surfaces may help improve the ozone simulation. As the modeling system is very sensitive to LAI and uncertainties exist in satellite products, quality assurance on MODIS input (processed LAI, FAR, and albedo) is important for the MODIS input to be used routinely in WRF/CMAQ simulations with the PX LSM for research applications and air quality regulatory decision-making. Further upgrades to the

updated WRF/CMAQ modeling system are ongoing by incorporating a biochemically-based photosynthesis-conductance scheme following the studies for climate LSMs [*Sellers et al*, 1996; *Calvet et al.1998; Dai et al.*, 2004; *Bonan et al.*, 2011; *Clark et al.*, 2011; *Kowalczyk et al.*, 2013; *Oleson et al.*, 2013]. The realistic MODIS vegetation input is crucial for the system to correctly model vegetation productivity in the photosynthesis-conductance scheme. With the photosynthesis-conductance scheme, the WRF/CMAQ system has the capabilities to dynamically respond to CO_2 concentration temporally and spatially and to simulate the coupling effect of climate, air quality (such as O_3), and vegetation in changing climate [*Sitch et al.*, 2007; *Lombardozzi et al.*, 2012].

REFERENCES

Alton, P. (2009), A simple retrieval of ground albedo and vegetation absorptance from MODIS satellite data for parameterisation of global land-surface models, Agricultural and Forest Meteorology, 149(10), 1769-1775.

Appel, K. W., K. M. Foley, J. O. Bash, P. W. Pinder, R. L. Dennis, D. J. Allen, and K. A. Pickering (2011a), Multi-resolution assessment of the Community Multiscale Air Quality (CMAQ) model v4.7 wet deposition estimates for 2002-2006, Geosci. Model Dev, 4, 357–371.

Appel, K. W., R. C. Gilliam, N. Davis, and A. Zubrow (2011b), Overview of the Atmospheric Model Evaluation Tool (AMET) v1.1 for evaluating meteorological and air quality models, Environ. Modell. Softw., 26(4), 434–443.

Baker, I. T., A. S. Denning, N. Hanan, L. Prihodko, P. L. Vidale, K. Davis, and P. Bakwin (2010), North American gross primary productivity: regional characterization and interannual variability, Tellus, 62B, 533–549.

Barbu, A. L., J. C. Calvet, J. F. Mahfouf, C. Albergel, and S. Lafont (2011), Assimilation of Soil Wetness Index and Leaf Area Index into the ISBA-A-gs land surface model: grassland case study, Biogeosciences, 8, 1971–1986.

Bhumralkar, C. M. (1975), Numerical experiments on the computation of ground surface temperature in an atmospheric general circulation model, Journal of Applied Meteorology, 14, 1246–1258.

Binkowski, F.S. and S. J. Roselle (2003), Models-3 Community Multiscale Air Quality (CMAQ) model aerosol component: 1. Model description, J. Geophys. Res., 108 (D6), 4183.

Blackadar, A. K. (1976), Modelling the nocturnal boundary layer. In Proceedings of the Third Symposium on Atmospheric Turbulence, Diffusion and Air Quality, American Meteorological Society, Boston, MA, 46–49.

Bonan, G. B. (2008), Ecological climatology: concepts and applications, Cambridge University Press, New York.

Bonan, G. B., P. J. Lawrence, K. W. Oleson, S. Levis, M. Jung, M. Reichstein, D. M. Lawrence, and S. C. Swenson (2011), Improving canopy processes in the Community Land Model version 4 (CLM4) using global flux fields empirically inferred from FLUXNET data, Journal of Geophysical Research: Biogeosciences (2005–2012), 116(G2).

Boussetta, S., G. Balsamo, E. Dutra, A. Beljaars, and C. Albergel (2015), Assimilation of surface albedo and vegetation states from satellite observations and their impact on numerical weather prediction, Remote Sensing of Environment, 163 (2015), 111-126.

Bouttier, F., J. F. Mahfouf, and J. Noilhan (1993), Sequential assimilation of soil moisture from atmospheric low-level parameters. Part I: Sensitivity and calibration studies, J. Appl. Meteor., 32, 1335–1351.

Budyko, M. I. (1974), Climate and Life. Academic Press, New York, 508 pp

Byun, D. W. and K. L. Schere (2006), Review of the governing equations, computational algorithms, and other components of the Models-3 Community Multiscale Air Quality (CMAQ) modeling system, Appl. Mech. Rev., 59, 51-77.

Calvet, J. C., J. Noilhan, J. L. Roujean, P. Bessemoulin, M. Cabelguenne, A. Olioso, and J. P. Wigneron (1998), An interactive vegetation SVAT model tested against data from six contrasting sites, Agric. For. Meteorol., 92,73– 95.

Camillo, P. J. and R. J. Gurney, 1986. A resistance parameter for bare-soil evaporation models, Soil Science, 141(2), 95-105.

Carvalho, D., A. Rocha, M. Gómez-Gesteira, and C. Silva Santos (2014), Sensitivity of the WRF model wind simulation and wind energy production estimates to planetary boundary layer parameterizations for onshore and offshore areas in the Iberian Peninsula, Applied Energy 135 (2014), 234-246.

Chen, J. M., P. M. Rich, S. T. Gower, J. M. Norman, and S. Plummer (1997), Leaf area index of boreal forests: theory, techniques, and measurements, Journal of Geophysical Research: Atmospheres (1984–2012), 102(D24), 29429-29443.

Clark, D. B., L. M. Mercado, S. Sitch, C. D. Jones, N. Gedney, M. Pryor, G. G. Rooney, R. L. H. Essery, E. Blyth1, O. Boucher, R. J. Harding, C. Huntingford, and P. M. Cox (2011), The joint UK land environment simulator (JULES), model description–Part 2: carbon fluxes and vegetation dynamics, Geoscientific Model Development, 4(3), 701-722.

Cohen, W. B., T. K. Maiersperger, D. P. Turner, W. D. Ritts, D. Pflugmacher, R. E. Kennedy, A. Kirschbaum, S.W. Running, M. Costa, and S. T. Gower (2006), MODIS land cover and LAI collection 4 product quality across nine sites in the western hemisphere, IEEE Transactions on Geoscience and Remote Sensing, 44,1843−1857.

Compton, J. E., J. A. Harrison, R. L. Dennis, T. L. Greaver, B. H. Hill, S. J. Jordan, H. Walker, and H. V. Campbell (2011), Ecosystem services altered by human changes in the nitrogen cycle: a new perspective for US decision making, Ecology Letters, 14, 804–815.

Dai, Y., R. E. Dickinson, and Y. P. Wang (2004), A two-big-leaf model for canopy temperature, photosynthesis, and stomatal conductance, J. Clim., 17, 2281-2299.

Deardorff, J. (1977), A parameterization of ground-surface moisture content for use in atmospheric prediction models, Journal of Applied Meteorology, 16(11), 1182-1185.

Dee, D. P., S. M. Uppala, A. J. Simmons, P. Berrisford, P. Poli, S. Kobayashi, ... and F. Vitart (2011), The ERA-Interim reanalysis: Configuration and performance of the data assimilation system, Quarterly Journal of the Royal Meteorological Society, 137(656), 553-597.

Douville, H., P. Viterbo, J. F. Mahfouf, and A. C. M. Beljaars (2000), Evaluation of the optimum interpolation and nudging techniques for soil moisture analysis using FIFE data, Mon. Wea. Rev., 128, 1733–1756.

Eder, B., D. Kang, R. Mathur, J. Pleim, S. Yu, T. Otte, and G. Pouliot (2009), A performance evaluation of the National Air Quality Forecast Capability for the summer of 2007, Atmospheric Environment, 43(14), 2312-2320.

Fang, H., C. Jiang, W. Li, S. Wei, F. Baret, J. Chen, J. Garcia-Haro, R. Liu, R. Myneni, R., B. Pinty, Z. Xiao, and Z. Zhu (2013), Characterization and intercomparison of global moderate resolution leaf area index (LAI) products: Analysis of climatologies and theoretical uncertainties, Journal of Geophysical Research – Biospheres, 118, 529-548.

Fensholt, R., I. Sandholt, and M. S. Rasmussen (2004), Evaluation of MODIS LAI, fAPAR and the relation between fAPAR and NDVI in a semi-arid environment using in situ measurements, Remote Sensing of Environment, 91(3), 490-507.

Foley, K. M., S. J. Roselle, K. W. Appel, P. V. Bhave, J. E. Pleim, T. L. Otte, R. Mathur et al. (2010), Incremental testing of the Community Multiscale Air Quality (CMAQ) modeling system version 4.7, Geoscientific Model Development, 3(1), 205-226.

Fuentes, J. D., T. J. Gillespie, G. den Hartog, G. and H. H. Neumann (1992), Ozone deposition onto a deciduous forest during dry and wet conditions, Agric. For. Meteorol., 62, 1-18.

Gao, F., J. Morisette, R. Wolfe, G. Ederer, J. Pedelty, E. Masuoka, R. Myneni, B. Tan, and J. Nightingale (2008), An Algorithm to Produce Temporally and Spatially Continuous MODIS-LAI Time Series, IEEE Geoscience and Remote Sensing Letters, 5(1), 60-64.

Gao, Y., N. Lu, and T. Yao T. (2011), Evaluation of a cloud-gap-filled MODIS daily snow cover product over the Pacific Northwest USA, Journal of Hydrology, 404, 157–165.

Gego, E., C. Hogrefe, G. Kallos, A. Voudouri, J.S. Irwin, and S.T., Rao (2005), Examination of model predictions at different horizontal grid resolutions, Environmental Fluid Mechanics, 5, 63–85.

Giard, D., and E. Bazile (2000), Implementation of a new assimilation scheme for soil and surface variables in a global NWP model, Mon. Wea. Rev., 128, 997–1015.

Gilliam, R. C., W. Appel, and S. Philips (2005), The Atmospheric Evaluation Tool (AMET): Meteorology module, Extended Abstracts, Fourth Annual Community Analysis and Modeling System Conf., Chapel Hill, NC, University of North Carolina Institute for the Environment, 6 pp. [Available online at

http://www.cmascenter.org/conference/2005/abstracts/6_1.pdf].

Gilliam, R. C., C. Hogrefe, and S. T. Rao (2006), New methods for evaluating meteorological models used in air quality applications, Atmospheric Environment, 40, 5073-5086.

Gilliam, R. C., and J. E. Pleim (2010), Performance assessment of new land surface and planetary boundary layer physics in the WRF-ARW, Journal of Applied Meteorology and Climatology, 49(4), 760-774.

Hogrefe, C., G. Pouliot, D. Wong, A. Torian, S. Roselle, J. Pleim, and R. Mathur (2014), Annual application and evaluation of the online coupled WRF–CMAQ system over North America under AQMEII phase 2, Atmospheric Environment.

Iacono, M.J., J. S. Delamere, E. J.Mlawer, M. W. Shephard, S. A. Clough, W. D. Collins (2008), Radiative forcing by long-lived greenhouse gases: calculations with the AER radiative transfer models, J. Geophys. Res., 113, D13103, doi:10.1029/2008JD009944.

Im, U., R. Bianconi, E. Solazzo, I. Kioutsioukis, A. Badia, A. Balzarini, ... and S. Galmarini (2014), Evaluation of operational on-line-coupled regional air quality models over Europe and North America in the context of AQMEII phase 2. Part I: Ozone, Atmospheric Environment.

Inness, A., F. Baier, A. Benedetti, I. Bouarar, S. Chabrillat, H. Clark, ... and C. Zerefos (2013), The MACC reanalysis: an 8 yr data set of atmospheric composition, Atmos. Chem. Phys., 13, 4073-109.

Jarvis P. G. (1976), The interpretation of the variations in leaf water potential and stomatal conductance found in canopies in the field, Philosophical Transactions of the Royal Society of London, Series B, 273, 593–610.

Jayalakshmy, M. S. and J. Philip (2010), Thermophysical properties of plant leaves and their influence on the environment temperature, International Journal of Thermophysics, 31(11-12), 2295-2304.

Kain, J. S. (2004), The Kain–Fritsch convective parameterization: An update. J. Appl. Meteor., 43, 170–181.

Kelly, J. T., K. R. Baker, J. B. Nowak, J. G. Murphy, M. Z. Markovic, T. C. VandenBoer, R. A. Ellis, …and C. Misenis (2014), Fine-scale simulation of ammonium and nitrate over the South Coast Air Basin and San Joaquin Valley of California during CalNex-2010, Journal of Geophysical Research: Atmospheres, 119(6), 3600-3614.

Kondo, J., N. Saigusa, and T. Sato (1990), A parameterization of evaporation from bare soil surfaces, Journal of Applied Meteorology, 29(5), 385-389.

Kowalczyk, E. A., L. Stevens, R. M. Law, M. Dix, Y. P. Wang, I. N. Harman, ... and T. Ziehn (2013), The land surface model component of ACCESS: description and impact on the simulated surface climatology, Australian Meteorological and Oceanographic Journal, 63(1), 65-82.

Lawrence, D., K. W. Oleson, M. G. Flanner, P. E. Thorton, S. C. Swenson, P. J. Lawrence, X. Zeng, Z. L. Yang, S. Levis, K. Skaguchi, G. B. Bonan and A. G. Slater (2011), Parameterization Improvements and Functional and Structural Advances in Version 4 of the Community Land Model, J. Adv. Model. Earth Syst., 3(1).

Lee, T. J. and R. A. Pielke (1992), Estimating the soil surface specific humidity, Journal of Applied Meteorology, 31(5), 480-484.

Leverenz, J. W., and T. M. Hinckley (1990), Shoot structure, leaf area index and productivity of evergreen conifer stands, Tree Physiology 6(2), 135-149.

Lewis, P., and M. J. Barnsley (1994), Influence of the sky radiance distribution on various formulations of the earth surface albedo, In 6th International Symposium on Physical Measurements and Signatures in Remote Sensing, ISPRS, 707-715.

Liang, X. Z., M. Xu, W. Gao, K. Kunkel, J. Slusser, Y. Dai, Q. Min, … and F. Gao (2005), Development of land surface albedo parameterization based on Moderate Resolution Imaging Spectroradiometer (MODIS) data, Journal of Geophysical Research: Atmospheres (1984–2012), 110(D11).

Lombardozzi, D., S. Levis, G. Bonan, and J. P. Sparks (2012), Predicting photosynthesis and transpiration responses to ozone: decoupling modeled photosynthesis and stomatal conductance, Biogeosciences, 9, 3113-3130, doi:10.5194/bg-9-3113-2012.

Los, S. O., N. H. Pollack, M. T. Parris, G. J. Collatz, C. J. Tucker, P. J. Sellers, ... and D. A. Dazlich (2000), A global 9-yr biophysical land surface dataset from NOAA AVHRR data, Journal of Hydrometeorology, 1(2), 183-199.

Lucht, W., C. B. Schaaf, and A. H. Strahler (2000), An algorithm for the retrieval of albedo from space using semiempirical BRDF models, IEEE Trans. Geosci. Remote Sens., 38, 977– 998, doi:10.1109/36.841980.

Mahfouf, J. F. (1991), Analysis of soil moisture from near-surface parameters: A feasibility study, J. Appl. Meteorol., 30, 506– 526.

Manzi, A. O., and S. Planton (1994), Implementation of the ISBA parameterization scheme for land surface processes in a GCM: An annual cycle experiment, J. Hydrol., 155, 355–389.

Moldrup, P., T. Olesen, T. Yamaguchi, P. Schjønning, and D. E. Rolston (1999), Modeling diffusion and reaction in soils: IX. The Buckingham-Burdine-Campbell equation for gas diffusivity in undisturbed soil, Soil Science, 164(8), 542-551.

Moore, N., N. Torbick, B. Lofgren, J. Wang, B. Pijanowski, J. Andresen, D. Y. Kim, and J. Olson (2010), Adapting MODIS-derived LAI and fractional cover into the RAMS in East Africa, Int. J. Clim., 30, 1954–1969.

Morrison, H., G. Thompson, V. Tatarskii (2009), Impact of Cloud Microphysics on the Development of Trailing Stratiform Precipitation in a Simulated Squall Line: Comparison of One– and Two–Moment Schemes, Mon. Wea. Rev., 137, 991–1007.

Mu, Q., F. A. Heinsch, M. Zhao, and S. W. Running (2011), Improvements to a MODIS global terrestrial evapotranspiration algorithm, Remote Sensing of Environment 115, 1781-1800.

Myneni, R., Y. Knyazikhin, and N. Shabanov (2011), Leaf Area Index and Fraction of Absorbed PAR Products from Terra and Aqua MODIS Sensors: Analysis, Validation, and Refinement. Land Remote Sensing and Global Environmental Change, Remote Sensing and Digital Image Processing, 11, 603-633.

Niu, G. Y., Z. L. Yang, K. E. Mitchell, F. Chen, M. B. Ek, M. Barlage, ... and Y. Xia (2011), The community Noah land surface model with multiparameterization options (Noah-MP): 1. Model description and evaluation with local-scale measurements, Journal of Geophysical Research: Atmospheres (1984–2012), 116(D12).

Noilhan, J. and S. Planton (1989), A simple parameterization of land surface processes for meteorological models, Mon. Wea. Rev., 117, 536-549.

Noilhan, J. and J. F.Mahfouf (1996), The ISBA land surface parameterisation scheme, Global and Planetary Change, 13(1), 145-159.

Oleson, K. W., D. M. Lawrence, G. B. Bonan, B. Drewniak, M. Huang, C. D. Koven, S. Levis, F. Li, W. J. Riley, Z. M. Subin, S. C. Swenson, P. E. Thornton, A. Bozbiyik, R. Fisher, E. Kluzek, J. F. Lamarque, P. J. Lawrence, L. R. Leung, W. Lipscomb, S. Muszala, D. M. Ricciuto, W. Sacks, Y. Sun, J. Tang, and Z. L. Yang (2013), Technical Description of version 4.5 of the Community Land Model (CLM). Ncar Technical Note NCAR/TN-503+STR, National Center for Atmospheric Research, Boulder, CO, 422 pp, DOI: 10.5065/D6RR1W7M.

Otte, T. L. and J. E. Pleim (2010), The Meteorology-Chemistry Interface Processor (MCIP) for the CMAQ modeling system: updates through MCIPv3. 4.1, Geoscientific Model Development, 3(1), 243-256.

Padro, J. (1996), Summary of ozone dry deposition velocity measurements and model estimates over vineyard, cotton, grass and deciduous forest in summer, Atmospheric Environment, 30(13), 2363-2369.

Pielke, R. A., R. Avissar, M. Raupach, A.J. Dolman, X. Zeng, and A.S. Denning (1998), Interactions between the atmosphere and terrestrial ecosystems: influence on weather and climate, Global Change Biology, 4(5), 461-475.

Pleim, J. E. (2007a), A combined local and nonlocal closure model for the atmospheric boundary layer. Part I: model description and testing, J. Appl. Meteor. Clim., 46, 1383–1395.

Pleim, J. E. (2007b), A combined local and nonlocal closure model for the atmospheric boundary layer. Part II: application and evaluation in a mesoscale meteorological model, J. Appl. Meteor. Clim., 46, 1396–1409.

Pleim, J. E., J. O. Bash, J. T. Walker, and E. J. Cooter (2013), Development and evaluation of an ammonia bidirectional flux parameterization for air quality models, Journal of Geophysical Research: Atmospheres, 118(9), 3794-3806.

Pleim J. E. and R. Gilliam (2009), An indirect data assimilation scheme for deep soil temperature in the Pleim-Xiu land surface model, J. Appl. Meteor. Clim., 48, 1362-1376.

Pleim, J. E. and L. Ran (2011), Surface Flux Modeling for Air Quality Applications, Atmosphere, 2(3), 271-302.

Pleim, J. E. and A. Xiu (1995), Development and testing of a surface flux and planetary boundary layer model for application in mesoscale models, J. Appl. Meteorol., 34, 16–32.

Pleim, J. E. and A. Xiu (2003), Development of a Land Surface Model. Part II: Data Assimilation, J. Appl. Meteor., 42, 1811–1822.

Pleim, J. E., A. Xiu, P. L. Finkelstein, and T. L. Otte (2001), A coupled land-surface and dry deposition model and comparison to field measurements of surface heat, moisture, and ozone fluxes. Water, Air and Soil Pollution: Focus, 1(5-6), 243-252.

Pleim, J., A. A. R. Gilliam, W. Appel, and L. Ran, 2015: Recent Advances in Modeling of the Atmospheric Boundary Layer and Land Surface in the Coupled WRF-CMAQ Model, 34th International Technical Meeting on Air Pollution Modelling and its Application, 4-8 May, 2015, Montpellier, France.

Pouliot, G., H. A. D. van der Gon, J. Kuenen, J. Zhang, M. D. Moran, and P. A. Makar (2014), Analysis of the emission inventories and model-ready emission datasets of Europe and North America for phase 2 of the AQMEII project, Atmospheric Environment.

Prentice, I. C., X. Liang, B. E. Medlyn, and Y-P. Wang (2015), Reliable, robust and realistic: the three R's of next-generation land-surface modelling, Atmospheric Chemistry and Physics , 15(10), 5987-6005.

Ran, L. and A. Hanna (2014), Spatial Allocator Raster Tools v4.2: User's Guide, the Community Modeling and System analysis at the University of North Carolina, Chapel Hill. Available at: https://www.cmascenter.org/sa-tools/documentation/4.2/html/raster/Raster_Users_Guide_4_2.pdf, (last access: September 2015), 15 pp.

Ran, L., R. Gilliam, F. S. Binkowski, A. Xiu, J. Pleim, and L. Band (2015), Sensitivity of the Weather Research and Forecast/Community Multiscale Air Quality modeling system to MODIS LAI, FPAR, and albedo, J. Geophys. Res. Atmos., 120, 8491–8511, doi:10.1002/2015JD023424.

Rasmussen, D. J., A. M. Fiore, V. Naik, L. W. Horowitz, S. J. McGinnis, M. G. Schultz (2012), Surface ozone-temperature relationships in the eastern US: A monthly climatology for evaluating chemistry-climate models, Atmospheric Environment, 47, 142-153.

Rawls, W. J., D. L. Brakensiek, and K. E. Saxton (1982), Estimation of soil water properties, Trans. of the ASAE, 25, 1316–1320.

Rogers, R. E., A. Deng, D. R. Stauffer, B. J. Gaudet, Y. Jia, S. T. Soong, and S. Tanrikulu (2013), Application of the Weather Research and Forecasting Model for Air Quality Modeling in the San Francisco Bay Area, Journal of Applied Meteorology & Climatology, 52(9).

Sakaguchi, K., and X. Zeng (2009), Effects of soil wetness, plant litter, and under-canopy atmospheric stability on ground evaporation in the Community Land Model (CLM3. 5), Journal of Geophysical Research: Atmospheres (1984–2012), 114(D1).

Schaaf, C. B., F. Gao, A. H. Strahler, W. Lucht, X. Li, T. Tsang, N. C. Strugnell, X. Zhang, Y. Jin, J. P. Muller, P. Lewis, M. Barnsley, P. Hobson, M. Disney, G. Roberts, M. Dunderdale, C. Doll, R. d'Entremont, B. Hu, S. Liang, and J. L. Privette (2002), First Operational BRDF, Albedo and Nadir Reflectance Products from MODIS, Remote Sens. Environ., 83, 135-148.

Schaaf, C. B., J. Liu, F. Gao and A. H. Strahler (2011), MODIS Albedo and Reflectance Anisotropy Products from Aqua and Terra, In Land Remote Sensing and Global Environmental Change: NASA's Earch Observing System and the Science of ASTER and MODIS, Remote Sensing and Digital Image Processing Series, Vol.11, edited by B. Ramachandran, C. Justice, and M. Abrams, Springer-Cerlag, 873 pp.

Sellers, P. J., M. D. Heiser, and F. G. Hall (1992), Relations between surface conductance and spectral vegetation indices at intermediate (100 m^2 to 15 km^2) length scales, Journal of Geophysical Research: Atmospheres (1984–2012), 97(D17), 19033-19059.

Sellers, P. J., D. A. Randall, G. J. Collatz, J. A. Berry, C. B. Field, D. A. Dazlich, C. Zhang, G. D. Collelo, and L. Bounoua (1996), A revised land surface parameterization (SiB2) for atmospheric GCMs. Part I: Model formulation, J. Clim., 9, 676–705.

Sellers, P., R. Dickinson, D. Randall, A. Betts, F. Hall, J. Berry, G. Collatz, A. Denning, A., H. Mooney, C. Nobre, N. Sato, C. Field, and A. Henderson-Sellers (1997), Modeling the exchanges of energy, water, and carbon between continents and the atmosphere, Science 275(5299), 502-509.

Skamarock, W. C., J. B. Klemp, J. Dudhia, D. O. Gill, D. M. Barker, W. Wang, and J. G. Powers (2008), A description of the advanced research WRF version 3. NCAR Tech Note, NCAR/TN 475+STR: 125 pp.

Sarwar G., H. Simon, K. Fahey, R. Mathur, W. S. Goliff, and W. R. Stockwell (2014), Impact of sulfur dioxide oxidation by Stabilized Criegee Intermediate on sulfate, Atmospheric Environment, 85, 204-214, ISSN 1352-2310.

Sitch, S., P. M. Cox, W. J. Collins, and C. Huntingford (2007), Indirect radiative forcing of climate change through ozone effects on the land-carbon sink, Nature, 448, 791–794.

Solazzo, E., R. Bianconi, G. Pirovano, M. D. Moran, R. Vautard, C. Hogrefe, K. W. Appel, V. Matthias, P. Grossi, B. Bessagnet, J. Brandt, C. Chemel, J. H. Christensen, R. Forkel, X. V. Francis, A. B. Hansen, S. McKeen, U. Nopmongcol, M. Prank, K. N. Sartelet, A. Segers, J. D. Silver, G. Yarwood, J. Werhahn, J. Zhang, S. T. Rao, S. Galmarini (2013), Evaluating the capability of regional-scale air quality models to capture the vertical distribution of pollutants, Geoscientific Model Development, 6, 791-818.

Stauffer, D. R., and N. L. Seaman (1990), Use of four-dimensional data assimilation in a limited-area mesoscale model, Part I: Experiments with synoptic-scale data, Mon. Wea. Rev., 118, 1250-1277.

Stauffer, D. R., N. L. Seaman, and F. S. Binkowski (1991), Use of four-dimensional data assimilation in a limited-area mesoscale model, Part II: Effects of data ssimilation within the planetary boundary layer, Mon. Wea. Rev., 119, 734-754.

Vautard, R., M. D. Moran, E. Solazzo, R. C. Gilliam, V. Matthias, R. Bianconi, ... and S. Galmarini (2012), Evaluation of the meteorological forcing used for the Air Quality Model Evaluation International Initiative (AQMEII) air quality simulations. Atmospheric Environment, 53, 15-37.

Wang, S. X., M. Zhao, J. Xing, Y. Wu, Y. Zhou, Y. Lei, K. B. He, L. X. Fu, and J. M. Hao (2010), Quantifying the air pollutants emission reduction during the 2008 Olympic Games in Beijing, Environ. Sci. Technol., 44, 2490-2496.

Wanner, W., X. Li, and A. H. Strahler (1995), On the derivation of kernels for kernel-driven models of bidirectional reflectance, J. Geophys. Res., 100, 21,077– 21,090.

Weiss, A. and J. M. Norman (1985), Partitioning solar radiation into direct and diffuse, visible and near-infrared components, Agricultural and Forest meteorology, 34(2), 205-213.

Wesely, M. L., J. A. Eastman, D. H. Stedman, and E. D. Yalvac (1982), An eddy correlation measurement of NO_2 flux to vegetation and comparison to O_3 flux, Atmos. Environ., 16, 815-820.

Whitten, G. Z., G. Heo, Y. Kimura, E. McDonald-Buller, D. Allen, W. P. L. Carter, and G. Yarwood (2010), A new condensed toluene mechanism for Carbon Bond: CB05-TU, Atmos. Environ., 44, 5346–5355.

Wyngaard, J. C. (2010), Turbulence in the Atmosphere, Cambridge University Press.

Xing, J., R. Mathur, J. Pleim, C. Hogrefe, C.-M. Gan, D. C. Wong, C. Wei, R. Gilliam, and G. Pouliot (2015), Observations and modeling of air quality trends over 1990–2010 across the Northern Hemisphere: China, the United States and Europe, Atmos. Chem. Phys., 15, 2723-2747, doi:10.5194/acp-15-2723-2015.

Xiu, A. and J. E. Pleim (2001), Development of a Land Surface Model. Part I: Application in a Mesoscale Meteorological Model, J. Appl. Meteor., 40, 192-209.

Yang, W., B. Tan, D. Huang, M. Rautiainen, N. V. Shabanov, Y. Wang, J. L. Privette, … and R. B. Myneni (2006), MODIS leaf area index products: From validation to algorithm improvement,Geoscience and Remote Sensing, IEEE Transactions, 44(7), 1885-1898.

Zhang, X., M. A. Friedl, and C. B. Schaaf (2006), Global vegetation phenology from Moderate Resolution Imaging Spectroradiometer (MODIS): Evaluation of global patterns and comparison with in situ measurements, Journal of Geophysical Research: Biogeosciences (2005–2012), 111(G4).

Yu, X., Z. Wu, W. Jiang, and X. Guo (2015), Predicting daily photosynthetically active radiation from global solar radiation in the Contiguous United States, Energy Conversion and Management, 89 (2015): 71-82.

CHAPTER 4: A PHOTOSYNTHESIS-BASED TWO-LEAF CANOPY STOMATAL CONDUCTANCE MODEL FOR WRF/CMAQ WITH MODIS INPUT

Abstract

A coupled photosynthesis-stomatal conductance model with single layer sunlit and shaded leaf canopy scaling is developed for the Pleim-Xiu land surface model (LSM) in the meteorology and air quality modeling system - WRF/CMAQ (Weather Research and Forecast model and Community Multiscale Air Quality model). The photosynthesis-based stomatal conductance model for the PX LSM (PX PSN) is implemented and evaluated in a diagnostic box model which has evapotranspiration and ozone deposition components taken directly from WRF/CMAQ. The PX PSN is validated for LH estimation at four selected FLUXNET sites with different vegetation types and landscape characteristics and at one FLUXNET site with ozone flux measurements in comparison with the simple Jarvis approach used in the current PX LSM. The model performance is influenced by many factors including model parameters, site-related input data, and measurement errors, in addition to physical process formulations. Overall, the PX PSN performs as well as the PX Jarvis does in simulating LH with varying performance at different sites. The PX PSN shows distinct advantages in simulating LH over landscapes with short vegetation such as grassland and cropland. Since the PX PSN treats C_3 and C_4 plants differently for CO_2 assimilation estimation, it has significant advantages in simulating LH over the C_4 grassland in comparison with the PX Jarvis approach. Simulations using Moderate Resolution Imaging Spectroradiometer (MODIS) LAI rather than LAI observations at each site were also performed to assess how the model would perform with the grid averaged data

available in the Eulerian grid model (WRF/CMAQ). While MODIS LAI generally follows the seasonality of the observed LAI, it cannot capture the extreme highs and lows of the site measurements. The MODIS LAI makes the model perform worse at all sites except one site with tall and old trees. The PX PSN performs especially well in simulating LH and ozone deposition velocity and flux at the ozone flux grassland site while the PX Jarvis significantly overestimates. The performance of the PX PSN over prevalent vegetation types (deciduous and coniferous forest, grassland, and cropland) at the selected sites demonstrates that the model is applicable for WRF/CMAQ simulations.

4.1 Introduction

The combined meteorology and air quality (AQ) modeling system composed of the Weather Research and Forecast (WRF) model [*Skamarock et al*., 2008] and Community Multiscale Air Quality (CMAQ) model [*Byun and Schere,* 2006] is an important decision support tool that is used to help understand the chemical and physical processes involved in air quality degradation and develop policy to mitigate harmful effects of air pollution on human health and the environment around the world [*Cohan et al*., 2007; *Wang et al*., 2010; *Compton et al*., 2011; *Hogrefe et al*., 2014; *Xing et al*., 2015]. Despite significant advances in AQ modeling systems over the past decade, there are still many uncertainties in the system [*Foley et al*., 2010; *Appel et al.* 2011]. For example, the system tends to overestimate ozone in the southeast and Gulf regions of the U.S. while ozone estimations in the north agree well with observations. The recent study by *Ran et al.* [2015b], using an improved WRF/CMAQ with and without Moderate Resolution Imaging Spectroradiometer (MODIS) vegetation and albedo input, shows that the model's tendency to overestimate O_3 in these regions persists (figure 4.1). Many components from this complex modeling system including emissions, transport, photochemistry, and land

surface exchange may contribute to these errors. This research focuses on improving land surface model (LSM) processes in the retrospective WRF/CMAQ system which includes both meteorological (heat, moisture, and momentum) and chemical (dry deposition and bi-directional exchange) surface fluxes.

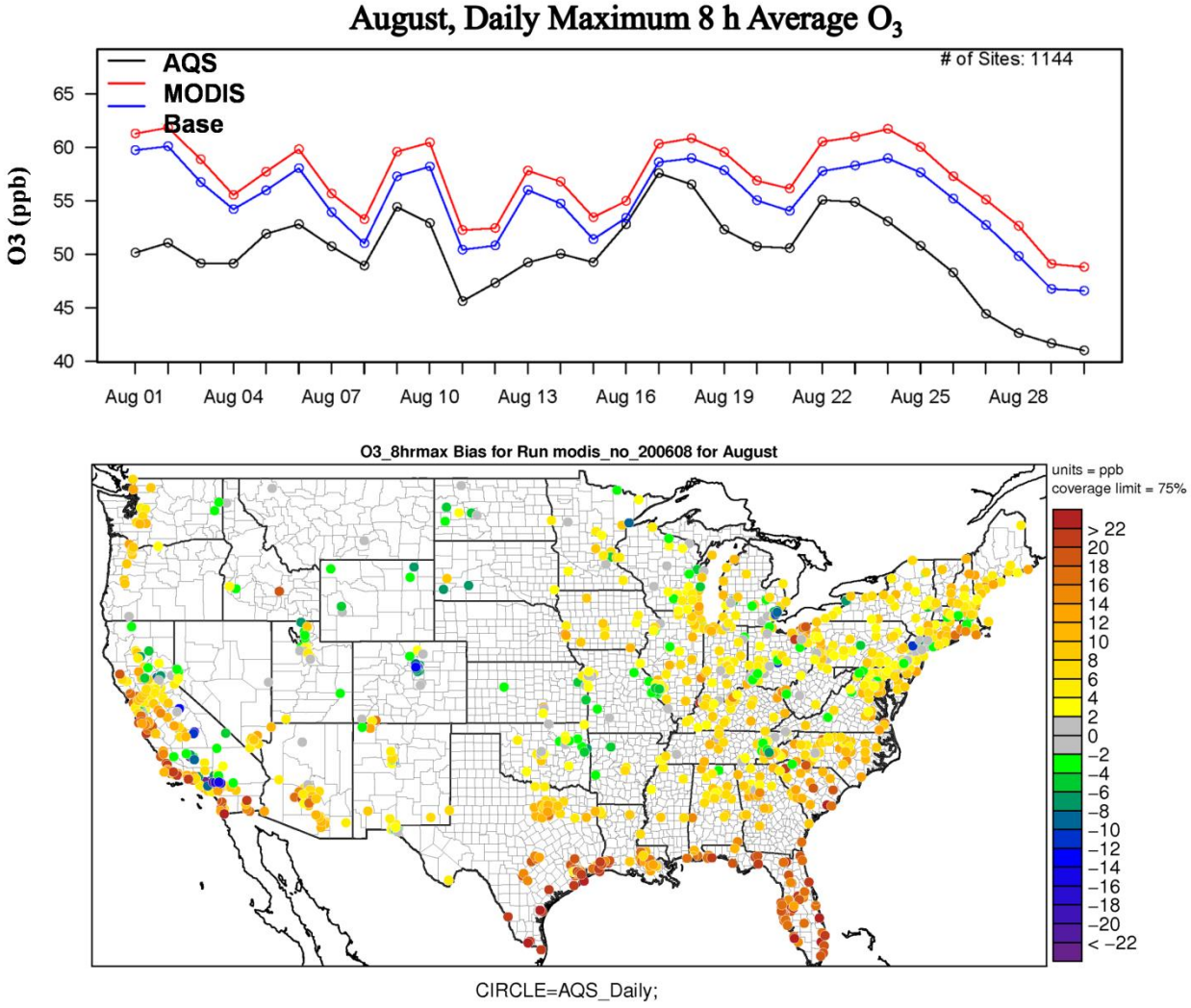

Figure 4.1. Evaluation of daily maximum 8 hour average O_3 (ppb) simulated from an improved WRF/CMAQ with/without MODIS vegetation and albedo input over August 2006 against the EPA Air Quality System (AQS) sites. The top plot displays mean of daily maximum 8 hour average O_3 from the base model (blue line), the model with MODIS input (red line) and all AQS sites (black line). The bottom plot is the mean bias spatial plot for daily maximum 8 hour

average O_3 simulated from the base model without MODIS input. The base model's vegetation is computed from vegetation parameters prescribed in land use category lookup tables using equations 2 and 3 in *Ran et al*. [2015a].

The Pleim-Xiu (PX) [*Pleim and Xiu*; 1995; *Xiu and Pleim*, 2001] and Noah [*Chen and Dudhia*, 2001] LSMs are two of WRF LSMs which are commonly used for meso-scale retrospective meteorology simulations. The PX LSM is routinely used in air quality simulations [*Eder et al*., 2009; *Kelly et al*., 2014; *Hogrefe et al*., 2014] because it is specifically designed for CMAQ which has a dry deposition model using the same stomatal and aerodynamic resistances computed in the PX LSM WRF and has the same planetary boundary layer (PBL) model, the Asymmetric Convective Model version 2 (ACM2) [*Pleim*, 2007a and 2007b], that can be consistently configured in WRF. Unlike climate LSMs [e.g. *Oleson et al.*, 2013; *Clark et al*., 2011] with complex hydrology and dynamic vegetation coupled with climate to model processes over decadal to century future periods, the PX and Noah LSMs have relatively simple prognostic soil water models (PX has 2 soil layers and Noah has 4) which rely heavily on data initialization and assimilation for high accuracy over relatively short periods (days to years). Thus, both the LSMs have simple canopy treatments with a big-leaf empirical function stomatal conductance following the approach described by *Noilhan and Planton* [1989] as well as simple soil hydrology and snow processes. Surface characteristics including vegetation parameters and surface albedo are specified in LSM land use look-up tables and plant phenological dynamics are modeled using simple time and temperature dependent functions. Land use data used in these LSMs are often out of date and created from certain periods in the past. With increasing needs to conduct year-long retrospective WRF/CMAQ simulations, these LSMs using simple canopy treatment with table prescribed surface representations from out of date land use data clearly

show limitations in capturing seasonal landscape changes (e.g. phenology and albedo) and disturbances (e.g. fires, storm damages) [*Ran et al.*,2015b]. In addition, lacking a biochemically-based photosynthesis-conductance scheme could limit not only the model's dynamic responses to environmental conditions such as temperature, air pollutants (e.g. O_3) and CO_2 concentration but also their applications in assessing the coupling effects of air quality and vegetation productivity in changing climate.

There are ongoing efforts to improve the surface representation in WRF/CMAQ. For instance, the high resolution 30-m National Land Cover Database (NLCD) as well as MODIS 500-m land cover data [*Pleim and Ran*, 2011, *Ran et al*., 2010, *Ran et al*., 2012] are used in WRF/CMAQ simulations with the PX LSM. Gridded 2011 NLCD/MODIS land cover data at the 9-arc second resolution for most of North America are available in the WRF Preprocessing System (WPS) for WRF/CMAQ with the PX LSM to use the 40-class NLCD/MODIS land cover data routinely. In addition, there are recent improvements to the vegetation, soil, and PBL processes in the WRF/CMAQ with the PX LSM and ACM2 [*Pleim et al.*, 2015]. *Ran et al.* [2015a and 2015b] incorporated MODIS vegetation and albedo products in the WRF/CMAQ modeling system with the PX LSM. They conclude that realistic vegetation characteristics and phenology from MODIS products help improve the 2 m mixing ratio (Q) simulation during the growing seasons. With EPA beginning to regulate greenhouse gases (GHGs) under the Clean Air Act ("CAA"), the simple vegetation treatment following the empirical function Jarvis stomatal conductance approach [*Jarvis*, 1976] without the CO_2 effect by the PX LSM [*Noilhan and Planton*,1989; *Pleim and Xiu*, 1995] is limited over extended simulations for regulatory and scientific research related to climate-air quality co-benefit studies. Therefore, incorporating the impacts of CO_2 in WRF/CMAQ through using a photosynthesis-based stomatal conductance

approach in the PX LSM will be an important advance in the modeling capabilities with changing CO_2 levels in space and time which can be captured by the EPA CO_2 emission inventory. This research furthers the study presented by *Ran et al*. [2015b] by enhancing the vegetation model using a photosynthesis-based stomatal physiology process model which is commonly used in Earth system models [*Bonan et al.*, 2011; *Clark et al*., 2011; *Kowalczyk et al*., 2013; *Oleson et al*., 2013].

The objective of the study is to develop, implement and evaluate a coupled leaf photosynthesis and stomatal conductance approach in the PX LSM for meteorology and air quality modeling with MODIS vegetation input. This paper focuses on the development and evaluation of a coupled photosynthesis and stomatal conductance approach in a diagnostic box model with the PX LSM and CMAQ dry deposition model components that are directly from the updated WRF/CMAQ system presented by *Ran et al*. [2015b]. The questions which the papers addresses are: (i) how does the PX LSM with a coupled leaf photosynthesis and stomatal conductance approach influence the performance of latent heat and ozone deposition and flux, (ii) can the photosynthesis approach PX LSM better represent diurnal variations in latent heat, and ozone deposition and flux than the current approach, and (iii) how does the PX LSM with a coupled leaf photosynthesis and stomatal conductance approach and with the input of MODIS leaf area index (LAI) and fraction of absorbed photosynthetically active radiation (FPAR) vegetation data influence latent heat?

A sunlit and shaded big leaf photosynthesis-based stomatal conductance approach developed and implemented in the diagnostic PX LSM box model is described in section 2 based on the 2006 flux measurements from the FLUXNET Harvard Forest US-Ha1 site. The photosynthesis-based approach is further evaluated and analyzed against the measurements from

four selected FLUXNET sites (Missouri Ozark/US-MOz, Mead Irrigated Rotation/US-Ne2, Fermi Prairie/US-IB2, and Wind River Field Station/US-Wrc) which have different vegetation types and against the 2013 ozone and surface flux measurements by EPA at Duke Forest Open Field, North Carolina. MODIS vegetation input to the diagnostic box model is also evaluated to demonstrate the advantages and limitations in using MODIS input to the advanced PX LSM. MODIS LAI is evaluated against observed LAI which are available at the four selected FLUXNET measurement sites. Conclusions and future work are presented in the last section.

4.2 Photosynthesis-based Stomatal Conductance Approach

Vegetation plays an important role not only in the surface energy budget but also water and carbon cycles [*Jarvis and McNaughton*, 1986; *Katul et al*., 2012]. In addition, it is the source and sink of atmospheric chemicals including CO_2 and gas-phase chemical species such as O_3, NH_3, NO_2, SO_2, and a wide array of volatile organic compounds (VOCs) [*Pleim and Ran*, 2011]. Plants open their stomata to obtain atmospheric CO_2 for photosynthesis while at the same time they lose water because of the diffusion of water molecules through leaf stomata to the atmosphere. A key function of LSMs is to estimate latent heat flux (λE), which is the product of latent heat of evaporation (λ) times evaporative water flux (E, also called evapotranspiration - ET). ET contains evaporation from leaf transpiration, water evaporation from soil, litter and vegetation surfaces, and open water bodies [*Bonan*, 2008]. In the growing seasons, transpiration is often dominant in controlling ET from vegetated lands [*Budyko*, 1974]. Because stomata control the amount of water transpired by vegetation, stomatal conductance and its scaling from leaf to canopy are key processes in estimating ET. The coupled photosynthesis-based stomatal conductance model with sunlit and shaded leaves for the PX LSM is developed for modeling ET and the carbon cycle between the atmosphere and vegetation based on approaches which are

applied in global climate models (GCMs) [*Dai et al*., 2004; *Cox et al*., 1998; *Bonan et al., 2011*; *Clark et al.,* 2011; *Kowalczyk et al.,* 2013; *Oleson et al.,* 2013] and ecosystem productivity models [*Campbell and Norman, 1998*; *Medlyn et al*., 2005; *Song et al*., 2009; *Evers et al*, 2010; Baker et al., 2010].

4.2.1 Stomatal Conductance

The current PX LSM models canopy stomatal conductance (G_{st}) to gasses based on the Jarvis approach [*Jarvis*, 1976], which is an empirical multiplicative model by linking the stomatal conductance to assumed-independent environmental functions. The PX LSM treats the whole canopy as a single leaf (big-leaf model) and the canopy fluxes from the big leaf are then calculated by summing the fluxes of individual leaves [*Jarvis*, 1995] using LAI. Following the Jarvis approach presented in the Interactions Soil Biosphere Atmosphere (ISBA) LSM [*Noilhan and Planton*, 1989] with modifications in the PX LSM [*Pleim and Xiu*, 1995], G_{st} is computed as:

$$G_{st} = LAI * \left[\frac{1}{R_{st\min}} F_1(PAR) F_2(w_2) F_3(RH_s) F_4(T_{ic}) \right] \tag{4.1}$$

where R_{stmin} is the minimum stomatal resistances for each land cover type specified in the LSM land cover lookup table. The functions $F_{1–4}$, which represent the fractional degree (0 to 1) of stomatal closure caused by the environmental factors: photosynthetically active radiation (*PAR*), root-depth soil moisture (w_2), relative humidity at the leaf surface (RH_s), and air temperature in the canopy (T_{ic}), are defined by *Xiu and Pleim* [2001]. The influence of ambient CO_2 concentration is not included in the current PX LSM with the assumption that the CO_2 concentration is constant for the relatively short periods typically used for mesoscale meteorology simulations. The advantage of this simple empirical approach is that it can be

easily implemented for large scale simulations with a small set of vegetation parameters such as LAI and R_{stmin} and it generally produces reasonable results for retrospective simulations with initial or real-time assimilated soil conditions [*Noilhan and Mahfouf*, 1996; *Chen and Dudhia*, 2001; *Xiu and Pleim*, 2001]. The weakness of the simplest models is that they depend on the limited number of multiplicative functions which are related to environment variables that are often not actually independent. Since the multiplicative big leaf model does not depend on measurable physiological or physical parameters, they have to be tuned against stand-level and canopy level eddy flux measurements. Although the big leaf model is simple and widely used in many disciplines, it is often criticized for ignoring canopy gradients and differences between plant and soil components within the canopy [*Jarvis*, 1995; *dePury and Farquhar*, 1997; *Wang and Leuning*, 1998].

The stomatal conductance (g_{st}) at the leaf scale in the photosynthesis-based PX LSM is modeled based on the commonly used the Ball-Woodrow-Berry (BWB) model [*Ball et al*., 1987], which connects g_{st} directly to net CO_2 assimilation rate (A_{net}) based on plant physiological processes. g_{st} is modeled in the PX LSM following the semi-empirical BWB model described by *Collatz et al*. [1991], applied in a GCM by *Sellers et al.* [1996], and implemented in the Community Land Model version 4 (CLM4.5) [*Bonan et al*., 2011; *Oleson et al*. 2013] within the Community Earth System Model (CESM) as:

$$g_{st} = g_0 + m_g \frac{A_{net}}{c_s} \frac{e_s}{e_i} P_a \tag{4.2}$$

where g_0 is set to 0.01 mol m^{-2} s^{-1} for C_3 plants and 0.04 mol m^{-2} s^{-1} for C_4 plants, m_g is a plant-type parameter which is 9 for C_3 plants and 4 for C_4 plants, c_s is the CO_2 partial pressure at the leaf surface, e_s is the vapor pressure at the leaf surface, e_i is the saturation vapor pressure inside the leaf stomata at the vegetation surface temperature (T_s), and P_a is the atmospheric pressure.

Soil moisture stress is considered similarly to the PX Jarvis LSM where the empirical function F_2 (eq. 4.3) is used to scale canopy stomatal and net CO_2 assimilation rate following the approach used by the Joint UK Land Environment Simulator (JULES) LSM model [*Clark et al*., 2011]. The function F_2 with a relatively smooth S shape very similar to the JULES soil stress factor is computed as:

$$F_2 = \frac{1}{\left[1+\exp\left\{-5\left(w_{2avl}/w_{2mxav} - \left(w_{2mxav}/3 + w_{wlt}\right)\right)\right\}\right]} \tag{4.3}$$

with

$$w_{2avl} = w_2 - w_{wlt}\,,\ w_{2mxav} = w_{fc} - w_{wlt}$$

where w_{fc} is the volumetric water content at field capacity and w_{wlt} is the wilting point.

4.2.2 Leaf-scale Photosynthesis

The net photosynthetic assimilation rate - A_{net} of C_3 and C_4 plants at the leaf scale for the PX LSM is estimated based on the biochemical model of photosynthesis described by *Farquhar et al*. [1980] and applied in GCMs [*Collatz et al*., 1991, and 1992, *Sellers et al*., 1996, *Cox et al.*, 1999, Clark et al., 2011, *Bonan et al*. 2011, *Oleson et al.*, 2013] and land surface exchange studies in modeling plant evaporation and productivity [*Medlyn et al*., 2005; *Song et al*., 2009; *Evers et al*, 2010; *Baker et al*., 2010]. A_{net} (mol CO_2 m^{-2} s^{-1}) is calculated based on colimitation among three potential assimilation rates (A_c, A_j, and A_e) limited by Rubisco (nitrogen related), light (photon related), and transport of photosynthetic products for C_3 plants and phosphoenolpyruvate (PEP) carboxylase limitation for C_4 plants. The Rubisco-limited assimilation rate (A_c mol CO_2 m^{-2} s^{-1}) is a function of the maximum rate of carboxylation of Rubisco (V_{cmax} mol CO_2 m^{-2} s^{-1}) and is formulated following JULES [*Clark et al., 2011*] as:

$$A_c = \begin{cases} V_{c\max}\left(\dfrac{c_i - c_c}{c_i + K_c(1+O_a/K_o)}\right) & \text{for } C_3 \text{ and } C_4 \text{ plants} \\ V_{c\max} \end{cases} \quad (4.4)$$

with

$$V_{c\max} = V_{c\max 25}\frac{2^{0.1(T_s-25)}}{[1+e^{0.3(T_s-T_{up})}][1+e^{0.3(T_{low}-T_s)}]} \quad (4.5)$$

$$c_c = \begin{cases} \dfrac{O_a}{2600(0.57^{0.1(Ts-25)})} & \text{for } C_3 \text{ and } C_4 \text{ plants} \\ 0 \end{cases} \quad (4.6)$$

where c_i (Pa) is the CO_2 partial pressure inside the leaf stomata, c_c (Pa) is the CO_2 compensation point in the absence of non-photorespiratory respiration, O_a (Pa) is the partial pressure of atmospheric oxygen, and K_c (Pa) and K_o (Pa) are the Michaelis-Menten constants for CO_2 and O_2. C_c, K_c, and K_o are computed based on parameters and equations used in JULES [*Cox et al*., 1998; *Clark et al*., 2011]. V_{cmax} at any leaf surface temperature is estimated based on the maximum rate of carboxylation of the enzyme Rubisco at 25°C (V_{cmax25} mol CO_2 m^{-2} s^{-1}). The average V_{cmax25} value is assumed to be related to leaf nitrogen concentration and is computed based on the top of the canopy V_{cmax25} (V_{cmax25_0}) integrated for sunlit and shaded leaves based on the equations described by *Bonan et al.* [2011] as:

$$V_{c\max 25}(sun) = V_{c\max 25\_0}(1-e^{-(K_n+K_{dir})LAI})\frac{1}{K_n+K_{dr}}\frac{1}{LAI_{sun}} \quad (4.7)$$

$$V_{c\max 25}(sha) = \left\{V_{c\max 25\_0}\left[(1-e^{-K_nLAI})\frac{1}{K_n}\right] - (1-e^{-(K_n+K_{dir})LAI})\frac{1}{K_n+K_{dir}}\right\}\frac{1}{LAI_{shd}} \quad (4.8)$$

where K_n is the foliage nitrogen decay coefficient, K_{dir} is the direct beam attenuation coefficient within the canopy (described by equation 4.19), and LAI_{sun} and LAI_{shd} are the LAI values for sunlit and shaded leaves (described by equations 4.17 and 4.18). As one of the most important

parameter in the photosynthesis approach, V_{cmax25} shows a range of values among and within plant function types (PFTs) [*Kattge et al*., 2009] mainly due to different nitrogen use efficienies. The value used is often tightly related to the foliage nitrogen decay coefficient (K_n) which also varies among models [*Bonan et al*., 2011]. The PX LSM photosynthesis model follows the V_{cmax25} values after nitrogen constraints and K_n = 0.17 based on the values analyzed by *Bonan et al.* [2011]. *Bonan et al.* [2011] uses K_n = 0.11 in their evaluation study; but the value is set to 0.3 in CLM4.5 for multi-layer model considerations. T_{up} and T_{low} are the limits of the optimal temperature range defined for PFT types in JULES [*Clark et al.*, 2011].

The lighted-limited assimilation rate (A_j mol CO_2 m^{-2} s^{-1}) is a function of the rate of electron transport (J mol electron m^{-2} s^{-1}) and is computed as:

$$A_j = \begin{cases} J\left(\dfrac{c_i - c_c}{4.5c_i + 10.5c_c}\right) & \text{for } C_3 \text{ and } C_4 \text{ plants} \\ \varepsilon\ I_{apar} \end{cases} \tag{4.9}$$

with

$$0.7J^2 - (\varepsilon_j I_{apar} + J_{\max})J + \varepsilon_j I_{apar} J_{\max} = 0 \tag{4.10}$$

$$\varepsilon_j = \varepsilon \frac{4(c_i + 2c_c)}{(c_i - c_c)} \tag{4.11}$$

$$J_{\max} = 1.97 V_{c\max} \tag{4.12}$$

where J is solved using the quadratic equation 4.10, ε is the quantum yield (mol CO_2 mol^{-1} photon) and ε_j (mol CO_2 mol^{-1} photon) is the computed electron transport quantum use efficiency following the studies by *Medlyn et al*. [2005] and applied in *Song et al.* [2009]. J_{max} is the maximum electron transport rate (mol electron m^{-2} s^{-1}) and the ratio 1.97 of *Jmax* over V_{CMAX} is used by *Bonan et al*. [2011]. I_{apar} (mol photon m^{-2} s^{-1}) is the absorbed photosynthetically active radiation (APAR) by the leaf. Though a number of alternative functions are used to model J_{max}

and V_{cmax} dependence on temperature across the literature, *Medlyn et al*. [2002] categorizes them into two basic types: the Arrhenius (such as the JULES approach) and the peaked function (such as the CLM4.5 approach). They also show that the peaked function represents the temperature-dependent J_{max} better for almost all species-based experiments in their review. For mesoscale simulations over relative short-time scales, compared with climate simulations, the photosynthesis-based PX LSM uses the Arrhenius function approach which requires fewer PFT-specific temperature constraint parameters.

The photosynthesis rate (A_e) limited by the transport of photosynthetic products (C_3 plants) and phosphoenolpyruvate (PEP) carboxylase limitation (C_4 plants) is computed following JULES [*Clark et al*., 2011] as:

$$A_e = \begin{cases} 0.5V_{c\max} \\ 20000V_{c\max}\dfrac{c_i}{p_a} \end{cases} \quad \text{For } C_3 \text{ and } C_4 \text{ plants, respectively} \qquad (4.13)$$

The final CO_2 assimilation rate (A) is computed by solving the colimitation equations described by *Bonan et al*. [2011] and the net assimilation rate is computed by subtracting leaf dark respiration from A as:

$$0.98A_i^2 - (A_c + A_j)A_i + A_c A_j = 0 \qquad (4.14)$$

$$0.95A^2 - (A_i + A_e)A + A_i A_e = 0 \qquad (4.15)$$

$$A_{net} = A - f_{dr}V_{c\max} \qquad (4.16)$$

where A_i is the smoothed minimum of A_c and A_j. A_i and A are the smallest roots of the quadratic equations. f_{dr} is the dark respiration coefficient which is set as 0.015 for C_3 plants and 0.025 for C_4 plants following JULES.

4.2.3 Leaf to Canopy Scaling

Up-scaling CO_2 assimilation rate and stomatal conductance for estimating canopy transpiration and productivity from the leaf to canopy is complicated by spatial heterogeneity within plant canopies in both the vertical and horizontal dimensions. LAI [*Chen et al*, 2006], leaf inclination angles and leaf clumping [*Pisek et al*. 2013], crown gappiness [*Song et al*. 2009], leaf nitrogen and photosynthetic capacity [*Leuning et al*., 1995; *Baldocchi and Meyers*, 1998] vary within the canopy collectively affecting canopy transpiration, CO_2 assimilation, and other flux processes. The non-linearity of many key processes such as leaf photosynthesis and transpiration with respect to radiation further complicates the difficulty in upscaling those processes [*Jarvis*, 1995; *Campbell and Norman***,** 1998]. In addition, physiological and physical processes such as leaf photosynthesis, stomatal conductance, and transpiration have non-linear relationships with many abiotic regulating variables (e.g. solar and terrestrial radiation, temperature, humidity, wind speed, and soil moisture). Leaf stomatal conductance in a canopy can be quite different at different positions due to both current and past varying abiotic and biotic conditions (e.g. age, height) [*Jarvis and McNaughton*, 1986; *Jarvis*, 1995]. Because of this complication, it is still a challenge to contemporary land surface scientists in ecology, climate, meteorology, and biogeochemistry for modeling and validating parameterized processes that govern land-surface fluxes across different time and space scales [*Moorcroft*, 2006]. Scaling methods from the leaf to canopy vary with different complexity from the simplest big leaf models [*Monteith*, 1981; *Jarvis*, 1995; *Pleim and Xiu*, 1995, *Chen and Dudhia*, 2001] to multi-layer models with 3-D arrays [*Kobayashi et al*., 2012]. A weakness of the simple big leaf model is that it treats sunlit and shaded leaves within the canopy equally. This equal treatment of the canopy leaves often results in overestimation of flux rates (e.g. CO_2) [*dePury and Farquhar*, 1997; *Wang and Leuning*, 1998]. The sunlit and shaded leaves have distinct differences in leaf

surface temperature which results in different surface vapor pressure. Thus, stomata will behave differently under varying micro-meteorological conditions within the canopy. *dePury and Farquhar* [1997] and *Wang and Leuning* [1998] demonstrated that a single-layer sunlit/shaded big leaf model is simpler and has equivalent capabilities to accurately predict CO_2 assimilation rate and latent heat in comparison with a multi-layer model. *Zhang et al*. (2001) also showed that the sunlit/shaded big leaf approach also compares well to multi-layer models for representing the stomatal pathway in dry deposition models. For the mesoscale modeling purpose, the photosynthesis-based PX LSM model also adopts the two-big leaf approach for canopy scaling. The sunlit and shaded leaf areas are computed using the equations described by *Campbell and Norman* [1998] and applied in many studies [e.g., *Song et al.*, 2009] as:

$$LAI_{sun} = \frac{1 - e^{-K_{dir} LAI}}{K_{dir}} \tag{4.17}$$

$$LAI_{shd} = LAI - LAI_{sun} \tag{4.18}$$

Campbell [1986] suggested a simple equation to compute the direct beam attenuation coefficient as:

$$K_{dir} = \frac{\sqrt{x^2 + \tan^{-2}(\theta_{sun})}}{x + 1.774(x + 1.182)^{-0.733}} \tag{4.19}$$

where θ_{sun} is the sun zenith angle, x is the canopy leaf orientation parameter with 0 for vertical leaves and 1 for spherical leaf orientation (randomly oriented). Following the work by *Goudriaan* [1977] and applied in many studies [e.g. *Song et al*., 2009], the transmittance of beam radiation for non-horizontal scattering leaves with leaf absorptivity (α_{leaf}) can be computed as:

$$\tau_{dir} = e^{-\sqrt{\alpha_{leaf}} K_{dir} LAI} \tag{4.20}$$

The extinction coefficient for diffuse light (K_{dif}) within the canopy can be estimated by first computing the transmittance for diffuse radiation for the entire upper hemisphere (τ_{dif}) as:

$$\tau_{dif} = \int_0^{\pi/2} \exp(-K_{dir}(\theta_{sun}) LAI) \sin(2\theta_{sun}) d\theta_{sun} \tag{4.21}$$

$$K_{dif} = -\frac{\ln(\tau_{dif})}{LAI} \tag{4.22}$$

The computed direct and diffuse extinction coefficients, the mean radiation intensity on the sunlit and shaded leaves from visible (or PAR) and near infrared (NIR) bands are estimated based on the direct and diffuse PAR and NIR radiation estimations at the top canopy using the methods described by *Song et al*. [2009]. The net radiation (R_{net}) for the sunlit and shaded leaves is computed individually as:

$$R_{net} = APAR + ANIR + LW_{floor} f_{LW} + LW_{air} f_{LW} - 2LW_{canopy} f_{LW} \tag{4.23}$$

with

$$f_{LW} = \frac{1 - \exp(-K_{dif} LAI)}{K_{dif} LAI} \tag{4.24}$$

where *APAR* and *ANIR* are the absorbed PAR and NIR at the leaf (sunlit or shaded) (W m^{-2}), LW_{floor}, LW_{air}, and LW_{canopy} are the long wave radiations (W m^{-2}) from the floor, air, and canopy computed following the methods of *Song et al.* [2009]. f_{LW} is the scaling factor of the longwave radiation to the canopy. The leaf temperature is computed following the method described by *Evers et al*. [2010] using the Penman-Monteith equation with *Rnet* computed for each leaf.

The canopy stomatal conductance (G_{st}) and net photosynthesis rate (A_{cnet}) for the whole canopy with the soil moisture constraint are then computed as:

$$G_{st} = \left(g_{st\_sun} \times LAI_{sun} + g_{st\_shd} \times LAI_{shd}\right) F2 \tag{4.25}$$

$$A_{cnet} = \left(A_{net\_sun} \times LAI_{sun} + A_{net\_shd} \times LAI_{shd}\right) F2 \tag{4.26}$$

where g_{st_sun}, g_{st_shd} (m s^{-1}), A_{net_sun}, and A_{net_shd} (mol m^{-2} s^{-1}) are computed leaf-scale stomatal conductance and net CO_2 assimilation rate for the sunlit and shaded leaves. The transpiration from the sunlit or shaded canopy leaf (TR_{c_sun} or TR_{c_shd}) with the soil moisture constraint on the stomatal conductance is computed following the PX LSM approach [*Pleim and Xiu*, 1995] as:

$$TR_{c\_sun} = \rho_a \frac{q_s(T_{s\_sun}) - q_a}{R_{bw} + R_a + 1/(LAI_{sun} \times g_{stw\_sun} \times F_2)} \tag{4.27}$$

where ρ_a is the air density (kg m^{-3}), $q_s(T_{s\_sun})$ is the saturated mixing ratio for water vapor at the sunlit leaf temperature T_{s_sun}, q_a is the ambient water vapor mixing ratio above the canopy, R_{bw} is the boundary resistance for water (m s^{-1}), R_a is the air dynamic resistance (m s^{-1}), and g_{stw_sun} is the sunlit leaf stomatal conductance for water (m s^{-1}) computed from g_{st} (eq. 4.2) for CO_2. The transpiration for the shaded leaf is computed using the same equation but with parameters for the shaded leaf. The transpiration (TR_c) for the whole canopy is then computed as:

$$TR_c = TR_{c\_sun} + TR_{c\_shd} \tag{4.28}$$

The evapotranspiration (ET_c) for the canopy is then computed as:

$$ET_c = TR_c + E_{ss} + E_{vs} \tag{4.29}$$

where E_{ss} and E_{vs} are the evaporation from the bare soil surface and vegetation surface and they are estimated based on the current PX LSM approach [*Pleim and Xiu*, 1995; *Ran et al.*, 2015b].

Both the photosynthesis-based model and current PX approach use the same estimated E_{ss} and E_{vs} in ET computation. Thus, the comparison of LH between the two approaches purely reflects the differences in modeled plant transpiration.

4.2.4 Box Model Implementation

The photosynthesis-based approach is implemented in a diagnostic box model with the ET and ozone deposition velocity routines from WRF/CMAQ with PX LSM described by *Ran et al*. [2015b]. This box model is designed to use as many observational data as possible from the FLUXNET L2 standardized data [*Baldocchi*, 2008] for evaluating modeled latent heat flux (LH) from the photosynthesis-based approach (PX PSN) in comparison with the current Jarvis approach (PX Jarvis) and observed LH. Since the box model is diagnostic and there is no energy budget calculation, observed sensible heat is used to compute aerodynamic surface temperature which is used as the leaf temperature in the PX Jarvis approach. Observed friction velocity (u_*) is used to compute the boundary layer resistance and aerodynamic resistance based on the Monin-Obukov similarity theory (MOST) [*Monin and Obukhov*, 1954; *Oleson et al.*, 2013; *Pleim and Ran*, 2011]. The computed aerodynamic surface temperature is not used in the PX PSN which estimates the sunlit and shaded leaf surface temperatures using the net radiation for sunlit and shaded leaves. Thus, the PX Jarvis approach may have some advantage in these box model experiments through using more observed data in estimating stomatal conductance and ET than are used by the PX PSN approach. The observed air temperature, wind speed, LH, PAR, soil moisture, CO_2 level, relative humidity, vapor pressure deficit, air pressure, precipitation, and LAI (if available) are read in and used in the box model for ET modeling. To solve the equations for each sunlit and shaded leaf, an iterative numerical scheme, similar to CLM4.5 [*Oleson et al*., 2013], is used to estimate the leaf surface CO_2 partial pressure (c_s Pa), g_{st}, A_{net}, and c_i until c_i

converges. At the same time, the leaf temperature is also numerically iterated outside the c_i iteration using the Penman-Monteith equation with R_{net} for each leaf. ET from the canopy is obtained by adding computed transpiration from the canopy (eq. 4.29) to the evaporation estimated from the soil and the leaf surface.

4.2.5 Photosynthesis-based Model

The key parameters for canopy scaling and canopy radiative transfer are evaluated in figure 4.2 based on the Harvard Forest US-Ha1 site data on 13 June 2006 at 12pm with changing parameters. The sunlit leaf is dominant at the lower LAI while the shaded leaf increases with the increase of LAI (top left in figure 4.2) for the assumed spherical leaf distribution of the broadleaf forest site. The sunlit leaf absorbs the majority of the incident PAR (top right in figure 4.2) at the top of the canopy; the absorbed fraction peaks for LAI around 4 with a slightly decreasing trend following the increase of LAI due to the increase of shaded leaf LAI. The changes of the sunlit/shaded LAI and absorbed PAR fractions are very similar to the parameters displayed by *Bonan et al*. [2011]. With an assumed LAI at 4, most of the leaves are shaded and the sunlit leaf fraction is greatest at 0 zenith angle (bottom left in figure 4.2). The shaded leaf LAI increases and the sunlit leaf LAI decreases with increasing zenith angle. The direct beam extinction coefficient (red line in the low right plot) increases with the zenith angle exponentially (particularly after 80°) and is greater than 1 for zenith angles greater than 60° which is consistent with *Campbell and Norman* [1998]. Since K_{dir} is multiplied by the incident direct beam PAR in estimating the total PAR on the sunlit leaves based on the method of *Campbell and Norman* [1998], high K_{dir} values give much higher estimated PAR on the sunlit leaves than the incident PAR at the top of the canopy during hours with high zenith angle (morning or evening) when the sunlit leaf is a small fraction of the canopy. This condition sometimes causes the sunlit leaf

temperature to be unrealistically high when u^* is exceptionally low in the early morning (very stable conditions with high boundary layer and aerodynamic resistances). The very small sunlit leaf fraction when sun is just rising and the much higher sunlit PAR due to high K_{dir} sometimes result in unstable numerical iteration without converging. Thus, K_{dir} is limited to 3 in the model. The diffuse beam extinction coefficient is a function of LAI (blue line in the bottom right plot) and it decreases exponentially with the increase of LAI.

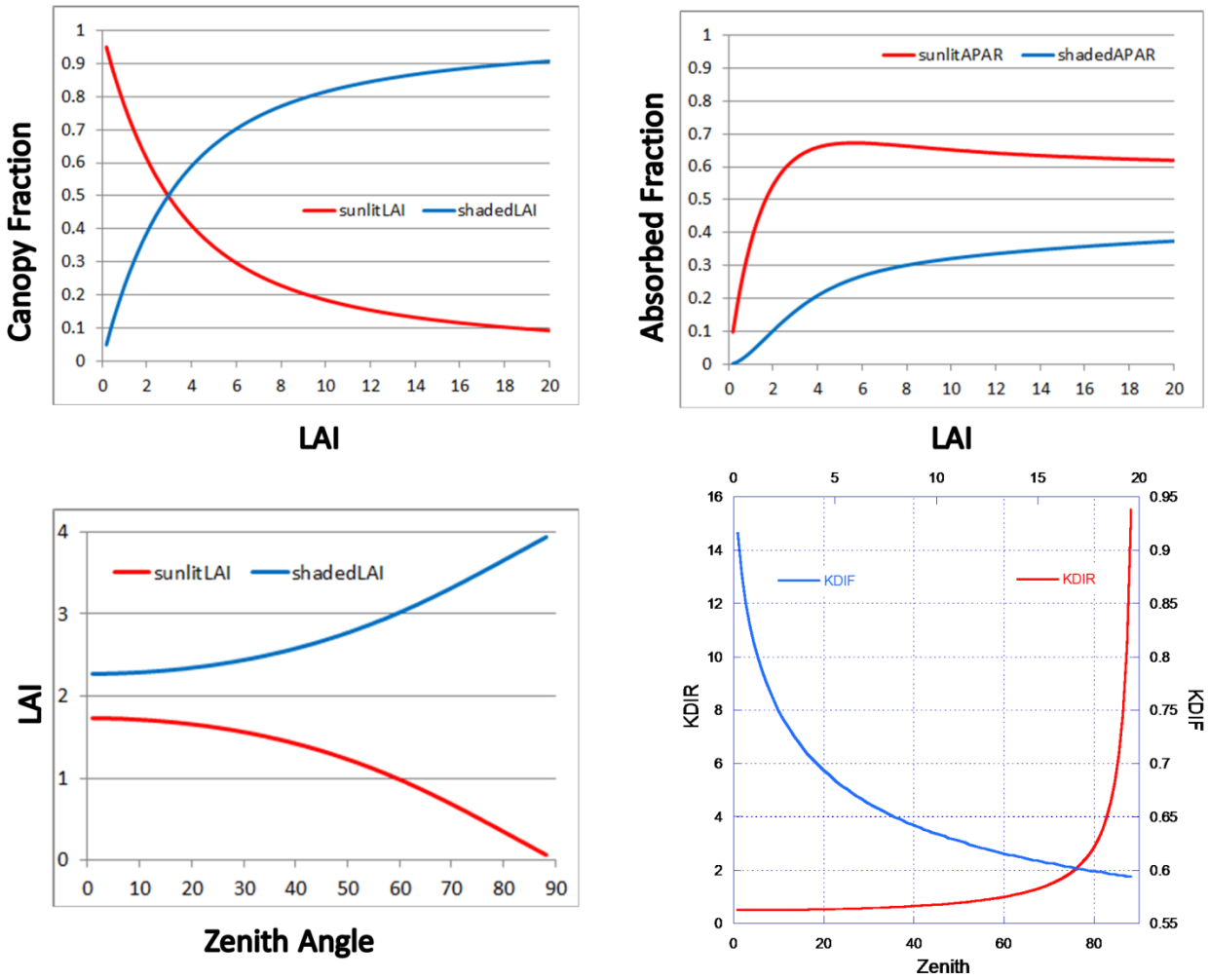

Figure 4.2. Canopy scaling and radiative transfer parameters plots. The top row plots are the leaf canopy fraction (top left) and the absorbed PAR fraction to the incident PAR (top right) for the sunlit and shaded leaves. The bottom row plots are the sunlit and shaded LAI (bottom left)

with changing zenith angle and the direct and diffuse extinction coefficients (bottom right) as a function of zenith angle and LAI. Parameters are computed based on US-Ha1 data on 13 June 2006 at 12pm with longitude = W 72.1715, latitude = N 42.5378, LAI = 4 ($m^2\ m^{-2}$), zenith angle = 20°, x = 1 (spherical leaf), α_{leaf} = 0.8 for PAR (leaf absorptivity), and α_{leaf} = 0.2 for NIR, forest floor reflectance = 0.10.

Figure 4.3 demonstrates the influence of deep soil moisture on the canopy transpiration, stomatal conductance, and net assimilation rate (eq. 4.25, 4.26, 4.28). The F_2 S shape function indicates that transpiration as well as stomatal conductance and net assimilation rate reaches the potential rate where the soil moisture is greater than field capacity and is severely limited below the wilting point. Since the development of the assimilation rate computation in the box PX LSM follows the components from JULES and methods used by *Song et al*. [2009], figure 4.4 compares median diurnal LH estimates from the PX PSN with the approaches used by JULES [*Clark et al.*, 2011] and *Song et al.* [2009] (implemented in the box model) against the results from the PX Jarvis and the US-Ha1 site measurements [*Urbanski et al*., 2007] for July 2006. Though all models perform well in comparison with the observations (black line), the JULES approach tends to overestimate LH around peak photosynthesis hours because the model does not have constraints on the absorbed PAR in estimating the rate of electron transport as the Song approach does. The Song approach is slightly higher because some constants used in the three assimilation rate computations are slightly different from the JULES approach. The PX PSN, which uses the JULES approach to compute A_c, A_e and the Song's approach to compute A_j with all constants from JULES, results in better LH estimation during the peak transpiration hours. The PX Jarvis does well except in the morning hours and late evening with relatively high LH estimation. All models tend to overestimate LH during the morning and late afternoon with the

photosynthesis approaches performing better in the morning. LH from the PX PSN is closest to the observations in the morning while the photosynthesis approaches perform the best around 6 pm. The much improved LH estimation around 6 pm has important implications for meteorology and air quality modeling as WRF/CMAQ tends to overestimate LH and pollutant concentrations during the evening transition when the model tends to stabilize too quickly. Lower LH estimation may help increase sensible heat flux, preventing premature stabilization at the surface, and thus reducing pollutant concentrations. The estimated canopy stomatal conductance and ozone deposition velocity from the PX Jarvis and PSN approaches over the 2 to 11 July 2006 period (chosen as an example of summer conditions for a short period without any missing data) are displayed in figure 4.6 to demonstrate the change of ozone deposition velocity due to the change of stomatal conductance. The PX Jarvis tends to have higher stomatal conductance during this period which results in slightly higher ozone deposition velocity. The ozone deposition involves several pathways including deposition to wet/dry cuticle surfaces, to soil surface, and via stomata including effects of mesophyll resistance [*Pleim and Ran*, 2011]. Thus, ozone deposition velocity is not simply linearly related to stomatal conductance as demonstrated by the comparison plots in figure 4.5.

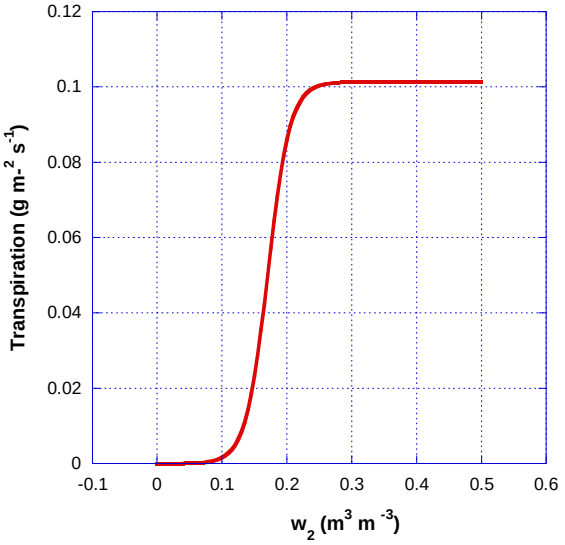

Figure 4.3. Transpiration as a function of deep soil moisture (F_2 function by eq. 4.3), computed based on US-Ha1 data on 2 July 2006 at 12pm with changing deep soil moisture (w_2). The box model uses the loam soil properties (w_{fc} = 0.24 m^3 m^{-3}, w_{sat} = 0.451 m^3 m^{-3}, w_{wlt}=0.155 m^3 m^{-3}) from the box PX LSM for the site.

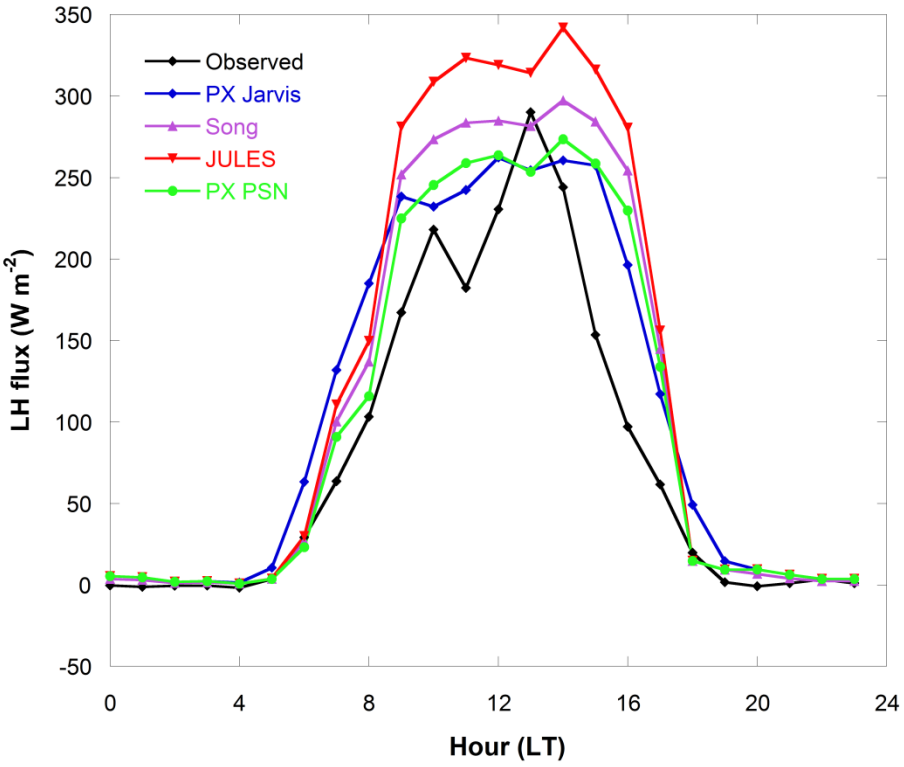

Figure 4.4. Diurnal median comparisons of the estimated latent heat (LH) from the photosynthesis approaches used by JULES [*Clark et al.*, 2011], *Song et al.* [2009], and photosynthesis-based PX LSM (PX PSN) to compute three potential assimilation rates (A_c, A_j, and A_e) in comparison with LH from the PX LSM Jarvis approach [*Pleim and Xiu*, 1995] and the observation data at the FLUXNET Harvard Forest US-Ha1 site [*Urbanski et al.*, 2007]. The broadleaf C_3 plant simulations are conducted in the PX box model using July 2006 US-Ha1 standardized L2 data with canopy height = 25 m, x = 1 (spherical leaf), α_{leaf} = 0.8 for PAR (leaf absorptivity), α_{leaf} = 0.2 for NIR, forest floor reflectance = 0.10, $V_{CMAX25\_0} = 30\times10^{-6}$ mol m^{-2} s^{-1}, k_n = 0.17, T_{low} = 0.0 °C, T_{up} = 36 °C, leaf scattering coefficient 0.15, quantum yield ε = 0.08 (mol CO2 mol^{-1} photon), and Jarvis R_{stmin} = 200 s m^{-1}.

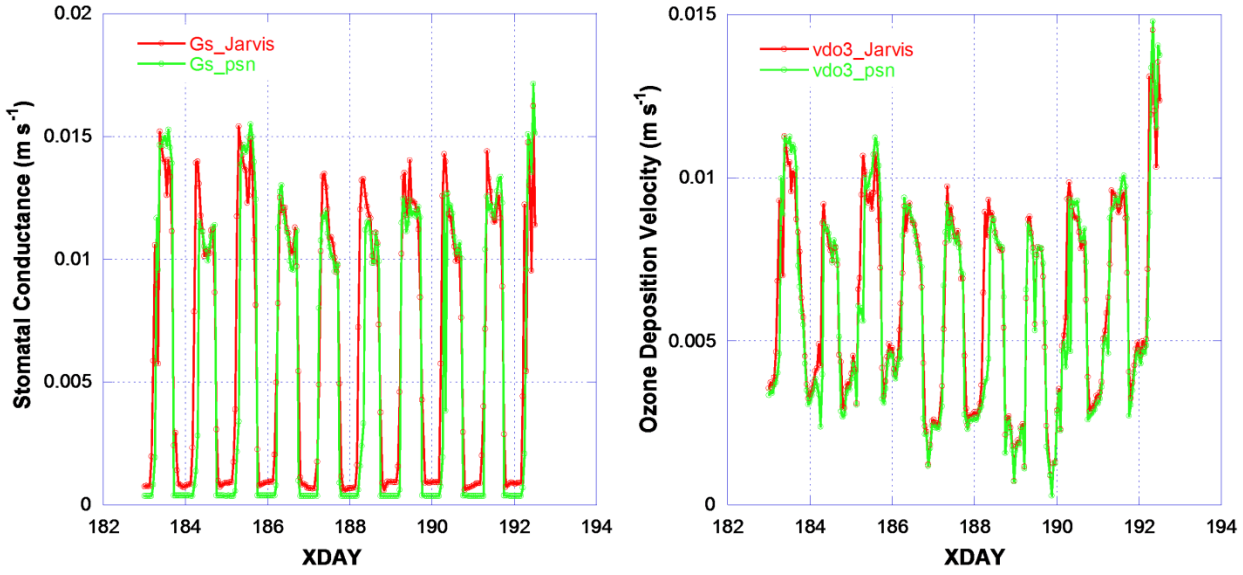

Figure 4.5. Stomatal conductance (m s^{-1}, left) and ozone deposition velocity (m s^{-1}, right) computed from the PX Jarvis and photosynthesis-based approach from 2 to 11 July 2006 with the modeling parameters described in the figure 4.4 caption.

4.3 Model Evaluation and Analysis

The PX PSN model is evaluated and analyzed for LH estimation at four selected FLUXNET sites with different vegetation types and landscape characteristics. The evaluation is conducted over the period with FLUXNET LAI measurements for each site and LAI is linearly interpolated for the days in between LAI observations. Additional model simulations are made using the 2006 gap-filled MODIS vegetation data processed for each land cover type within a WRF/CMAQ 12 km grid cell to show the model performance and limitations when using the averaged MODIS vegetation for each PFT within a grid cell for typical mesoscale applications. The gap-filled MODIS LAI data are processed from 2006 MODIS Collection 5 LAI and FPAR data (MOD15A2GFS) at 1 km resolution and every 8 days [*Gao et al.*, 2008; *Myneni et al.*, 2011] from the North American Carbon Program as used in the previous studies by *Ran et al.* [2015a and 2015b]. The model is further evaluated based on the 2013 ozone flux measurements

at the Duke Forest Open Field - US-Dk1, made by U.S. EPA [*Almand-Hunter et al.,* 2015], to assess the impact of the photosynthesis-based approach on LH, ozone deposition velocity, and ozone flux. Site descriptions, key parameters adopted from CLM4.5 [*Oleson et al*., 2013], JULES [Clarks et al., 2011], and PX LSM [*Xiu and Pleim*, 2001; *Pleim et al*., 2013] based on site PFT, and simulation year for the four FLUXNET sites and one EPA ozone measurement site are presented in table 4.1. There are two soil moisture measurements at two different depths available in the FLUXNET Level 2 (L2) standardized file. At some sites the soil moisture measurements are at the same depth as the soil temperature measurements while at other sites they are at different depths and some sites, such as Harvard forest, there are no soil moisture measurements at all. Depending on the seasons, the model responses to the two soil moisture measurements differently, as plants tend to use shallow water with more nutrients when there is no water stress but tap into deeper soil water when the upper layers are dry during the hot summer. Interpolated soil water between the two measurements generally does not help model performance without weighting by root distribution. Therefore, the model uses the soil moisture measurement which fits model performance best for the simulation periods at each site.

Table 4.1. Site and key parameters for selected four FLUXNET sites and EPA flux ozone site.

Site Name	Info.	Key Parameters
FLUXNET Measurments:		
2006 Missouri Ozark/US-Moz	Deciduous Broadleaf C3, location(-92.2, 38.7441), Elevation 219 m, Missouri, *Gu et al.* [2006]	Canopy height = 24 m, OBS LAI, x =1 (spherical leaf), $\alpha leaf$ PAR = 0.8, $\alpha leaf$ NIR = 0.2, forest floor reflectance = 0.10, V_{CMAX25_0} = 30×10-6 mol m-2 s-1, k_n = 0.17, T_{low} = 0 C, T_{up} = 36 C, leaf scattering coefficient 0.15, quantum yield ε = 0.08 (mol CO2 mol-1 photon), and Jarvis R_{stmin} = 200 s m-1 (same as Harvard Forest US-Ha1 site), silt loam with w_{sat} = 0.485, w_{fc} = 0.255, w_{wlt} = 0.178
2008 Wind River Field Station/US-Wrc	Evergreen Needleleaf C3, location(-121.9519, 45.8205), Elevation 371 m, Wahsington, Paw U et al. *[2004]*	Canopy height = 56 m, LAI = 8.6, x = 1 (spherical leaf), $\alpha leaf$ PAR = 0.8, $\alpha leaf$ NIR = 0.2, forest floor reflectance = 0.10, V_{CMAX25_0} = 55×10-6 mol m-2 s-1, k_n = 0.17, T_{low} = -10 C, T_{up} = 26 C, leaf scattering coefficient 0.17, quantum yield ε = 0.08 (mol CO2 mol-1 photon), and Jarvis R_{stmin} = 175 s m-1, silt loam with w_{sat} = 0.485, w_{fc} = 0.255, w_{wlt} = 0.178
2006 Fermi Prairie/US-IB2	Grasslands C4, location(-88.241, 41.8406), elevation 226 m, Illinois, *Allison et al*. [2005]	Canopy height = 1 m, OBS LAI, x = 0.85, $\alpha leaf$ PAR = 0.8, $\alpha leaf$ NIR = 0.2, forest floor reflectance = 0.10, V_{CMAX25_0} = 25×10-6 mol m-2 s-1, k_n = 0.17, T_{low} = 13 C, T_{up} = 45 C, leaf scattering coefficient 0.17, quantum yield ε = 0.06 (mol CO2 mol-1 photon), and Jarvis R_{stmin} = 100 s m-1, silty clay loam with w_{sat} = 0.477, w_{fc} = 0.322, w_{wlt} = 0.218
2006 Mead Irrigated Rotation/US-Ne2	Soybean C3, location(-96.4701, 41.1649), elevation 362 m, Nebraska, *Verma et al*. [2005]	Canopy height varies with OBS LAI, x = 0.81, $\alpha leaf$ PAR = 0.8, $\alpha leaf$ NIR = 0.2, forest floor reflectance = 0.10, V_{CMAX25_0} = 90×10-6 mol m-2 s-1, k_n = 0.17, T_{low} = 0 C, T_{up} = 36 C, leaf scattering coefficient 0.15, quantum yield ε = 0.08 (mol CO2 mol-1 photon), and Jarvis R_{stmin} = 70 s m-1, silty clay loam with w_{sat} = 0.477, w_{fc} = 0.322, w_{wlt} = 0.218
U.S. EPA Measurments:		
2013 Duke Forest Open Field/US-Dk1	Grasslands C3, location(-79.0934, 35.9712), elevation 168 m, North Carolina, *Almand-Hunter et al. [2015]*	Canopy height = 1 m, LAI = 3, x = 0.85, $\alpha leaf$ PAR = 0.8, $\alpha leaf$ NIR = 0.2, forest floor reflectance = 0.10, V_{CMAX25_0} = 26×10-6 mol m-2 s-1, k_n = 0.17, T_{low} = 0 C, T_{up} = 36 C, leaf scattering coefficient 0.15, quantum yield ε = 0.12 (mol CO2 mol-1 photon), and Jarvis R_{stmin} = 100 s m-1, loam with w_{sat} = 0.451, w_{fc} = 0.24, w_{wlt} = 0.155

Estimated fluxes are evaluated using diurnal median comparisons between the two approaches against observations. In addition, the two approaches are evaluated using scatter plots of daily values of estimated fluxes (e.g. latent heat and O_3 flux) against observations with computed normalized mean bias (NMB) and normalized mean error (NME) from daily flux estimations. The NMB and NME metrics for model estimations are calculated as [e.g. *Yu et al*., 2006]:

$$NMB = \frac{\sum (M_i - O_i)}{\sum O_i} \times 100 \tag{4.30}$$

$$NME = \frac{\sum |M_i - O_i|}{\sum O_i} \times 100 \tag{4.31}$$

where M_i and O_i are the estimated and observed daily total fluxes for day i. The two relative metrics in percent are useful to evaluate errors of modeling results against observations for fluxes which can have quite different magnitude and variability across the different sites.

4.3.1 FLUXNET Site Simulations

Missouri Ozark/US-Moz site

The simulated LH from the PX PSN approach at the Missouri Ozark/US-Moz FLUXNET site [*Gu et al.*, 2006] is evaluated against the LH simulated from the PX Jarvis approach and the observed LH in figure 4.6. The measured LAI is much lower than the MODIS LAI for this deciduous broadleaf land cover type in the CMAQ 12km grid cell in which the site is located. However, the seasonal change of MODIS LAI (phenology) parallels the measured LAI (middle plot in figure 4.6). Using the observed LAI, the PX PSN and Jarvis approaches perform reasonably well in general (left plot in figure 4.6) for simulations from 9 July (day 190) - 14 November (day 318) 2006. However, the PX PSN tends to overestimate LH for most of the hours after 9am until the evening. Using the MODIS LAI, both models overestimate LH (right plot in figure 4.6) due to higher LAI from MODIS and the PX PSN still has higher LH than the Jarvis approach following the same pattern as the simulations with observed LAI. The scatter plots of estimated daily total LH estimations against the observations (figure 4.7) also demonstrate that the PX Jarvis approach performs slightly better than the PX PSN approach. Ideally the fitted regression line in the scatter plot should have a slope = 1, a y-intercept = 0, and R = 1. While the R value is quite high indicating good correlation with the observations, the slope > 1 shows a general tendency to overestimate LH by both approaches.

In contrast to the pattern at the Harvard Forest US-Ha1 site with the same PFT (deciduous broadleaf), the PX PSN tends to overestimate LH from mid-morning to evening at

the US-Moz site over the much longer simulation period (July to November versus one month for the US-Ha1 site). Though both sites have the same vegetation PFT, the species are different. Red oak, red maple, mature hemlock, and white pine are dominant at the Harvard Forest US-Ha1 site [*Urbanski et al*., 2007] while the Missouri Ozark/US-Moz site is in an oak-hickory forest which is uniquely located in an important transitional zone between hardwood and grassland in the central States. Thus, the model, which classifies both sites in the same PFT and therefore the same V_{cmax}, plant absorptivity, and other parameters, is unable to differentiate varying physiology from different trees within the same PFT at the two sites. In addition, soil moisture plays a key role in controlling the performance for the Moz site. There are only two soil moisture measurements, at 10 cm and 100 cm, available in the standardized L2 dataset. The soil moisture at 100 cm is almost above the field capacity for most of the year while the soil moisture at 10 cm varies rapidly. For the first half year with almost constant deep soil moisture above the field capacity, both approaches overestimate LH significantly. During the growing season after early July, the deep soil moisture shows more variation allowing the model to be more responsive to soil moisture conditions. Thus, the simulation is conducted and analyzed over the period after early July for this site. Through testing with soil moisture data at different depths for some of the selected sites, both models seem to perform best when using the soil moisture measured at root zone depth which is generally from 25 cm to 60 cm deep depending on the region and vegetation type (such as much deeper rooted trees in western drylands). Thus, it is crucial to choose the right soil moisture and temperature measurement for the diagnostic simulation because the measurement depths are usually different in the standardized L2 files for each FLUXNET site. Although both models use the same soil moisture limiting function F_2, the PX PSN tends to overestimate LH when soil moisture is not limiting while the Jarvis approach

generally performs better. It is possible that the aerodynamic surface temperature, which is calculated from observed sensible heat and used by the PX Jarvis computation, helps minimize the error in LH estimation for the tall canopy.

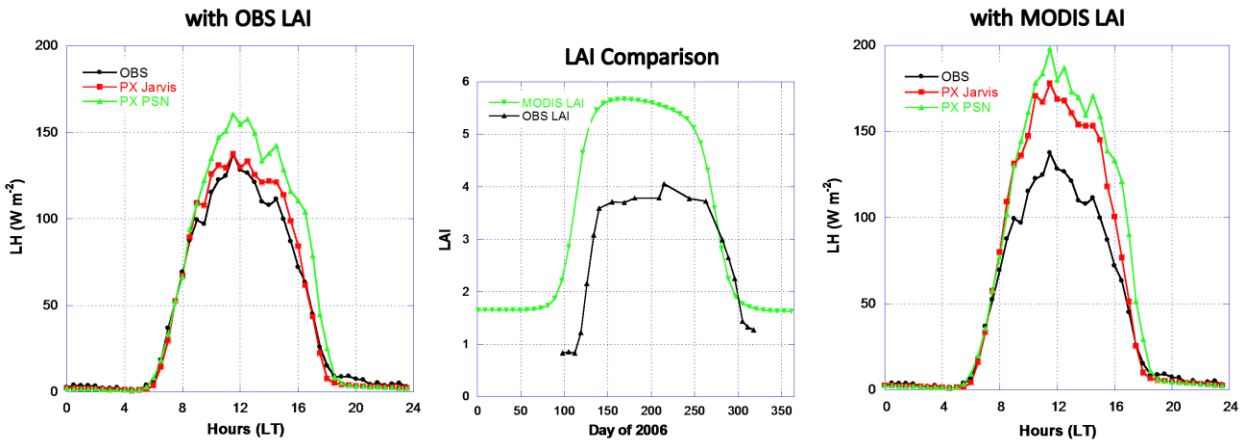

Figure 4.6. Missouri Ozark/US-Moz site LH diurnal median comparisons. LH is simulated with the photosynthesis-based and Jarvis approaches using the observed LAI (left plot) and the MODIS LAI (right plot) from 9 July (190) - 14 November (318) 2006. The observed LAI from the site 2006 biological data and processed 2006 MODIS LAI for the deciduous broadleaf land cover type at the 12 km CMAQ grid cell are displayed in the middle plot. Soil moisture measurements at 100 cm deep are used.

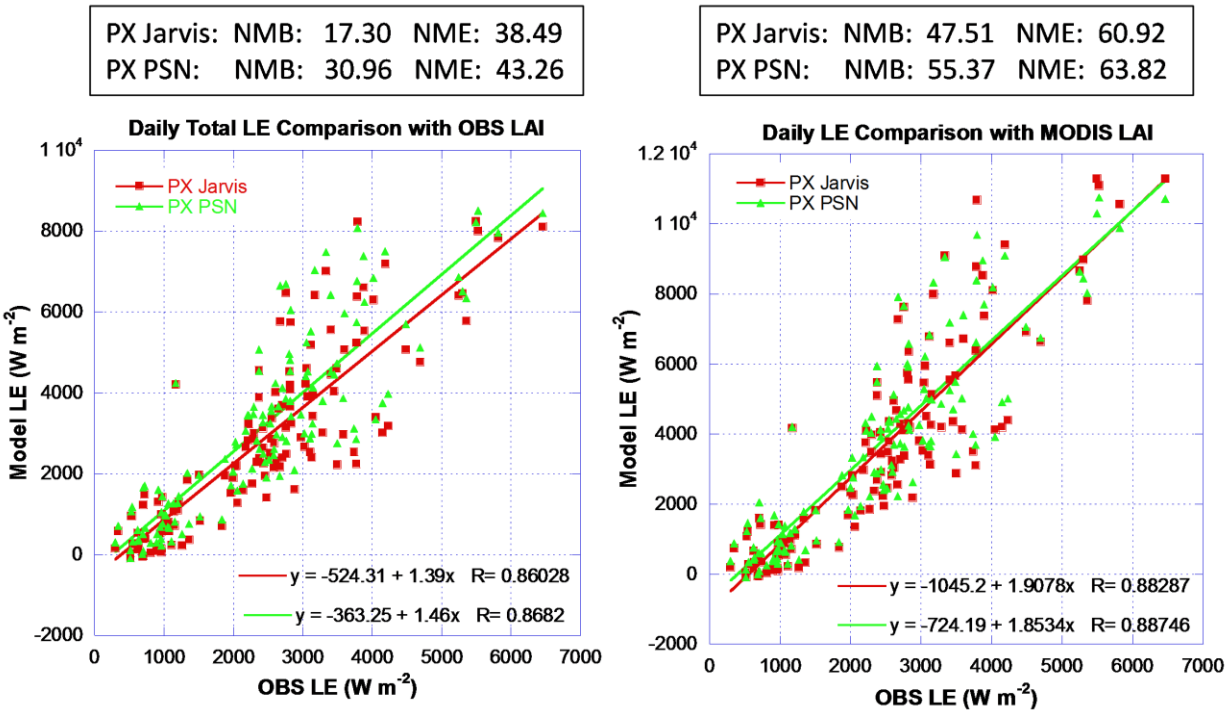

Figure 4.7. Missouri Ozark/US-Moz site scatter plot comparisons of daily total LH estimations.

Wind River Field Station/US-Wrc site

Simulation of LH at the Wind River Field Station/US-Wrc site is particularly challenging using the two stomatal conductance approaches [*Jarvis*, 1976; *Farquhar*, 1980; *Ball et al*., 1987; *Collatz et al*., 1991] in the box model. The old growth forest site is dominated by tall Douglas-fir (more than 60 m tall) more than 500 years old and tall western hemlock (more than 50 m tall). Using the observed LAI 8.6 (m^2 m^{-2}) at the site [*Thomas and Winner*, 2000], both approaches significantly overestimate LH by more than 50 W m^{-2} (left plot in figure 4.8) for simulations from 7 January (day 7) - 28 November (day 333) 2008. Using 2006 MODIS LAI for the evergreen needleleaf land cover type reduces the over estimation of LH significantly (right plot in figure 4.8) because the MODIS LAI (maximum around 5.3 m^2 m^{-2}) is much less than the observed LAI at the site. The MODIS LAI and FPAR algorithm tends to be saturated at high LAI (Yang et al. 2006). The PX PSN has higher estimation of LH than the PX Jarvis approach

in general for this site. With MODIS LAI, the PX PSN slightly overestimates LH while the PX Jarvis approach slightly underestimates around the peak radiation hour. From the late afternoon, both the approaches overestimate LH. The scatter plot evaluation is not conducted for this site due to the poor performance from the both approaches over the long simulation period. The 2008 FLUXNET measurement data is used for the modeling because the 2006 measurements have too many gaps and most of the soil moisture data are missing. Since FLUXNET does not have the biological data with measured LAI for this site, the observed LAI [*Thomas and Winner*, 2000] over late 1990s and available 2006 MODIS LAI for WRF/CMAQ are used for the simulation with the assumption that LAI does not change too much for this PFT old growth site. The MODIS LAI does show seasonal variation of LAI which peaks in late spring for the vegetation in this area with wet cool winters and hot dry summers. As the site is located in the subtle divide between the Wind River and Trout River in the north-south oriented Cascade Mountains, the soil moisture is limited during the hot summer [*Paw U et al*., 2004, *Shaw et al.*, 2004].

Similar to other sites, the model seems to be very sensitive to the soil moisture data used for LH estimation at the Wind River site. Soil moisture measurements are available at eight different depths between 0 to 2 m for this site. The measurement at 40 cm which shows most reasonable variations during the hot summer is selected for modeling. However, the soil moisture is mostly above the field capacity during the rest of the year which results in LH overestimation for the first of the half year (similar to the situation at the US-Moz site). With most plant roots within 0.5 m, deep roots extending to 1 – 2 m deep, and fine roots in the top 0 – 0.3 m deep [*Shaw et al*, 2004], it seems that the soil moisture measurements used for the modeling are too deep for the cool seasons but about right for the dry seasons. This indicates

that the optimal soil moisture depth for modeling plant transpiration not only varies with different sites and vegetation composition but also with different seasons depending on the soil moisture demand by vegetation. This may be particularly important for the US-Wrc site which has diverse vegetation species composition and canopy structures [*Thomas and Winner,* 2000]. Furthermore, the more than 500 year old tall Douglas-fir and western hemlock that are dominant at the site present ecological modeling complexity regarding age, height, biomass, and under/over story structures. Many studies [*McDowell et al.*, 2002; *Phillips et al*., 2002; *Wharton et al*., 2009; *Pangle et al*., 2015] have investigated the relationship between the canopy flux and tree height since *Ryan and Yoder* [1997] first proposed the hydraulic limitation hypothesis. With the increased path from soil to the canopy stoma for tall trees, it is assumed that leaf-specific hydraulic conductance may decrease resulting in reduced stomatal conductance. *McDowell et al*. [2002] and *Phillips et al*. [2002] tested the hypothesis at the US-Wrc site with young and old Douglas-fir trees and their results do not support the hypothesis as there is no observed decrease of stomatal conductance and photosynthesis for the old-growth trees compared to the younger shorter trees from their summer observations. They suggest that old tall Douglas-fir trees may evolve to compensate for the hydraulic limitation by having more efficient sap conductance. The study by *Pangle et al*. [2015] shows that the hydraulic limitation hypothesis is supported by all species they measured including western hemlock except Douglas-fir in the Pacific Northwest. Also, since FLUXNET measurements are based on the eddy covariance method to directly measure the flux density above the canopy, the direct measurement method comes with the assumption that the terrain is flat and with uniform vegetation and that the atmosphere is in steady state. Thus, eddy covariance derived fluxes include significant uncertainties due to non-ideal conditions in natural heterogeneous landscapes, which is particularly true for this site with

measurement height at 85 m above the ground over the tops of the clumped conifer canopy with diverse understory species. Accuracy of turbulent fluxes from this method is around 5-15% for the sensible heat and 10-20% for latent heat [*Mauder et al*., 2006; *Foken et al*., 2008] with systemic errors from sensor configurations and turbulence data processing around 5–10% and random errors from natural variation in vegetation and atmospheric turbulence around 5% [*Baldocchi*, 2008]. Since only the flux from the small eddies is measured at almost all FLUXNET network sites, some portion of the flux from larger eddies and advection is missing [*Finnigan et al*., 2003]. Larger eddies may play an important role because of the 85 m measurement height at the site and drainage flows from surrounding hills [*Shaw et al.*, 2004]. Finally, turbulent flux computation in LSMs use empirically determined non-dimensional profile functions in accordance with MOST even though MOST is defined under ideal environments. The validity of MOST is limited to flat terrain with homogeneous landscape and land cover and to a steady and horizontally homogeneous flow by averaging from 10 minutes to around an hour [*Monin and Obukhov*, 1954]. Even under ideal environments, MOST has around 10–20% errors [*Foken*, 2006]. In non-ideal conditions, MOST-based model calculations will be less accurate and result in more uncertainties in estimating aerodynamic resistance [*Wang and Dickinson*, 2012]. Since the uncertainty associated with flux measurement and computation applied to both models and observations at all sites, the interpretation of the model performance differences needs to be cautious.

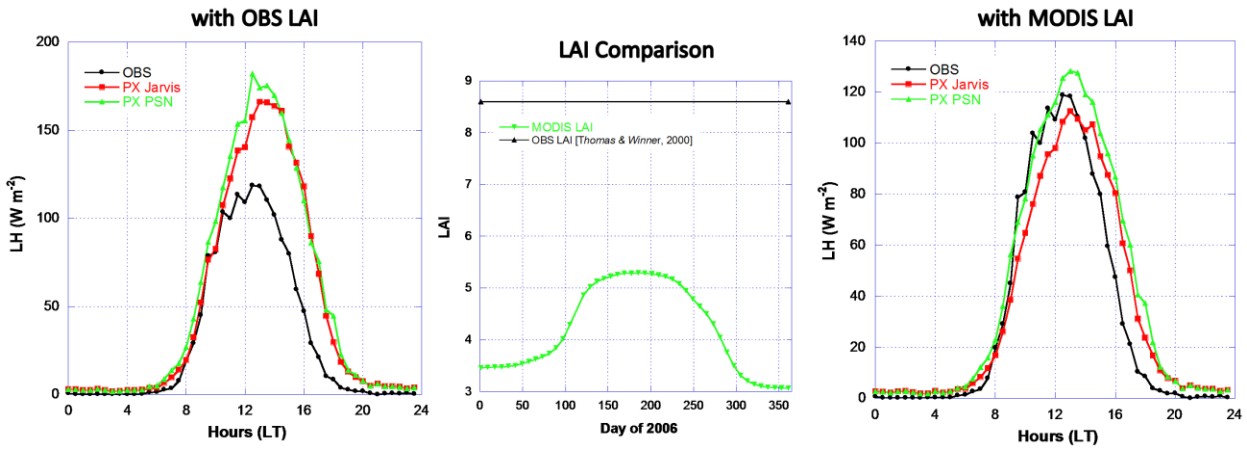

Figure 4.8. Wind River Field Station/US-Wrc site LH diurnal medium comparisons. LH is simulated with the photosynthesis-based and Jarvis approaches using the observed LAI (left plot) and the MODIS LAI (right plot) from 7 January (7) - 28 November (333) 2008. The observed LAI of the C_3 vegetation from the study by *Thomas and Winner* [2000] and processed 2006 MODIS LAI for the evergreen needleleaf land cover type at the 12 km CMAQ grid cell are displayed in the middle plot. Soil moisture measurements at 40 cm deep are used.

Fermi Prairie/US-IB2 site

The performance of simulated LH from 22 May (day 142) - 20 September (day 263) 2006 for the C_4 tall grass prairie at the Fermi Prairie/US-IB2 site is evaluated and shown in Figure 4.9. Soil moisture measurements at 25 cm deep (not in the standardized L2 data) are used for the modeling. Using the observed LAI, the PX PSN performs well while the PX Jarvis underestimates LH by around 50 (W m^{-2}) around peak radiation hours. Both approaches tend to underestimate LH in early morning and evening hours. Since the PX PSN treats C_3 and C_4 plants differently in modeling CO_2 assimilation, it seems to have advantages in modeling LH through the coupled photosynthesis and stomatal conductance approach with the consideration of the C_4 photosynthetic carbon cycle efficiency for the adaptation to high light, dry, and hot

environments. The peak MODIS LAI (around 1.75 $m^2 m^{-2}$) is much lower than the observed LAI (around 3 $m^2 m^{-2}$, middle plot in figure 4.9). But, the MODIS LAI peaks coincident with the observed LAI peak in late July and early August. In general, the MODIS LAI cannot capture the peak and low LAI values compared to site observations (exception at the US-Moz site) due to averaging at the WRF/CMAQ 12 km modeling resolution [*Ran et al*., 2015a]. With MODIS LAI, both the approaches underestimate LH with the PX PSN by around 50 (W m^{-2}) and the PX Jarvis by around 100 (W m^{-2}) around noon (right plot in figure 4.9). Both approaches have high uncertainties in the daily total LH estimations as indicated by the relatively low R value (figure 4.10). The PX PSN has lower NMB and higher NME for daily total LH estimations than the Jarvis approach for simulations with observed LAI. For MODIS LAI simulations, the PX PSN performs better with lower NMB and NME. Since this tall grassland site has rather uniform landscape with homogeneous vegetation and flat terrain [*Allison et al*., 2005], it meets the assumptions of the eddy covariance FLUXNET measurement and the turbulent flux computation by MOST relatively well in comparison with the previous two FLUXNET sites located in landscape transitional zones. Thus, both measurements and flux computations are likely to be less error prone and the demonstrated strength of the PX PSN approach is likely to be robust.

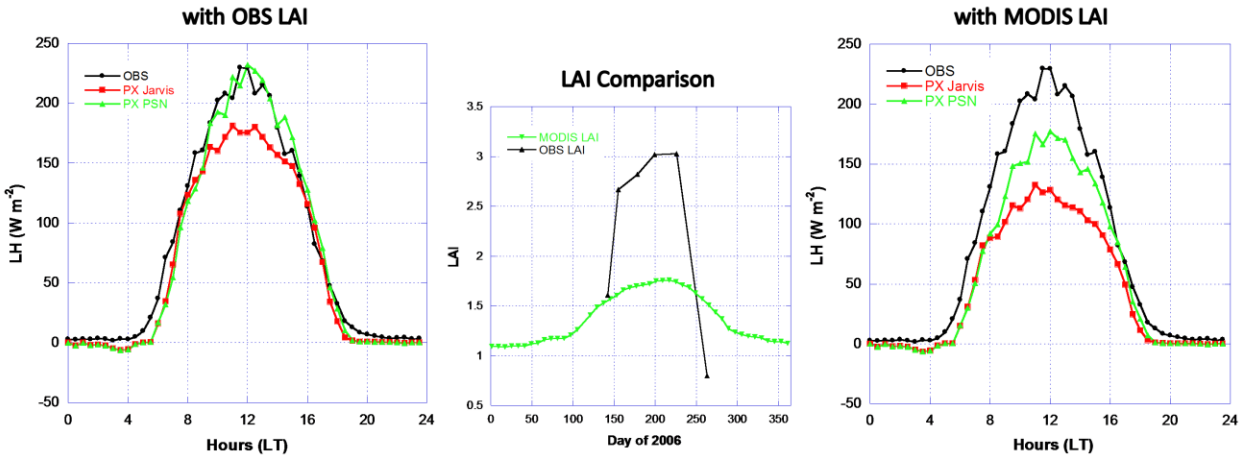

Figure 4.9. Fermi Prairie/US-IB2 site LH diurnal median comparisons. LH is simulated with the photosynthesis-based and Jarvis approaches using the observed LAI (left plot) and the MODIS LAI (right plot) from 22 May (142) - 20 September (263) 2006. The observed LAI of the C_4 grassland from the site 2006 biological data and processed 2006 MODIS LAI for the grassland land cover type at the 12 km CMAQ grid cell are displayed in the middle plot. Soil moisture measurements at 25 cm deep are used.

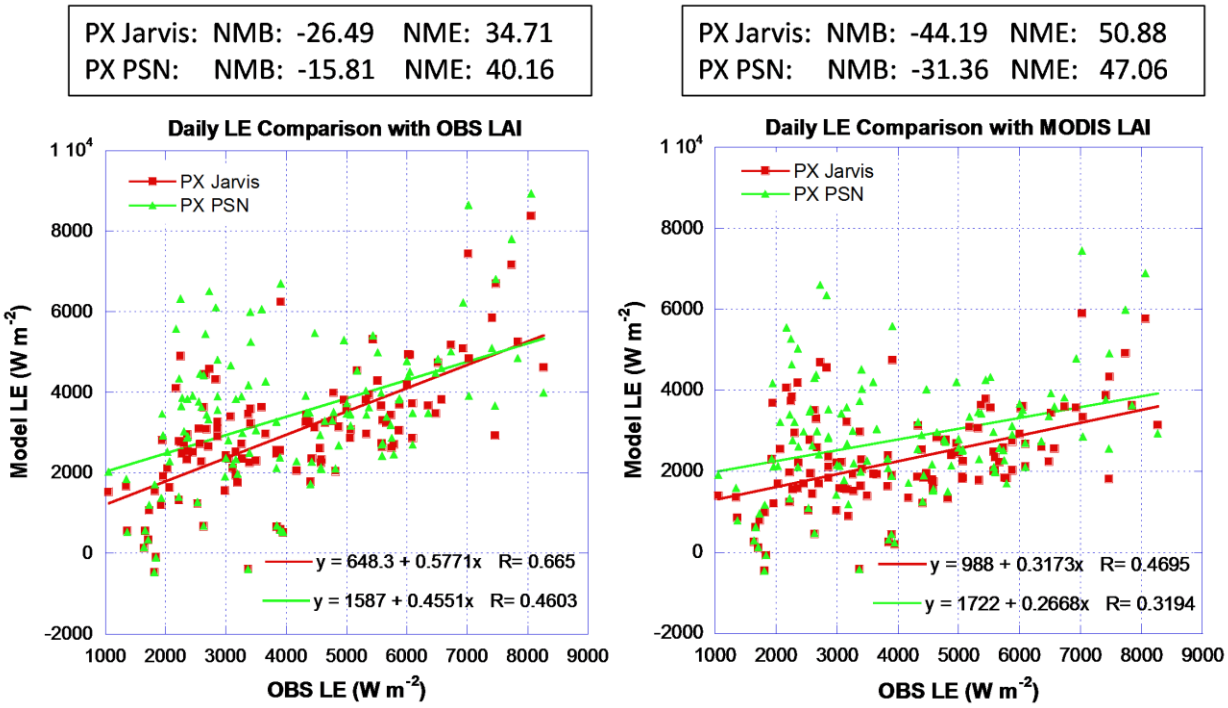

Figure 4.10. Fermi Prairie/US-IB2 site scatter plot comparisons of daily total LH estimations.

Mead Irrigated Rotation/US-Ne2 site

The box model is further evaluated for soybean crop at the Mead Irrigated Rotation/US-Ne2 site [*Verma et al.*, 2005] from 12 June (day 163) - 5 October (day 278) 2006. Soil moisture is set to field capacity due to irrigation. Distinct from the other sites with constant plant height, the measured seasonally varying crop height along with LAI from the site biological dataset are used in the simulation. While both models perform well with the observed LAI and crop height (left plot in figure 4.11), in the early morning the two models tend to underestimate LH but the PX PSN tends to overestimate LH in the early afternoon while the PX Jarvis slightly underestimates. The PX Jarvis LSM was originally developed based on soybean measurements in Kentucky [*Pleim et al.* 2001; *Pleim and Xiu*, 2003] thus it performs well at this site for soybeans. The fact that the PX PSN performs as well as the PX Jarvis for this crop validates its capabilities for modeling agricultural lands. The peak LAI for soybeans can reach 5 (m^2 m^{-2})

with canopy height around 1 m, but the peak MODIS LAI is only around 2.75 (m^2 m^{-2}). The height of the plant follows the LAI until the crop turns brown (greenness or LAI declining to zero) just before harvesting. The soybeans were planted on 1 May (day 121) and harvested on 5 October (day 278) for 2006. According to the measurements, it took almost a month after planting for the plants to have measurable LAI. Similar to other sites, the MODIS LAI peaks coincident with the observations but cannot capture the high and low of the observed LAI at the site. With MODIS LAI, both models overestimate LH because the peak soybean LAI period is short and on average MODIS LAI is higher than the observations over the modeling period. Using the MODIS LAI, the estimated LH median from the PX PSN is close to observations around noon while the Jarvis approach overestimates LH by around 50 (W m^{-2}) and both models tend to underestimate LH in the early morning hours. The two approaches perform well in daily total LH estimations with lower NMB and NME from the Jarvis approach (left plot in figure 4.12) in simulations with the observed LAI. However, both approaches do not perform well with the MODIS LAI which results in much higher errors and scatter (much lower R values) despite lower bias (right plot in figure 4.12). Thus, accurate LAI as well as crop height is crucial for simulations over crop lands. Because crop lands are treated as one land cover category in the current WRF/CMAQ system the mesoscale model cannot distinguish LAI and crop height associated with planting, fertilizing, irrigating, and harvesting of different crops. Although MODIS LAI tends to be low for the peak growing season at this soybean site, it does provide some information on plant LAI changes which are related to natural (e.g. temperature and precipitation) and human influences in comparison with the table-prescribed landscape in the current system.

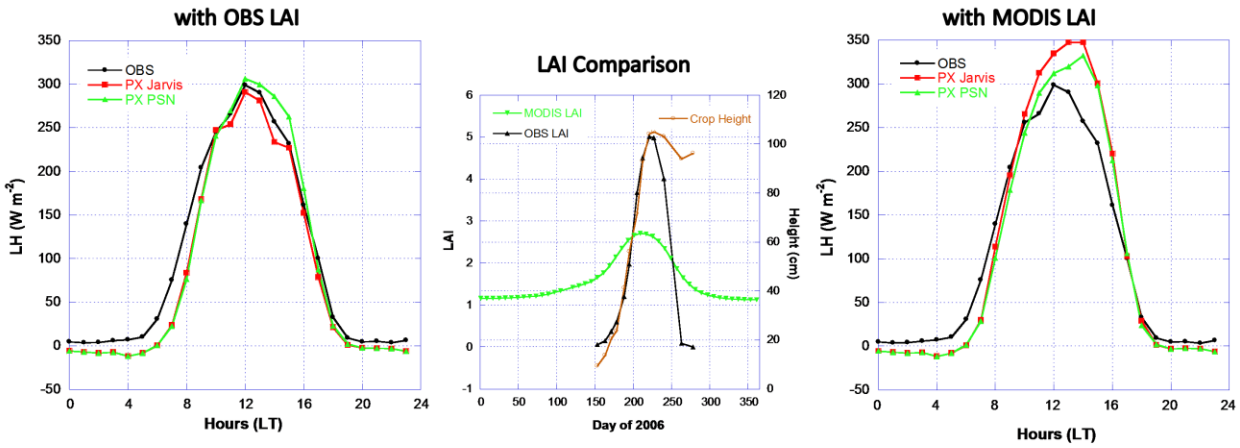

Figure 4.11. Mead Irrigated Rotation/US-Ne2 site LH diurnal median comparisons. LH is simulated with the photosynthesis-based and Jarvis approaches using the observed LAI (left plot) and the MODIS LAI (right plot) from 12 June (163) - 5 October (278) 2006. The observed LAI of C_3 soybean from the site 2006 biological data and processed 2006 MODIS LAI for the cropland land cover type at the 12 km CMAQ grid cell are displayed in the middle plot. Soil moisture is set to field capacity.

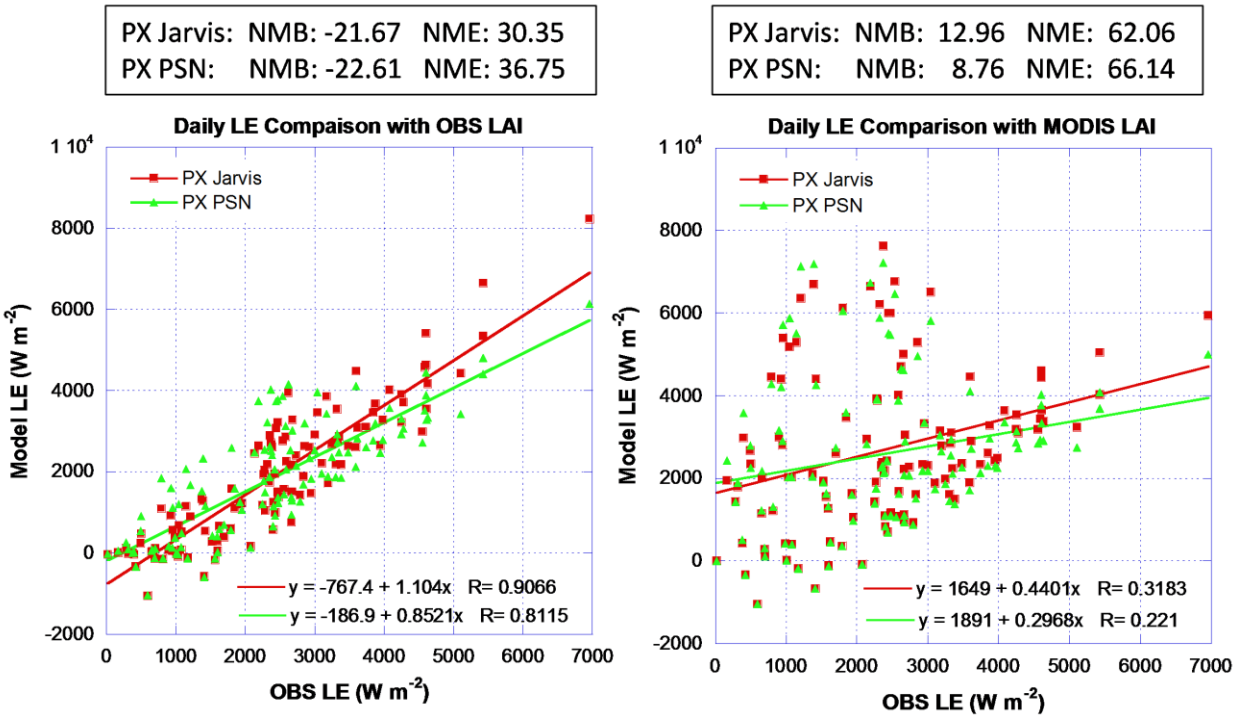

Figure 4.12. Mead Irrigated Rotation/US-Ne2 site scatter plot comparisons of daily total LH estimations.

4.3.2 Ozone Site Simulations

Simulated LH, stomatal conductance, and ozone deposition and flux from the PX Jarvis and PSN approaches over 40 days from 17 May to 18 June and 18 to 28 September 2013 are evaluated against the flux measurements conducted by U.S. EPA at the Duke Forest Open Field/US-Dk1 site [*Almand-Hunter et al.*, 2015]. Soil temperature and volumetric water content used are the average measurements over 0 - 5 cm depth, which are provided by EPA and used in site measurement data processing. Figure 4.13 shows the diurnal median statistics (left plot) for the simulations and selected 5-day hourly estimations (right plot) of LH using the two models against the observations. The PX Jarvis significantly overestimates LH by a factor of around 2 (~ 170 W m^{-2}) while the PSN overestimates LH by about 50 W m^{-2}. The hourly estimation plot for the selected 5 days shows a similar pattern with significant overestimation from PX Jarvis

while the PX PSN underestimates LH for the first two days (days 145 and 146) and overestimates LH for the last three days. The stomatal conductance estimated from the PX Jarvis is much greater than that from the PX PSN (by about a factor of 2, left plot in figure 4.14). Similarly, ozone deposition velocity and computed ozone flux based on ozone concentration measurements are also higher from the PX Jarvis but by a smaller margin because of influences of other ozone deposition pathways. The peak ozone deposition velocity from the PX PSN is lower than the observation peak but the peak timing follows the observations well in the early morning (middle plot in figure 4.14). In contrast to LH which is often highest around noon with roughly symmetric trends for morning and afternoon hours, ozone deposition velocity normally peaks in the early morning (around 8 am for the site), similar to stomatal conductance, with gradual decline throughout the daylight hours. Stomatal conductance usually decreases as relative humidity declines with increasing temperature. While low relative humidity reduces stomatal conductance, it also drives the fluxes from stomata to the ambient atmosphere due to increasing moisture gradient. Thus, the two influences often cancel out for LH resulting in the symmetric shape of the LH diurnal profile. Diurnal ozone flux also peaks around noon with a similar symmetric shape as LH because as deposition velocity declines in the afternoon the ozone concentration usually increases.

The middle and right plots in figure 4.14 show that the estimated ozone diurnal distribution and ozone flux from the PX PSN match the observations much better than the estimations from the PX Jarvis. However, estimated ozone deposition velocity and flux are high in both models from the afternoon to late evening with the PX PSN over-estimating to a much lesser degree. The daily total LH and O_3 flux estimations both show better agreement with the observation from the PX PSN with much lower NMB and NME (figure 4.15). While the scatter

plots show good correlations for both LH and O_3 fluxes (R values > 0.85), a factor of 2 over prediction by PX Jarvis for LH is reflected in the slope of the regression line (slope > 2). The over prediction of O_3 flux is by the PX Jarvis is evident from the scatter plot with all but 4 points above the 1-to-1 line. The low slope of the regression line and high y-intercept for PX PSN indicates a tendency to over predict at the low end and under predict at the high end.

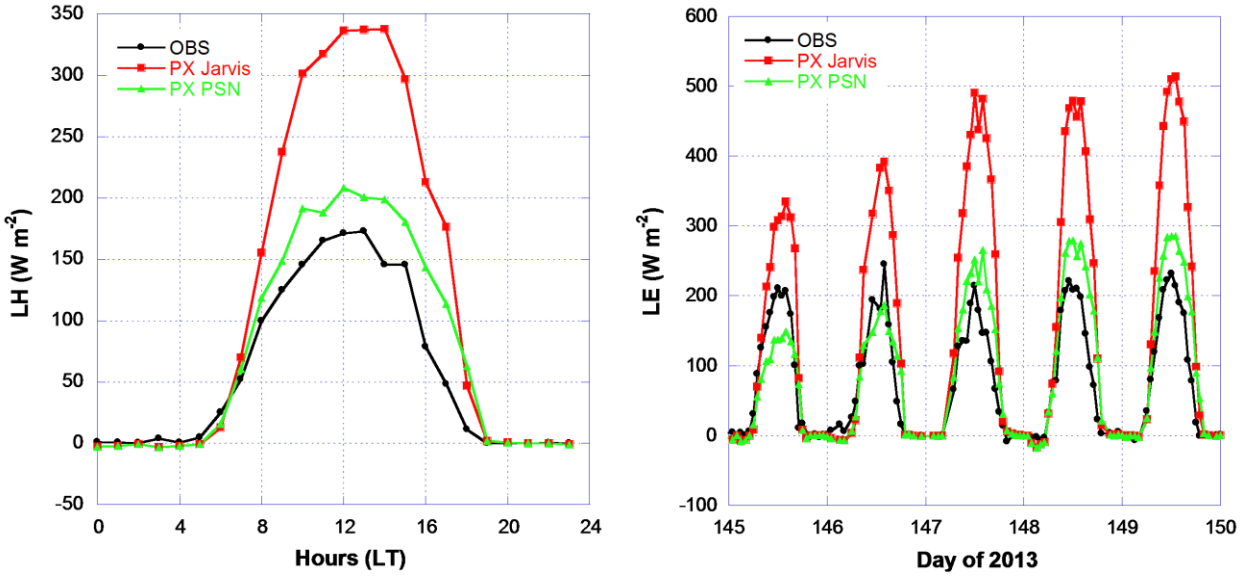

Figure 4.13. Duke Forest Open Field/US-Dk1 site LH diurnal median (left plot) and selected hourly (right plot) comparisons. Simulations are conducted based on LAI = 3 (m^2 m^{-2}) and other parameters listed in table 4.1 for the periods of 17 May (day 137) to 18 June (day 169) and 18 to 28 September (day 261 to 271) 2013 with measurements. Hourly display is for 25 to 30 May 2013 (day 145 to 150).

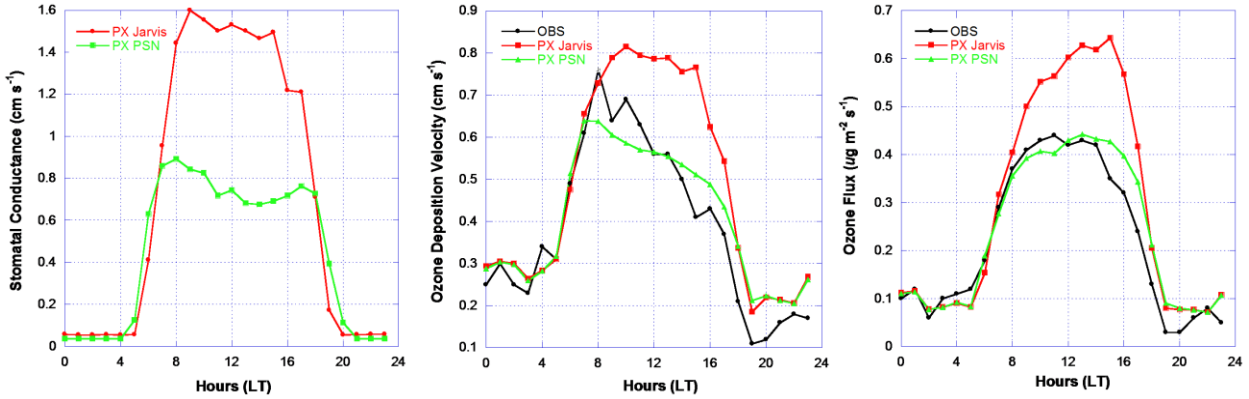

Figure 4.14. Duke Forest Open Field/US-Dk1 site diurnal median comparisons for estimated stomatal conductance (cm s^{-1}, left plot), ozone deposition velocity (cm s^{-1}, middle plot), and ozone flux (μg m^{-2} s^{-1}, right plot).

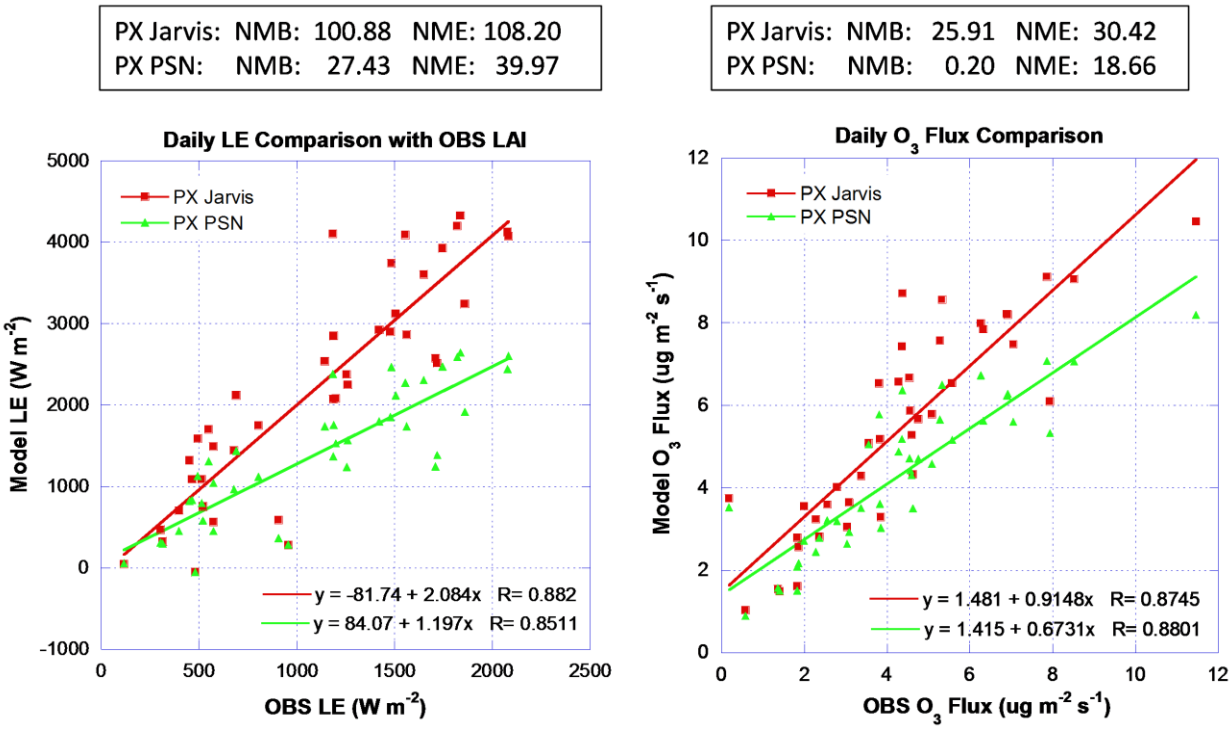

Figure 4.15. Duke Forest Open Field/US-Dk1 site scatter plot comparisons of daily total LH and ozone flux estimations.

The PX Jarvis has much higher estimation of stomatal conductance than the PX PSN for the displayed 5 day period from 25 to 30 May 2013 (left plot in figure 4.16). However, the PX PSN estimates ozone deposition velocity and flux better for the first three days while the PX Jarvis does better for the last two days (middle and right plots in figure 4.16). The spikes of the observed ozone deposition velocity and flux are not realistic and likely caused by some issues with the measurement. The big difference between the two models at this site seems to be much larger than the differences demonstrated by the four FLUXNET site LH evaluations discussed above. The use of measured sensible heat flux by the PX Jarvis for computing the aerodynamic surface temperature to be used in stomatal conductance computation as the leaf surface temperature may be degrading the model performance at this site. This approach seems to benefit the PX Jarvis at the Missouri Ozark/US-Moz and Wind River Field Station/US-Wrc sites which have tall tree canopies that serves as a barrier between the ground and the atmosphere. Since the surface energy budget is dominated by the canopy at these forest sites, the aerodynamic surface temperature is a good surrogate for leaf temperature. At the Duke site, the computed aerodynamic surface temperature is much higher than the ambient temperature around the noon hours (e.g. around 6 C°) because the surface energy is more influenced by the ground rather since the grasses have much less mass and volume than forest. Thus, the aerodynamic surface temperature is not as good of a surrogate for the leaf temperature. The higher leaf temperature results in a higher mixing ratio gradient between the leaf stomata and the ambient atmosphere which drives greater LH flux. In the full PX LSM with WRF/CMAQ, the difference between the two approaches are likely to be much smaller because there is full energy budget with sophistical radiation models and dynamic feedbacks which will be equally applied to both approaches at a time scale of less than 40 seconds.

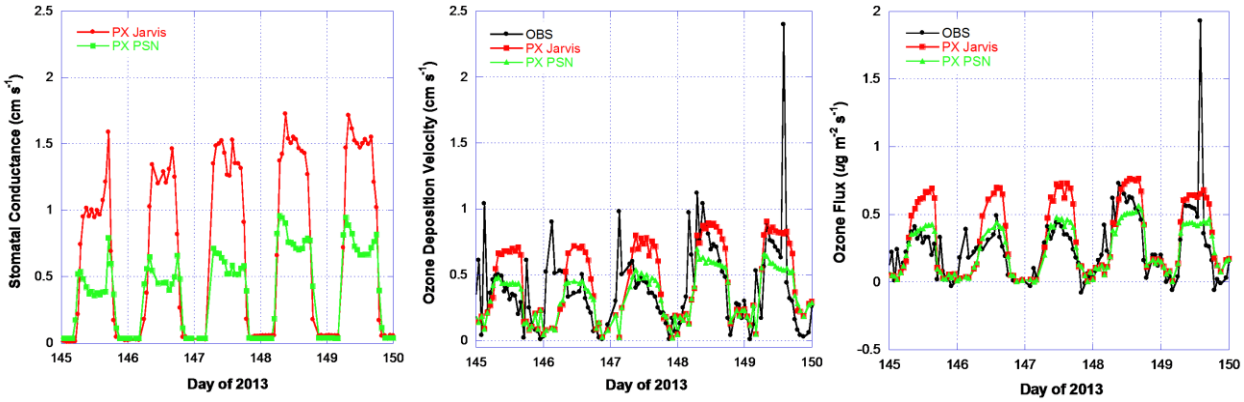

Figure 4.16. Duke Forest Open Field/US-Dk2 site hourly comparisons for estimated stomatal conductance (cm s^{-1}, left plot), ozone deposition velocity (cm s^{-1}, middle plot), and ozone flux (μg m^{-2} s^{-1}, right plot) over the period of 25 to 30 May 2013 (day 145 to 150).

4.4 Conclusions and Future Work

A coupled photosynthesis and stomatal conductance approach with simple parameterization is developed, implemented, and evaluated in a diagnostic box model with ET and ozone deposition components from WRF/CMAQ with the PX LSM. The performance of the diagnostic model is influenced by many factors including parametrizations based on broad PFTs, site-related input data, and measurement errors in addition to physical process formulations. Results from the box model comparisons should be interpreted with caution because off-line simulations cannot completely represent the performance in the full scale model with real-time feedbacks [*Samuelsson et al.,* 2003; *Qu and Henderson-Sellers,* 1998]. The purpose for this study is not to develop a site-specific model which matches measurements; but rather to develop applicable algorithms to be applied to the multi-scale (urban, region to global) WRF/CMAQ simulations for realistic treatments of grid cell average surface fluxes of heat, moisture, and trace chemical species. The performance of the developed model over varieties of vegetation and landscape types at the selected sites demonstrates that the model is applicable in large scale

modeling domains for the most prevalent vegetated land surface environments across the globe (i.e. deciduous and coniferous forest, grassland, and cropland).

The photosynthesis-based stomatal conductance model with two-leaf scaling is constrained by many additional model parameters, particularly related to photosynthesis such as the maximum rate of carboxylation of Rubisco - V_{cmax}, the foliage nitrogen decay coefficient – K_n, maximum electron transport rate - J_{max}, and quantum yield – ε. This gives the model advantages in distinguishing plants with different photosynthesis mechanism (C_3 and C_4) and efficiency among PFTs (such evergreen or deciduous from boreal, temperate, or tropic regions, different crops). However, those parameter values vary among and within PFTs across literature and different models. It is important to choose the values which represent plant types for the modeling approach including scaling implemented in the full Eulerian grid model. The model performs differently even at the sites with same PFT (such as US-Ha1 and US-Moz sites with broadleaf deciduous trees) using the same photosynthesis-related parameters due to different vegetation composition. In addition, LAI and soil moisture and texture influence the performance of the both approaches.

The evaluation using observed LAI and MODIS LAI at the WRF/CMAQ 12 km grid domain shows that accurate LAI is important for matching site measurements. With the MODIS LAI input, both approaches perform worse except at the Wind River Field Station US-Wrc site where lower LAI from averaged MODIS LAI at WRF/CMAQ grid cells help reduce LH and match the observations well. Although the MODIS LAI is generally different from the observed LAI; the change of MODIS LAI over the growing season does peak with the observed LAI. Thus, MODIS LAI captures the seasonality (or phenology) of vegetation, that is consistent with the results from *Ran et al*. [2015a and 2015b]. Note that, in the full Eulerian grid model LSM

performance is improved through real-time soil moisture and temperature nudging in the WRF PX LSM [*Pleim and Xiu,* 2003; *Pleim and Gilliam,* 2009] which continually adjusts soil moisture and temperature to reduce errors in LH flux thereby reducing air temperature and humidity errors. This scheme compensates for model errors due to inaccurate parameters as well as over-simplified canopy and soil algorithms. Thus, even though the box model simulations are using whatever soil moisture measurements that are available, the overestimation of LH which is observed at most sites is likely to be corrected in WRF simulations with the PX LSM soil nudging scheme and dynamic feedbacks.

The photosynthesis-based approach is evaluated at the Harvard Forest (US-Ha1) FLUXNET site for July 2006 and the model performs well in comparison with the current PX Jarvis approach and two other CO_2 assimilation methods compared to observations. The advanced approach can simulate LH as well as the PX Jarvis approach in general for four selected FLUXNET sites (US-Moz, US-Wrc, US-IB2, and US-Ne2) though the performance varies at different sites. For the US-Moz and US-Wrc sites with tall forest canopy, the PX Jarvis approach shows some advantage during the peak noon hours. The photosynthesis-based approach shows clear improvement in modeling short vegetation (e.g. grassland and soybean), particularly for the C_4 grassland at the Fermi Prairie US-IB2 site by distinguishing C_3 and C_4 plants in modeling the CO_2 assimilation rate. Both the approaches significantly overestimate LH at the Wind River Field Station US-Wrc site with observed LAI because of the complex landscape dominated by old growth tall Douglas-fir and western hemlock. The hydraulic limitation, which is one of many factors which may contribute to the overestimation, seems to apply to western hemlock but not to Douglas-fir [*McDowell et al*., 2002; *Phillips et al*., 2002; *Pangle et al*., 2015] at this site. As the developed photosynthesis-bases model is a single layer

two-leaf model for meso-scale modeling, it shows limitation in modeling sites with complex canopy structures including different species at different heights. For the complex canopy, a multi-layer model [*Baldocchi and Meyers*, 1998; *Meyers et al*., 1998] likely performs better. The advanced model performs much better than the Jarvis approach at the Duke Forest Open Field US-Dk1 grassland site in simulating LH and ozone flux. The photosynthesis model shows the ability to simulate the diurnal shape of ozone deposition velocity which usually peaks in the early morning. The Jarvis approach is known to have difficulty in simulating the diurnal shape [*Finkelstein et al*., 2000; *Pleim et al*., 2001] and this deficiency is clearly demonstrated at the site. The simulated ozone flux from the advanced approach matches the observations much better than that from the Jarvis approach which overestimates ozone flux by around 50%.

The current PX WRF/CMAQ uses 20-class NLCD land cover types for the U.S. and 20-class MODIS IGBP classes for areas outside the U.S. There is an ongoing effort at EPA to develop new land cover classes with detailed PFTs for vegetation from boreal, temperate, tropical, and dryland regions and with major crop categories including irrigation information. The new land cover types with more specific PFTs are more suitable for the photosynthesis-based PX LSM than the current land cover types used in the system. With realistic vegetation and albedo from MODIS products being ingested into WRF/CMAQ [*Ran et al*., 2015a and 2015b], the system has more accurate vegetation and surface representation which helps improve not only spatial and temporal characteristics of vegetation and land surface but also improves the meteorology performance. The next step is to implement the evaluated photosynthesis-based stomatal conductance model into WRF/CMAQ PX LSM with MODIS input and new land cover types. Thus, the system with improved land surface representation and vegetation processes can be used in research and applications in coupling air quality, climate, and vegetation productivity

directly with CO_2 concentration which changes temporally and spatially. In addition, the effects of air pollutants such as O_3 on ecosystem productivity can also be easily implemented in this advanced approach [*Sitch et al.*, 2007; *Lombardozzi et al.*, 2012] for EPA's secondary standard assessments under the Clean Air Act to protect the environment.

REFERENCES

Allison, V. J., R. M. Miller, J. D. Jastrow, R. Matamala, and D. R. Zak (2005), Changes in soil microbial community structure in a tallgrass prairie chronosequence, Soil Sci. Soc. Am. J., 69 (5), 1412–1421.

Almand-Hunter, B. B., Walker, J. T., Masson, N. P., Hafford, L., Hannigan, M. P. (2015), Development and validation of inexpensive, automated, dynamic flux chambers, Atmospheric Measurement Techniques, 8, 267-280.

Appel, K. W., K. M. Foley, J. O. Bash, P. W. Pinder, R. L. Dennis, D. J. Allen, and K. A. Pickering (2011), Multi-resolution assessment of the Community Multiscale Air Quality (CMAQ) model v4.7 wet deposition estimates for 2002-2006, Geosci. Model Dev, 4, 357–371.

Baker, I. T., A. S. Denning, N. Hanan, L. Prihodko, P. L. Vidale, K. Davis, and P. Bakwin (2010), North American gross primary productivity: regional characterization and interannual variability, Tellus, 62B, 533–549.

Baldocchi, D. (2008), TURNER REVIEW No. 15, 'Breathing' of the terrestrial biosphere: lessons learned from a global network of carbon dioxide flux measurement systems, Australian Journal of Botany, 56:(1),1-26.

Baldocchi, D. D. and T. Meyers (1998), On using eco-physiological, micrometeorological and biogeochemical theory to evaluate carbon dioxide, water vapor and trace gas fluxes over vegetation: a perspective, Agricultural and Forest Meteorology, 90(1-2), 1-25.

Ball, M. C., I. E. Woodrow, and J. A. Berry (1987), A model predicting stomatal conductance and its contribution to the control of photosynthesis under different environmental conditions, In Progress in Photosynthesis Research (ed J. Biggins), Martinus Nijhoff Publishers, Dordrecht, Netherlands 221–224.

Bonan, G. B. (2008), Ecological climatology: concepts and applications, Cambridge University Press, New York.

Bonan, G. B., P. J. Lawrence, K. W. Oleson, S. Levis, M. Jung, M. Reichstein, D. M. Lawrence, and S. C. Swenson (2011), Improving canopy processes in the Community Land Model version 4 (CLM4) using global flux fields empirically inferred from FLUXNET data, Journal of Geophysical Research: Biogeosciences (2005–2012), 116(G2).

Budyko, M., 1974. Climate and life, Academic, New York.

Byun, D. W. and K. L. Schere (2006), Review of the governing equations, computational algorithms, and other components of the Models-3 Community Multiscale Air Quality (CMAQ) modeling system, Appl. Mech. Rev., 59, 51-77.

Campbell, G. S. (1986), Extinction coefficients for radiation in plant canopies calculated using an ellipsoidal inclination angle distribution, Agricultural and forest meteorology, 36(4), 317-321.

Campbell, G. S., and J. M. Norman (1998), An introduction to environmental biophysics. Springer Science & Business Media.

Chen, F., and J. Dudhia (2001), Coupling an advanced land-surface/hydrology model with the Penn State/NCAR MM5 modeling system. Part I: Model implementation and sensitivity, Mon. Wea. Rev., 129, 569-585.

Chen, J. M., A. Govind, O. Sonnentag, Y. Zhang, A. Barr, and B. Amiro (2006), Leaf area index measurements at Fluxnet-Canada forest sites, Agricultural and Forest Meteorology, 140(1), 257-268.

Clark, D. B., L. M. Mercado, S. Sitch, C. D. Jones, N. Gedney, M. Pryor, G. G. Rooney, R. L. H. Essery, E. Blyth1, O. Boucher, R. J. Harding, C. Huntingford, and P. M. Cox (2011), The joint UK land environment simulator (JULES), model description–Part 2: carbon fluxes and vegetation dynamics, Geoscientific Model Development, 4(3), 701-722.

Cohen, W. B., T.K. Maiersperger, D.P. Turner, W.D. Ritts, D. Pflugmacher, R.E. Kennedy, Kirschbaum, S.W. Running, N. Costa, and S.T. Gower, 2006. MODIS land cover and LAI collection 4 product quality across nine sites in the western hemisphere. IEEE Transactions on Geoscience and Remote Sensing 44:1843−1857.

Collatz, G. J., J. T. Ball, C. Grivet, and J. A. Berry (1991), Physiological and environmental regulation of stomatal conductance, photosynthesis and transpiration: a model that includes a laminar boundary layer, Agricultural and Forest Meteorology, 54(2), 107-136.

Collatz, G. J., M. Ribas-Carbo, and J. A. Berry (1992), Coupled photosynthesis-stomatal conductance model for leaves of C_4 plants, Aust. J. Plant Physiol., 19, 519–538.

Compton, J. E., J. A. Harrison, R. L. Dennis, T. L. Greaver, B. H. Hill, S. J. Jordan, H. Walker, and H. V. Campbell (2011), Ecosystem services altered by human changes in the nitrogen cycle: a new perspective for US decision making, Ecology Letters, 14, 804–815.

Cox, P. M., C. Huntingford, and R. J. Harding (1998), A canopy conductance and photosynthesis model for use in a GCM land surface scheme, Journal of Hydrology 212 (1998), 79-94.

Dai, Y., R. E. Dickinson, and Y. P. Wang (2004), A two-big-leaf model for canopy temperature, photosynthesis, and stomatal conductance, J. Clim., 17, 2281-2299.

de Pury, D. G. G. and G. D. Farquhar (1997), Simple scaling of photosynthesis from leaves to canopies without the errors of big-leaf models, Plant Cell Environ., 20, 537–557.

Eder, B., D. Kang, R. Mathur, J. Pleim, S. Yu, T. Otte, and G. Pouliot (2009), A performance evaluation of the National Air Quality Forecast Capability for the summer of 2007, Atmospheric Environment, 43(14), 2312-2320.

Evers, J. B., J. Vos, X. Yin, P. Romero, P. E. L. Van Der Putten, and P. C. Struik (2010), Simulation of wheat growth and development based on organ-level photosynthesis and assimilate allocation, Journal of Experimental Botany, 61(8), 2203-2216.

Farquhar, G. D., S. von Caemmerer, and J. A. Berry (1980), A biochemical model of photosynthetic CO2 assimilation in leaves of C_3 species, Planta, 149, 78–90.

Finkelstein, P. L., T. G. Ellestad, J. F. Clarke, T. P. Meyers, D. B. Schwede, E. O. Hebert, and J. A. Neal (2000), Ozone and sulfur dioxide dry deposition to forests: Observations and model evaluation, Journal of Geophysical Research: Atmospheres (1984–2012), 105(D12), 15365-15377.

Finnigan, J. J., R. Clement, Y. Malhi, R. Leuning, and H.A. Cleugh (2003), A reevaluation of long-term flux measurement techniques part I: averaging and coordinate rotation, Boundary-Layer Meteorology, 107, 1–48.

Foley, K. M., S. J. Roselle, K. W. Appel, P. V. Bhave, J. E. Pleim, T. L. Otte, R. Mathur et al. (2010), Incremental testing of the Community Multiscale Air Quality (CMAQ) modeling system version 4.7, Geoscientific Model Development, 3(1), 205-226.

Foken, T. (2006), 50 years of the Monin-Obukhov similarity theory, Bound.-Layer Meteorol. 119, 431–447.

Foken, T. (2008), The energy balance closure problem: An overview, Ecol. Appl., 18(6), 1351–1367.

Gao, F., J. Morisette, R. Wolfe, G. Ederer, J. Pedelty, E. Masuoka, R. Myneni, B. Tan, and J. Nightingale (2008), An Algorithm to Produce Temporally and Spatially Continuous MODIS-LAI Time Series, IEEE Geoscience and Remote Sensing Letters, 5(1), 60-64.

Goudriaan, J. (1977), Crop micrometeorology: a simulation study, Pudoc, Center for Agricultural Publishing and Documentation.

Gu, L., T. Meyers, S. G. Pallardy, P. J. Hanson, B. Yang, M. Heuer, K. P. Hosman, J. S. Riggs, D. Sluss, and S. D. Wullschleger (2006), Direct and indirect effects of atmospheric conditions and soil moisture on surface energy partitioning revealed by a prolonged drought at a temperate forest site, Journal of Geophysical Research: Atmospheres (1984–2012), 111, D16.

Hogrefe, C., G. Pouliot, D. Wong, A. Torian, S. Roselle, J. Pleim, and R. Mathur (2014), Annual application and evaluation of the online coupled WRF–CMAQ system over North America under AQMEII phase 2, Atmospheric Environment.

Jarvis P. G. (1976), The interpretation of the variations in leaf water potential and stomatal conductance found in canopies in the field, Philosophical Transactions of the Royal Society of London, Series B, 273, 593–610.

Jarvis, P.G., and K.G. McNaughton (1986), Stomatal control of transpiration: Scaling up from lead to region, Adv. in Ecol. Res. 15:1-49.

Jarvis, P.G. (1995), Scaling Processes and Problems. Plant Cell and Environment, 18(10):1079-1089.

Katul, G. G., S. Manzoni, S. Palmroth, R. Oren (2010), A stomatal optimization theory to describe the effects of atmospheric CO2 on leaf photosynthesis and transpiration, Ann. Bot. 105(3):431–442.

Kelly, J. T., K. R. Baker, J. B. Nowak, J. G. Murphy, M. Z. Markovic, T. C. VandenBoer, R. A. Ellis, …and C. Misenis (2014), Fine-scale simulation of ammonium and nitrate over the South Coast Air Basin and San Joaquin Valley of California during CalNex-2010, Journal of Geophysical Research: Atmospheres, 119(6), 3600-3614.

Kobayashi, H., D. D. Baldocchi, Y. Ryu, Q. Chen, S. Ma, J. L. Osuna, and S. L. Ustin (2012), Modeling energy and carbon fluxes in a heterogeneous oak woodland: A three-dimensional approach, Agricultural and Forest Meteorology, 152 (2012), 83-100.

Kowalczyk, E. A., L. Stevens, R. M. Law, M. Dix, Y. P. Wang, I. N. Harman, ... and T. Ziehn (2013), The land surface model component of ACCESS: description and impact on the simulated surface climatology, Australian Meteorological and Oceanographic Journal, 63(1), 65-82.

Leuning, R., F. M. Kelliher, D. G. G. Depury, and E. D. Schulze (1995), Leaf Nitrogen, Photosynthesis, Conductance and Transpiration - Scaling from Leaves to Canopies, Plant Cell and Environment, 18(10), 1183-1200.

Lombardozzi, D., S. Levis, G. Bonan, and J. P. Sparks (2012), Predicting photosynthesis and transpiration responses to ozone: decoupling modeled photosynthesis and stomatal conductance, Biogeosciences, 9, 3113-3130, doi:10.5194/bg-9-3113-2012.

Mauder, M., C. Liebethal, M. Go¨ ckede, J.-P. Leps, F. Beyrich, and T. Foken (2006), Processing and quality control of flux data during LITFASS-2003, Boundary-Layer eteorology, 121, 67–88.

McDowell, N. G., N. Phillips, C. Lunch, B. J. Bond, and M. G. Ryan (2002), An investigation of hydraulic limitation and compensation in large, old Douglas-fir trees, Tree Physiology 22 (11), 763-774.

Medlyn, B. E., E. Dreyer, D. Ellsworth, M. Forstreuter, P. C. Harley, M. U. F. Kirschbaum, X. Le Roux, P. Montpied, J. Strassemeyer, A. Walcroft, K. Wang, and D. Loustau (2002), Temperature response of parameters of a biochemically based model of photosynthesis. II. A review of experimental data. Plant, Cell & Environment, 25(9), 1167-1179.

Medlyn, B.E., A. P. Robinson, R. Clement, and R. E. McMurtrie (2005), On the validation of models of forest CO2 exchange using eddy covariance data: some perils and pitfalls, Tree Physiology, 25(7), 839-857.

Meyers, T. P., P. L. Finkelstein, J. Clarke, T. G. Ellestad, and P. F. Sims (1998), A multilayer model for inferring dry deposition using standard meteorological measurements, J. Geophys. Res.,103, 22645–22661.

Monin, A. S. and A. Obukhov (1954), Basic laws of turbulent mixing in the surface layer of the atmosphere, Contrib. Geophys. Inst. Acad. Sci., USSR, 151, 163-187.

Monteith, J. L. (1981), Evaporation and Surface-Temperature, Quarterly Journal of the Royal

Meteorological Society, 107 (451), 1-27.

Moorcroft, P. R. (2006), How close are we to a predictive science of the biosphere? Trends in Ecology & Evolution, 21(7), 400-407.

Myneni, R., Y. Knyazikhin, and N. Shabanov (2011), Leaf Area Index and Fraction of Absorbed PAR Products from Terra and Aqua MODIS Sensors: Analysis, Validation, and Refinement. Land Remote Sensing and Global Environmental Change, Remote Sensing and Digital Image Processing, 11, 603-633.

Noilhan, J. and S. Planton (1989), A simple parameterization of land surface processes for meteorological models, Mon. Wea. Rev., 117, 536-549.

Noilhan, J. and J. F. Mahfouf (1996), The ISBA land surface parameterisation scheme, Global and Planetary Change, 13(1), 145-159.

Oleson, K. W., D. M. Lawrence, G. B. Bonan, B. Drewniak, M. Huang, C. D. Koven, S. Levis, F. Li, W. J. Riley, Z. M. Subin, S. C. Swenson, P. E. Thornton, A. Bozbiyik, R. Fisher, E. Kluzek, J. F. Lamarque, P. J. Lawrence, L. R. Leung, W. Lipscomb, S. Muszala, D. M. Ricciuto, W. Sacks, Y. Sun, J. Tang, and Z. L. Yang (2013), Technical Description of version 4.5 of the Community Land Model (CLM). Ncar Technical Note NCAR/TN-503+STR, National Center for Atmospheric Research, Boulder, CO, 422 pp, DOI: 10.5065/D6RR1W7M.

Pangle, R. E., K. Kavanagh, and R. Duursma (2015), Decline in canopy gas exchange with increasing tree height, atmospheric evaporative demand, and seasonal drought in co-occurring inland Pacific Northwest conifer species, Canadian Journal of Forest Research ja.

Paw U, K. T., M. Falk, T. H. Suchanek, S. L. Ustin, … and A. A. Matista (2004), Carbon dioxide exchange between an old growth forest and the atmosphere. Ecosystems, 7, 513–524.

Phillips, N., B. J. Bond, N. G. McDowell, and M. G. Ryan (2002), Canopy and hydraulic conductance in young, mature and old Douglas-fir trees, Tree Physiology, 22(2-3), 205-211.

Pisek, J., O. Sonnentag, A. D. Richardson, and M. Mõttus (2013), Is the spherical leaf inclination angle distribution a valid assumption for temperate and boreal broadleaf tree species?, Agricultural and Forest Meteorology, 169, 186-194.

Pleim, J. E. (2007a), A combined local and nonlocal closure model for the atmospheric boundary layer. Part I: model description and testing, J. Appl. Meteor. Clim., 46, 1383–1395.

Pleim, J. E. (2007b), A combined local and nonlocal closure model for the atmospheric boundary layer. Part II: application and evaluation in a mesoscale meteorological model, J. Appl. Meteor. Clim., 46, 1396–1409.

Pleim J. E. and R. Gilliam (2009), An indirect data assimilation scheme for deep soil temperature in the Pleim-Xiu land surface model, J. Appl. Meteor. Clim., 48, 1362-1376.

Pleim, J. E. and L. Ran (2011), Surface Flux Modeling for Air Quality Applications, Atmosphere, 2(3), 271-302.

Pleim, J. E. and A. Xiu (1995), Development and testing of a surface flux and planetary boundary layer model for application in mesoscale models, J. Appl. Meteorol., 34, 16–32.

Pleim, J. E. and A. Xiu (2003), Development of a Land Surface Model. Part II: Data Assimilation, J. Appl. Meteor., 42, 1811–1822.

Pleim, J. E., A. Xiu, P. L. Finkelstein, and T. L. Otte (2001), A coupled land-surface and dry deposition model and comparison to field measurements of surface heat, moisture, and ozone fluxes. Water, Air and Soil Pollution: Focus, 1(5-6), 243-252.

Pleim, J., A. A. R. Gilliam, W. Appel, and L. Ran, 2015: Recent Advances in Modeling of the Atmospheric Boundary Layer and Land Surface in the Coupled WRF-CMAQ Model, 34th International Technical Meeting on Air Pollution Modelling and its Application, 4-8 May, 2015, Montpellier, France.

Qu, W.Q., and A. Henderson-Sellers (1998), Comparing the scatter in PILPS off-line experiments with that in AMIP I coupled experiments, Global and Planetary Change, 19, 209-223.

Ran, L., J. Pleim, A.R. Gilliam, W. Benjey, A. Hanna (2012), Application and Evaluation of 2006 NLCD and MODIS in the WRF/CMAQ System Part I: Meteorology Simulations, the 2012 CMAS Conference, Chapel Hill, NC Oct. 15 – 17, 2012 (oral presentation).

Ran, L., J. Pleim, A.R. Gilliam (2010), Impact of High Resolution Land-Use Data in Meteorology and Air Quality Modeling Systems, In Air Pollution Modeling and Its Application XX. Springer, the Netherlands 3-7.

Ran, L., R. Gilliam, F. S. Binkowski, A. Xiu, J. Pleim, and L. Band (2015a), Sensitivity of the Weather Research and Forecast/Community Multiscale Air Quality modeling system to MODIS LAI, FPAR, and albedo, J. Geophys. Res. Atmos., 120, 8491–8511, doi:10.1002/2015JD023424.

Ran, L., J. Pleim, R. Gilliam, F. S. Binkowski, C. Hogrefe, and L. Band (2015b), Improved Meteorology from an Updated WRF/CMAQ Modeling System with MODIS Vegetation and Albedo, submitted to J. Geophys. Res. Atmosphere.

Ryan, M. G., and B. J. Yoder (1997), Hydraulic limits to tree height and tree growth, BioScience, 47, 235–242, doi:10.2307/1313077.

Samuelsson, P., B. Bringfelt, L. P. Graham (2003), The role of aerodynamic roughness for runoff and snow evaporation in land-surface schemes - comparison of uncoupled and coupled simulations, Global and Planetary Change, 38, 93-99.

Sellers, P. J., D. A. Randall, G. J. Collatz, J. A. Berry, C. B. Field, D. A. Dazlich, C. Zhang, G. D. Collelo, and L. Bounoua (1996), A revised land surface parameterization (SiB2) for atmospheric GCMs. Part I: Model formulation, J. Clim., 9, 676–705.

Shaw, D. C., J. F. Franklin, K. Bible, J. Klopatek, E. Freeman, S. Greene, and G. G. Parker (2004), Ecological setting of the Wind River old-growth forest, Ecosystems, 7(5), 427-439.

Sitch, S., P. M. Cox, W. J. Collins, and C. Huntingford (2007), Indirect radiative forcing of climate change through ozone effects on the land-carbon sink, Nature, 448, 791–794.

Skamarock, W. C., J. B. Klemp, J. Dudhia, D. O. Gill, D. M. Barker, W. Wang, and J. G. Powers (2008), A description of the advanced research WRF version 3. NCAR Tech Note, NCAR/TN 475+STR: 125 pp.

Song, C., G. Katul, R. Oren, L. E. Band, C. L. Tague, P. C. Stoy, and H. R. McCarthy (2009), Energy, water, and carbon fluxes in a loblolly pine stand: Results from uniform and gappy canopy models with comparisons to eddy flux data, Journal of Geophysical Research: Biogeosciences (2005–2012) 114(G4).

Thomas, S. C., and W. E. Winner (2000), Leaf area index of an old-growth Douglas-fir forest estimated from direct structural measurements in the canopy, Canadian Journal of Forest Research, 30(12), 1922-1930.

Urbanski, S., C. Barford, S. Wofsy, C. Kucharik, E. Pyle, J. Budney, K. McKain, D. Fitzjarrald, M. Czikowsky, and J. W. Munger (2007), Factors controlling CO2 exchange on timescales from hourly to decadal at Harvard Forest, J. Geophys. Res., 112(G2), G02020, doi:10.1029/2006JG000293.

Verma, S. B., A. Dobermann, K. G. Cassman, D. T. Walters, J. M. Knops, T. J. Arkebauer, ... and E. A. Walter-Shea (2005). Annual carbon dioxide exchange in irrigated and rainfed maize-based agroecosystems, Agricultural and Forest Meteorology, 131(1), 77-96.

Wang, K., and R .E. Dickinson (2012), A review of global terrestrial evapotranspiration: Observation, modeling, climatology, and climatic variability, Reviews of Geophysics 50(2).

Wang, S. X., M. Zhao, J. Xing, Y. Wu, Y. Zhou, Y. Lei, K. B. He, L. X. Fu, and J. M. Hao (2010), Quantifying the air pollutants emission reduction during the 2008 Olympic Games in Beijing, Environ. Sci. Technol., 44, 2490-2496.

Wang, Y. P., and R. Leuning (1998), A two - leaf model for canopy conductance, photosynthesis and partitioning of available energy. I: Model description and comparison with a multi-layered model, Agric., For. Meteorol., 91, 89–111, doi:10.1016/S0168-1923(98)00061-6.

Wang, S. X., M. Zhao, J. Xing, Y. Wu, Y. Zhou, Y. Lei, K. B. He, L. X. Fu, and J. M. Hao (2010), Quantifying the air pollutants emission reduction during the 2008 Olympic Games in Beijing, Environ. Sci. Technol., 44, 2490-2496.

Wharton, S., M. Schroeder, K. Bible, and M. Falk (2009), Stand-level gas-exchange responses to seasonal drought in very young versus old Douglas-fir forests of the Pacific Northwest, USA, Tree physiology, 29(8), 959-974.

Xing, J., R. Mathur, J. Pleim, C. Hogrefe, C.-M. Gan, D. C. Wong, C. Wei, R. Gilliam, and G. Pouliot (2015), Observations and modeling of air quality trends over 1990–2010 across the Northern Hemisphere: China, the United States and Europe, Atmos. Chem. Phys., 15, 2723-2747, doi:10.5194/acp-15-2723-2015.

Xiu, A. and J. E. Pleim (2001), Development of a Land Surface Model. Part I: Application in a Mesoscale Meteorological Model, J. Appl. Meteor., 40, 192-209.

Yang, W., N. V. Shabanov, D. Huang, W. Wang, R. E. Dickinson, R. R. Nemani, Y. Knyazikhin, and R. B. Myneni (2006), Analysis of leaf area index products from combination of MODIS Terra and Aqua data, Remote Sensing of Environment, 104(3), 297-312.

Yu, S., B. Eder, R. Dennis, S. H. Chu, and S. E. Schwartz (2006), New unbiased symmetric metrics for evaluation of air quality models, Atmospheric Science Letters, 7(1), 26-34.Zhang, L., M.D. Moran, J.R. Brook (2001), A comparison of models to estimate in-canopy photosynthetically active radiation and their influence on canopy stomatal resistance, Atmos. Environ., 35, 4463–4470.

CHAPTER 5: SYNTHESIS

5.1 Summary

Vegetation transpiration is a crucial component in the surface energy budget and the water and carbon cycles. In air quality modeling, vegetation is also a source and sink of many atmospheric pollutants and precursor chemicals such as O_3, oxidized and reduced nitrogen, and volatile organic compounds (VOCs). The commonly used PX LSM for the combined meteorology and air quality modeling system, WRF/CMAQ, relies on lookup table prescribed parameters to describe albedo and vegetation with plant phenological dynamics modeled using simple time and temperature dependent functions. A simple empirical function Jarvis approach is used to estimate canopy stomatal conductance in modeling vegetation transpiration and pollutant deposition. This research aims to (1) improve the land surface representation in WRF/CMAQ using satellite vegetation and albedo and to (2) advance the vegetation processes with a biochemically-based photosynthesis-stomatal conductance approach. The two components of this research are synergistic because accurate vegetation representation is essential for estimating canopy CO_2 assimilation and stomatal conductance using the biochemically-based photosynthesis approach.

The first step of this research is to evaluate model performance using the prescribed vegetation and albedo in the current system and assess sensitivities to replacement with satellite vegetation and albedo input. The PX LSM intentionally exaggerates the vegetation coverage, particularly in the western dryland areas, in order to optimize its soil moisture nudging scheme for reducing errors in 2 m *T* and *Q* for meteorology simulations. Using MODIS vegetation and

albedo products containing much more accurate spatial and temporal surface representation is clearly a significant advance adding more realism to the system. However, evaluations comparing model simulations including the MODIS inputs and the base model demonstrate mixed results. MODIS inputs have the largest effects in the western drylands because of substantially less vegetation coverage from MODIS LAI and FPAR, where the current PX LSM look-up table yields unrealistically high vegetation coverage. The more accurate MODIS vegetation coverage results in reduced latent heat flux, 2 m *Q*, and ozone dry deposition velocity, and increased surface skin *T*, 2 m *T*, PBLH, and surface ozone concentrations. Sensitivity evaluation of the WRF and CMAQ simulations with MODIS input generally indicates reduced error and bias in 2 m *Q* but greater error and bias in 2 m *T* and ozone with reduced bias in 2 m *T* and ozone concentrations at the high end of the observed range. While MODIS albedo input results in higher albedo in western barrens and deserts causing lower surface skin *T*, 2 m *T*, and PBLH and lower albedo for coniferous forests in the southeast, boreal regions and high mountains in the west resulting in higher skin *T*, 2 m *T*, and PBLH, overall domain-wide evaluation statistics show that MODIS albedo has much less impact on the system in comparison with MODIS vegetation. Thus, this research mainly focuses on sensitivities of model performance due to vegetation differences. An important conclusion from the mixed results due to the use of more realistic satellite surface representation is that improvements should be made in the model physics, particularly the LSM which likely uses the exaggerated base vegetation coverage and LAI in the western drylands to compensate for an inherent model tendency toward hot biases in low vegetation areas.

The second step of this research is to update the WRF/CMAQ modeling system with MODIS input by including recent model improvements in vegetation, soil, and PBL processes.

The updated system is evaluated against the simulations from the previous study over a short period in the summer (August-September 2006). The system is further evaluated for the advantages in using satellite input to describe seasonal changes through yearlong meteorology simulations and selected three-month (April, August, and October) air quality simulations. The updated processes in WRF/CMAQ clearly improve 2 m *T* and *Q*, 10 m WS, and near surface ozone concentration estimations for both MODIS and base simulations over the short summer period. The system seems to respond well to the updated soil resistance which uses a soil water diffusion approach and has a more gradual change when soil moisture is approaching field capacity, with reduction in domain-wide warm biases, particularly in sparsely vegetated western regions. The ozone concentration estimations from both the MODIS and base cases show significant improvements due to the improved meteorology.

Evaluations of the yearlong meteorology simulations and selected three-month air quality simulations using the updated system focus on 2 m *Q* and surface ozone with the change of vegetation. MODIS input improves the system through not only better spatial and temporal representation but also different LAI magnitudes from diverse natural and cultivated vegetation types which the LSM land cover look-up tables cannot adequately distinguish. The green-up from the PX LSM vegetation is too fast for 2006 but the green down is similar to the MODIS vegetation. Consistently higher LAI in the Pacific temperate rain forest and lower LAI in Canadian boreal forests and southeast coniferous forests in MODIS LAI are distinct throughout the entire year. The MODIS vegetation results in overall bias reduction for 2 m *Q* during the growing seasons from April to September with the differences in simulated latent heat and 2 m *Q* between the MODIS and base cases closely following the differences in LAI. Areas with improved 2 m *Q* from MODIS input move from the southeast following the green up in April

towards the west and north following the LAI changes in the natural and cultivated lands to the central Plains through August. Despite the overall improvement of meteorology simulations, many sites also show increased bias and error, particularly dry bias in the southwest from August through September with MODIS input. The consistent dry bias condition in this region (which is not unique to this system) during the hot summer is likely to be associated with uncertainties in other parts of the system (e.g. influences of the Gulf circulation and the North American monsoon). From October to March with inactive vegetation, MODIS input does not have big impact on the system as large scale meteorology is often dominant in the cold seasons. The updated system with MODIS input increases the high bias of ozone concentrations but by no more than 3 ppb on average for April, August, and October. The high ozone bias, concentrated in the areas where MODIS input has much lower LAI in comparison with the base model for all selected months, suggests that improvements may be needed in the CMAQ dry deposition model for low LAI areas where deposition to the bare soil is important.

With the improved meteorology from realistic spatial and temporal MODIS vegetation using the improved WRF/CMAQ, the final step in this research is to advance the vegetation processes by incorporating a coupled photosynthesis-stomatal conductance approach into the PX LSM. This research is conducted by developing a photosynthesis-based approach in a diagnostic box model, which includes the current PX Jarvis approach, for modeling ET and ozone dry deposition velocity. The purpose for this final step research is not to develop a site-specific model which matches measurements, but rather to develop applicable algorithms in the WRF/CMAQ modeling system for grid cell average surface flux estimations of heat, moisture, and trace chemical species. The photosynthesis-based approach is developed based on the FLUXNET measurements at the Harvard Forest US-Ha1 site following the photosynthesis

approaches applied in climate earth systems and ecosystem productivity models. The model is evaluated using the FLUXNET measurements at four selected sites (US-Moz, US-Wrc, US-IB2, and US-Ne2) with different vegetation types and landscape characteristics and using the ozone measurements at the Duke Forest Open Field US-Dk1 operated by EPA.

The performance of the photosynthesis-based approach and current Jarvis approach varies at different sites due to the influence of many factors including parametrizations based on broad PFTs, site-related input data, and measurement errors in addition to the underlying physical process formulations. For mesoscale modeling purposes, site vegetation parameters are specified based on parameter values defined in climate earth system models according to site PFT even though photosynthesis parameters (e.g. *Vcmax, Jmax*) can vary within a PFT for different sites. While the two approaches perform well in LH estimation at the US-Ha1 site for the development, the Jarvis approach shows some advantage in estimating LH at the two forest evaluation sites (US-Moz and US-Wrc) with some overestimation of LH around peak noon hours from the photosynthesis-based approach. Both approaches do not perform well at the Wind River Field Station US-Wrc site because the single-layer canopy does not well represent the complex old growth canopy which includes very tall 500 year old Douglas fir and shorter western Hemlock with overall LAI around 9. The photosynthesis-based approach demonstrates clear advantage in LH estimation for short vegetation (e.g. grassland and soybean), particularly for the C_4 grassland at the Fermi Prairie US-IB2 site possibly because it distinguishes C_3 and C_4 plants in modeling the CO_2 assimilation rate.

The MODIS LAI is generally lower than the observed LAI except at the US-Moz site, but the peak of MODIS LAI over the growing season follows the seasonality of the observed LAI. With MODIS LAI input, both approaches perform worse at all sites except at the Wind River

Field Station US-Wrc sites. The photosynthesis-based approach performs much better than the Jarvis approach at the Duke Forest Open Field US-Dk1 grassland site in LH, ozone deposition velocity, and ozone flux estimations. In particular, the photosynthesis-based approach demonstrates the ability to simulate the peak of diurnal ozone deposition velocity which is often in the early morning. Using the vegetation processes applied in climate earth systems and ecosystem models and with the performance demonstrated in evaluation over varieties of vegetation and landscape types at the selected sites, the developed photosynthesis-based model in PX LSM is applicable for large scale WRF/CMAQ modeling domains which have vegetation coverage ranging from deciduous and coniferous forests to grass and crop lands across the world.

5.2 Future Plans

The performance of the final box model comparisons cannot completely represent the performance in full scale model simulations of grid cell average surface fluxes of heat, moisture, and trace chemical species with dynamic feedback. The future work is to implement the evaluated photosynthesis-based stomatal conductance model into WRF/CMAQ PX LSM with MODIS input. Currently, the PX LSM Jarvis approach in WRF/CMAQ models stomatal conductance for grid cell averaged vegetation characteristics in each cell. For the photosynthesis-based approach, the simulation has to be conducted for each PFT type within a grid cell. Since the PX LSM already uses fractional vegetation input, the change of vegetation modeling from the average approach to the mosaic of PFT types should be feasible. Yearlong simulations over the continental U.S. should be conducted using the implemented system with the advanced vegetation processes and MODIS input for full model evaluation at different grid resolutions (e.g. 12-km, 4-km, and 1-km). Domain-wide modeling results can be compared with meteorological and air quality measurements as well as results from this research. Changes in

simulated surface fluxes from the advanced LSM should propagate through modeled LH and PBL height to affect clouds, precipitation, and winds. Changes to these meteorology fields will consequently affect chemical concentrations as well. The AQ simulations will also be directly affected by changes in canopy conductance for dry deposition (e.g. O_3) as demonstrated in the diagnostic box model simulations.

In addition, more research can be conducted from the simulation results with MODIS albedo input from this research to investigate how albedo affects meteorology and air quality in shorter time periods (days to weeks). MODIS albedo not only provides better spatial variations to the system but also realistic diurnal and seasonable changes in comparison with the current PX LSM table prescribed albedo values. Furthermore, the yearlong WRF simulations and selected month CMAQ simulations can be further evaluated using site measurements with vertical information along with PBL height observations. This research demonstrates LAI is an important parameter in LH and deposition simulation. As uncertainties exist in MODIS LAI and FPAR, processed MODIS LAI and FPAR need to have further quality assurance in order for the data to be used in operational WRF/CMAQ simulations for the scientific and regulatory communities. Finally, the impacts of air pollutants such as O_3 on CO_2 assimilation and stomatal conductance can be implemented in the photosynthesis-based model to assist EPA's secondary standard assessments under the Clean Air Act for protecting the environment.

5.3 Significance

This research results in reduced uncertainty in the meteorology and air quality modeling for air pollution studies. Replacing the current empirical Jarvis-type stomatal conductance scheme with the biochemically-based photosynthesis-conductance scheme will improve the model's dynamic responses to environmental conditions such as temperature and CO_2

concentration, which will enhance performance over extended simulations in changing climate. Furthermore, remotely-sensed dynamic vegetation data will result in more faithful representation of seasonal changes in natural and cultivated vegetation and changes in vegetation due to disturbances such as severe drought, fire damage, pest infestation, construction activities, and storm damage. Integrated modeling systems across multiple media are being developed that involve meteorology and AQ modeling components. For example, WRF and CMAQ are being linked with ecosystem, agricultural, and hydrology models so that impacts of atmospheric pollutants via wet and dry deposition can be consistently integrated with cropland, watershed, river, and estuary models for comprehensive assessments of ecosystem pollution and impairment of ecosystem services. Clearly, improved surface fluxes, including dry deposition, will be particularly beneficial for modeling atmospheric inputs to watershed and agricultural models. Similarly, the WRF/CMAQ system is being linked to human exposure models for human health impact assessment. Improved spatial and temporal distributions of modeled air pollutant concentrations particularly O_3 that should result from this research will reduce the uncertainties involved in quantifying exposure. The WRF/CMAQ system is an important decision support tool that is used to mitigate harmful effects of air pollution on human health and ecosystems. Improving the tool through development of more advanced science processes and incorporation of satellite observations will have direct benefit to society.